

# The Driving of Mean Flows by Convection

Laura Kathryn Currie

Submitted in accordance with the requirements for the degree of Doctor of Philosophy

The University of Leeds  
Department of Applied Mathematics

June 2014



The candidate confirms that the work submitted is her own and that appropriate credit has been given within the thesis where reference has been made to the work of others.

This copy has been supplied on the understanding that it is copyright material and that no quotation from the thesis may be published without proper acknowledgement.

©2014 The University of Leeds and Laura Kathryn Currie.

The right of Laura Kathryn Currie to be identified as Author of this work has been asserted by her in accordance with the Copyright, Designs and Patents Act 1988.



# Acknowledgements

First and foremost, I would like to thank my supervisor, Prof. Steve Tobias, primarily for his enthusiasm, advice and patience but also for the countless conversations about football. In addition, I would like to acknowledge my examiners Prof. Mike Proctor and Prof. Chris Jones for helpful comments regarding the presentation of this thesis.

I would also like to extend my gratitude to all the members of the Geophysical and Astrophysical Fluid Dynamics research group at the University of Leeds. Specifically, I would like to mention Ben, Julian, Nikolai, Rob and Tina for their support and friendship during the last four years.

More personally, I would like to thank my parents and grandparents, as without their support and encouragement I would not have been able to get to this stage. Further thanks go to my brothers and to Barnsley Ladies Football Club for providing a fun life outside of academia. Finally, I would like to thank my best friend and husband, James, for being the best.

This research has been funded by a PhD studentship from STFC.



# Abstract

The interaction of convection with rotation and magnetic fields plays an important role in determining the dynamics of many geophysical and astrophysical phenomena. In particular, this interaction is thought to be associated with the generation of large-scale mean flows as observed, for example, in the atmospheres of the giant planets and in the interior of the Sun. This study examines the interaction of convection with rotation and magnetic fields in a simplified, two-dimensional, plane layer model. We consider the case where the fluid rotates about an axis that is oblique to gravity, and is in the presence of a horizontal magnetic field. Also considered, is the case where a horizontal temperature gradient maintains a thermal wind. The fluid is taken to be either incompressible, using the Boussinesq approximation, or compressible, using the anelastic approximation. An examination of the linear behaviour is undertaken to investigate the conditions required for the onset of convection, in a number of different regimes. The existence of an unexpected symmetry is proved in the anelastic case. A pseudospectral numerical code, developed in order to solve the nonlinear equations, is then described. The code is employed to investigate the dynamics in the nonlinear regime and determine the underlying physical interactions for mean flow maintenance. It is shown that whether convection acts to decrease or increase the thermal wind shear, depends on the Prandtl number and the angle of tilt of the rotation vector. Furthermore, the asymmetries introduced when a background stratification is present, manifest themselves in the time-dependent nature of the mean flows driven. We also show that an imposed horizontal magnetic field not only inhibits mean flow generation but also affects the vertical structure of the flows. To finish, a discussion of the applicability of the work to astrophysical phenomena is given.



# Contents

Acknowledgements . . . . .	v
Abstract . . . . .	vii
Contents . . . . .	ix
List of figures . . . . .	xv
List of tables . . . . .	xxix
<b>1 Introduction</b>	<b>1</b>
1.1 Motivation . . . . .	1
1.2 Examples of mean flows . . . . .	1
1.2.1 The Sun . . . . .	2
1.2.2 Jupiter . . . . .	5
1.2.3 Other examples . . . . .	7
1.3 Mechanisms for mean flow generation . . . . .	9
1.4 Convection . . . . .	10
1.4.1 Rayleigh-Bénard convection . . . . .	10
1.4.2 Experiments . . . . .	11
1.4.3 Nonlinear studies . . . . .	11
1.5 Hathaway model . . . . .	14
1.6 Thesis outline . . . . .	15

---

<b>2</b>	<b>Derivation of governing equations</b>	<b>17</b>
2.1	Fluid and MHD equations . . . . .	17
2.1.1	Continuity equation . . . . .	17
2.1.2	Momentum equation . . . . .	18
2.1.3	Temperature equation . . . . .	18
2.1.4	Induction equation . . . . .	19
2.1.5	Equation of state . . . . .	19
2.2	Model setup . . . . .	20
2.3	Boussinesq approximation . . . . .	21
2.3.1	Boundary conditions . . . . .	22
2.3.2	Basic state . . . . .	23
2.3.3	Perturbation equations . . . . .	25
2.3.4	Nondimensionalisation . . . . .	26
2.3.5	Nondimensionalisation of the basic state . . . . .	27
2.4	Anelastic approximation . . . . .	28
2.4.1	Governing equations . . . . .	28
2.4.2	Preliminary scalings . . . . .	29
2.4.3	Anelastic scalings . . . . .	32
2.4.4	Lantz formulation . . . . .	35
2.4.5	Reference state . . . . .	36
2.4.6	Alternative nondimensionalisation . . . . .	37
2.4.7	Boundary conditions . . . . .	39
2.4.8	Basic state . . . . .	39
2.5	Summary . . . . .	40

---

<b>3</b>	<b>Linear Boussinesq Convection</b>	<b>41</b>
3.1	Introduction . . . . .	41
3.2	Linear theory . . . . .	42
3.2.1	Linearisation of the governing equations . . . . .	42
3.2.2	Normal mode decomposition . . . . .	43
3.2.3	Boundary conditions . . . . .	45
3.3	Numerical method . . . . .	46
3.3.1	Eigenfunctions . . . . .	47
3.4	Numerical results . . . . .	48
3.5	Hydrodynamic results ( $\mathbf{B} = 0$ ) . . . . .	48
3.5.1	Prandtl number effects . . . . .	49
3.5.2	Effect of $T_y$ on the onset of convection . . . . .	53
3.6	Effects of a horizontal magnetic field . . . . .	54
3.6.1	Analytical results . . . . .	54
3.6.2	Numerical solutions . . . . .	58
3.6.3	Two-dimensional solutions . . . . .	59
3.6.4	Eigenvalue diagrams . . . . .	63
3.6.5	Three-dimensional solutions . . . . .	65
3.7	Summary . . . . .	67
<b>4</b>	<b>Linear Anelastic Convection</b>	<b>69</b>
4.1	Introduction . . . . .	69
4.2	Linear equations . . . . .	70
4.3	Numerical results . . . . .	72
4.3.1	Effect of $Ta$ on the onset of convection . . . . .	72
4.3.2	Eigenfunctions . . . . .	79

---

4.3.3	Three-dimensional solutions . . . . .	81
4.3.4	NS rolls - effect of $\phi$ and $Pr$ . . . . .	82
4.3.5	Effect of $\theta$ on the onset of convection . . . . .	85
4.4	Symmetry considerations . . . . .	89
4.4.1	Eigenfunctions . . . . .	91
4.4.2	Proof of symmetry when $k = 0$ . . . . .	92
4.5	Summary . . . . .	94
<b>5</b>	<b>Nonlinear Numerical Method</b>	<b>97</b>
5.1	Introduction to pseudospectral methods . . . . .	97
5.2	Governing equations . . . . .	98
5.2.1	Boundary conditions . . . . .	100
5.3	Method of solution . . . . .	100
5.3.1	Coordinate transformation . . . . .	100
5.3.2	Fourier Expansion . . . . .	101
5.3.3	Chebyshev expansion . . . . .	102
5.3.4	Application to the problem . . . . .	105
5.3.5	A note on calculating spectral coefficients . . . . .	107
5.3.6	Nonlinear terms . . . . .	107
5.3.7	Dealiasing . . . . .	107
5.3.8	Time stepping . . . . .	108
5.3.9	Application of the time stepping method . . . . .	109
5.3.10	Thual algorithm . . . . .	113
5.4	Testing the code . . . . .	116
5.5	Useful diagnostics . . . . .	116
5.5.1	Mean flows . . . . .	117

---

5.5.2	Nusselt number . . . . .	117
5.5.3	Kinetic energies . . . . .	118
5.6	Extending the method to solve the MHD equations . . . . .	118
5.6.1	Boundary conditions . . . . .	120
5.6.2	Testing the MHD code . . . . .	121
5.6.3	Useful diagnostics . . . . .	121
5.7	Extending the method to solve the anelastic equations . . . . .	121
5.7.1	Testing the anelastic code . . . . .	124
5.7.2	Useful diagnostics . . . . .	124
5.8	Summary . . . . .	125
<b>6</b>	<b>Nonlinear Hydrodynamic Convection</b>	<b>127</b>
6.1	Introduction . . . . .	127
6.2	Numerical results . . . . .	127
6.2.1	No thermal wind . . . . .	128
6.2.2	Transition to chaos . . . . .	129
6.2.3	Nonlinear solutions . . . . .	130
6.2.4	Large-scale solutions . . . . .	132
6.2.5	Decreasing $Pr$ . . . . .	135
6.3	Mean flows . . . . .	140
6.3.1	Effect of $\phi$ on mean flows . . . . .	140
6.3.2	Effect of $Pr$ on mean flows . . . . .	141
6.3.3	Reynolds stresses . . . . .	145
6.4	Addition of a thermal wind . . . . .	149
6.4.1	Nonlinear solutions . . . . .	151
6.4.2	Interaction between convection and thermal wind shear . . . . .	152

---

6.4.3	Reynolds Stresses . . . . .	158
6.5	Summary . . . . .	162
<b>7</b>	<b>Nonlinear Anelastic Convection</b>	<b>165</b>
7.1	Introduction . . . . .	165
7.2	Numerical results . . . . .	165
7.2.1	Mean flows . . . . .	172
7.2.2	Mean flow equations . . . . .	179
7.2.3	Linear approximation . . . . .	184
7.3	Summary . . . . .	187
<b>8</b>	<b>Nonlinear rotating convection in the presence of a horizontal magnetic field</b>	<b>189</b>
8.1	Introduction . . . . .	189
8.2	Numerical results . . . . .	190
8.2.1	Mean flows . . . . .	191
8.2.2	Mean fields . . . . .	196
8.2.3	Increasing $Ra$ . . . . .	199
8.2.4	Mean flow equations . . . . .	199
8.2.5	Linear approximation . . . . .	205
8.2.6	Effect of $\zeta$ . . . . .	208
8.2.7	Effect of $Pr$ . . . . .	212
8.3	Summary . . . . .	219
<b>9</b>	<b>Conclusions</b>	<b>221</b>
9.1	Summary of results and discussion . . . . .	221
9.2	Further work . . . . .	226
	<b>Bibliography</b>	<b>229</b>

# List of figures

- 1.1 Interior structure of the Sun. The core extends to 20-25% of the radius and is surrounded by the radiation zone which extends to approximately 70% of the radius. The outer 30% is occupied by the convection zone. Image source: <http://phys.org/news/>. . . . . 2
- 1.2 Rotation profile of the Sun. The radiation zone is in solid body rotation, whereas the convection zone is differentially rotating. In between these two regions is a thin layer known as the tachocline. Image from Schou *et al.* (1998). . . . . 4
- 1.3 Solar butterfly diagram. The location of sunspots as a function of time and latitude. In each eleven year cycle, sunspots increase in number, move towards the equator and then decrease in number. Image from Hathaway (2010). . . . . 5
- 1.4 Magnetic butterfly diagram. The polarity of the magnetic field associated with sunspots switches after each 11 year cycle, resulting in a complete cycle period of 22 years. Image source: David Hathaway, NASA. . . . . 5
- 1.5 (a) Image of Jupiter showing the distinct array of zonal jets present in its atmosphere. Image source: <http://astronomy.nyu.edu.cn>. (b) Data relating to the zonal flows obtained from the Voyager and Cassini missions, the two sets of data are very similar. Image from Porco *et al.* (2003). . . . . 6
- 1.6 Circulation of air in the Earth's atmosphere. There exist three distinct cells of meridional circulation in each hemisphere: (i) the Hadley cell, (ii) the Ferrel cell and (iii) the Polar cell. In addition, large-scale zonal flows exist in the form of the polar and subtropical jets. Image source: [www.srh.noaa.gov](http://www.srh.noaa.gov). . . . . 8
- 1.7 Observed zonal flow profiles of Jupiter, Saturn, Uranus and Neptune. Figure adapted from figure 2 of Sukoriansky *et al.* (2002). . . . . 9

1.8 Hathaway model. A schematic of the model used by Hathaway *et al.* (1980). It consists of a plane layer taken at a latitude  $\phi$  on a spherical body. As a result the rotation vector is oblique to gravity and is given by  $\mathbf{\Omega} = (0, \Omega \cos \phi, \Omega \sin \phi)$ .  $z$  is directed upwards,  $y$  is directed northwards and  $x$  (into the page) is directed eastwards. . . . . 14

2.1 Configuration: Our model consists of a rotating plane layer rotating with velocity  $\mathbf{\Omega} = (0, \Omega \cos \phi, \Omega \sin \phi)$ .  $x$  is directed eastwards,  $y$  is directed northwards and  $z$  is directed upwards. A horizontal magnetic field is imposed and a temperature gradient in both the  $y$  and  $z$  directions is imposed. . . . . 20

3.1 Critical Rayleigh number ( $Ra_{\text{crit}}$ ) and critical wavenumber ( $a_{\text{crit}}$ ) against Taylor number ( $Ta$ ) for NS (solid line) and EW (dashed line) convection rolls, in a layer with  $\phi = \frac{\pi}{4}$ . This figure exactly replicates figure 2 of HTG and provides good support for the accuracy of our numerical code. . . . . 49

3.2 Critical values for NS rolls. (a) Critical Rayleigh number,  $Ra_{\text{crit}}$ , (b) critical wavenumber,  $k_{\text{crit}}$ , and (c) critical frequency,  $\omega_{\text{crit}}$ , of NS rolls against Taylor number,  $Ta$ , for different  $Pr$  in a layer at  $\phi = \frac{\pi}{4}$ . The black line represents direct modes and all other lines represent oscillatory modes. In black  $Pr = 1$ , blue  $Pr = 0.1$ , green  $Pr = 0.05$ , red  $Pr = 0.025$ , purple  $Pr = 0.0125$  and orange  $Pr = 0.00625$ . . . . . 50

3.3 Critical values for EW rolls. (a) Critical Rayleigh number,  $Ra_{\text{crit}}$ , (b) critical wavenumber,  $l_{\text{crit}}$ , and (c) critical frequency,  $\omega_{\text{crit}}$ , of EW rolls against Taylor number,  $Ta$ , for different  $Pr$  in a layer at  $\phi = \frac{\pi}{4}$ . The black line represents direct modes and all other lines represent oscillatory modes. In black  $Pr = 1$ , blue  $Pr = 0.1$ , green  $Pr = 0.05$ , red  $Pr = 0.025$ , purple  $Pr = 0.0125$  and orange  $Pr = 0.00625$ . . . . . 51

3.4 Eigenfunctions  $w(y, z)$ ,  $\theta(y, z)$  and  $\zeta(y, z)$  at  $Ra_{\text{crit}}$ ,  $l_{\text{crit}}$  and  $\omega_{\text{crit}}$  for  $Pr = 0.05, Ta = 10^5$  and (a)  $T_y = 0, \phi = \frac{\pi}{2}$ , (b)  $T_y = 0, \phi = \frac{\pi}{4}$ , (c)  $T_y = -0.5, \phi = \frac{\pi}{2}$ , (d)  $T_y = -0.5, \phi = \frac{\pi}{4}$ , (e)  $T_y = 0.5, \phi = \frac{\pi}{2}$ , (f)  $T_y = 0.5, \phi = \frac{\pi}{4}$ . . . . . 52

- 3.5 (a) Critical Rayleigh number ( $Ra_{\text{crit}}$ ), (b) critical wavenumber ( $l_{\text{crit}}$ ) and (c) critical frequency ( $\omega_{\text{crit}}$ ), as a function of  $T_y$ , for  $Pr = 1$  (black) and  $Pr = 0.1$  (blue) with  $Ta$  fixed at  $10^5$ . The  $Pr = 1$  solutions are steady and the  $Pr = 0.1$  solutions are oscillatory. . . . . 54
- 3.6 Rayleigh number against wavenumber for a layer with  $Q = 1000$ ,  $Pr = 1$  and  $\zeta = 0.1$ . The blue symbols represent the numerical results generated by the code and the red symbols the theoretical expression as given by Arter (1983). The two coincide. The upper lines are the results for the steady solution and the lower lines are for the oscillatory solution. . . . . 59
- 3.7 Critical values for case (i). Critical Rayleigh number (a), wavenumber (b) and frequency (c) as a function of  $Q$  for  $Pr = 1$  and  $\zeta = 0.1$  with  $Ta = 10^5$ . The direct mode is shown in blue and the oscillatory mode in red. In this case only the magnetic oscillatory mode exists. . . . . 61
- 3.8 Critical values for case (ii). Critical Rayleigh number (a), wavenumber (b) and frequency (c) as a function of  $Q$  for  $Pr = 0.1$  and  $\zeta = 1.1$  with  $Ta = 10^5$ . The direct mode is shown in blue and the oscillatory mode in green. In this case only the rotating oscillatory mode exists. . . . . 62
- 3.9 Critical values for case (iii). Critical Rayleigh number (a), wavenumber (b) and frequency (c) as a function of  $Q$  for  $Pr = 0.1$  and  $\zeta = 0.1$  with  $Ta = 10^5$ . The direct mode is shown in blue, the (magnetic) oscillatory mode in red and the (rotating) oscillatory mode in green. . . . . 62
- 3.10 Eigenvalue diagram for  $l = 10$ ,  $Q = 500$ ,  $Ta = 10^5$ ,  $Pr = 1$  and  $\zeta = 0.1$ . The arrows indicate the direction of increasing Rayleigh number. . . . . 63
- 3.11 Eigenvalue diagram for a layer with  $Ta = 10^5$ ,  $Pr = 0.1$  and  $\zeta = 1.1$ . In a)  $Q = 930$  and  $l = 0.7$ ; in b)  $Q = 1000$  and  $l = 0.7$ . The arrows indicate the direction of increasing Rayleigh number. . . . . 64
- 3.12 Eigenvalue diagram for a layer with  $Ta = 10^5$ ,  $Pr = 0.1$ ,  $\zeta = 0.1$ . and  $Q = 900$ . In a)  $k = 0.9$ , in b)  $k = 1.7$ , in c)  $k = 2$ , in d)  $k = 3.5$ , in e)  $k = 4.6$ , and in f)  $l = 6$ . The arrows indicate the direction of increasing Rayleigh number. . . . . 66

3.13 Critical Rayleigh number, ( $Ra_{\text{crit}}$ , top left), critical wavenumber ( $k_{\text{crit}}$ , bottom left,  $l_{\text{crit}}$ , bottom right) and critical frequency ( $\omega_{\text{crit}}$ , top right) as a function of  $Q$  for  $Pr = 0.1$  and  $\zeta = 0.1$  with  $Ta = 10^5$  for three-dimensional perturbations. The direct mode is shown in blue, the (magnetic) oscillatory mode in red and the (rotating) oscillatory mode in green. . . . . 67

4.1  $Ra_{\text{crit}}$  (top),  $k_{\text{crit}}$  (centre) and  $\omega_{\text{crit}}$  (bottom) against  $Ta$  for NS rolls when  $Pr = 0.1$  and  $\phi = \frac{\pi}{4}$ . In black  $\theta = 0$ , in red  $\theta = -0.37$ , in green  $\theta = -0.79$  and in blue  $\theta = -0.95$ . Solutions with positive preferred frequency are denoted with a '+' , solutions with negative preferred frequency are denoted with a 'o' and the cases where only marginal solutions with a negative frequency exist are denoted by a '.' . . . . . 73

4.2  $w(x, z, t)$  at onset over one time period for NS rolls when  $Pr = 0.1$ ,  $\phi = \frac{\pi}{4}$ ,  $\theta = -0.79$  and (a)  $\omega_{\text{crit}} > 0$  (left travelling wave), (b)  $\omega_{\text{crit}} < 0$  (right travelling wave). . . . . 75

4.3  $\sigma_R$  plotted against  $\sigma_I$  for (a)  $k = 2$ ,  $Ta = 10^2$  and  $\theta = 0$ , (b)  $k = 1$ ,  $Ta = 10^3$  and  $\theta = 0$ , (c)  $k = 2$ ,  $T = 2000$  and  $\theta = -0.95$  and (d)  $k = 2$ ,  $T = 5000$  and  $\theta = -0.95$ . Oscillatory bifurcations occur when  $\sigma_R = 0$  for  $\sigma_I \neq 0$ . . . . . 77

4.4  $Ra_{\text{crit}}$  (top),  $l_{\text{crit}}$  (centre) and  $\omega_{\text{crit}}$  (bottom) against  $Ta$  for EW rolls when  $Pr = 0.1$  and  $\phi = \frac{\pi}{4}$ . In black  $\theta = 0$ , in red  $\theta = -0.37$ , in green  $\theta = -0.79$  and in blue  $\theta = -0.95$ . For EW rolls, the solutions with positive and negative frequency have the same  $Ra_{\text{crit}}$ , so both are preferred modes at onset. . . . . 78

4.5  $\sigma_R$  plotted against  $\sigma_I$  for  $\theta = -0.79$ ,  $k = 0$ ,  $l = 3$ , and (a)  $Ta = 50$ , (b)  $Ta = 10^5$ . Oscillatory bifurcations occur when  $\sigma_R = 0$  for  $\sigma_I \neq 0$ . . . . . 79

4.6 Eigenfunctions  $w$ ,  $s$  and  $\zeta$  at  $Ra_{\text{crit}}$  and  $a_{\text{crit}}$  for  $Pr = 0.1$ ,  $Ta = 10^7$  and (a)  $\theta = 0$ ,  $\phi = \frac{\pi}{2}$ ,  $l = 0$ , (b)  $\theta = 0$ ,  $\phi = \frac{\pi}{4}$ ,  $l = 0$ , (c)  $\theta = 0$ ,  $\phi = \frac{\pi}{4}$ ,  $k = 0$ , (d)  $\theta = -0.95$ ,  $\phi = \frac{\pi}{2}$ ,  $l = 0$ , (e)  $\theta = -0.95$ ,  $\phi = \frac{\pi}{4}$ ,  $l = 0$ , and (f)  $\theta = -0.95$ ,  $\phi = \frac{\pi}{4}$ ,  $k = 0$ . . . . . 80

4.7 Amplitude function  $|W(z)|$  as a function of  $z$  for NS rolls,  $\phi = \frac{\pi}{4}$ ,  $Pr = 0.1$  and  $\theta = 0$  (blue),  $\theta = -0.37$  (red),  $\theta = -0.79$  (green) and  $\theta = -0.95$  (black) for (a)  $Ta = 10^3$  and (b)  $Ta = 10^7$ . . . . . 81

- 4.8 Contours of Rayleigh number against  $k$  and  $l$  for (a)  $Ta = 1200$ ,  $\theta = -0.37$  and (b)  $Ta = 10000$ ,  $\theta = -0.79$ . In (a) the preferred mode (white cross) is oblique and  $Ra_{\text{crit}} = 1427$ ,  $k_{\text{crit}} = 1.8250$ ,  $l_{\text{crit}} = 1.5900$  and  $\omega_{\text{crit}} = -1.6105$ , whereas in (b), the preferred mode (white cross) is oriented NS and  $Ra_{\text{crit}} = 1915$ ,  $k_{\text{crit}} = 2.6200$ ,  $l_{\text{crit}} = 0$  and  $\omega_{\text{crit}} = -6.1293$ . . . . . 82
- 4.9  $Ra_{\text{crit}}$  (top)  $k_{\text{crit}}$  (centre) and  $\omega_{\text{crit}}$  (bottom) against  $Ta$  for NS rolls when  $Pr = 0.1$ . Black (red), blue (orange) and green (turquoise) symbols denote  $\phi = \frac{\pi}{2}$ ,  $\phi = \frac{\pi}{4}$  and  $\phi = \frac{\pi}{6}$  respectively for  $\theta = 0$  ( $\theta = -0.95$ ). The symbol shape has the same interpretation as in figure 4.1. . . . . 84
- 4.10  $Ra_{\text{crit}}$  (top)  $k_{\text{crit}}$  (centre) and  $\omega_{\text{crit}}$  (bottom) against  $Ta$  for NS rolls when  $\phi = \frac{\pi}{4}$ . Black (red), blue (orange), green (turquoise) and purple (grey) symbols denote  $Pr = 1$ ,  $Pr = 0.1$ ,  $Pr = 0.01$ ,  $Pr = 0.001$  respectively for  $\theta = 0$  ( $\theta = -0.95$ ). The symbol shape has the same interpretation as in figure 4.1. . . . . 86
- 4.11  $Ra_{\text{crit}}$  (left)  $k_{\text{crit}}$  (centre) and  $\omega_{\text{crit}}$  (right) against  $|\theta|$  for NS rolls when  $Pr = 0.1$ ,  $\phi = \frac{\pi}{4}$ . Solid lines represent solutions with  $\omega_{\text{crit}} > 0$  and dashed lines represent solutions with  $\omega_{\text{crit}} < 0$ . In red  $Ta = 10^4$ , in blue  $Ta = 10^5$ , in black  $Ta = 10^6$  and in purple  $Ta = 10^7$  . . . . . 87
- 4.12  $Ra_{\text{crit}}$  (left)  $l_{\text{crit}}$  (centre) and  $\omega_{\text{crit}}$  (right) against  $|\theta|$  for EW rolls when  $Pr = 0.1$ ,  $\phi = \frac{\pi}{4}$ . In red  $Ta = 10^4$ , in blue  $Ta = 10^5$ , in black  $Ta = 10^6$  and in purple  $Ta = 10^7$  . . . . . 87
- 4.13  $Ra_{\text{crit}}$  (left),  $k_{\text{crit}}$  (centre) and  $\omega_{\text{crit}}$  (right) against  $|\theta|$  for NS rolls when  $Pr = 0.1$ . Black (red), blue (orange) and green (turquoise) symbols correspond to  $\phi = \frac{\pi}{2}$ ,  $\phi = \frac{\pi}{4}$  and  $\phi = \frac{\pi}{6}$  respectively for  $Ta = 10^4$  ( $Ta = 10^7$ ). Solid lines correspond to solutions with  $\omega_{\text{crit}} > 0$  and dashed lines to solutions with  $\omega_{\text{crit}} < 0$ . . . . . 88
- 4.14  $Ra_{\text{crit}}$  (left),  $k_{\text{crit}}$  (centre) and  $\omega_{\text{crit}}$  (right) against  $|\theta|$  for NS rolls when  $\phi = \frac{\pi}{4}$ . Black (blue), red (orange) and (grey) symbols correspond to  $Ta = 10^7$ ,  $Ta = 10^9$  and  $Ta = 10^{11}$  respectively for  $Pr = 0.01$  ( $Pr = 0.001$ ). Solid lines correspond to solutions with  $\omega_{\text{crit}} > 0$  and dashed lines to solutions with  $\omega_{\text{crit}} < 0$ . . . . . 89
- 4.15 Real and imaginary parts of growth rate plotted against each other for different  $Ra$  whilst  $Ta = 10^5$ ,  $Pr = 0.1$ ,  $\phi = \frac{\pi}{4}$ ,  $\theta = -0.9$ . In (a)  $l = 0$ ,  $k = 3$ , in (b)  $k = 0$ ,  $l = 3$  and in (c)  $k = 3$ ,  $l = 3$ . When  $k = 0$  the symmetry is not broken. . . 90

4.16 Eigenfunctions. The solutions  $|W(z)|$ ,  $|Z(z)|$  and  $|S(z)|$  as a function of  $z$  for  $k = 0$ ,  $l = 2$ ,  $Ta = 10^5$ ,  $Pr = 0.1$ ,  $\phi = \frac{\pi}{4}$ ,  $Ra = 2 \times 10^5$  and (a)  $\theta = 0$ , (b)  $\theta = -0.95$ . The solid line corresponds to the solutions with  $\omega > 0$  and the dotted lines to solutions with  $\omega < 0$ . . . . . 91

6.1 Regime diagram for solutions at fixed  $\phi$  and  $Ra$  for  $Pr = 1$ ,  $\phi = \frac{\pi}{2}$ ,  $\frac{\pi}{4}$  and  $\frac{\pi}{6}$ . Red squares represent steady solutions, blue circles represent periodic solutions, green triangles represent quasi-periodic solutions and light blue stars represent chaotic solutions. The results are plotted against (a)  $Ra$ , and (b)  $\frac{Ra}{Ra_c}$ . . . . . 128

6.2 Time series of Nusselt number ( $Nu$ ) and kinetic energy ( $KE_{\text{pert}}$ ) for the case when  $Pr = 1$ ,  $\phi = \frac{\pi}{4}$  and in (a),  $Ra = 40000$ , in (b),  $Ra = 50000$ , in (c),  $Ra = 63000$ , and in (d),  $Ra = 75000$ . . . . . 130

6.3 Phase space and alongside it a Poincaré section for each of the cases in figure 6.2. In (a),  $Ra = 40000$  and the section is taken at  $KE_{\bar{u}} = 0.1307$ , in (b),  $Ra = 50000$  and the section is taken at  $KE_{\bar{u}} = 6$ , in (c),  $Ra = 63000$  and the section is taken at  $KE_{\bar{u}} = 100$  and in (d),  $Ra = 75000$  and the section is taken at  $KE_{\bar{u}} = 200$ . . . . . 131

6.4 Contours of the streamfunction  $\psi(y, z)$  in a settled state, for the case with  $Pr = 1$  and  $\phi = \frac{\pi}{4}$ . In (a),  $Ra = 40000$ , in (b),  $Ra = 63000$ , in (c),  $Ra = 75000$  and in (d),  $Ra = 2 \times 10^5$ . . . . . 132

6.5 Contours of the temperature  $T(y, z)$  after the final time step for the case with  $Pr = 1$  and  $\phi = \frac{\pi}{4}$ . In (a),  $Ra = 40000$ , in (b),  $Ra = 63000$ , in (c),  $Ra = 75000$  and in (d),  $Ra = 2 \times 10^5$ . . . . . 133

6.6 Time-averaged, mean temperature profiles  $\bar{T}$ , for the cases shown in figure 6.5. The solid line represents  $Ra = 40000$ , the dashed line represents  $Ra = 63000$ , the dot-dashed line represents  $Ra = 75000$  and the dotted line represents  $Ra = 2 \times 10^5$ . Increasing  $Ra$  acts to make the interior of the fluid layer more isothermal. 134

6.7 Nusselt number ( $Nu$ ) against Rayleigh number ( $Ra$ ) for  $Pr = 1$ ,  $\phi = \frac{\pi}{6}$ ,  $Ta = 10^5$ . As  $Ra$  is increased the solution changes regimes. In particular, at  $Ra = 6 \times 10^5$  the solution is chaotic but at  $Ra = 7 \times 10^5$  the solution is steady. This change in regime coincides with an increase in  $Nu$ . . . . . 134

- 6.8 Contours of  $\psi(y, z)$  for steady solutions taken from two different steady regimes. In a)  $Ra = 40000$  and in (b)  $Ra = 8 \times 10^5$ . The larger  $Ra$  solution exhibits a much larger length scale and the cells are not aligned with the rotation vector, as they are in (a). . . . . 135
- 6.9 (a) Temperature as a function of  $y$  and  $z$ . (b) Horizontally averaged temperature as a function of  $z$ . In both cases,  $Ra = 8 \times 10^5$ ,  $Pr = 1$ ,  $\phi = \frac{\pi}{4}$ ,  $Ta = 10^5$ . The bulk of the fluid is isothermal except for the two thin boundary layers. . . . . 135
- 6.10 Regime diagram for solutions at fixed  $\phi$  and  $Ra$  for  $Pr = 0.1$ ,  $\phi = \frac{\pi}{2}$ ,  $\frac{\pi}{4}$  and  $\frac{\pi}{6}$ . Red squares represent steady solutions, blue circles represent periodic solutions, green triangles represent quasi-periodic solutions, black dots relaxation oscillations and light blue stars represent chaotic solutions. The results are plotted against (a)  $Ra$ , and (b)  $\frac{Ra}{Ra_c}$ . . . . . 136
- 6.11 (a) Time series of Nusselt number ( $Nu$ ) and kinetic energy ( $KE_{\text{pert}}$ ) for the case when  $Pr = 0.1$ ,  $\phi = \frac{\pi}{4}$  and  $Ra = 70000$ . (b) shows plots of the kinetic energy in  $\bar{u}$  (blue) and  $\bar{v}$  (red) against time for the same case. . . . . 137
- 6.12 Phase space and alongside it a Poincaré section for the relaxation oscillation case shown in figure 6.11. The cut through phase space is taken at  $KE_{\bar{u}} = 300$ . . . . . 137
- 6.13 Ratios of the kinetic energy in  $\bar{u}$  and  $\bar{v}$  to the kinetic energy in the perturbations calculated using, in (a), the variability measure ( $\langle KE_{\bar{\xi}} \rangle$ ), and in (b), the mean measure ( $KE_{\langle \bar{\xi} \rangle}$ ), for  $Pr = 1$ ,  $\phi = \frac{\pi}{2}$  (blue, crosses),  $\phi = \frac{\pi}{4}$  (red, dots) and  $\phi = \frac{\pi}{6}$  (green, squares). In each case, the top row shows plots of the ratios against  $Ra$  and the bottom row against  $\frac{Ra}{Ra_c}$ . . . . . 142
- 6.14 Contour plots of the mean flows  $\bar{u}(z, t)$ ,  $\bar{v}(z, t)$  and their corresponding time-average  $\langle \bar{u} \rangle$ ,  $\langle \bar{v} \rangle$  as a function of  $z$ . In all cases,  $Pr = 1$  and  $Ra = 2 \times 10^5$  but  $\phi$  is varied. In (a)  $\phi = \frac{\pi}{2}$ , in (b)  $\phi = \frac{\pi}{4}$ , and in (c)  $\phi = \frac{\pi}{6}$ . . . . . 143
- 6.15 Ratios of the kinetic energy in  $\bar{u}$  and  $\bar{v}$  to the kinetic energy in the perturbations calculated using, in (a), the variability measure ( $\langle KE_{\bar{\xi}} \rangle$ ) and in (b), the mean measure ( $KE_{\langle \bar{\xi} \rangle}$ ), for  $\phi = \frac{\pi}{4}$ ,  $Pr = 1$  (blue, crosses) and  $Pr = 0.1$  (red, dots). The top row shows plots of the ratios against  $Ra$  and the bottom row against  $\frac{Ra}{Ra_c}$ . . . . . 144

6.16 Contour plots of the mean flows  $\bar{u}(z, t)$ ,  $\bar{v}(z, t)$  and their corresponding time-average  $\langle \bar{u} \rangle$ ,  $\langle \bar{v} \rangle$  as a function of  $z$ . In (a),  $\phi = \frac{\pi}{4}$ ,  $Ra = 2 \times 10^5$  and  $Pr = 1$ , in (b),  $\phi = \frac{\pi}{4}$ ,  $Ra = 2 \times 10^5$  and  $Pr = 0.1$ , in (c),  $\phi = \frac{\pi}{4}$ ,  $Ra \approx 20Ra_c$ ,  $Ra = 7 \times 10^5$  and  $Pr = 1$ , and in (d),  $\phi = \frac{\pi}{4}$ ,  $Ra \approx 20Ra_c$ ,  $Ra = 1.5 \times 10^5$  and  $Pr = 0.1$ . . . . . 146

6.17 Contour plots of the Reynolds stresses terms given by  $\frac{\partial}{\partial z}(\overline{vw})$  in (a) and (c) and  $\frac{\partial}{\partial z}(\overline{uw})$  in (b) and (d). In all cases,  $Pr = 1$  and  $Ra = 2 \times 10^5$  but in (a) and (b),  $\phi = \frac{\pi}{2}$ , and in (c) and (d),  $\phi = \frac{\pi}{4}$ . . . . . 147

6.18 Top: each of the terms in equation (6.3.3) driving  $\bar{u}$ . Bottom: each of the terms in equation (6.3.4) driving  $\bar{v}$ . In both cases the terms are plotted as a function of  $z$  for  $Ra = 2 \times 10^5$ ,  $Ta = 10^5$  and  $\phi = \frac{\pi}{4}$ . The solid lines represent  $Pr = 1$  and the dashed lines represent  $Pr = 0.1$ . In blue are the mean flow terms, in red are the Reynolds stress terms and in green are the viscous terms. Also plotted are the mean flows (black) without the  $Pr$  factor. . . . . 148

6.19 Top: each of the terms in equation (6.3.3) driving  $\bar{u}$ . Bottom: each of the terms in equation (6.3.4) driving  $\bar{v}$ . In both cases the terms are plotted as a function of  $z$  for  $Ra = 27Ra_c$ ,  $Ta = 10^5$  and  $\phi = \frac{\pi}{4}$ . The solid lines represent  $Pr = 1$  and the dashed lines represent  $Pr = 0.1$ . In blue are the mean flow terms, in red are the Reynolds stress terms and in green are the viscous terms. Also plotted are the mean flows (black) without the  $Pr$  factor. . . . . 149

6.20 Regime diagram for solutions at fixed  $\phi$  and  $Ra$  for  $T_y = -0.5$ ,  $Pr = 1$ ,  $\phi = \frac{\pi}{2}$  and  $\phi = \frac{\pi}{4}$ . Red squares represent steady solutions, blue circles represent periodic solutions, green triangles represent quasi-periodic solutions and light blue stars represent chaotic solutions. The results are plotted against (a)  $Ra$ , and (b)  $\frac{Ra}{Ra_c}$ . . . . . 150

6.21 Contours of the streamfunction  $\psi(y, z)$  in a settled state for the case with  $Pr = 1$ ,  $\phi = \frac{\pi}{4}$  and  $T_y = -0.5$ . In (a),  $Ra = 40000$ , in (b),  $Ra = 55000$ , in (c),  $Ra = 60000$  and in (d),  $Ra = 2 \times 10^5$ . . . . . 152

6.22 (a) Contours of the basic state temperature,  $T_{BS} = 1 - z + T_y y$ . (b) Contours of the total temperature  $T(y, z) = 1 - z + T_y y + \theta(y, z)$  after the system has been allowed to evolve in time, for the case with  $Pr = 1$ ,  $\phi = \frac{\pi}{4}$ ,  $T_y = -0.5$ , and  $Ra = 2 \times 10^5$ . . . . . 152

- 6.23 Ratio of the KE in the mean flows to KE in the perturbations calculated using (a) the variability measure and (b) the mean measure. The solid lines are for  $T_y = -0.5$  and the dotted lines are for  $T_y = 0$ . In (c), the ratio of the KE in  $\bar{u}_{total}$  to total KE is presented with dashed lines corresponding to the KE in  $U_{BS}$ . In all cases,  $Pr = 1$ , and the blue lines correspond to  $\phi = \frac{\pi}{2}$  and the red lines to  $\phi = \frac{\pi}{4}$ . . . . . 154
- 6.24 Ratio of the KE in the mean flows to KE in the perturbations calculated using (a) the variability measure and (b) the mean measure. The solid lines are for  $T_y = -0.5$  and the dotted lines are for  $T_y = 0$ . In (c), the ratio of the KE in  $\bar{u}_{total}$  to total KE is presented with dashed lines corresponding to the KE in  $U_{BS}$ . In all cases,  $\phi = \frac{\pi}{4}$ , and the blue lines correspond to  $Pr = 1$  and the red lines to  $Pr = 0.1$ . . . . . 156
- 6.25 Contour plots of the mean flows  $\bar{u}(z, t)$ ,  $\bar{v}(z, t)$  and their corresponding time-average  $\langle \bar{u} \rangle$ ,  $\langle \bar{v} \rangle$  as a function of  $z$ . In (a) and (b),  $Pr = 1$ ,  $T_y = -0.5$  and  $Ra = 2 \times 10^5$  but  $\phi$  is varied. In (a)  $\phi = \frac{\pi}{2}$  and in (b)  $\phi = \frac{\pi}{4}$ . . . . . 157
- 6.26 Contour plots of the mean flows  $\bar{u}(z, t)$ ,  $\bar{v}(z, t)$  and their corresponding time-average  $\langle \bar{u} \rangle$ ,  $\langle \bar{v} \rangle$  as a function of  $z$ . In both cases  $\phi = \frac{\pi}{4}$ ,  $T_y = -0.5$  and  $Ra = 2 \times 10^5$  but in (a)  $Pr = 1$  and in (b)  $Pr = 0.1$ . . . . . 157
- 6.27 Regime diagram to show for which parameters the shear is increased, and for which the shear is reduced and energy extracted from the shear. Red dots indicate a decrease in shear and black crosses indicate an increase. In all cases  $T_y = -0.5$ . 158
- 6.28 Contour plots of the Reynolds stresses terms given by  $\frac{\partial}{\partial z}(\overline{vw})$  in (a) and (c) and  $\frac{\partial}{\partial z}(\overline{uw})$  in (b) and (d). In all cases,  $Pr = 1$ ,  $Ra = 2 \times 10^5$  and  $T_y = -0.5$  but in (a) and (b),  $\phi = \frac{\pi}{2}$  and in (c) and (d),  $\phi = \frac{\pi}{4}$ . . . . . 159
- 6.29 Top: each of the terms in equation (6.3.3) driving  $\bar{u}$ . Bottom: each of the terms in equation (6.3.4) driving  $\bar{v}$ . In both cases the terms are plotted as a function of  $z$  for  $Ra = 2 \times 10^5$ ,  $T_y = -0.5$ ,  $Ta = 10^5$  and  $\phi = \frac{\pi}{4}$ . The solid lines represent  $Pr = 1$  and the dashed lines represent  $Pr = 0.1$ . In blue are the mean flow terms, in red are the Reynolds stress terms and in green are the viscous terms. Also plotted are the mean flows (black) without the  $Pr$  factor. . . . . 160

6.30 Top: each of the terms in equation (6.3.3) driving  $\bar{u}$ . Bottom: each of the terms in equation (6.3.4) driving  $\bar{v}$ . In both cases the terms are plotted as a function of  $z$  for  $Ra = 27Ra_c$ ,  $T_y = -0.5$ ,  $Ta = 10^5$  and  $\phi = \frac{\pi}{4}$ . The solid lines represent  $Pr = 1$  and the dashed lines represent  $Pr = 0.1$ . In blue are the mean flow terms, in red are the Reynolds stress terms and in green are the viscous terms. Also plotted are the mean flows (black) without the  $Pr$  factor. . . . . 161

7.1 A regime diagram to show the types of solution that occur in our system, for different values of  $\theta$  and  $Ra$ . Steady solutions are denoted by a square, quasi-periodic solutions by a triangle, chaotic solutions by a cross and relaxation oscillation solutions by a dot. In all cases  $Pr = 1$ . . . . . 166

7.2 Time series of  $KE_{\text{pert}}$  for  $Pr = 1$ ,  $\theta = -0.79$  for a chaotic solution in (a) at  $Ra = 2 \times 10^5$  and a relaxation oscillation solution in (b) at  $Ra = 5 \times 10^5$ . . . . 167

7.3 Relative distribution of  $KE_{\text{pert}}$  for the same parameters as used in figure 7.2. In (a) the mean is 4432.7951 and the standard deviation 566.7354. In (b), the mean is 31556.0515 and the standard deviation is 7743.3476 . . . . . 168

7.4 Velocity plots indicating the direction of flow in the layer for different  $\theta$ . In (a)  $\theta = -0.37$ , in (b)  $\theta = -0.66$ , in (c)  $\theta = -0.79$  and in (d)  $\theta = -0.95$ . In all cases  $Pr = 1$  and  $Ra = 5 \times 10^5$ . The asymmetry of the layer increases with  $|\theta|$ . 169

7.5 Contours of the total entropy,  $\bar{s} + s$ , corresponding to the velocity plots in figure 7.4. In (a)  $\theta = -0.37$ , in (b)  $\theta = -0.66$ , in (c)  $\theta = -0.79$  and in (d)  $\theta = -0.95$ . In all cases  $Pr = 1$  and  $Ra = 5 \times 10^5$ . The amount of mixing that occurs in the layer decreases as  $|\theta|$  increases. . . . . 170

7.6 Vertical structure of the mean entropy,  $\bar{s}_{\text{tot}}$ , for the parameters used in figure 7.5. In red,  $\theta = -0.37$ , in blue,  $\theta = -0.66$ , in black,  $\theta = -0.79$  and in purple,  $\theta = -0.95$ . The dashed lines correspond to the basic state entropy and the solid lines to  $\bar{s}_{\text{tot}}$  after the simulations have been carried out. . . . . 171

7.7 Kinetic energy in the perturbations as a function of  $\theta$  for  $Pr = 1$  and  $Ra = 2 \times 10^5$  (crosses), from the chaotic regime and  $Ra = 5 \times 10^5$  (dots), from the relaxation oscillation regime. . . . . 172

- 7.8 Energy in the mean flows  $\bar{u}$  and  $\bar{v}$  as calculated by the mean measure (red crosses) and the variability measure (blue dots) for the case corresponding to figure 7.7, i.e.,  $Pr = 1$  and  $Ra = 5 \times 10^5$ . . . . . 174
- 7.9 Contour plots of  $\bar{v}$  in two different regimes. In (a) the solution is chaotic and in (b) the solution is from the relaxation oscillation regime. In both cases,  $Pr = 1$ ,  $\theta = -0.79$  with  $Ra = 2 \times 10^5$  in (a) and  $Ra = 5 \times 10^5$  in (b). . . . . 175
- 7.10 Contour plots of the mean flows  $\bar{u}$  and  $\bar{v}$ . In (a)  $\theta = -0.24$ , in (b)  $\theta = -0.66$  and in (c)  $\theta = -0.79$ . In all cases  $Pr = 1$  and  $Ra = 2 \times 10^5$ . . . . . 176
- 7.11 Mean (black curve) and standard deviation (error bars) of  $\bar{u}$  and  $\bar{v}$  for  $Pr = 1$ ,  $Ra = 2 \times 10^5$ , (a)  $\theta = -0.24$  and (b)  $\theta = -0.79$ . As  $|\theta|$  is increased the more systematic flow occurs at lower  $z$ . . . . . 177
- 7.12 Standard deviation of (a)  $\bar{u}$  and (b)  $\bar{v}$  as a function of layer depth for different stratifications. In black  $\theta = -0.24$ , in purple  $\theta = -0.37$ , in orange  $\theta = -0.66$ , in turquoise  $\theta = -0.79$  and in blue  $\theta = -0.95$ . . . . . 178
- 7.13 Time-averaged mean flows  $\langle \bar{u} \rangle$  (top) and  $\langle \bar{v} \rangle$  (bottom) as a function of  $z$ . In this case  $Pr = 1$ ,  $Ra = 2 \times 10^5$  and in black  $\theta = -0.24$ , in purple  $\theta = -0.37$ , in orange  $\theta = -0.66$ , in turquoise  $\theta = -0.79$  and in blue  $\theta = -0.95$ . . . . . 179
- 7.14 Terms of the mean flow equations (7.2.1) (top axes) and (7.2.2) (bottom axes) as a function of  $z$  for  $Pr = 1$ ,  $Ra = 2 \times 10^5$  and in (a),  $\theta = 0$ , whilst in (b),  $\theta = -0.79$ . The blue lines represent the mean flow terms, the orange the RS terms, the green the viscous terms and red the mean flows  $\bar{u}$  and  $\bar{v}$ . In case (a), the mean flow terms are equivalent to the mean flows themselves. . . . . 181
- 7.15 Left-hand column: Contour plots of the RS term  $\frac{\partial}{\partial z}(\overline{\rho v w})$  that drive  $\bar{u}$ . Right-hand column: Contour plots of the RS term  $\frac{\partial}{\partial z}(\overline{\rho u w})$  that drive  $\bar{v}$ . In (a),  $\theta = -0.24$ , in (b),  $\theta = -0.66$  and in (c),  $\theta = -0.79$  and in all cases,  $Pr = 1$  and  $Ra = 2 \times 10^5$ . They correspond to the mean flows depicted in figure 7.10. . . . . 182
- 7.16 Time-averaged RS terms that drive  $\bar{u}$  (top) and  $\bar{v}$  (bottom) as a function of  $z$ . In this case  $Pr = 1$ ,  $Ra = 2 \times 10^5$  and in black  $\theta = -0.24$ , in purple  $\theta = -0.37$ , in orange  $\theta = -0.66$ , in turquoise  $\theta = -0.79$  and in blue  $\theta = -0.95$ . These plots correspond to the mean flows in figure 7.13. . . . . 183

7.17 Mean (black curve) and standard deviation (error bars) of the RS terms that drive  $\bar{u}$  (left) and  $\bar{v}$  (right) for  $Pr = 1$ ,  $Ra = 2 \times 10^5$  and (a)  $\theta = -0.24$ , (b)  $\theta = -0.79$ . 185

7.18 The RS terms calculated from the nonlinear code (solid lines) and the RS terms calculated from linear eigenfunctions (dashed lines) for  $Pr = 1$  and (a)  $Ra = 2 \times 10^5$ , (b)  $Ra = 10^6$ . The agreement is generally poor. The linear calculation provides a rough estimate at  $\theta = -0.37$  and  $Ra = 2 \times 10^5$  but the approximation gets worse as  $|\theta|$  and  $Ra$  are increased. . . . . 186

8.1 Kinetic energy (left) and magnetic energy (right) in the perturbations plotted against  $Q$  for  $Pr = 1$ ,  $\zeta = 1.1$ ,  $Ra = 5 \times 10^5$ . Solutions from the chaotic regime are marked with a cross and solutions from the steady regime with a dot. . 191

8.2 Contours of  $\psi(y, z)$  (left-hand column) and  $A(y, z)$  (right-hand column) at a snapshot in time for  $Pr = 1$ ,  $\zeta = 1.1$ ,  $Ra = 5 \times 10^5$  and in (a)  $Q = 100$ , in (b)  $Q = 1500$  and in (c)  $Q = 10000$ . (a) and (b) correspond to chaotic solutions and (c) is a steady solution. . . . . 192

8.3 Kinetic energies in the mean flow for  $Pr = 1$ ,  $\zeta = 1.1$ ,  $Ra = 5 \times 10^5$  and a range of  $Q$ . The top row gives the mean measure of the energy in  $\bar{u}$  (left) and  $\bar{v}$  (right) in red and the variability measure of the energy in blue. Chaotic solutions are marked with a cross and steady solutions with a dot. The bottom row gives the ratio of the energy in the mean flow to the kinetic energy in the perturbations. 193

8.4 Time-dependent  $\bar{u}$  (left) and  $\bar{v}$  (right) for  $Pr = 1$ ,  $\zeta = 1.1$ ,  $Ra = 5 \times 10^5$  and (a)  $Q = 100$ , (b)  $Q = 1500$ . . . . . 195

8.5  $\bar{u}$  (top) and  $\bar{v}$  (bottom) for  $Pr = 1$ ,  $\zeta = 1.1$ ,  $Ra = 5 \times 10^5$ . Each  $Q$  is represented by a different colour; blue represents  $Q = 0$ , red represents  $Q = 100$ , green represents  $Q = 500$ , pink represents  $Q = 1000$ , light blue represents  $Q = 2000$ , black represents  $Q = 5000$  and orange represents  $Q = 10000$ .  $Q = 0$  to  $Q = 1000$  are chaotic solutions, whereas  $Q = 2000$  to  $Q = 10000$  are steady solutions. Notice that  $\bar{v}$  is bigger than  $\bar{u}$ . . . . . 196

8.6 Time-dependent  $\bar{B}_1$  (left) and  $\bar{B}_2$  (right) for  $Pr = 1$ ,  $\zeta = 1.1$ ,  $Ra = 5 \times 10^5$  and (a)  $Q = 100$ , (b)  $Q = 1500$ . . . . . 197

- 8.7  $\bar{B}_1$  (top) and  $\bar{B}_2$  (bottom) for  $Pr = 1$ ,  $\zeta = 1.1$ ,  $Ra = 5 \times 10^5$ . Each  $Q$  is represented by a different colour; red represents  $Q = 100$ , green represents  $Q = 500$ , pink represents  $Q = 1000$ , light blue represents  $Q = 2000$ , black represents  $Q = 5000$  and orange represents  $Q = 10000$ . In blue is the basic state magnetic field,  $\mathbf{B}_{BS} = (0, 1, 0)$ .  $Q = 100$  to  $Q = 1000$  are chaotic solutions, whereas  $Q = 2000$  to  $Q = 10000$  are steady solutions. . . . . 198
- 8.8 Kinetic energies in the mean flow for  $Pr = 1$ ,  $\zeta = 1.1$ ,  $Ra = 5 \times 10^6$  and a range of  $Q$ . The top row gives the mean measure of the energy in  $\bar{u}$  (left) and  $\bar{v}$  (right) in red and the variability measure of the energy in blue. Chaotic solutions are marked with a cross, relaxation oscillation solutions with a plus sign, periodic solutions with a square and steady solutions with a dot. The bottom row gives the ratio of the energy in the mean flow to the kinetic energy in the perturbations. . . . . 200
- 8.9 Terms of the mean flow equations, (8.2.8) (top) which drive  $\bar{u}$ , and (8.2.9) (bottom) which drive  $\bar{v}$ , plotted for different  $Q$  and  $Pr = 1$ ,  $\zeta = 1.1$  and  $Ra = 5 \times 10^5$ . In orange are the RS terms, in black are the MS terms, in green are the viscous terms and in blue are the mean flow terms. . . . . 203
- 8.10 Typical sizes of the terms in the mean flow equations (as given by (8.2.10) and (8.2.11)). In red are the RS terms, in black the MS terms and in green the viscous terms for  $Pr = 1$ ,  $\zeta = 1.1$  and (a),  $Ra = 5 \times 10^5$  and (b),  $Ra = 5 \times 10^6$ . The different symbols represent the same solution regimes as they did in figures 8.3 and 8.8. . . . . 206
- 8.11 The RS terms (left-hand column) and MS terms (right-hand column) calculated from the nonlinear code (solid lines) and the RS terms calculated from linear eigenfunctions (dashed lines) for  $Pr = 1$ ,  $\zeta = 1.1$ ,  $Ra = 5 \times 10^5$  and (a)  $Q = 100$ , (b)  $Q = 1000$  and (c)  $Q = 10000$ . The agreement is better for larger  $Q$ . . . . . 207
- 8.12 Kinetic energies in the mean flow for  $Pr = 1$ ,  $\zeta = 0.1$ ,  $Ra = 5 \times 10^5$  and a range of  $Q$ . The top row gives the mean measure of the energy in  $\bar{u}$  (left) and  $\bar{v}$  (right) in red and the variability measure of the energy in blue. Chaotic solutions are marked with a cross and steady solutions with a dot. The bottom row gives the ratio of the energy in the mean flow to the energy in the perturbations. . . . . 209
- 8.13  $\bar{u}$  (left) and  $\bar{v}$  (right) for  $Pr = 1$ ,  $\zeta = 0.1$ ,  $Ra = 5 \times 10^5$  and (a)  $Q = 10000$ , (b)  $Q = 50000$ . . . . . 210

- 8.14 Terms of the mean flow equations, (8.2.8) (top) which drive  $\bar{u}$ , and (8.2.9) (bottom) which drive  $\bar{v}$ , for  $Pr = 1$ ,  $\zeta = 0.1$ ,  $Q = 50000$  and  $Ra = 5 \times 10^5$ . In orange are the RS terms, in black are the MS terms, in green are the viscous terms and in blue are the mean flow terms. . . . . 211
- 8.15 Ratio of the typical sizes of MS to RS terms that drive (a)  $\bar{u}$  and (b)  $\bar{v}$ , as a function of  $Q$ , for  $Pr = 1$  and  $Ra = 5 \times 10^5$ . In black,  $\zeta = 1.1$ , in red,  $\zeta = 0.5$  and in green,  $\zeta = 0.1$ . . . . . 212
- 8.16 Standard deviation,  $\sigma$ , in  $\langle \bar{u} \rangle$  (left) and  $\langle \bar{v} \rangle$  (right) as a function of (a)  $Q$  and (b)  $\zeta Q$ , for  $Pr = 1$ ,  $Ra = 5 \times 10^5$  and  $\zeta = 1.1$  (black) and  $\zeta = 0.1$  (green). . . . . 213
- 8.17 Energies in the kinetic energy and magnetic energy for  $Pr = 0.1$ ,  $\zeta = 0.5$ ,  $Ra = 5 \times 10^5$  and a range of  $Q$ . Chaotic solutions are marked with a cross and quasi-periodic solutions with a triangle. . . . . 214
- 8.18 Energies in the mean flow for  $Pr = 0.1$ ,  $\zeta = 0.5$ ,  $Ra = 5 \times 10^5$  and a range of  $Q$ . The mean measure of the energy is given in red and the variability measure in blue. Chaotic solutions are marked with a cross and quasi-periodic solutions with a triangle. The bottom row presents the ratios of the energies in the mean flows to the energy in the perturbations. . . . . 215
- 8.19  $KE_{\text{pert}}$  (a),  $ME_{\text{pert}}$  (b),  $\theta^2$  (c) and  $Nu$  (d) as a function of  $Ra$  for  $Pr = 0.1$ ,  $\zeta = 0.5$  and  $Q = 25000$  (crosses),  $Q = 50000$  (dots). . . . . 216
- 8.20 Time-dependent  $\bar{u}$  (left) and  $\bar{v}$  (right) for  $Pr = 0.1$ ,  $\zeta = 0.5$ ,  $Ra = 5 \times 10^5$  and (a)  $Q = 20000$ , (b)  $Q = 35000$ . . . . . 217
- 8.21 Terms of the mean flow equations, (8.2.8) (top) which drive  $\bar{u}$ , and (8.2.9) (bottom) which drive  $\bar{v}$ , for  $Pr = 0.1$ ,  $\zeta = 0.5$ ,  $Q = 35000$  and  $Ra = 5 \times 10^5$ . In orange are the RS terms, in black are the MS terms, in green are the viscous terms, in blue are the mean flow terms and in red are the mean flows themselves. 218
- 8.22 Ratio of the typical sizes of MS to RS terms that drive (a)  $\bar{u}$  and (b)  $\bar{v}$ , as a function of  $Q$ , for  $\zeta = 0.5$  and  $Ra = 5 \times 10^5$ . In black,  $Pr = 1$  and in red,  $Pr = 0.1$ . . . 219

## List of tables

- 3.1 A table of solutions to the equations (3.6.60) and (3.6.61) for  $Pr = 0.1$ ,  $\zeta = 0.1$ ,  $Q = 10000$  and  $\phi = \frac{\pi}{2}$ . These are an example of the solutions used as an initial estimate in the numerical code that solves for the solution when  $\phi = \frac{\pi}{4}$ . . . . . 58
- 6.1 A table to show in which runs large-scale steady solutions occur. Also shown, are runs with parameters close to those runs which have large-scale solutions but which are not found to reach the high  $Nu$ , steady states in which the large-scale structures are observed. . . . . 139



# Chapter 1

## Introduction

### 1.1 Motivation

For centuries, scientists have been observing the Sun and its Solar System. With the advent of new observational techniques an ever clearer picture of the Universe is being built, though many of the phenomena observed can not be well explained. It is our hope that by studying such phenomena through mathematical modelling, and relating the results to observations, our understanding will be improved.

In particular, large-scale mean flows have long been observed in many systems of geophysical and astrophysical importance, such as planets, stars, galaxies and accretion disks. Despite this, mean flow generation is not a well understood process; neither is the interaction of mean flows with other physical processes such as magnetic field generation. Well-known examples of mean flows include the differential rotation in the Sun, the large-scale zonal jets on Jupiter and the jet streams in the Earth's atmosphere. The next section examines these examples in more detail and describes the physical mechanisms that might cause them.

### 1.2 Examples of mean flows

To begin, we define loosely what is meant by a mean flow. Fluid flow can be split into a mean part and a fluctuating part, where the mean flow is the part of the fluid velocity that remains after an averaging process (e.g., Reynolds decomposition). We will define this more rigorously in due course. Often, the mean flow is much larger than the small-scale turbulence that occurs along

with it. We now describe some of these large-scale flows, the physical situations in which they occur and their implications.

### 1.2.1 The Sun

The Sun is a mass of plasma that lies at the centre of the Solar System. It has a radius of approximately  $6.955 \times 10^8$  m and a mass of approximately  $1.989 \times 10^{30}$  kg (Williams (2004)). The physical processes occurring in the Sun have a large effect on space weather (National Research Council (1997)) and so it is important to understand them. This activity can have terrestrial implications, for example, the Sun ejects large quantities of matter and radiation in so-called coronal mass ejections and these can cause damage to satellites and disrupt communication networks (National Research Council (2008)). Observations of the Sun, over many years, have enabled us to gain a deeper understanding of the structure of the Sun. A detailed review of the Sun and its properties is found in Priest (1984) or Stix (2004); we outline some key features in the following sections.

#### Structure of the Sun

The Sun can be thought of as consisting of a number of distinct regions, defined by the material in the region and the physical processes that occur there, see figure 1.1. At the centre of the

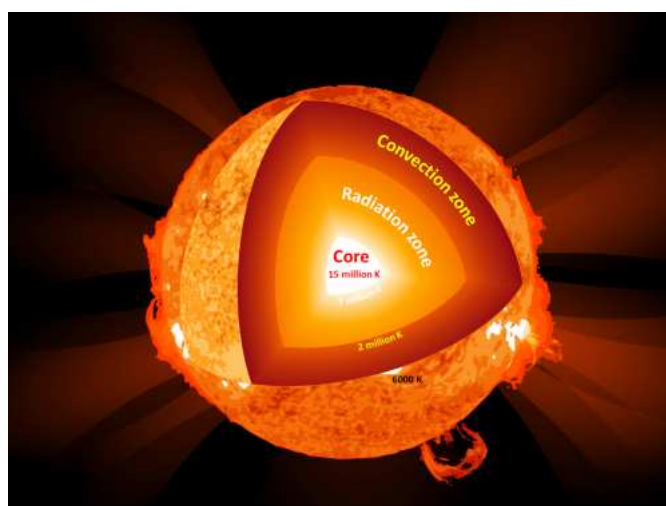


Figure 1.1: Interior structure of the Sun. The core extends to 20-25% of the radius and is surrounded by the radiation zone which extends to approximately 70% of the radius. The outer 30% is occupied by the convection zone. Image source: <http://phys.org/news/>.

Sun is the solar core which extends to 20-25% of the radius. In the core, temperatures are hot enough for nuclear fusion to take place, so that hydrogen can be converted into helium, and in doing so, create vast amounts of energy. This energy is carried outwards by radiation into the next region, known as the radiative zone, where the energy continues to be radiated outwards, until approximately 70% of the distance of the solar radius is reached. In the region occupied by the outer 30% by radius, the Sun is convectively unstable and this region is therefore known as the convective zone. The region between the radiative and convective zones is a shallow region of radial shear, known as the tachocline (Spiegel & Zahn (1992)), it will be described in more detail later. In the convective zone, energy is transported by the convection towards the surface. At the photosphere, i.e., the visible surface of the Sun, hotter material that has been convected outwards from the interior is cooled and therefore its density increases, this causes the material to sink towards the base of the convection zone and the process begins again. These convective motions are characterised at the surface as solar granules and supergranules. Above the photosphere is the solar atmosphere, but we are interested in the physical processes that occur in the solar interior, more specifically in the convection zone and so we shall not delve deeper into the solar atmosphere here.

It has been known for some time that, by tracking visible surface features, the Sun is rotating faster at the equator than it is at the poles - it is differentially rotating (see e.g., Ward (1966)). However, little was known about the internal rotation profile of the Sun until relatively recently, when a technique known as helioseismology was developed. Helioseismology measures Doppler shifts at the solar surface that result from wave oscillations in the interior and the data obtained can be inverted to infer information about the large-scale structure and rotation of the solar interior. Details of the technique are given in Christensen-Dalsgaard (2002). Using this technique, the rotation profile given in figure 1.2 has been deduced. From the profile we see that the radiative zone is in solid body rotation but the convection zone is rotating faster at the equator than it is at the poles, with lines of constant rotation rate being radial, thus confirming the differential rotation previously observed. The period of rotation at the poles is approximately 33 days whereas at the equator it is only 25 days (Schou *et al.* (1998)). The smooth transition between the radiation and convection zones occurs at the tachocline and as a result the tachocline is a layer of strong shear (Hughes *et al.* (2007)). It is the convective turbulence in the convective zone that appears to drive motions that result in differential rotation, these motions persist on averaging and are an example of a mean flow. This thesis aims to provide simple models for examining such a convectively driven mean flow.

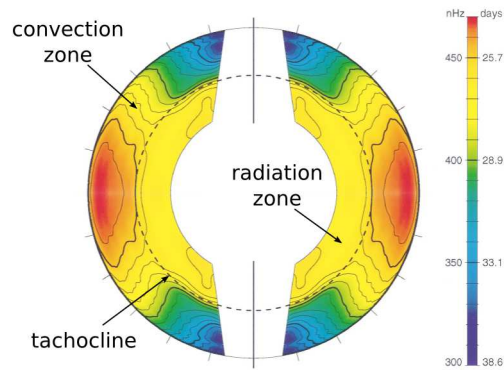


Figure 1.2: Rotation profile of the Sun. The radiation zone is in solid body rotation, whereas the convection zone is differentially rotating. In between these two regions is a thin layer known as the tachocline. Image from Schou *et al.* (1998).

### Magnetic nature of the Sun

The Sun consists of electrically conducting fluid which allows it to have a magnetic field. The process by which this field is generated is known as dynamo action and is an active research topic in its own right (see Ossendrijver (2003) or Tobias & Weiss (2007) for a review) but it is believed that differential rotation assists the dynamo process. The Sun's active magnetic field affects the physical processes occurring in the Sun and therefore, ideally, the effect of a field should be considered in any solar model. For example, the differential rotation of the Sun causes magnetic field lines to twist and, over time, cause magnetic field loops to erupt from the Sun's surface, this leads to the emergence of so-called sunspots which can be observed as dark spots on the Sun's surface (e.g., Tobias (2002)). Observations of sunspots over many years have led to the recognition of a sunspot cycle - the periodic change in number and location of sunspots over time. An illustration of this cycle is given in figure 1.3. For obvious reasons, this diagram is known as a butterfly diagram (Maunder (1904)) and from it we can observe that the sunspot cycle has an eleven year period. During this cycle, sunspots increase in number and move towards the equator before decreasing in number, then the cycle starts again. Each time the cycle starts again, the magnetic field switches polarity and as a result the complete magnetic cycle actually occurs over a 22 year period, as shown by figure 1.4. For a comprehensive review of sunspots, see Thomas & Weiss (2008).

Clearly, to understand the Sun, it is necessary to understand how convection interacts with rotation and magnetic fields. This is a primary aim of our study.

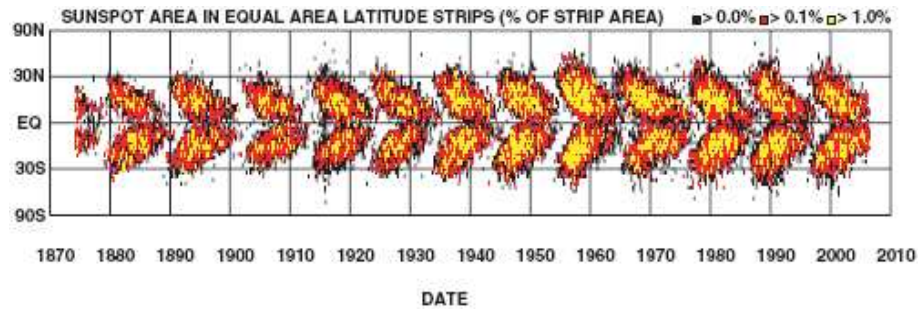


Figure 1.3: Solar butterfly diagram. The location of sunspots as a function of time and latitude. In each eleven year cycle, sunspots increase in number, move towards the equator and then decrease in number. Image from Hathaway (2010).

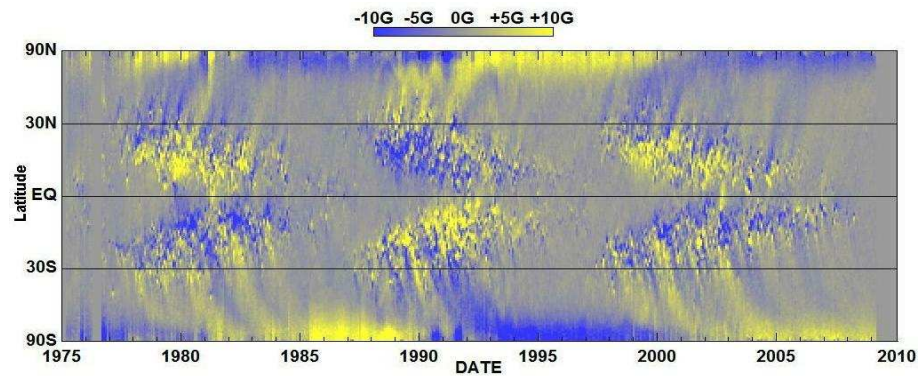


Figure 1.4: Magnetic butterfly diagram. The polarity of the magnetic field associated with sunspots switches after each 11 year cycle, resulting in a complete cycle period of 22 years. Image source: David Hathaway, NASA.

## 1.2.2 Jupiter

With a radius of approximately  $7 \times 10^7$  m and a mass of approximately  $1.9 \times 10^{27}$  kg (Williams (2007)), Jupiter is the largest planet in the Solar System. It is believed to consist of a dense metallic core surrounded by an outer layer atmosphere of hydrogen and helium (Stevenson & Salpeter (1976), Guillot *et al.* (2004)). The atmosphere is thought to be about  $1.5 \times 10^7$  m in extent and it is in the atmosphere that mean flows are observed. It is known that Jupiter has a magnetic field, which like the Sun is believed to be driven by dynamo action. Though the mechanism is not fully understood, it is thought the magnetic field is generated in the metallic core, see e.g., Jones (2011). The mean flows on Jupiter result in the very distinct, banded structure we observe, see figure 1.5(a). This banded structure is made up of an array of prograde and retrograde zonal flows and whilst they have been observed for centuries it is not fully understood what causes them.

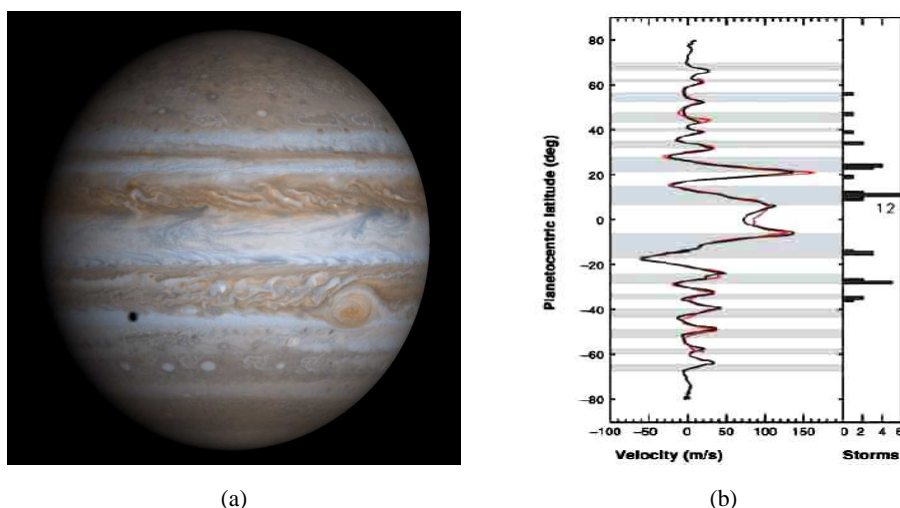


Figure 1.5: (a) Image of Jupiter showing the distinct array of zonal jets present in its atmosphere. Image source: <http://astronomy.nyu.edu.cn>. (b) Data relating to the zonal flows obtained from the Voyager and Cassini missions, the two sets of data are very similar. Image from Porco *et al.* (2003).

Data relating to the zonal flows was obtained on two separate missions by the Voyager (Limaye (1986)) and Cassini spacecraft (Porco *et al.* (2003)), see figure 1.5(b). Despite these missions being 20 years apart, the data for the zonal flows was found to be almost identical, highlighting the steady nature of the jets.

There have been different models proposed to describe the banded structure and the origin of the jets. One model, introduced by Busse (1976), suggests that the zonal flows are driven by convection in the deep interior. A second model, proposes the zonal flows are confined to a stably stratified region at the surface (Williams (1979), Dowling & Ingersoll (1989)) in which case, the flows are driven by small-scale turbulence, perhaps caused by thunderstorms. Both models have shortcomings when trying to reproduce the exact banded structure of the Jovian atmosphere. The deep convection models are often able to reproduce the prograde equatorial jet and its flanking jets, e.g., Christensen (2001, 2002), Heimpel *et al.* (2005), but do not reproduce the high latitude jets. On the other hand, the shallow layer models are able to produce high-level jets but not the equatorial flows, e.g., Cho & Polvani (1996). Although more recently, Scott & Polvani (2007) and Warnford & Dellar (2014) have had some success by incorporating Newtonian cooling into their shallow layer models. Vasavada & Showman (2005) provided a review of observations, theory, experiments and simulations of Jupiter's atmosphere, they concluded that Jupiter's dynamics are probably a result of both deep and shallow processes.

### 1.2.3 Other examples

We have discussed the mean flows of the Sun and Jupiter in some detail but there are many other examples of large-scale mean flows in nature. We describe some of them briefly here.

#### Earth's atmosphere

The circulation in the Earth's atmosphere is another example of a large-scale flow present in nature. An extensive description of the circulation in the atmosphere can be found in Vallis (2006). We describe the key aspects briefly here. There are two main types of circulation: the meridional circulation, i.e., along lines of constant longitude, and the zonal flows, i.e., along lines of constant latitude. The circulation is driven by the rotation of the Earth and solar heating; they act to transport energy from the equator to the poles by convection. There are three distinct circulation cells acting meridionally in each hemisphere, as shown in figure 1.6. The cell closest to the equator is known as the Hadley cell (Hadley (1735)) and it works as follows: the warmer air at the equator rises and moves polewards and then sinks in the subtropics. Some of the air that sinks to the surface at the subtropic latitudes returns to the equator to complete the Hadley cell. The rest of the sinking air moves towards the poles where, at roughly  $60^\circ$  latitude, it meets cold air moving down from the poles. The low surface pressure at  $60^\circ$  latitude causes the air to rise; some of this air returns to  $30^\circ$  latitude to complete the Ferrel cell. The third circulation cell is known as the Polar cell, and it is completed when some of the air circulated towards the equator from the poles, meets the Ferrel cell and is returned to the poles.

The zonal flows, known as jet streams, arise because the air from the equatorial region is warm compared to the air in the Ferrel cell, and so there is a strong temperature gradient between the two air masses. The resulting jets, known as subtropical jets, flow from west to east in both hemispheres - the wind does not flow from hot to cold directly but is deflected by the Coriolis effect (i.e., to the right in the northern hemisphere and to the left in the southern hemisphere). Similarly, the meeting of the warm air from mid-latitudes and the cold air from the poles causes another jet to form above the air masses, in much the same way as the subtropical jets. Again these jets occur in each hemisphere and they are known as the polar jets.

In this thesis, we focus on mean flows driven in astrophysical bodies such as the Sun, we mention the Earth's atmosphere as another example of the ubiquitous nature of mean flows only and will not consider it any further.

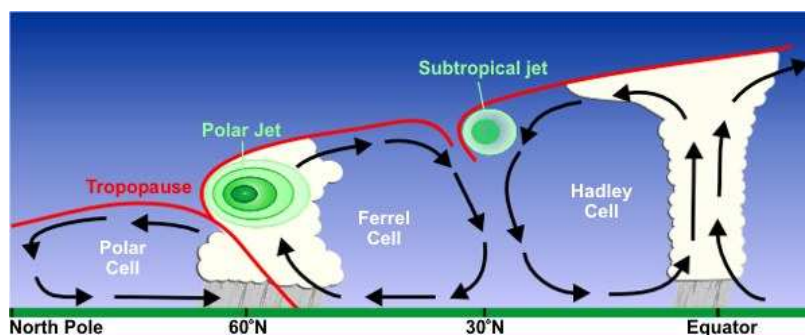


Figure 1.6: Circulation of air in the Earth's atmosphere. There exist three distinct cells of meridional circulation in each hemisphere: (i) the Hadley cell, (ii) the Ferrel cell and (iii) the Polar cell. In addition, large-scale zonal flows exist in the form of the polar and subtropical jets. Image source: [www.srh.noaa.gov](http://www.srh.noaa.gov).

### Other planets

In addition to data about Jupiter, the Cassini mission provided details about Saturn (see Porco *et al.* (2005)). Along with images from the Hubble telescope (Pérez-Hoyos *et al.* (2005)), this data has been able to enlighten us about the zonal flow pattern on Saturn. Like Jupiter, Saturn's atmosphere consists of a prograde equatorial jet with multiple smaller-scale jets at higher latitudes. However, Saturn's equatorial jet is broader than Jupiter's, and the bands are less striking in colour, hence Saturn is a less well-known example of strong zonal flow. Porco *et al.* (2005) also showed that at higher latitudes on Saturn, there are only three prograde jets in each hemisphere, in contrast to many more on Jupiter. Moreover, there is very little retrograde surface flow on Saturn, again in contrast to Jupiter.

As well as the gas giant planets, Jupiter and Saturn, the ice giant planets, Uranus and Neptune, are also known to have strong zonal flows. Imaging data from the Hubble and Keck telescopes has provided information about the zonal flow on these planets (see Hammel *et al.* (2001, 2005)). In contrast to Jupiter and Saturn, the equatorial jets on Uranus and Neptune are retrograde and the higher latitudes do not contain multiple jets. Instead, there is a high-latitude prograde jet in each hemisphere. The zonal flow profiles of Jupiter, Saturn, Uranus and Neptune as found in Sukoriansky *et al.* (2002) are shown in figure 1.7.

As explained before, shallow layer systems have been used to model atmospheres of giant planets and they often result in retrograde equatorial jets, in agreement with the observations for Uranus and Neptune. Therefore, these models have been favoured for investigating the zonal flows on the ice giant planets (e.g., Cho & Polvani (1996)). As an alternative, Aurnou *et al.* (2007) used

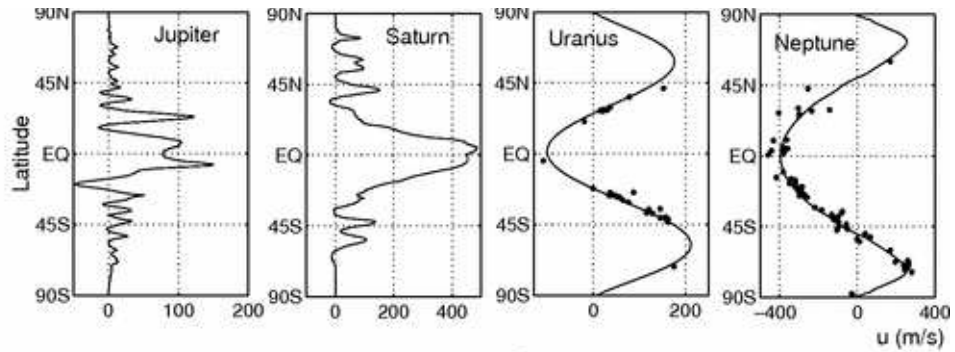


Figure 1.7: Observed zonal flow profiles of Jupiter, Saturn, Uranus and Neptune. Figure adapted from figure 2 of Sukoriansky *et al.* (2002).

three-dimensional convection models to examine the flows on Uranus and Neptune.

### Other stars

Whilst we have described the Sun in some detail, it is not the only star that exhibits differential rotation. For example, the rapidly rotating star system, AB Doradus, is also believed to be differentially rotating (Donati & Collier Cameron (1997)). The interior rotation rate profile of the Sun is well known from helioseismology (see section 1.2.1) but for some time, the Sun was the only star for which we had measurements of its internal rotation rate. Although, by tracking surface features, the surface rotation rate of other stars could be deduced, (see e.g., Donati *et al.* (1999) and Collier Cameron *et al.* (2002)). More recently, asteroseismology missions have been carried out to probe the internal rotation profiles of other stars e.g., the Kepler mission (see Gilliland *et al.* (2010)). Such missions, as well as the previous surface measurements, showed that other stars are also differentially rotating.

Whilst the aim of this study is to examine the interaction of convection, rotation, magnetic fields and the driving of mean flows in a simplified model, the work has been conducted with applications to stellar physics in mind.

## 1.3 Mechanisms for mean flow generation

In the previous section, we described some examples of mean flows observed in a geophysical and astrophysical context. The mechanisms of their generation depends upon the exact physical setting in which they are found. We have seen that the interaction of convection with rotation

and magnetic fields results in the observed solar differential rotation. Whereas, the mechanism for zonal flow in Jupiter's atmosphere is still not fully understood. As we have seen, it is thought that the flow may be a result of convective processes in the deep interior, or a result of processes occurring in a stably stratified weather layer, or possibly a combination of the two. This thesis examines convection as a mechanism for mean flow generation and therefore we will focus on convection hereafter.

## 1.4 Convection

As has been discussed in the preceding sections, convection is an important mechanism in the driving of mean flows. Broadly, convection is a process that transports heat energy in a fluid by fluid motions. The general idea behind thermal convection is that a parcel of warm fluid is less dense than a cooler parcel, and so, if a fluid parcel is warmed, it will become less dense than its surroundings and rise because of buoyancy effects. On the other hand, the cooler fluid will sink to replace the initial fluid, resulting in motions within the fluid. This convective motion transports heat energy in the fluid and leads to fluid mixing.

### 1.4.1 Rayleigh-Bénard convection

The most simple mathematical description of convection is encapsulated in the Rayleigh-Bénard system, named after Henri Bénard and Lord Rayleigh. Bénard conducted experiments on a layer heated from below (Bénard (1900, 1901)) and Rayleigh (1916) carried out a mathematical linear stability analysis of the same system. The Rayleigh-Bénard system consists of a fluid layer where the lower boundary is maintained at a higher temperature than the upper boundary. Initially, the fluid is taken to be at rest. As described above, the hotter, less dense fluid will want to rise due to buoyancy and the system is unstable. The natural tendency of the fluid to redistribute itself to form a stable configuration is opposed by the fluid viscosity. Therefore, the temperature gradient must be large enough to overcome this opposition before the instability will onset. Rayleigh showed that whether a fluid layer heated from below is stable or not can be determined from a dimensionless parameter that relates the size of the temperature gradient to the size of the viscous effects. This parameter is known as the Rayleigh number and will play an important role throughout this thesis; it will be defined in section 2.3.4.

In subsequent years, the simple Rayleigh-Bénard model was built upon and generalised in Jeffreys (1926, 1928). Chandrasekhar (1961) provides a comprehensive review of the mathematical linear

theory for a number of different situations. Details of other work relating to the linear theory of convection is given in Chapters 3 and 4.

### 1.4.2 Experiments

A useful tool for studying convection is through experiments. Often, experiments can explore parameter regimes that cannot be studied theoretically or numerically. There has been an abundance of experimental studies of convection, beginning with the experiments of Bénard in 1900. Schmidt & Milverton (1935) confirmed experimentally the predicted onset of convection, as derived by Rayleigh. In subsequent years, the experiments were repeated by many, including Malkus (1954), who was able to achieve greater precision. Rossby (1969) added rotation to the systems of previous studies. As experimental techniques were improved and new ones developed, experiments involving convection in deeper layers were performed, e.g., Castaing *et al.* (1989), they not only had a deeper layer but were able to reach higher Rayleigh numbers. Liu & Ecke (1997) studied rotating experiments in a deeper layer than in the earlier experiments such as those undertaken by Rossby (1969). More recently, experimentalists have tried to develop scaling laws relating to heat transport, for example, King *et al.* (2009, 2012) try to establish laws for the dependence of the efficiency of heat transfer (as measured by the Nusselt number) on the thermal driving (as measured by the Rayleigh number) in rotating Rayleigh-Bénard convection.

### 1.4.3 Nonlinear studies

Linear theory, as introduced by Rayleigh and described by Chandrasekhar (1961), is only capable of determining whether a system is convectively stable or not and if not, at what rate we would expect to see growth. It is not able to tell us anything about the dynamics of the fluid after the initial period of growth. To determine this behaviour, it is required that the nonlinear effects are accounted for in the mathematical description of the convection. Early studies of nonlinear convection were carried out by Malkus & Veronis (1958), they analysed the nonlinear stability of the system to finite amplitude perturbations and established whether or not a system would reach a thermal equilibrium. Veronis (1959) extended this idea to incorporate rotation.

There is only so much progress that can be made analytically when studying the nonlinear regime, but with the advent of computers, techniques were developed to solve the equations numerically. Veronis (1966) was one of the first to do this when he studied two-dimensional Rayleigh-Bénard convection using a numerical algorithm to solve the equations. He later added rotation to the

system and solved it using a similar algorithm, see Veronis (1968). Because of the lack of computing power at the time, these simulations were only conducted at very moderate Rayleigh numbers. Moore & Weiss (1973) studied two-dimensional Rayleigh-Bénard convection using a different numerical approach to Veronis (1966) and found they were able to study a much larger range of parameters. With the development of faster, more efficient computers and better numerical algorithms, Rayleigh-Bénard convection was able to be studied in a lot more depth numerically. For example, Vincent & Yuen (1999, 2000) were able to reach Rayleigh numbers of up to several orders of magnitude higher than in previous studies in their two-dimensional simulations, this led to the discovery of behaviour not seen before, or predicted by any theory. Computing resources now allow for the study of fully nonlinear convection in three dimensions.

As mean flow generation is a nonlinear process, the ability to solve the nonlinear equations numerically has led to a large number of studies of convection-driven mean flows. Mean flows generated by convection have been studied using a variety of different models. Earlier models tended to treat the fluid as incompressible and use the Boussinesq approximation (described in section 2.3) as this is computationally the simplest thing to do. Hathaway & Somerville (1983) performed three-dimensional simulations of Boussinesq convection in a so-called tilted  $f$ -plane geometry, which can be used as a local approximation to a region of a spherical body. The tilted  $f$ -plane is a plane layer in which the rotation vector can be oblique to gravity (see section 1.5 for more details). The plane layer geometry is considered the simplest to handle computationally. Hathaway & Somerville (1986, 1987), extended the work of Hathaway & Somerville (1983) to investigate the interaction between convection, rotation and shear flows by imposing a background shear flow. Other work relating to Boussinesq convection on a tilted  $f$ -plane was done by Julien & Knobloch (1998) who used asymptotic theory to establish constraints on the transport properties of the flows. They compared the results of their asymptotic analysis to the results of the numerical simulations of Hathaway & Somerville (1983) and found good agreement. Saito & Ishioka (2011) revisited the problem of the interaction of convection with rotation in an imposed shear flow. They were able to examine a larger region of parameter space than Hathaway & Somerville (1987) and identified a feedback mechanism resulting in an accelerated mean flow.

The plane layer model, as just described, is a local model, and when the axis of rotation is allowed to vary from the direction of gravity, it can be used to represent a local region at different latitudes of a spherical body, but this is a crude approximation. In order to capture some of effects of the curvature of a spherical body, Busse (1970) introduced an annulus model. This geometry has been used in attempts to model the zonal flow on Jupiter, for example, Jones *et al.* (2003)

used a rotating annulus model in a two-dimensional study and incorporated the possibility of boundary friction which allowed for the more realistic multiple jet solutions to be found more easily. Rotvig & Jones (2006) examined this annulus model more extensively and identified a bursting mechanism that occurs in the convection in some cases. Three-dimensional Boussinesq simulations were carried out in a spherical shell geometry by Christensen (2001, 2002) who was using the zonal winds on large gas planets as his motivation.

As pointed out by many of these Boussinesq studies, they are only to be treated as a starting point for the investigation of mean flows in astrophysical situations, since in reality there exist large density gradients across the fluid in question and the Boussinesq approximation neglects these. This has led to the consideration of models with a compressible fluid, but because of the particularly demanding nature of the computations involved in solving the fully compressible equations, the anelastic approximation is often used (see section 2.4 for a description of the anelastic approximation). Jones & Kuzanyan (2009) used the anelastic approximation with a spherical shell geometry to perform three-dimensional simulations of the zonal flow of giant planets. They also comment on the differences between the Boussinesq and compressible cases.

In the late 20th century, an anelastic code was developed for use on parallel architecture to greatly help with large three-dimensional simulations. The code is based upon spherical harmonic decomposition and is therefore given the name Anelastic Spherical Harmonic (ASH) code, see Clune *et al.* (1999). The code has since been used to perform a large number of simulations of astrophysical flows. For example, Elliott *et al.* (2000) and Brun & Toomre (2002) used the code to simulate differential rotation and meridional circulation in the Sun. The early simulations using the ASH code did not include the effects of a magnetic field, but later, such effects have been included in simulations of the anelastic magnetohydrodynamic (MHD) equations. These have been used to study stellar convection and dynamos, for example, Browning (2008) studied fully convective stars, Brun *et al.* (2005a) studied dynamos in A-type stars and Brown *et al.* (2007), Brown *et al.* (2011) examined dynamos in rapidly rotating suns and young solar type stars respectively.

Even though fully compressible simulations are extremely computationally demanding, there have been some three-dimensional simulations of fully compressible convection. These include Brummell *et al.* (1996), Brummell *et al.* (1998) and Chan (2001) who are concerned with differential rotation in fully convective, plane layer models. In this thesis we will only investigate Boussinesq and anelastic models.

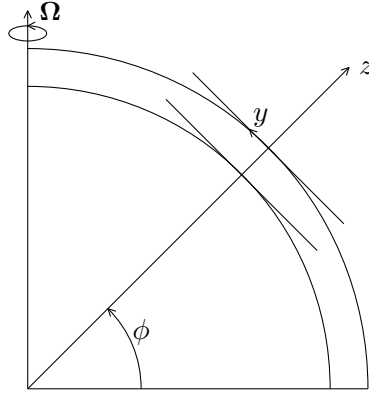


Figure 1.8: Hathaway model. A schematic of the model used by Hathaway *et al.* (1980). It consists of a plane layer taken at a latitude  $\phi$  on a spherical body. As a result the rotation vector is oblique to gravity and is given by  $\mathbf{\Omega} = (0, \Omega \cos \phi, \Omega \sin \phi)$ .  $z$  is directed upwards,  $y$  is directed northwards and  $x$  (into the page) is directed eastwards.

## 1.5 Hathaway model

The tilted f-plane geometry, as briefly discussed in the previous section, is a plane layer where the rotation vector is oblique to gravity. Hathaway *et al.* (1979, 1980) utilised a tilted plane layer model for studying the onset of convection when both a vertical and a horizontal temperature gradient are imposed. We describe their system as it is used as the starting point of our study and the tilted f-plane will be the geometry we use for the models considered throughout this thesis. The model of Hathaway *et al.* (1980) consists of a local plane layer of fluid rotating about an axis that is oblique to gravity, used to represent different latitudes on a spherical body (see figure 1.8). Gravity is in the vertical direction and the rotation vector is at an angle  $\phi$  from the horizontal.  $z$  is measured upwards,  $y$  is measured northwards and  $x$  is measured eastwards. The rotation vector is then given by  $\mathbf{\Omega} = \Omega(0, \cos \phi, \sin \phi)$ . A temperature gradient is imposed in both the vertical ( $z$ ) and horizontal ( $y$ ) directions. Hathaway *et al.* (1980) enforce a fixed temperature, no slip boundary condition on the top and bottom boundaries. This model will form the basis of our study, however we will adapt and extend the model to examine different physical situations. A mathematical description of the model we use is derived in the next chapter.

## 1.6 Thesis outline

Having described the motivation for studying convection-driven mean flows and given an overview of existing models for such a study, our objective is to extend the work of others to investigate the effects of a horizontal temperature gradient, magnetic field and compressibility on mean flows driven by convection. To this end, this thesis is organised in the following way.

In Chapter 2, we introduce our model, which is an extension of the model of Hathaway *et al.* (1980), as described in section 1.5. We then present a derivation of the governing equations for our system, and cast them into different forms for use in later chapters.

Chapters 3 and 4 lay important foundations for a nonlinear study by considering the linear theory. Chapter 3 extends the work of Hathaway *et al.* (1980) to more physically relevant regimes and to incorporate a horizontal magnetic field. Chapter 4 introduces an oblique rotation vector into a plane layer model of stratified convection, where previous models have only considered vertical rotation.

Further groundwork for a nonlinear study is carried out in Chapter 5, where a detailed description of the numerical methods used to solve the fully nonlinear equations is given. The construction of an efficient, pseudospectral Fourier-Chebyshev code is first described for the purely hydrodynamic system. The chapter then finishes by explaining how extensions to include the effects of a magnetic field and stratification are implemented.

With the foundations in place, Chapters 6-8 are devoted to a nonlinear study of convection, with a focus on establishing the behaviour of mean flows in a number of different systems. Chapter 6 investigates the effect of a horizontal temperature gradient, Chapter 7 examines the effect of imposing a background density stratification on the fluid layer and Chapter 8 considers the inhibition of mean flow generation by a magnetic field.

To conclude the thesis, Chapter 9 summarises the main results, discusses applications and limitations of the work presented, before indicating how the work might be extended.



## Chapter 2

# Derivation of governing equations

The models used to study many of the phenomena described in Chapter 1 make different assumptions depending on their motivation, and therefore, the equations used to describe them take different forms, but the majority have their origins in the fluid and magnetohydrodynamic (MHD) equations. There are a number of textbooks that give a comprehensive introduction to these equations, e.g., Chandrasekhar (1961), Batchelor (2000), Davidson (2001). In this chapter, we introduce the model we use to study convection, and derive the equations governing such a model. We also manipulate the equations into a number of different forms that we will utilise in later chapters. Furthermore, we discuss some of the approximations that go into the models and their physical relevance.

### 2.1 Fluid and MHD equations

To begin our study, we require the equations governing the magnetohydrodynamic flow of an electrically conducting, viscous fluid with varying density and temperature and the associated magnetic field. We shall denote by  $\rho(\mathbf{x}, t)$  the fluid density, by  $\mathbf{u}(\mathbf{x}, t) = (u, v, w)$  the fluid velocity, by  $T(\mathbf{x}, t)$  the fluid temperature and by  $\mathbf{B}(\mathbf{x}, t) = (B_1, B_2, B_3)$  the magnetic field at a position  $\mathbf{x}$  and time  $t$ .

#### 2.1.1 Continuity equation

The first equation we shall be concerned with is the continuity equation, this is a statement of conservation of mass and is given by

$$\frac{\partial \rho}{\partial t} + \nabla \cdot (\rho \mathbf{u}) = 0. \quad (2.1.1)$$

### 2.1.2 Momentum equation

The second equation is the momentum equation (also called the Navier-Stokes equation or equation of motion) and is given in an inertial frame by

$$\rho \left( \frac{\partial \mathbf{u}}{\partial t} + (\mathbf{u} \cdot \nabla) \mathbf{u} \right) = -\nabla P + \mathbf{F} + \nabla \cdot (\mu \boldsymbol{\tau}), \quad (2.1.2)$$

where  $\boldsymbol{\tau}$  is the viscous stress tensor given by

$$\tau_{ij} = \frac{\partial u_i}{\partial x_j} + \frac{\partial u_j}{\partial x_i} - \frac{2}{3} \nabla \cdot \mathbf{u} \delta_{ij}, \quad (2.1.3)$$

$P$  is the isotropic pressure and  $\mu$  is the dynamic viscosity. We have assumed that the fluid is Newtonian and so the stress is proportional to the rate of strain of the fluid.  $\mathbf{F}$  is the external force acting on the fluid.

There are two external forces that are of importance in this thesis:

1. The buoyancy force due to gravity, given by  $\rho \mathbf{g} = \rho(0, 0, -g)$ , where  $\mathbf{g}$  is the acceleration due to gravity.
2. The Lorentz force due to the magnetic field, given by  $\mathbf{j} \times \mathbf{B}$ , where  $\mathbf{j} = (j_1, j_2, j_3) = \frac{1}{\mu_0} (\nabla \times \mathbf{B})$  is the (non-relativistic) current and  $\mu_0$  is the permeability of free space.

In addition, as we are interested in rotating fluids, we have to consider the Coriolis effect which results in a modification to the governing equations. The Coriolis force is a pseudo-force that results from the acceleration of a non-inertial reference frame; it is given by  $2\rho \boldsymbol{\Omega} \times \mathbf{u}$ , where  $\boldsymbol{\Omega}$  is the angular velocity vector.

With these external forces and the Coriolis effect considered, the momentum equation (2.1.2) in a rotating frame becomes

$$\rho \left( \frac{\partial \mathbf{u}}{\partial t} + (\mathbf{u} \cdot \nabla) \mathbf{u} \right) = -\nabla p - \rho g \hat{\mathbf{e}}_z - 2\rho \boldsymbol{\Omega} \times \mathbf{u} + \frac{1}{\mu_0} (\nabla \times \mathbf{B}) \times \mathbf{B} + \nabla \cdot (\mu \boldsymbol{\tau}), \quad (2.1.4)$$

where  $p = P - \frac{1}{2} |\boldsymbol{\Omega} \times \mathbf{x}|^2$  is a modified pressure to account for the centrifugal acceleration which can be written  $-\frac{1}{2} \nabla (|\boldsymbol{\Omega} \times \mathbf{x}|^2)$ .

### 2.1.3 Temperature equation

The third governing equation results from conservation of energy and leads to a relevant equation for heat conduction (see e.g., Hurlburt *et al.* (1996))

$$\rho \frac{\partial}{\partial t} (c_v T) + \rho (\mathbf{u} \cdot \nabla) (c_v T) = k \nabla^2 T - p \nabla \cdot \mathbf{u} + \Phi + \Upsilon, \quad (2.1.5)$$

where  $\Phi$  represents viscous heating and is given by  $\Phi_{ij} = \frac{\mu}{2}(\frac{\partial u_i}{\partial x_j} + \frac{\partial u_j}{\partial x_i})^2 - \frac{2}{3}\mu(\nabla \cdot \mathbf{u})^2$  and  $\Upsilon = \frac{\eta}{\mu_0}(\nabla \times \mathbf{B})^2$  represents ohmic heating, with  $\eta$  being the magnetic diffusivity.  $c_v$  represents the specific heat at constant volume and  $k$  is the thermal conductivity.

### 2.1.4 Induction equation

Our final equation is an evolution equation for the magnetic field, it can be obtained in the following way: Ohm's law, for a moving conductor, gives us that the electric field,  $\mathbf{E}$ , is related to the magnetic field by

$$\begin{aligned}\mathbf{E} &= \frac{\mathbf{j}}{\sigma} - \mathbf{u} \times \mathbf{B} \\ &= \frac{1}{\mu_0\sigma}(\nabla \times \mathbf{B}) - \mathbf{u} \times \mathbf{B},\end{aligned}\tag{2.1.6}$$

where  $\sigma$  is the conductivity of the fluid. Note, we have made the MHD approximation which assumes the above form for Ohm's law and that all speeds are non-relativistic. Equation (2.1.6), when combined with Faraday's law, which is given by

$$\nabla \times \mathbf{E} = -\frac{\partial \mathbf{B}}{\partial t},\tag{2.1.7}$$

gives

$$\frac{\partial \mathbf{B}}{\partial t} = \nabla \times (\mathbf{u} \times \mathbf{B}) + \eta \nabla^2 \mathbf{B},\tag{2.1.8}$$

where we have set  $\eta = \frac{1}{\mu_0\sigma}$  to be constant and used the vector identity  $\nabla \times (\nabla \times \mathbf{B}) = -\nabla^2 \mathbf{B}$ , which relies on the fact the magnetic field is solenoidal ( $\nabla \cdot \mathbf{B} = 0$ ). Equation (2.1.8) is known as the induction equation.

### 2.1.5 Equation of state

An equation of state is required to complete the description of the fluid system. In general it is a thermodynamic equation relating state variables of the fluid, e.g., an equation relating the density of a fluid to its pressure and temperature, i.e.,

$$\rho = \rho(p, T).\tag{2.1.9}$$

The equation of state we use depends on the approximations we are making, we will give the appropriate equations of state for each model as they are introduced.

## 2.2 Model setup

In this thesis, we will use a local plane layer model, similar to the one used by Hathaway *et al.* (1980), which was described in section 1.5. However, we adapt and extend the model to suit a number of different physical situations. Our model consists of a plane layer of fluid rotating about an axis that is oblique to gravity, see figure 2.1. The layer can be interpreted as a local model for a layer taken at a latitude  $\phi$  on a spherical body (cf. figure 1.8), so that the rotation vector is given by

$$\boldsymbol{\Omega} = \Omega(0, \cos \phi, \sin \phi). \quad (2.2.10)$$

The  $x$ -direction is measure eastwards, the  $y$ -direction is measured northwards and the  $z$ -direction is measured upwards. Gravity points vertically downwards. To drive convection, a vertical temperature gradient is imposed, where the lower boundary is maintained at a higher temperature than the upper boundary. In addition, we impose a horizontal temperature gradient representative of latitudinal temperature gradients that exist in, for example, stars (Hathaway *et al.* (1980)). Our model described so far, is exactly as the one used in Hathaway *et al.* (1980) and described in section 1.5. However, additional to the Hathaway model, we will also impose a horizontal magnetic field  $\mathbf{B}_0$  in the initial configuration (see figure 2.1), since horizontal fields are more relevant to stars than vertical fields, see e.g., Galloway & Weiss (1981). In further contrast to Hathaway *et al.* (1980), we impose stress free conditions on the top and bottom boundaries.

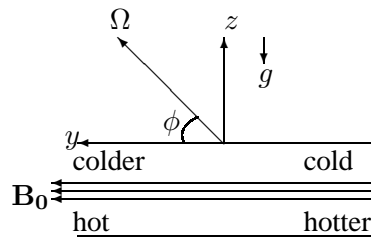


Figure 2.1: Configuration: Our model consists of a rotating plane layer rotating with velocity  $\boldsymbol{\Omega} = (0, \Omega \cos \phi, \Omega \sin \phi)$ .  $x$  is directed eastwards,  $y$  is directed northwards and  $z$  is directed upwards. A horizontal magnetic field is imposed and a temperature gradient in both the  $y$  and  $z$  directions is imposed.

The equations governing the behaviour of our model were described in section 2.1. These equations give a full description for a compressible fluid in a rotating frame, but they are computationally demanding to solve. To simplify things, we will consider two approximations: (i)

the Boussinesq approximation and (ii) the anelastic approximation. We begin with the Boussinesq approximation in the next section, before describing the anelastic approximation in section 2.4.

### 2.3 Boussinesq approximation

As was first recognised by Boussinesq (1903), there are situations where the full governing equations, described in section 2.1, can be simplified. Spiegel & Veronis (1960) and Chandrasekhar (1961) give details of the so-called Boussinesq approximation, but the two key assumptions are that (i) density is linearly related to temperature so that fluctuations in the density result from thermal (and not pressure) effects and (ii) that the depth of the motions is less than the scale heights of the system. These approximations are well suited to a liquid. As a result of the Boussinesq approximation, we can neglect density perturbations in all terms except the buoyancy term and so sound waves are filtered from the system. The fluctuations are required to remain in the buoyancy term as the acceleration due to gravity is large compared to characteristic accelerations. We denote the constant density by  $\rho_0$ .

Applying the Boussinesq approximation to equations (2.1.1) and (2.1.4) gives

$$\nabla \cdot \mathbf{u} = 0, \quad (2.3.11)$$

$$\frac{\partial \mathbf{u}}{\partial t} + (\mathbf{u} \cdot \nabla) \mathbf{u} = -\frac{1}{\rho_0} \nabla p - \frac{\rho}{\rho_0} g \hat{\mathbf{e}}_z - 2\boldsymbol{\Omega} \times \mathbf{u} + \frac{1}{\rho_0 \mu_0} (\nabla \times \mathbf{B}) \times \mathbf{B} + \nu \nabla^2 \mathbf{u}, \quad (2.3.12)$$

where we have assumed  $\mu$  to be constant and defined  $\nu = \frac{\mu}{\rho_0}$  to be the kinematic viscosity. We have also used the fact that  $\nabla \cdot (\mu \boldsymbol{\tau}) = \mu \nabla \cdot \boldsymbol{\tau} = \mu (\nabla^2 \mathbf{u} + \frac{1}{3} \nabla (\nabla \cdot \mathbf{u})) = \mu \nabla^2 \mathbf{u}$  for an incompressible fluid.

In the temperature equation (2.1.5), we ignore the terms resulting from viscous and ohmic heating, and take  $c_v$  and  $k$  to be constant to give

$$\frac{\partial T}{\partial t} + (\mathbf{u} \cdot \nabla) T = \kappa \nabla^2 T, \quad (2.3.13)$$

where  $\kappa = \frac{k}{\rho_0 c_v}$  is the thermal diffusivity. The induction equation (2.1.8) remains as

$$\frac{\partial \mathbf{B}}{\partial t} = \nabla \times (\mathbf{u} \times \mathbf{B}) + \eta \nabla^2 \mathbf{B}, \quad (2.3.14)$$

with the solenoidal constraint

$$\nabla \cdot \mathbf{B} = 0 \quad (2.3.15)$$

still holding true.

An appropriate equation of state for the Boussinesq system relates density to temperature and is given by (see e.g., Chandrasekhar (1961))

$$\rho = \rho_0(1 - \tilde{\alpha}(T - T_0)), \quad (2.3.16)$$

where  $\tilde{\alpha}$  is the coefficient of thermal expansion and  $T_0$  is the temperature at which  $\rho = \rho_0$ .

### 2.3.1 Boundary conditions

At the top ( $z = d$ ) and bottom ( $z = 0$ ) boundaries, we enforce no normal flow. This requires

$$\mathbf{u} \cdot \hat{\mathbf{n}} = w = 0 \quad \text{on } z = 0, d. \quad (2.3.17)$$

For stress free boundaries, we enforce that the tangential stress must vanish on the boundaries.

Equation (2.1.3) suggests that this requires

$$\tau_{13} = \frac{\partial u}{\partial z} + \frac{\partial w}{\partial x} = 0, \quad (2.3.18)$$

$$\tau_{23} = \frac{\partial v}{\partial z} + \frac{\partial w}{\partial y} = 0 \quad (2.3.19)$$

on  $z = 0$  and  $z = d$ .

Since  $w = 0$  on the boundaries for all  $x$  and  $y$ , we have  $\frac{\partial w}{\partial x} = \frac{\partial w}{\partial y} = 0$  on the boundaries and so equations (2.3.18) and (2.3.19) reduce to

$$\frac{\partial u}{\partial z} = \frac{\partial v}{\partial z} = 0 \quad \text{on } z = 0, d. \quad (2.3.20)$$

These conditions allow us to find an additional condition on  $w$ . First, calculate

$$\frac{\partial}{\partial z} \nabla \cdot \mathbf{u} = \frac{\partial^2 u}{\partial x \partial z} + \frac{\partial^2 v}{\partial y \partial z} + \frac{\partial^2 w}{\partial z^2} = 0 \quad (2.3.21)$$

then, using (2.3.20), we obtain

$$\frac{\partial^2 w}{\partial z^2} = 0 \quad \text{on } z = 0, d. \quad (2.3.22)$$

A condition on the vorticity can be obtained if we consider its vertical component given by  $\varphi = \frac{\partial v}{\partial x} - \frac{\partial u}{\partial y}$ , differentiating  $\varphi$  with respect to  $z$  gives

$$\frac{\partial \varphi}{\partial z} = \frac{\partial^2 v}{\partial x \partial z} - \frac{\partial^2 u}{\partial y \partial z} = 0 \quad \text{on } z = 0, d, \quad (2.3.23)$$

using (2.3.20).

Since the convection is driven by a temperature difference,  $\Delta T$ , across the layer we have

$$T(y) = T_0(y) + \Delta T \quad \text{on } z = 0 \quad (2.3.24)$$

$$T(y) = T_0(y) \quad \text{on } z = d. \quad (2.3.25)$$

Note, in this setup,  $T$  is allowed to vary with  $y$  on the boundaries.

The magnetic boundary conditions are obtained by assuming there is no normal magnetic field at the boundary, i.e.,

$$\mathbf{B} \cdot \hat{\mathbf{n}} = B_3 = 0 \quad \text{on } z = 0, d, \quad (2.3.26)$$

and by taking

$$\frac{\partial B_1}{\partial z} = \frac{\partial B_2}{\partial z} = 0 \quad \text{on } z = 0, d. \quad (2.3.27)$$

These conditions allow us to find an additional condition on  $B_3$ . First, we calculate

$$\frac{\partial}{\partial z} \nabla \cdot \mathbf{B} = \frac{\partial^2 B_1}{\partial x \partial z} + \frac{\partial^2 B_2}{\partial y \partial z} + \frac{\partial^2 B_3}{\partial z^2} = 0 \quad (2.3.28)$$

then, using (2.3.27), we obtain

$$\frac{\partial^2 B_3}{\partial z^2} = 0 \quad \text{on } z = 0, d. \quad (2.3.29)$$

Roberts & Jones (2000) call these magnetic boundary conditions illustrative, but they are also known as perfectly conducting boundary conditions.

### 2.3.2 Basic state

We now seek a basic state to the system. A basic state is a (usually) simple solution to the governing equations of the system. Perturbations can then be added to this state to investigate the stability of the system.

Throughout this thesis, we assume a time-independent, or steady, basic state and whenever a magnetic field is present, we assume a horizontal basic state field given by

$$\mathbf{B}_{BS} = B_0(\cos \alpha, \sin \alpha, 0), \quad (2.3.30)$$

where  $\alpha$  is the angle describing the orientation of the field.

We assume the basic state temperature varies in  $y$ , to account for latitudinal temperature gradients (see section 2.2), then we must have a balance between the pressure gradient, buoyancy and Coriolis terms in the momentum equation, (2.3.12), which leads to a thermal wind.

We wish for the flow induced by the horizontal temperature gradient to be in the east-west, or  $x$ -direction. We therefore choose a simple, steady basic state flow of the form  $\mathbf{u}_{BS} = (U(z), 0, 0)$ , then, from equation (2.3.13), we have  $\nabla^2 T_{BS} = 0$ . Therefore, we can assume

$$T_{BS} = T_0 + \frac{\partial T}{\partial z} z + \frac{\partial T}{\partial y} y, \quad (2.3.31)$$

where  $\frac{\partial T}{\partial z}$  gives our vertical temperature gradient and  $\frac{\partial T}{\partial y}$  gives our horizontal temperature gradient. With these assumptions, the  $x$ -component of the curl of the momentum equation (equation (2.3.12)) in the basic state, i.e., the thermal wind equation, becomes

$$2 \frac{dU}{dz} \Omega \sin \phi + \tilde{\alpha} \frac{\partial T}{\partial y} g = 0. \quad (2.3.32)$$

Hence, the thermal wind shear is given by

$$\frac{dU}{dz} = -\frac{\tilde{\alpha} \frac{\partial T}{\partial y} g}{2\Omega \sin \phi}, \quad (2.3.33)$$

which, upon integrating, leads to a basic state zonal flow given by

$$U(z) = -\frac{\tilde{\alpha} \frac{\partial T}{\partial y} g}{2\Omega \sin \phi} \left( z - \frac{d}{2} \right), \quad (2.3.34)$$

where we have chosen the constant of integration such that the flow is antisymmetric about the mid-plane,  $z = \frac{d}{2}$ .

We can then use the basic state velocity and temperature to find the basic state density and pressure. Equation (2.3.16) with equation (2.3.31) gives

$$\rho_{BS} = \rho_0 \left( 1 - \tilde{\alpha} \left( \frac{\partial T}{\partial z} z + \frac{\partial T}{\partial y} y \right) \right). \quad (2.3.35)$$

The  $z$ -component of the momentum equation (2.3.12) in the basic state is given by

$$\frac{dp_{BS}}{dz} = -\rho_{BS} g + 2\rho_0 U(z) \Omega \cos \phi. \quad (2.3.36)$$

Substituting for  $\rho_{BS}$  from equation (2.3.35), for  $U$  from equation (2.3.34) and integrating leads to the following expression for  $p_{BS}$

$$p_{BS} = p_0 - \rho_0 g z \left( 1 - \frac{\tilde{\alpha} z}{2} \frac{\partial T}{\partial z} \right) - \rho_0 g \tilde{\alpha} \frac{\partial T}{\partial y} \left[ \frac{\cos \phi}{\sin \phi} \frac{z}{2} (z - d) - zy \right], \quad (2.3.37)$$

where  $p_0$  is a constant of integration.

Note, when  $\frac{\partial T}{\partial y}$  is zero, i.e., there is no horizontal temperature gradient and hence no thermal wind, we reduce to the standard case studied in Chandrasekhar (1961) and we have hydrostatic balance (balance between the pressure gradient and buoyancy). Also, when  $\phi = \frac{\pi}{2}$ , our system is closely related to the Eady problem, see Drazin & Reid (1981).

### 2.3.3 Perturbation equations

Having defined our basic state, we can introduce perturbations to this basic state. Primed quantities will denote the perturbations, except for the temperature fluctuation which we denote by  $\theta$ . So, we let each of the variables be a sum of the basic state and a perturbation, i.e.,

$$\mathbf{u} = \mathbf{u}_{BS} + \mathbf{u}', \quad p = p_{BS} + p', \quad \rho = \rho_{BS} + \rho', \quad (2.3.38)$$

$$T = T_{BS} + \theta, \quad \mathbf{B} = \mathbf{B}_{BS} + \mathbf{B}'. \quad (2.3.39)$$

We note that the perturbations may contain both a mean (horizontally averaged) part and a fluctuation to that mean. This terminology will be important later when we consider mean flows (Chapters 6, 7 and 8).

At this stage, we have made no assumption about the size of the perturbations relative to the basic state. On substituting these expansions into the equations (2.3.11)-(2.3.16) we obtain the following set of perturbation equations. Note we have cancelled the basic state terms and some terms are zero because of their lack of time or spatial dependence.

$$\begin{aligned} \frac{\partial \mathbf{u}'}{\partial t} + (U + u') \frac{\partial}{\partial x} \mathbf{u}' + v' \frac{\partial}{\partial y} \mathbf{u}' + w' \frac{\partial}{\partial z} (\mathbf{u}_{BS} + \mathbf{u}') &= -\frac{1}{\rho_0} \nabla p' - \frac{\rho'}{\rho_0} g \hat{\mathbf{e}}_z \\ &- 2\Omega \times \mathbf{u}' + \frac{1}{\mu_0 \rho_0} [(\nabla \times \mathbf{B}') \times (\mathbf{B}_{BS} + \mathbf{B}')] + \nu \nabla^2 \mathbf{u}', \end{aligned} \quad (2.3.40)$$

$$\nabla \cdot \mathbf{u}' = 0, \quad (2.3.41)$$

$$\frac{\partial \theta}{\partial t} + (U + u') \frac{\partial}{\partial x} \theta + v' \frac{\partial}{\partial y} (T_{BS} + \theta) + w' \frac{\partial}{\partial z} (T_{BS} + \theta) = \kappa \nabla^2 \theta, \quad (2.3.42)$$

$$\rho' = -\rho_0 \tilde{\alpha} \theta, \quad (2.3.43)$$

$$\frac{\partial \mathbf{B}'}{\partial t} = \nabla \times [(\mathbf{u}_{BS} + \mathbf{u}') \times \mathbf{B}' + (\mathbf{u}' \times \mathbf{B}_{BS})] + \eta \nabla^2 \mathbf{B}', \quad (2.3.44)$$

$$\nabla \cdot \mathbf{B}' = 0. \quad (2.3.45)$$

We can eliminate  $\rho'$  by using equation (2.3.43) in equation (2.3.40). These equations constitute the fully nonlinear equations describing rotating magnetoconvection in a horizontal field.

The impenetrable, stress free boundary conditions for the velocity, given by equations (2.3.17), (2.3.20) and (2.3.22) translate to the following boundary conditions on the perturbations

$$w' = 0, \quad \frac{\partial u'}{\partial z} = \frac{\partial v'}{\partial z} = 0, \quad \frac{\partial^2 w'}{\partial z^2} = 0, \quad \text{on } z = 0, d. \quad (2.3.46)$$

The condition on the vertical component of the vorticity, (2.3.23), becomes

$$\frac{\partial \varphi'}{\partial z} = 0, \quad \text{on } z = 0, d, \quad (2.3.47)$$

where  $\varphi' = \frac{\partial v'}{\partial x} - \frac{\partial u'}{\partial y}$ . Throughout this thesis, the boundaries will be held at a fixed temperature and so any perturbation to the temperature basic state must vanish on the boundaries. The boundary conditions on the temperature perturbation are therefore

$$\theta = 0 \quad \text{on } z = 0, d. \quad (2.3.48)$$

Finally, the perfectly conducting magnetic boundary conditions given by (2.3.26), (2.3.27) and (2.3.29), translate to the following conditions on the perturbations

$$B'_3 = 0, \quad \frac{\partial B'_1}{\partial z} = \frac{\partial B'_2}{\partial z} = 0, \quad \frac{\partial^2 B'_3}{\partial z^2} = 0, \quad \text{on } z = 0, d. \quad (2.3.49)$$

### 2.3.4 Nondimensionalisation

It is useful to put the equations into a dimensionless form. To do this we need to choose some typical values over which to scale the variables. For the length scale, we choose  $d$ , the depth of the layer, meaning that the layer extends from  $z = 0$  to  $z = 1$  in dimensionless terms. For the time scale we choose the thermal diffusion time,  $\frac{d^2}{\kappa}$ , this is the time scale over which a temperature perturbation is diffused, over a length scale  $d$ . The pressure will scale with  $\frac{\rho_0 \kappa \nu}{d^2}$  and temperature with  $|\frac{\partial T}{\partial z}|d$ . We take  $B_0$  to be the size of the magnetic field. We therefore let

$$\mathbf{x} = d\tilde{\mathbf{x}}, \quad t = \frac{d^2}{\kappa}\tilde{t}, \quad p' = \frac{\rho_0 \kappa \nu}{d^2}\tilde{p}, \quad \mathbf{u}' = \frac{\kappa}{d}\tilde{\mathbf{u}}, \quad \theta = |\frac{\partial T}{\partial z}|d\tilde{\theta}, \quad \mathbf{B}' = B_0\tilde{\mathbf{B}}. \quad (2.3.50)$$

With this, equations (2.3.40)-(2.3.45) become

$$\begin{aligned} \frac{\partial \tilde{\mathbf{u}}}{\partial \tilde{t}} + (U + \tilde{u})\frac{\partial \tilde{\mathbf{u}}}{\partial \tilde{x}} + \tilde{v}\frac{\partial}{\partial \tilde{y}}\tilde{\mathbf{u}} + \tilde{w}\frac{\partial}{\partial \tilde{z}}(\mathbf{U}_{BS} + \tilde{\mathbf{u}}) &= -Pr\tilde{\nabla}\tilde{p} + RaPr\tilde{\theta}\hat{\mathbf{e}}_z \\ &\quad - Ta^{\frac{1}{2}}Pr\tilde{\Omega} \times \tilde{\mathbf{u}} + Q\zeta Pr[(\tilde{\nabla} \times \tilde{\mathbf{B}}) \times (\mathbf{B}_{BS} + \tilde{\mathbf{B}})] + Pr\tilde{\nabla}^2\tilde{\mathbf{u}}, \end{aligned} \quad (2.3.51)$$

$$\tilde{\nabla} \cdot \tilde{\mathbf{u}} = 0, \quad (2.3.52)$$

$$\frac{\partial \tilde{\theta}}{\partial \tilde{t}} + (U + \tilde{u})\frac{\partial \tilde{\theta}}{\partial \tilde{x}} + \tilde{v}\frac{\partial}{\partial \tilde{y}}(T_{BS} + \tilde{\theta}) + \tilde{w}\frac{\partial}{\partial \tilde{z}}(T_{BS} + \tilde{\theta}) = \tilde{\nabla}^2\tilde{\theta}, \quad (2.3.53)$$

$$\frac{\partial \tilde{\mathbf{B}}}{\partial \tilde{t}} = \tilde{\nabla} \times [(\mathbf{U}_{BS} + \tilde{\mathbf{u}}) \times \tilde{\mathbf{B}} + (\tilde{\mathbf{u}} \times \mathbf{B}_{BS})] + \zeta\tilde{\nabla}^2\tilde{\mathbf{B}}, \quad (2.3.54)$$

$$\tilde{\nabla} \cdot \tilde{\mathbf{B}} = 0. \quad (2.3.55)$$

These are the dimensionless perturbation equations for Boussinesq convection. They will be a starting point for a number of investigations in the coming chapters.

We have introduced the following dimensionless numbers

$$Ra = \frac{g\tilde{\alpha}d^4|\frac{\partial T}{\partial z}|}{\kappa\nu}, \quad Pr = \frac{\nu}{\kappa}, \quad Ta = \frac{4\Omega^2d^4}{\nu^2}, \quad Q = \frac{B_0^2d^2}{\mu_0\rho_0\nu\eta}, \quad \zeta = \frac{\eta}{\kappa}. \quad (2.3.56)$$

$Ra$  is the Rayleigh number and is a measure of the strength of the convective driving of the system. It is the ratio of the buoyancy force to diffusive forces.  $Pr$  is the fluid Prandtl number and is the ratio of the kinematic viscosity to thermal diffusivity - it is a property of the fluid. For  $Pr > 1$ , momentum will diffuse faster than heat and for  $Pr < 1$ , momentum will diffuse slower than heat.  $Ta$  is the Taylor number and is the ratio of the Coriolis to viscous forces. Increasing  $Ta$  increases the effect of rotation on the system.  $Q$  is the Chandrasekhar number and is a measure of the strength of the magnetic field through the ratio of the Lorentz force to viscous forces. Increasing  $Q$  increases the effect of the magnetic field on the system.  $\zeta$  is the ratio of magnetic diffusivity to thermal diffusivity and is again a property of the fluid. For  $\zeta > 1$ , magnetic field will diffuse faster than heat and for  $\zeta < 1$ , magnetic field will diffuse slower than heat. We also note here that the commonly used magnetic Prandtl number,  $Pm$  can be formed from  $Pr$  and  $\zeta$  in the following way

$$Pm \equiv \frac{\nu}{\eta} = \frac{\nu \kappa}{\kappa \eta} = \frac{Pr}{\zeta}. \quad (2.3.57)$$

### 2.3.5 Nondimensionalisation of the basic state

The basic state we defined in section 2.3.2 was dimensional. Now that we have introduced some dimensionless parameters to the governing equations, (2.3.51)-(2.3.55), it makes sense to express our basic state in terms of these parameters. The basic state temperature (2.3.31) becomes

$$\tilde{T}_{BS} = \tilde{T}_0 + T_z \tilde{z} + T_y \tilde{y} \quad (2.3.58)$$

where  $T_z = \frac{\partial T}{\partial z}$  and  $T_y = \frac{\partial T}{\partial y}$ . This results in  $T_z = 1$  for stable stratifications and  $T_z = -1$  for unstable stratifications. Throughout this thesis we consider convectively unstable basic state stratifications and so we take  $T_z = -1$ .  $T_y$  will be kept as a variable used to characterise the size of the thermal wind.

The only nonzero component of the basic state flow is the  $x$ -component given by (2.3.34), in dimensionless terms this becomes

$$\tilde{U} = -\frac{Ra T_y}{Ta^{\frac{1}{2}} \sin \phi} \left( \tilde{z} - \frac{1}{2} \right). \quad (2.3.59)$$

The magnetic field basic state (2.3.30) simply reduces to

$$\tilde{\mathbf{B}}_{BS} = (\cos \alpha, \sin \alpha, 0). \quad (2.3.60)$$

As the pressure and density basic states no longer appear in the governing equations we shall not express them in dimensionless terms.

## 2.4 Anelastic approximation

The Boussinesq equations, derived in the section 2.3, do not allow for the effects of compressibility and stratification of the fluid, but in many physical situations it is important to include such effects. For example, the interiors of stars are characterised by many density scale heights and it is thought that this density stratification plays an important role in governing the dynamics. However, using the fully compressible equations is computationally intensive and so, as an alternative, the anelastic approximation can be used to capture the effects of compressibility. This, like in the Boussinesq system, is an approximation and so its validity must be kept in mind.

The anelastic approximation filters the sound waves from the system (as did the Boussinesq approximation). It is the sound waves that make the fully compressible equations so computationally expensive to deal with. But, unlike the Boussinesq approximation, we no longer need to assume that the typical layer depth is small compared with the pressure scale height.

The anelastic equations were first derived by Batchelor (1953) in the context of the Earth's atmosphere. Ogura & Phillips (1962) later performed a more formal scale analysis and Gough (1969) extended the approximation to allow for time-dependent basic states, though we shall focus solely on the time-independent case in this thesis. The anelastic approximation has since been used to study a number of problems in geophysical and astrophysical fluids. For example, convection in A-type stars (Toomre *et al.* (1976)), the geodynamo (Glatzmaier & Roberts (1996)), solar convection (Miesch *et al.* (2000)), solar differential rotation (Brun & Toomre (2002)), the solar dynamo (Brun *et al.* (2005b), Browning *et al.* (2006)) and rapidly rotating stars (Brown *et al.* (2008)). Some of these examples involve the presence of a magnetic field, but in this thesis we shall restrict ourselves to only applying the anelastic approximation to the purely hydrodynamic equations, i.e.,  $\mathbf{B} = 0$ .

### 2.4.1 Governing equations

We begin with the fully compressible equations of section 2.1 and derive the anelastic equations by making suitable assumptions, as discussed above. We use a procedure similar to that used by Lantz & Fan (1999). A detailed description of the derivation is also given in Roxburgh (2007) and Berkoff (2011) for non-rotating magnetoconvection.

As detailed in section 2.1, the governing equations for fully compressible, rotating, hydrodynamic convection are:

the momentum equation

$$\rho \left[ \frac{\partial \mathbf{u}}{\partial t} + (\mathbf{u} \cdot \nabla) \mathbf{u} \right] = -\nabla p - \rho g \hat{\mathbf{e}}_z - 2\rho \boldsymbol{\Omega} \times \mathbf{u} + \nabla \cdot (\mu \boldsymbol{\tau}), \quad (2.4.61)$$

where

$$\tau_{ij} = \frac{\partial u_i}{\partial x_j} + \frac{\partial u_j}{\partial x_i} - \frac{2}{3} \nabla \cdot \mathbf{u} \delta_{ij} \quad (2.4.62)$$

is the viscous stress tensor and we take a tilted rotation vector of the form

$$\boldsymbol{\Omega} = \Omega(0, \cos \phi, \sin \phi), \quad (2.4.63)$$

as shown in figure 2.1. The continuity equation is given by

$$\frac{\partial \rho}{\partial t} + \nabla \cdot (\rho \mathbf{u}) = 0, \quad (2.4.64)$$

and instead of a temperature formulation (such as equation (2.1.5)) we will use an entropy formulation of the energy equation given by

$$\rho T \left[ \frac{\partial s}{\partial t} + (\mathbf{u} \cdot \nabla) s \right] = \nabla \cdot \left[ \frac{k_T}{c_p} T \nabla s \right] + \mu \frac{\boldsymbol{\tau}^2}{2}, \quad (2.4.65)$$

where we take the turbulent thermal conductivity  $k_T = c_p \rho \kappa = \text{constant}$ . Here,  $s$  is the entropy, it is related to other thermodynamic variables by the following expression

$$s = c_v \ln \left( \frac{p}{\rho^\gamma} \right), \quad (2.4.66)$$

where  $\gamma = \frac{c_p}{c_v}$  is the ratio of the specific heat capacity at constant pressure to the specific heat capacity at constant volume. In equation (2.4.65), we have assumed the turbulent thermal conductivity to be much larger than the molecular thermal conductivity, and so (2.4.65) contains an entropy diffusion term but not a thermal diffusion term. We note that both terms are retained in some models, see e.g., Braginsky & Roberts (1995).

Compared with the equation of state used in the Boussinesq equations, (2.3.16), we consider a more general equation of state, it is also known as the ideal gas law and is given by

$$p = \mathcal{R} \rho T, \quad (2.4.67)$$

where  $\mathcal{R} = c_p - c_v$  is the gas constant.

## 2.4.2 Preliminary scalings

To derive the equations of the anelastic approximation, we express all variables as the sum of a reference state variable and a perturbation to that reference state, i.e.,

$$f(x, y, z, t) = \bar{f}(z) + f^*(x, y, z, t), \quad (2.4.68)$$

where an overbar denotes a reference state quantity and a star a perturbation quantity. Note, as in the Boussinesq case (section 2.3.3), the perturbation quantity may contain both a horizontally averaged, mean part and a fluctuation to that mean.

We use a reference atmosphere that depends on the vertical coordinate  $z$  only. The atmosphere is in hydrostatic equilibrium and so we have

$$\frac{d\bar{p}}{dz} = -\bar{\rho}g. \quad (2.4.69)$$

The reference variables are also related by

$$\bar{p} = \mathcal{R}\bar{\rho}\bar{T}, \quad (2.4.70)$$

$$\bar{s} = c_v \ln \left( \frac{\bar{p}}{\bar{\rho}^\gamma} \right). \quad (2.4.71)$$

In addition, we assume a reference atmosphere that is very close to being adiabatic and therefore we introduce a small parameter,  $\epsilon$ , that measures the departure from adiabaticity of the reference state, i.e.,

$$\epsilon \equiv \frac{l}{H_r} \left( \frac{\partial \ln \bar{T}}{\partial \ln \bar{p}} - \frac{\partial \ln \bar{T}}{\partial \ln \bar{p}} \Big|_{\text{ad}} \right) = -\frac{l}{T_r} \left[ \left( \frac{d\bar{T}}{dz} \right)_r + \frac{g}{c_p} \right] = -\frac{l}{c_p} \left( \frac{d\bar{s}}{dz} \right)_r, \quad (2.4.72)$$

where  $l$  is a typical length scale of the system,  $H_r = \frac{\bar{p}}{g\bar{\rho}} = -\frac{dz}{d \ln \bar{p}}$  is the pressure scale height, the subscript  $\text{ad}$  indicates the value for an adiabatic atmosphere and a subscript  $r$  denotes a reference value taken at  $z = 0$ .  $\epsilon$  will also be a measure of the relative magnitude of the perturbations and we assume

$$\frac{|p^*|}{\bar{p}} \approx \frac{|\rho^*|}{\bar{\rho}} \approx \frac{|T^*|}{\bar{T}} \approx |s^*| \approx \epsilon \ll 1, \quad (2.4.73)$$

so that the fluctuations are small compared to the reference state. Note also that the relative pressure, density and temperature fluctuations are of the same order, this is different to the assumption made in the Boussinesq approximation.

To begin the derivation of the anelastic equations, we use preliminary scalings, denoted by the subscript  $s$ . Let

$$p = p_s(\bar{p} + \epsilon p^*), \quad T = T_s(\bar{T} + \epsilon T^*), \quad \rho = \rho_s(\bar{\rho} + \epsilon \rho^*), \quad (2.4.74)$$

$$\mathbf{u} = u_s \mathbf{u}^*, \quad t = t_s t^*, \quad g = g_s, \quad (2.4.75)$$

$$\nabla = \frac{1}{l_s} \nabla^*, \quad c_p = c_{p,s}, \quad \mu = \mu_s, \quad (2.4.76)$$

$$\Omega = \Omega_s \Omega^*, \quad k_T = k_{T,s}, \quad \nu = \nu_s, \quad (2.4.77)$$

$$\kappa = \kappa_s. \quad (2.4.78)$$

Note that these scalings may depend on  $\epsilon$ . We wish to develop scalings that are independent of  $\epsilon$ . The reference state is nearly adiabatic and so we must have that the reference and fluctuating entropy enter at the same order and hence  $s = \text{const} + s_s c_{p,s}(\bar{s} + s^*)$ , but the constant term does not appear in any equations and so we will neglect it from now on. Since any departure from the reference state is small we can assume hydrostatic balance. As in Gough (1969), we take the pressure scale height  $l_s = H_r$  to be our characteristic length scale. The characteristic velocity  $u_s$  is obtained from equating the kinetic energy of a bubble of gas and the work done by the buoyancy force over the characteristic length. This gives (ignoring the effects of pressure fluctuations and viscous stresses)

$$u_s^2 = g l_s \frac{\rho^*}{\bar{\rho}} \approx g H_r \epsilon. \quad (2.4.79)$$

It follows that the characteristic time is

$$t_s = \frac{l_s}{u_s} = \left( \frac{H_r}{\epsilon g} \right)^{\frac{1}{2}}. \quad (2.4.80)$$

So that the required terms enter at leading order we require  $\rho_s = \rho_r$  and  $T_s = T_r$ . Gravity is assumed constant across the layer and since at leading order we must have hydrostatic balance, it follows that  $g_s = g_r$ . The pressure scaling should be consistent with  $H_r = \frac{\bar{p}}{g\bar{\rho}}$  and therefore  $p_s = g_r H_r \rho_r$ . The gas constant  $\mathcal{R}$  does not fluctuate and so  $c_{p,s} = c_{p,r}$ .

To see how the other terms scale, we substitute our preliminary scalings into the governing equations, then, from equation (2.4.61), after dividing through by  $\rho_r g_r$  we have

$$\begin{aligned} \epsilon(\bar{\rho} + \epsilon\rho^*) \left[ \frac{\partial \mathbf{u}^*}{\partial t^*} + (\mathbf{u}^* \cdot \nabla^*) \mathbf{u}^* \right] &= -\nabla^*(\bar{p} + \epsilon p^*) - (\bar{\rho} + \epsilon\rho^*) \hat{\mathbf{e}}_z \\ &\quad - \frac{2\Omega_s(H_r g_r \epsilon)^{\frac{1}{2}}}{g_r} (\bar{\rho} + \epsilon\rho^*) \boldsymbol{\Omega}^* \times \mathbf{u}^* + \frac{(g_r H_r \epsilon)^{\frac{1}{2}}}{\rho_r g_r H_r^2} \nabla^* \cdot (\mu_s \boldsymbol{\tau}^*). \end{aligned} \quad (2.4.81)$$

At  $\mathcal{O}(1)$  we must satisfy hydrostatic balance and all other terms must enter at  $\mathcal{O}(\epsilon)$ . The left hand side clearly satisfies this ordering. For the third term on the right-hand side to be  $\mathcal{O}(\epsilon)$  we require  $\Omega_s = \epsilon^{\frac{1}{2}} \Omega_r$ . Similarly, the last term on the right hand side requires  $\mu_s = \epsilon^{\frac{1}{2}} \mu_r$ . Then, since  $\mu = \rho\nu$ , it follows that  $\nu_s = \epsilon^{\frac{1}{2}} \nu_r$ . Introducing the preliminary scalings into the energy equation (2.4.65) gives

$$\begin{aligned} \rho_r T_r s_s c_{p,r} \left( \frac{\epsilon g_r}{H_r} \right)^{\frac{1}{2}} (\bar{\rho} + \epsilon\rho^*) (\bar{T} + \epsilon T^*) \left[ \frac{\partial(\bar{s} + s^*)}{\partial t^*} + (\mathbf{u}^* \cdot \nabla^*) (\bar{s} + s^*) \right] \\ = \frac{k_{T,s} T_r s_s c_{p,r}}{c_{p,r} H_r^2} \nabla^* [(\bar{T} + \epsilon T^*) \nabla^* (\bar{s} + s^*)] + \mu_r \epsilon^{\frac{1}{2}} \frac{g_r H_r \epsilon}{H_r^2} \frac{\boldsymbol{\tau}^{*2}}{2}. \end{aligned} \quad (2.4.82)$$

For all the terms to balance at  $\mathcal{O}(\epsilon^{\frac{3}{2}})$  we need  $s_s = \epsilon$  and  $k_{T,s} = \epsilon^{\frac{1}{2}}k_{T,r}$ . This latter scaling means that, since  $k_T = \rho c_p \kappa$ , we must have  $\kappa_s = \epsilon^{\frac{1}{2}}\kappa_r$ . We have now developed scalings which are independent of  $\epsilon$ . The next section uses these to derive the full anelastic equations.

### 2.4.3 Anelastic scalings

With knowledge of the scalings from the previous section we have the following anelastic scalings which are independent of  $\epsilon$ :

$$p = \rho_r g_r H_r (\bar{p} + \epsilon p^*), \quad T = T_r (\bar{T} + \epsilon T^*), \quad \rho = \rho_r (\bar{\rho} + \epsilon \rho^*), \quad (2.4.83)$$

$$\mathbf{u} = (g_r H_r \epsilon)^{\frac{1}{2}} \mathbf{u}^*, \quad t = \left( \frac{H_r}{\epsilon g_r} \right)^{\frac{1}{2}} t^*, \quad g = g_r, \quad (2.4.84)$$

$$\nabla = \frac{1}{H_r} \nabla^*, \quad c_p = c_{p,r}, \quad \mu = \epsilon^{\frac{1}{2}} \mu_r, \quad (2.4.85)$$

$$\boldsymbol{\Omega} = \Omega_r \epsilon^{\frac{1}{2}} \boldsymbol{\Omega}^*, \quad k_T = \epsilon^{\frac{1}{2}} k_{T,r}, \quad \nu = \epsilon^{\frac{1}{2}} \nu_r, \quad (2.4.86)$$

$$\kappa = \epsilon^{\frac{1}{2}} \kappa_r, \quad s = \epsilon c_{p,r} (\bar{s} + s^*). \quad (2.4.87)$$

Now, substituting these scalings into equation (2.4.61) gives

$$\begin{aligned} \epsilon \rho_r g_r (\bar{\rho} + \epsilon \rho^*) \left[ \frac{\partial \mathbf{u}^*}{\partial t^*} + (\mathbf{u}^* \cdot \nabla^*) \mathbf{u}^* \right] &= -\frac{\rho_r g_r H_r}{H_r} \nabla^* (\bar{p} + \epsilon p^*) - \rho_r g_r (\bar{\rho} + \epsilon \rho^*) \hat{\mathbf{e}}_z \\ &\quad - 2\rho_r \Omega_r \epsilon (g_r H_r)^{\frac{1}{2}} (\bar{\rho} + \epsilon \rho^*) \boldsymbol{\Omega}^* \times \mathbf{u}^* + \frac{\epsilon g_r^{\frac{1}{2}}}{H_r^{\frac{3}{2}}} \nabla^* \cdot (\mu_r \boldsymbol{\tau}^*). \end{aligned} \quad (2.4.88)$$

Then, by dividing by  $\rho_r g_r$ , we obtain

$$\begin{aligned} \epsilon (\bar{\rho} + \epsilon \rho^*) \left[ \frac{\partial \mathbf{u}^*}{\partial t^*} + (\mathbf{u}^* \cdot \nabla^*) \mathbf{u}^* \right] &= -\nabla^* (\bar{p} + \epsilon p^*) - (\bar{\rho} + \epsilon \rho^*) \hat{\mathbf{e}}_z \\ &\quad - \frac{2\Omega_r \epsilon (g_r H_r)^{\frac{1}{2}}}{g_r} (\bar{\rho} + \epsilon \rho^*) \boldsymbol{\Omega}^* \times \mathbf{u}^* + \frac{\epsilon g_r^{\frac{1}{2}}}{\rho_r g_r H_r^{\frac{3}{2}}} \nabla^* \cdot (\mu_r \boldsymbol{\tau}^*). \end{aligned} \quad (2.4.89)$$

At leading order,  $\mathcal{O}(\epsilon)$ , this yields

$$\bar{\rho} \left[ \frac{\partial \mathbf{u}^*}{\partial t^*} + (\mathbf{u}^* \cdot \nabla^*) \mathbf{u}^* \right] = -\nabla^* p^* - \rho^* \hat{\mathbf{e}}_z - \frac{2\Omega_r H_r^{\frac{1}{2}}}{g_r^{\frac{1}{2}}} \bar{\rho} \boldsymbol{\Omega}^* \times \mathbf{u}^* + \frac{1}{\rho_r g_r^{\frac{1}{2}} H_r^{\frac{3}{2}}} \nabla^* \cdot (\mu_r \boldsymbol{\tau}^*). \quad (2.4.90)$$

Introducing the anelastic scalings (2.4.83)-(2.4.87) to the traditional nondimensional numbers (defined in 2.3.4) gives the following:

$$Ra = -\frac{g H_r^4}{c_p \kappa \nu} \left( \frac{d\bar{s}}{dz} \right)_r = \frac{g H_r^3 \epsilon}{\kappa \nu} = \frac{g H_r^3}{\kappa_r \nu_r}, \quad (2.4.91)$$

$$Ta = \frac{4\Omega^2 H_r^4}{\nu^2} = \frac{4\Omega_r^2 H_r^4}{\nu_r^2} \quad (2.4.92)$$

and

$$Pr = \frac{\nu}{\kappa} = \frac{\nu_r}{\kappa_r}. \quad (2.4.93)$$

Equation (2.4.90) can then be written as

$$\bar{\rho} \left[ \frac{\partial \mathbf{u}^*}{\partial t^*} + (\mathbf{u}^* \cdot \nabla^*) \mathbf{u}^* \right] = -\nabla^* p^* - \rho^* \hat{\mathbf{e}}_z - \left( \frac{TaPr}{Ra} \right)^{\frac{1}{2}} \bar{\rho} \boldsymbol{\Omega}^* \times \mathbf{u}^* + \left( \frac{Pr}{Ra} \right)^{\frac{1}{2}} \nabla^* \cdot \boldsymbol{\varsigma}^*, \quad (2.4.94)$$

where we have used  $\mu_r = \rho_r \bar{\rho} \nu_r$ , taken  $\nu$  to be constant and  $\boldsymbol{\varsigma}$  is given by  $\varsigma_{ij} = \bar{\rho} \tau_{ij} = \bar{\rho} \left( \frac{\partial u_i}{\partial x_j} + \frac{\partial u_j}{\partial x_i} - \frac{2}{3} \nabla \cdot \mathbf{u} \delta_{ij} \right)$ . As we did for the momentum equation, we can use the anelastic scalings (2.4.83)-(2.4.87) with the continuity equation given by equation (2.4.64). This gives

$$\rho_r \left( \frac{\epsilon g_r}{H_r} \right)^{\frac{1}{2}} \frac{\partial (\bar{\rho} + \epsilon \rho^*)}{\partial t^*} + \frac{\rho_r (g_r H_r \epsilon)^{\frac{1}{2}}}{H_r} \nabla^* \cdot ((\bar{\rho} + \epsilon \rho^*) \mathbf{u}^*) = 0, \quad (2.4.95)$$

which at leading order, after dividing by  $\rho_r \left( \frac{g_r}{H_r} \right)^{\frac{1}{2}}$ , yields

$$\nabla^* \cdot (\bar{\rho} \mathbf{u}^*) = 0. \quad (2.4.96)$$

Note that this is the same form as the incompressibility condition in Boussinesq convection (cf. equation (2.3.11)) but now it is  $\bar{\rho} \mathbf{u}$  that is divergence free and not just  $\mathbf{u}$ .

Next, on substitution of the anelastic scalings (2.4.83)-(2.4.87), the energy equation (2.4.65) becomes

$$\begin{aligned} & \rho_r T_r c_{p,r} \epsilon^{\frac{3}{2}} \left( \frac{g_r}{H_r} \right)^{\frac{1}{2}} (\bar{\rho} + \epsilon \rho^*) (\bar{T} + \epsilon T^*) \left[ \frac{\partial (\bar{s} + s^*)}{\partial t^*} + (\mathbf{u}^* \cdot \nabla^*) (\bar{s} + s^*) \right] \\ & = \frac{k_{T,r} T_r c_{p,r} \epsilon^{\frac{3}{2}}}{c_{p,r} H_r^2} \nabla^* [(\bar{T} + \epsilon T^*) \nabla^* (\bar{s} + s^*)] + \mu_r \epsilon^{\frac{3}{2}} \frac{g_r}{H_r} \frac{\boldsymbol{\tau}^{*2}}{2}. \end{aligned} \quad (2.4.97)$$

Dividing by  $\frac{\rho_r T_r c_{p,r} g_r^{\frac{1}{2}}}{H_r^2}$  gives

$$\begin{aligned} & \epsilon^{\frac{3}{2}} (\bar{\rho} + \epsilon \rho^*) (\bar{T} + \epsilon T^*) \left[ \frac{\partial (\bar{s} + s^*)}{\partial t^*} + (\mathbf{u}^* \cdot \nabla^*) (\bar{s} + s^*) \right] \\ & = \epsilon^{\frac{3}{2}} \frac{k_{T,r} T_r}{H_r^2} \frac{H_r^{\frac{1}{2}}}{\rho_r T_r c_{p,r} g_r^{\frac{1}{2}}} \nabla^* [(\bar{T} + \epsilon T^*) \nabla^* (\bar{s} + s^*)] + \mu_r \epsilon^{\frac{3}{2}} \frac{g_r^{\frac{1}{2}}}{\rho_r T_r c_{p,r} H_r^{\frac{1}{2}}} \frac{\boldsymbol{\tau}^{*2}}{2}, \end{aligned} \quad (2.4.98)$$

which, at  $\mathcal{O}(\epsilon^{\frac{3}{2}})$ , gives

$$\bar{\rho} \bar{T} \left[ \frac{\partial s^*}{\partial t^*} + (\mathbf{u}^* \cdot \nabla^*) (\bar{s} + s^*) \right] = \frac{k_{T,r}}{H_r^{\frac{3}{2}} \rho_r c_{p,r} g_r^{\frac{1}{2}}} \nabla^* [\bar{T} \nabla^* (\bar{s} + s^*)] + \frac{\mu_r g_r^{\frac{1}{2}}}{\rho_r T_r c_{p,r} H_r^{\frac{1}{2}}} \frac{\boldsymbol{\tau}^{*2}}{2}. \quad (2.4.99)$$

Alternatively, after introducing combinations of the nondimensional numbers defined in equations (2.4.91) - (2.4.93), this can be written as

$$\bar{\rho}\bar{T} \left[ \frac{\partial s^*}{\partial t^*} + (\mathbf{u}^* \cdot \nabla^*)(\bar{s} + s^*) \right] = \left( \frac{1}{RaPr} \right)^{\frac{1}{2}} \nabla^* [\bar{T} \nabla^* (\bar{s} + s^*)] + \frac{g_r H_r}{T_r c_{p,r}} \left( \frac{Pr}{Ra} \right)^{\frac{1}{2}} \frac{1}{\bar{\rho}} \frac{\mathbf{s}^{*2}}{2}. \quad (2.4.100)$$

The equation of state (2.4.67) becomes

$$g_r \rho_r H_r (\bar{p} + \epsilon p^*) = \mathcal{R} \rho_r T_r (\bar{\rho} + \epsilon \rho^*) (\bar{T} + \epsilon T^*) \quad (2.4.101)$$

but, from the zero order equation we have  $\bar{p} = \frac{\mathcal{R} T_r}{g_r H_r} \bar{\rho} \bar{T}$  and so

$$\begin{aligned} g_r H_r \rho_r \epsilon p^* &= \mathcal{R} T_r \rho_r (\bar{\rho} \epsilon T^* + \epsilon \rho^* \bar{T} + \epsilon^2 \rho^* T^*) \\ \Rightarrow p^* &= \frac{\mathcal{R} T_r}{g_r H_r} (\bar{\rho} T^* + \rho^* \bar{T} + \epsilon \rho^* T^*) \end{aligned} \quad (2.4.102)$$

which at leading order, using  $\frac{\mathcal{R} T_r}{g_r H_r} = \frac{\bar{p}}{\bar{\rho} \bar{T}}$ , gives

$$\frac{p^*}{\bar{p}} = \frac{T^*}{\bar{T}} + \frac{\rho^*}{\bar{\rho}}. \quad (2.4.103)$$

Finally, we consider the thermodynamic relation  $s = c_v \ln \left( \frac{p}{\rho^\gamma} \right)$ . Substituting in the anelastic scalings (2.4.83)-(2.4.87) gives

$$\epsilon c_{p,r} (\bar{s} + s^*) = c_v \ln [\rho_r g_r H_r (\bar{p} + \epsilon p^*)] - \gamma c_v \ln [\rho_r (\bar{\rho} + \epsilon \rho^*)]. \quad (2.4.104)$$

Then, from the zero order equation we have

$$\epsilon c_{p,r} \bar{s} = c_v \ln \rho_r g_r H_r \bar{p} - \gamma c_v \ln \rho_r \bar{\rho}, \quad (2.4.105)$$

and so we can write

$$\epsilon c_{p,r} s^* = c_v \ln \left( 1 + \epsilon \frac{p^*}{\bar{p}} \right) - c_p \ln \left( 1 + \epsilon \frac{\rho^*}{\bar{\rho}} \right). \quad (2.4.106)$$

But, from (2.4.73),  $\frac{p^*}{\bar{p}}$  and  $\frac{\rho^*}{\bar{\rho}}$  are small, allowing us to expand the logarithmic terms as Taylor series, leaving, at order  $\epsilon$ ,

$$\begin{aligned} c_p s^* &= c_v \frac{p^*}{\bar{p}} - c_p \frac{\rho^*}{\bar{\rho}} \\ \Rightarrow s^* &= \frac{1}{\gamma} \frac{p^*}{\bar{p}} - \frac{\rho^*}{\bar{\rho}}. \end{aligned} \quad (2.4.107)$$

Thus, we have formulated the nonlinear anelastic equations for rotating hydrodynamic convection, they are summarised below

$$\bar{\rho} \left[ \frac{\partial \mathbf{u}}{\partial t} + (\mathbf{u} \cdot \nabla) \mathbf{u} \right] = -\nabla p - \rho \hat{\mathbf{e}}_z - \left( \frac{TaPr}{Ra} \right)^{\frac{1}{2}} \bar{\rho} \boldsymbol{\Omega} \times \mathbf{u} + \left( \frac{Pr}{Ra} \right)^{\frac{1}{2}} \nabla \cdot \boldsymbol{\varsigma}, \quad (2.4.108)$$

$$\nabla \cdot (\bar{\rho} \mathbf{u}) = 0, \quad (2.4.109)$$

$$\bar{\rho} \bar{T} \left[ \frac{\partial s}{\partial t} + (\mathbf{u} \cdot \nabla)(\bar{s} + s) \right] = \left( \frac{1}{RaPr} \right)^{\frac{1}{2}} \nabla [\bar{T} \nabla (\bar{s} + s)] + \frac{g_r H_r}{T_r c_{p,r}} \left( \frac{Pr}{Ra} \right)^{\frac{1}{2}} \frac{1}{\bar{\rho}} \frac{\boldsymbol{\zeta}^2}{2}, \quad (2.4.110)$$

$$\frac{p}{\bar{p}} = \frac{T}{\bar{T}} + \frac{\rho}{\bar{\rho}}, \quad (2.4.111)$$

$$s = \frac{1}{\gamma} \frac{p}{\bar{p}} - \frac{\rho}{\bar{\rho}}. \quad (2.4.112)$$

Note, for clarity, we have removed the \*'s from the perturbation quantities.

#### 2.4.4 Lantz formulation

We can reduce the number of thermodynamic variables in the equations by employing a technique first used by Lantz (1992), and independently by Braginsky & Roberts (1995), (see also Lantz & Fan (1999)). We first divide the momentum equation (2.4.108) by  $\bar{\rho}$  to give

$$\left[ \frac{\partial \mathbf{u}}{\partial t} + (\mathbf{u} \cdot \nabla) \mathbf{u} \right] = -\frac{\nabla p}{\bar{\rho}} - \frac{\rho}{\bar{\rho}} \hat{\mathbf{e}}_z - \left( \frac{TaPr}{Ra} \right)^{\frac{1}{2}} \boldsymbol{\Omega} \times \mathbf{u} + \left( \frac{Pr}{Ra} \right)^{\frac{1}{2}} \frac{1}{\bar{\rho}} \nabla \cdot \boldsymbol{\zeta}. \quad (2.4.113)$$

Now, in particular, consider the first two terms on the right-hand side which can be written as

$$\begin{aligned} & -\frac{\nabla p}{\bar{\rho}} - \left( \frac{1}{\gamma} \frac{p}{\bar{p}} - s \right) \hat{\mathbf{e}}_z \\ &= -\nabla \left( \frac{p}{\bar{\rho}} \right) + s \hat{\mathbf{e}}_z - \left[ \frac{1}{\gamma} - \bar{p} \frac{d}{dz} \left( \frac{1}{\bar{\rho}} \right) \right] \frac{p}{\bar{p}} \hat{\mathbf{e}}_z \end{aligned} \quad (2.4.114)$$

Then, if we assume a polytropic atmosphere, we have  $\bar{p} \propto \bar{\rho}^{\frac{m+1}{m}}$ , where  $m$  is the polytropic index. In addition, the reference atmosphere is in hydrostatic equilibrium and so we can rewrite the second term in the square brackets in (2.4.114) to give

$$-\nabla \left( \frac{p}{\bar{\rho}} \right) + s \hat{\mathbf{e}}_z - \left[ \frac{1}{\gamma} - \frac{m}{m+1} \right] \frac{p}{\bar{p}} \hat{\mathbf{e}}_z. \quad (2.4.115)$$

For an atmosphere close to adiabatic,  $m \approx 1.5$  and so for a perfect, monotonic gas (where  $\gamma = \frac{5}{3}$ ) the term in the square brackets is small. With this simplification, the momentum equation (2.4.108) becomes

$$\left[ \frac{\partial \mathbf{u}}{\partial t} + (\mathbf{u} \cdot \nabla) \mathbf{u} \right] = -\nabla \frac{p}{\bar{\rho}} + s \hat{\mathbf{e}}_z - \left( \frac{TaPr}{Ra} \right)^{\frac{1}{2}} \boldsymbol{\Omega} \times \mathbf{u} + \left( \frac{Pr}{Ra} \right)^{\frac{1}{2}} \frac{1}{\bar{\rho}} \nabla \cdot \boldsymbol{\zeta}, \quad (2.4.116)$$

and so now we are in a position to eliminate the pressure by taking a curl and reduce the number of thermodynamic variables.

### 2.4.5 Reference state

The reference state we consider will be independent of time. In addition, the reference variables are related by

$$\bar{p} = \mathcal{R}\bar{\rho}\bar{T}, \quad (2.4.117)$$

$$\bar{s} = c_v \ln \left( \frac{\bar{p}}{\bar{\rho}^\gamma} \right) \quad (2.4.118)$$

and they must satisfy the zero order governing equations, i.e., they must satisfy

$$\nabla \cdot \left[ \frac{k_T}{c_p} \bar{T} \nabla \bar{s} \right] = 0, \quad (2.4.119)$$

$$\nabla \bar{p} = -\bar{\rho}g\hat{\mathbf{e}}_z. \quad (2.4.120)$$

The equations have a trivial, static solution that takes the form of a polytrope, i.e.,  $\bar{p} = A\bar{\rho}^{(1+\frac{1}{m})}$  where  $m$  is the polytropic index and  $A$  is a constant. The hydrostatic condition then gives

$$\left( 1 + \frac{1}{m} \right) A\bar{\rho}^{\frac{1}{m}} \frac{d\bar{\rho}}{dz} = -\bar{\rho}g. \quad (2.4.121)$$

Separating variables and integrating gives

$$\bar{\rho} = \left( \frac{-gz}{A(m+1)} + C \right)^m \quad (2.4.122)$$

and hence

$$\bar{p} = A \left( \frac{-gz}{A(m+1)} + C \right)^{m+1}. \quad (2.4.123)$$

From these we can establish  $\bar{T}$ , which is given by

$$\bar{T} = \frac{\bar{p}}{\mathcal{R}\bar{\rho}} = \frac{A}{\mathcal{R}} \left( \frac{-gz}{A(m+1)} + C \right). \quad (2.4.124)$$

This is the dimensional reference state.

In addition, it will be useful to have the reference state in dimensionless form. From equation (2.4.124), the thermal gradient is

$$\frac{d\bar{T}}{dz} = \frac{-g}{\mathcal{R}(m+1)}, \quad (2.4.125)$$

which in dimensionless form gives

$$\frac{T_r}{H_r} \frac{d\bar{T}}{dz} = \frac{-g}{\mathcal{R}(m+1)}, \quad (2.4.126)$$

or,

$$\frac{d\bar{T}}{dz} = \frac{-g}{\mathcal{R}(m+1)} \frac{H_r}{T_r} \equiv \theta. \quad (2.4.127)$$

Defining  $\theta$  is such a way, allows us to write the reference state in dimensionless form as

$$\bar{T} = (1 + \theta z), \quad (2.4.128)$$

$$\bar{\rho} = (1 + \theta z)^m, \quad (2.4.129)$$

$$\bar{p} = -\frac{(1 + \theta z)^{m+1}}{\theta(m+1)} = (1 + \theta z)^{m+1}, \quad (2.4.130)$$

$$\bar{s} = \frac{m+1-\gamma m}{\gamma \epsilon} \ln(1 + \theta z) + \text{const} = -\frac{1}{\theta} \ln(1 + \theta z) + \text{const} \quad (2.4.131)$$

where  $\frac{m+1-\gamma m}{\gamma} = -\frac{\epsilon}{\theta} = \mathcal{O}(\epsilon)$ . Equation (2.4.131) follows from the relation (2.4.118) in conjunction with the definition of  $\epsilon$  in (2.4.72).

## 2.4.6 Alternative nondimensionalisation

Equations (2.4.109), (2.4.110) and (2.4.116) are dimensionless governing equations for anelastic convection. However, the typical scales over which they have been derived differ from those used in the nondimensionalisation of the Boussinesq equations in section 2.3.4. We wish to be able to reduce the anelastic equations to the Boussinesq equations easily. We therefore rescale our dimensionless anelastic equations so that they are dimensionless with respect to the layer depth,  $d$ , and the thermal diffusion time scale,  $\frac{d^2}{\kappa}$ . To do this, we let

$$\nabla = \frac{H_r}{d} \tilde{\nabla}, \quad t = \frac{d^2}{\kappa_r} \left( \frac{g_r}{H_r} \right)^{\frac{1}{2}} \tilde{t}, \quad \mathbf{u} = \frac{\kappa_r}{d} \frac{1}{(g_r H_r)^{\frac{1}{2}}} \tilde{\mathbf{u}}, \quad p = \frac{\kappa_r^2}{d^2} \frac{1}{g_r H_r} \tilde{p}, \quad (2.4.132)$$

where a tilde denotes the dimensionless quantities with respect to the new nondimensionalisation. With these new scalings, the momentum equation (2.4.116), after dividing by  $\frac{\kappa_r^2}{g_r d^3}$ , becomes

$$\left[ \frac{\partial \tilde{\mathbf{u}}}{\partial \tilde{t}} + (\tilde{\mathbf{u}} \cdot \tilde{\nabla}) \tilde{\mathbf{u}} \right] = -\tilde{\nabla} \frac{\tilde{p}}{\tilde{\rho}} + \frac{g_r d^3}{\kappa_r^2} s \hat{\mathbf{e}}_z - \frac{2\Omega_r d^2}{\kappa_r^2} \tilde{\boldsymbol{\Omega}} \times \tilde{\mathbf{u}} + \frac{1}{\rho_r \kappa_r} \tilde{\nabla} \cdot (\mu_r \tilde{\boldsymbol{\tau}}), \quad (2.4.133)$$

which can be written as

$$\left[ \frac{\partial \tilde{\mathbf{u}}}{\partial \tilde{t}} + (\tilde{\mathbf{u}} \cdot \tilde{\nabla}) \tilde{\mathbf{u}} \right] = -\tilde{\nabla} \left( \frac{\tilde{p}}{\tilde{\rho}} \right) + Ra Pr s \hat{\mathbf{e}}_z - Ta^{\frac{1}{2}} Pr \tilde{\boldsymbol{\Omega}} \times \tilde{\mathbf{u}} + \frac{Pr}{\tilde{\rho}} \tilde{\nabla} \cdot \tilde{\boldsymbol{\zeta}}, \quad (2.4.134)$$

where

$$Ta = \frac{4\Omega_r^2 d^4}{\nu_r^2}, \quad Ra = \frac{g d^3}{\kappa_r \nu_r}, \quad Pr = \frac{\nu_r}{\kappa_r}. \quad (2.4.135)$$

The continuity equation (2.4.109) keeps the same form and becomes

$$\tilde{\nabla} \cdot (\tilde{\rho} \tilde{\mathbf{u}}) = 0. \quad (2.4.136)$$

The energy equation (2.4.110) becomes

$$\frac{\kappa_r H_r^{\frac{1}{2}}}{d^2 g_r^{\frac{1}{2}}} \bar{\rho} \bar{T} \left[ \frac{\partial \tilde{s}}{\partial \tilde{t}} + (\tilde{\mathbf{u}} \cdot \tilde{\nabla})(\bar{s} + \tilde{s}) \right] = \frac{k_{T,r} H_r^2}{H_r^{\frac{3}{2}} \rho_r c_{p,r} g_r^{\frac{1}{2}} d^2} \tilde{\nabla} \cdot [\bar{T} \tilde{\nabla}(\bar{s} + \tilde{s})] + \frac{\mu_r g_r^{\frac{1}{2}} H_r^2 \kappa_r^2}{\rho_r T_r c_{p,r} d^4 g_r H_r^{\frac{3}{2}}} \frac{\tilde{\boldsymbol{\tau}}^2}{2}, \quad (2.4.137)$$

which, after dividing by  $\frac{\kappa_r}{d^2} \left( \frac{H_r}{g_r} \right)^{\frac{1}{2}}$  gives

$$\bar{\rho} \bar{T} \left[ \frac{\partial \tilde{s}}{\partial \tilde{t}} + (\tilde{\mathbf{u}} \cdot \tilde{\nabla})(\bar{s} + \tilde{s}) \right] = \frac{k_{T,r}}{\kappa_r \rho_r c_{p,r}} \tilde{\nabla} \cdot [\bar{T} \tilde{\nabla}(\bar{s} + \tilde{s})] + \frac{\mu_r \kappa_r}{\rho_r T_r c_{p,r} d^2} \frac{\tilde{\boldsymbol{\tau}}^2}{2}. \quad (2.4.138)$$

Now,  $\theta = -\frac{gd}{c_p T_r}$  and  $k_{T,r} = \kappa_r \rho_r c_{p,r}$  which gives

$$\bar{\rho} \bar{T} \left[ \frac{\partial \tilde{s}}{\partial \tilde{t}} + (\tilde{\mathbf{u}} \cdot \tilde{\nabla})(\bar{s} + \tilde{s}) \right] = \tilde{\nabla} \cdot [\bar{T} \tilde{\nabla}(\bar{s} + \tilde{s})] - \frac{\theta}{\bar{\rho} Ra} \frac{\tilde{\boldsymbol{\zeta}}^2}{2}. \quad (2.4.139)$$

With this new nondimensionalisation, the reference state, given by (2.4.128)-(2.4.131), becomes

$$\bar{T} = 1 + \theta z, \quad \bar{\rho} = (1 + \theta z)^m, \quad \bar{p} = -\frac{Ra Pr}{\theta(m+1)} (1 + \theta z)^{m+1}, \quad (2.4.140)$$

$$\bar{s} = \frac{m+1-\gamma m}{\gamma \epsilon} \ln(1 + \theta z) + \text{const} \quad \text{with} \quad \frac{m+1-\gamma m}{\gamma} = -\frac{\epsilon}{\theta} = \mathcal{O}(\epsilon). \quad (2.4.141)$$

We note here that  $z$  is increasing upwards consistent with our Boussinesq formalism, this is in contrast to many anelastic studies where  $z$  increases downwards, see e.g., Roxburgh (2007).

Now that we have defined our reference state we can substitute it into our equations (2.4.134), (2.4.136) and (2.4.139) to give the equations for the perturbations as

$$\frac{\partial \mathbf{u}}{\partial t} + (\mathbf{u} \cdot \nabla) \mathbf{u} = -\nabla \left( \frac{p}{\bar{\rho}} \right) + Ra Pr s \hat{\mathbf{e}}_z - Ta^{\frac{1}{2}} Pr (\boldsymbol{\Omega} \times \mathbf{u}) + Pr \nabla^2 \mathbf{u} \\ + \frac{Pr m \theta}{1 + \theta z} \left[ \frac{\partial \mathbf{u}}{\partial z} + \frac{2}{3} \nabla w + \frac{1}{3} (1 + 2m) \theta \frac{w}{1 + \theta z} \hat{\mathbf{e}}_z \right], \quad (2.4.142)$$

$$\nabla \cdot \mathbf{u} = -\frac{m\theta}{1 + \theta z} w, \quad (2.4.143)$$

$$\frac{\partial s}{\partial t} + \mathbf{u} \cdot \nabla s = \frac{w}{1 + \theta z} + \frac{1}{\bar{\rho}} \nabla^2 s + \frac{\theta}{(1 + \theta z)^{m+1}} \frac{\partial s}{\partial z} \\ - \frac{\theta}{Ra(1 + \theta z)} \left[ 2 \sum_{i=1}^3 \left( \frac{\partial u_i}{\partial x_i} \right)^2 + \sum_{i < j} \left( \frac{\partial u_i}{\partial x_j} + \frac{\partial u_j}{\partial x_i} \right)^2 - \frac{2}{3} (\nabla \cdot \mathbf{u})^2 \right], \quad (2.4.144)$$

where we have removed the tildes from the perturbation variables. These equations are similar to those given in Mizerski & Tobias (2011). The key difference here however is the introduction of a tilted rotation vector,  $\boldsymbol{\Omega} = (0, \cos \phi, \sin \phi)$ .

### 2.4.7 Boundary conditions

For the anelastic system, the boundary conditions we use are slightly different to the ones used in the Boussinesq system. Instead of conditions on the temperature at the boundaries, we impose conditions on the entropy. We will assume the entropy to be fixed on the top and bottom boundaries, so that any perturbation to the basic state entropy must vanish on the boundaries, i.e.,

$$s = 0 \quad \text{on } z = 0, 1. \quad (2.4.145)$$

As in the Boussinesq case, we assume impenetrable, stress free boundaries, and so we have

$$w = 0, \quad \frac{\partial u}{\partial z} = \frac{\partial v}{\partial z} = 0 \quad \text{on } z = 0, 1. \quad (2.4.146)$$

But, since  $\nabla \cdot \mathbf{u} \neq 0$  in the anelastic system, the conditions (2.4.146) translate to a different condition on  $w$  than the one in the Boussinesq case, see equation (2.3.46). To derive the new condition, we consider  $\frac{\partial}{\partial z} \nabla \cdot \mathbf{u}$ , from equation (2.4.143) we have

$$\frac{\partial}{\partial z} \nabla \cdot \mathbf{u} = \frac{\partial^2 u}{\partial z \partial x} + \frac{\partial^2 v}{\partial z \partial y} + \frac{\partial^2 w}{\partial z^2} = -\frac{m\theta}{1+\theta z} \frac{\partial w}{\partial z} + \frac{m\theta^2}{(1+\theta z)^2} w. \quad (2.4.147)$$

Then, using (2.4.146), this gives

$$\frac{\partial^2 w}{\partial z^2} = -\frac{m\theta}{1+\theta z} \frac{\partial w}{\partial z} \quad \text{on } z = 0, 1. \quad (2.4.148)$$

The condition on the vertical component of the vorticity remains as in the Boussinesq case, i.e.,

$$\frac{\partial \varphi}{\partial z} = 0 \quad \text{on } z = 0, 1. \quad (2.4.149)$$

### 2.4.8 Basic state

The basic state can be slightly different to the reference state. But here we consider a static, steady basic state in which

$$\mathbf{u}_{BS} = \mathbf{0}, \quad \rho_{BS} = p_{BS} = s_{BS} = T_{BS} = 0. \quad (2.4.150)$$

Therefore, in this case, the reference state and basic state are equivalent. However, if for example, we were to consider the addition of a magnetic field, then the reference state would remain as non-magnetic and the magnetic field would be introduced through the basic state.

## 2.5 Summary

In this chapter, we introduced the model we will use throughout this thesis (see section 2.1). The model is based upon the one used by Hathaway *et al.* (1980), as described in section 1.5, i.e., we consider a plane layer of fluid rotating about an axis that is oblique to gravity. The basic state involves the imposition of both a horizontal and a vertical temperature gradient so that the basic state velocity contains a zonal thermal wind with vertical shear. However, extra to the Hathaway model, we impose a horizontal basic state magnetic field and we replace the no-slip boundary conditions of Hathaway *et al.* (1980), with stress free boundary conditions.

We presented the fully compressible fluid and MHD equations describing our system, in a rotating frame, but, as these equations are computationally demanding to solve, we discussed two approximations which we invoke in subsequent chapters.

1. **The Boussinesq approximation** was introduced in section 2.3 and allows density variations to be neglected in all terms except the buoyancy term. We derived perturbation equations under this approximation and recast them into dimensionless form. In Chapter 3, we consider the linearisation of these equations and in Chapters 6 and 8 we solve the nonlinear Boussinesq equations.
2. **The anelastic approximation** was introduced in section 2.4 and allows for density stratification in the fluid layer, whilst still filtering out the fast sound waves present in the fully compressible system. We derived the perturbation equations under this approximation, and considered the simplest basic state, so that there is no thermal wind or magnetic field to consider. In doing so, we have extended the system of Mizerski & Tobias (2011) to include a tilted rotation vector. We perform a linear study of these equations in Chapter 4 and a nonlinear study in Chapter 7.

## Chapter 3

# Linear Boussinesq Convection

### 3.1 Introduction

In Chapter 2, we derived the equations that describe the evolution of perturbations to a basic state of the hydrodynamic variables. The perturbations were of arbitrary size but in this chapter we assume them to be small enough that we can treat all products of perturbations to be negligible. By neglecting such products, we linearise the system of equations. Once we have the linear equations we are able to perform a normal mode decomposition and analyse the stability of the system. This is a well documented procedure and details can be found in Chandrasekhar (1961), Drazin & Reid (1981), amongst others.

There have been many studies of the linear stability of convection in a Boussinesq system. Early studies in a spherical geometry were performed by Roberts (1968) and Busse (1970), but these works were later shown to have shortcomings. Jones *et al.* (2000) improved on this early work and their results also agreed with the numerical simulations carried out by Zhang (1992). Dormy *et al.* (2004) considered the onset of convection in rotating spherical shells. The spherical geometry adds an extra level of complexity to computations and so other geometries have been studied for their relative computational ease. A setup that has been able to capture some of the features seen in a full spherical model is that of the annulus model (Busse (1970)). However, often considered the simplest of geometries to examine, is that of a plane layer as described in section 1.5 of the introduction.

The linear stability of a plane layer of fluid that is rotating about an axis parallel to gravity has been widely investigated, Chandrasekhar (1961) gives the most comprehensive review of the stability of this setup, but we also highlight some other studies. Eltayeb (1972) used linear stability

analysis to study hydromagnetic convection in a rapidly rotating fluid layer for four different orientations of rotation vector and magnetic field (see also Eltayeb (1975)), although they do not examine the case where the rotation vector is oblique to gravity and the imposed magnetic field is horizontal. In addition, Roberts & Jones (2000) considered a plane layer rotating about a vertical axis in the presence of a horizontal magnetic field at large Prandtl number. Arter (1983) investigated non-rotating convection in an imposed horizontal magnetic field, whilst this was primarily a nonlinear study, he did derive results from linear theory.

In the hydrodynamic regime, Teed *et al.* (2010) considered the effect of a thermal wind on plane layer convection but rotating about an axis parallel to gravity. As well as thermal instabilities they allowed for the possibility of baroclinic instabilities in a stably stratified fluid. They found, for a strong enough thermal wind, the system could be unstable even if the the layer was stably stratified.

A plane layer with vertical rotation is appropriate for modelling regions close to the poles on a spherical body, but if the layer is allowed to rotate at an angle oblique to gravity (the vertical direction) then it can be used to represent different latitudes on a spherical body. The linear stability of this setup was considered by Hathaway *et al.* (1979, 1980), who also imposed horizontal temperature gradients in the basic state to produce a thermal wind. This model was discussed in more detail in section 1.5.

We begin by deriving the linear equations for the Hathaway model, but, in addition, we will allow for the presence of a horizontal magnetic field. In other words, we linearise the nonlinear equations derived in Chapter 2.

## 3.2 Linear theory

### 3.2.1 Linearisation of the governing equations

On neglecting terms which are quadratic in the perturbations, the nondimensional equations (2.3.51)-(2.3.55) become

$$\frac{\partial \mathbf{u}}{\partial t} + U \frac{\partial \mathbf{u}}{\partial x} + w \frac{d\mathbf{u}_{BS}}{dz} = -Pr \nabla p + Ra Pr \theta \hat{\mathbf{e}}_z - Ta^{\frac{1}{2}} Pr \Omega \times \mathbf{u} + Q \zeta Pr [(\nabla \times \mathbf{B}) \times \mathbf{B}_{BS}] + Pr \nabla^2 \mathbf{u}, \quad (3.2.1)$$

$$\nabla \cdot \mathbf{u} = 0, \quad (3.2.2)$$

$$\frac{\partial \theta}{\partial t} + U \frac{\partial \theta}{\partial x} + T_y v - w = \nabla^2 \theta, \quad (3.2.3)$$

$$\frac{\partial \mathbf{B}}{\partial t} = \nabla \times [(\mathbf{u}_{BS} \times \mathbf{B}) + (\mathbf{u} \times \mathbf{B}_{BS})] + \zeta \nabla^2 \mathbf{B}, \quad (3.2.4)$$

$$\nabla \cdot \mathbf{B} = 0. \quad (3.2.5)$$

For clarity, we have removed the tildes from the perturbation quantities. Recall from equations (2.3.46)-(2.3.49), the boundary conditions we impose when solving these equations are

$$w = 0, \quad \frac{\partial^2 w}{\partial z^2} = 0, \quad \frac{\partial \varphi}{\partial z} = 0, \quad \theta = 0, \quad B_3 = 0, \quad \frac{\partial B_1}{\partial z} = 0 \quad (3.2.6)$$

on  $z = 0, 1$ .

### 3.2.2 Normal mode decomposition

To solve the system of equations (3.2.1)-(3.2.5) subject to the boundary conditions (3.2.6), we consider wave-like disturbances of the form

$$\theta(x, y, z, t) = \text{Re} \{ \Theta(z) f(x, y, t) \}, \quad (3.2.7)$$

where  $f(x, y, t) = e^{ikx + ily + \sigma t}$ ,  $\Theta$  is the amplitude,  $k$  and  $l$  are the real wavenumbers in the  $x$  and  $y$  directions respectively, and  $\sigma$  is the complex growth rate. Note we can write the growth rate as  $\sigma = \sigma_R + i\sigma_I$  where  $\sigma_R$  represents the growth rate of the disturbance and  $\sigma_I$  is the frequency of oscillations of the mode. Furthermore, in some cases, it will be convenient to write the frequency as  $\sigma_I = \omega$  and in what follows, both representations of the frequency will be used. Now, since  $\nabla \cdot \mathbf{u} = 0$ , we can write

$$\mathbf{u} = \nabla \times (\tilde{Z} \hat{\mathbf{z}}) + \nabla \times (\nabla \times \tilde{W} \hat{\mathbf{z}}),$$

where  $\tilde{Z}(z) = \frac{Z}{a^2} f(x, y, t)$  and  $\tilde{W} = \frac{W(z)}{a^2} f(x, y, t)$  and therefore

$$(u, v, w) = \text{Re} \left\{ \left[ \frac{ik}{a^2} DW + \frac{il}{a^2} Z, \frac{il}{a^2} DW - \frac{ik}{a^2} Z, W \right] f(x, y, t) \right\}, \quad (3.2.8)$$

where  $D \equiv \frac{d}{dz}$  and  $a^2 = k^2 + l^2$  is the total horizontal wavenumber. In this expansion,  $W(z)$  is the amplitude function for the vertical velocity and  $Z(z)$  the amplitude function for the vertical vorticity, i.e.,

$$\varphi = \frac{\partial v}{\partial x} - \frac{\partial u}{\partial y} = \text{Re} \left\{ Z(z) e^{ikx + ily + \sigma t} \right\}, \quad (3.2.9)$$

where  $\varphi$  is the  $z$ -component of the vorticity,  $\nabla \times \mathbf{u}$ . Similarly, since  $\nabla \cdot \mathbf{B} = 0$  we can write

$$\mathbf{B} = \nabla \times (\tilde{\mathcal{T}} \hat{\mathbf{z}}) + \nabla \times (\nabla \times \tilde{\mathcal{P}} \hat{\mathbf{z}})$$

where  $\tilde{\mathcal{T}} = \frac{\mathcal{T}}{a^2} f(x, y, t)$  and  $\tilde{\mathcal{P}} = \frac{\mathcal{P}(z)}{a^2} f(x, y, t)$  and therefore

$$(B_1, B_2, B_3) = \text{Re} \left\{ \left[ \frac{ik}{a^2} D\mathcal{P} + \frac{il}{a^2} \mathcal{T}, \frac{il}{a^2} D\mathcal{P} - \frac{ik}{a^2} \mathcal{T}, \mathcal{P} \right] f(x, y, t) \right\}. \quad (3.2.10)$$

By writing  $\mathbf{u}$  and  $\mathbf{B}$  in such a way means that  $\nabla \cdot \mathbf{u} = 0$  and  $\nabla \cdot \mathbf{B} = 0$  are automatically satisfied.

To eliminate the pressure perturbation we take the curl of equation (3.2.1), i.e., we form the vorticity equation. The vertical component of this equation is given by

$$\begin{aligned} \frac{\partial \varphi}{\partial t} + U \frac{\partial \varphi}{\partial x} - \frac{\partial w}{\partial y} DU = -PrTa^{\frac{1}{2}} \left[ \sin \phi \left( \frac{\partial u}{\partial x} + \frac{\partial v}{\partial y} \right) - \cos \phi \frac{\partial w}{\partial y} \right] + Pr \nabla^2 \varphi \\ + Q\zeta Pr \left[ \left( \cos \alpha \frac{\partial}{\partial x} + \sin \alpha \frac{\partial}{\partial y} \right) \left( \frac{\partial B_2}{\partial x} - \frac{\partial B_1}{\partial y} \right) \right]. \end{aligned} \quad (3.2.11)$$

Then, by assuming solutions of the form (3.2.7)-(3.2.10), we obtain

$$\begin{aligned} \sigma Z + ikUZ - ilW DU = PrTa^{\frac{1}{2}} (\sin \phi DW + il \cos \phi W) + Pr(D^2 - a^2)Z \\ + Q\zeta Pr (\cos \alpha ik + \sin \alpha il) \mathcal{T}, \end{aligned} \quad (3.2.12)$$

where we have used  $\frac{\partial w}{\partial z} = -\left(\frac{\partial u}{\partial x} + \frac{\partial v}{\partial y}\right)$  from  $\nabla \cdot \mathbf{u} = 0$ , and  $\frac{\partial B_2}{\partial x} - \frac{\partial B_1}{\partial y} = \mathcal{T}$  from equation (3.2.10).

Now, if we take the  $z$ -component of the curl of the vorticity equation, i.e., the curl of the curl of equation (3.2.1), then we obtain

$$\begin{aligned} \frac{\partial}{\partial t}(-\nabla^2 w) + U \frac{\partial}{\partial x}(-\nabla^2 w) = -RaPr \left( \frac{\partial^2 \theta}{\partial x^2} + \frac{\partial^2 \theta}{\partial y^2} \right) + PrTa^{\frac{1}{2}} \left( \cos \phi \frac{\partial \varphi}{\partial y} + \sin \phi \frac{\partial \varphi}{\partial z} \right) \\ + Pr \nabla^2(-\nabla^2 w) + Q\zeta Pr \left[ \left( \cos \alpha \frac{\partial}{\partial x} + \sin \alpha \frac{\partial}{\partial y} \right) (-\nabla^2 B_3) \right], \end{aligned} \quad (3.2.13)$$

where we have used the vector relation  $\nabla \times (\nabla \times \mathbf{u}) = -\nabla^2 \mathbf{u}$  (since  $\nabla \cdot \mathbf{u} = 0$ ). Assuming normal mode solutions in equation (3.2.13) gives

$$\begin{aligned} -\sigma(D^2 - a^2)W - Uik(D^2 - a^2)W = -a^2 RaPr \Theta + PrTa^{\frac{1}{2}} (\cos \phi ilZ + \sin \phi DZ) \\ - Pr(D^2 - a^2)^2 W - Q\zeta Pr (ik \cos \alpha + il \sin \alpha) (D^2 - a^2) \mathcal{P}. \end{aligned} \quad (3.2.14)$$

Normal mode decomposition of the heat equation (3.2.3) gives

$$[\sigma + ikU] a^2 \Theta + T_y (ilDW - ikZ) + T_z a^2 W = a^2 (D^2 - a^2) \Theta. \quad (3.2.15)$$

Regarding the evolution of the magnetic field, the  $z$ -component of the induction equation (3.2.4) is given by

$$\frac{\partial B_3}{\partial t} = \frac{\partial}{\partial x} (-UB_3 + w \cos \alpha) - \frac{\partial}{\partial y} (-w \sin \alpha) + \zeta \nabla^2 B_3, \quad (3.2.16)$$

which, on substitution of the separable solutions (3.2.8) and (3.2.10) gives

$$\sigma \mathcal{P} = -ikU \mathcal{P} + ikW \cos \alpha + ilW \sin \alpha + \zeta (D^2 - a^2) \mathcal{P}, \quad (3.2.17)$$

and the  $z$ -component of the curl of the induction equation (3.2.4) gives

$$\begin{aligned} \frac{\partial}{\partial t} \left( \frac{\partial B_2}{\partial x} - \frac{\partial B_1}{\partial y} \right) &= \sin \alpha \left( -\frac{\partial^2 w}{\partial x \partial z} - \frac{\partial^2 u}{\partial x^2} - \frac{\partial^2 u}{\partial y^2} \right) + \cos \alpha \left( \frac{\partial^2 v}{\partial x^2} + \frac{\partial^2 v}{\partial y^2} + \frac{\partial^2 w}{\partial y \partial z} \right) \\ &\quad - U \left( \frac{\partial^2 B_2}{\partial x^2} + \frac{\partial^2 B_2}{\partial y^2} + \frac{\partial^2 B_3}{\partial y \partial z} \right) - DU \frac{\partial B_3}{\partial y} + \zeta \nabla^2 \left( \frac{\partial B_2}{\partial x} - \frac{\partial B_1}{\partial y} \right), \end{aligned} \quad (3.2.18)$$

which in separable form can be written as

$$\sigma \mathcal{T} = \sin \alpha i l Z + \cos \alpha i k Z + \zeta (D^2 - a^2) \mathcal{T} - i l D U \mathcal{P} - i k U \mathcal{T} \quad (3.2.19)$$

using  $\nabla \cdot \mathbf{u} = \nabla \cdot \mathbf{B} = 0$ .

So, in summary, our governing equations for linearised Boussinesq convection are

$$\begin{aligned} [\sigma + i k U(z)] (D^2 - a^2) W + Pr T a^{\frac{1}{2}} (i l \cos \phi Z + \sin \phi D Z) &= -a^2 Pr Ra \Theta \\ &\quad + Pr (D^2 - a^2)^2 W + Q \zeta Pr (i l \sin \alpha + i k \cos \alpha) (D^2 - a^2) \mathcal{P}, \end{aligned} \quad (3.2.20)$$

$$\begin{aligned} [\sigma + i k U(z)] Z - i l D U W - Pr T a^{\frac{1}{2}} (i l \cos \phi W + \sin \phi D W) &= \\ Pr (D^2 - a^2) Z + Q \zeta Pr (i l \sin \alpha + i k \cos \alpha) \mathcal{T}, \end{aligned} \quad (3.2.21)$$

$$[\sigma + i k U(z)] a^2 \Theta + T_y (i l D W - i k Z) - a^2 W = a^2 (D^2 - a^2) \Theta, \quad (3.2.22)$$

$$[\sigma + i k U(z)] \mathcal{P} - (i l \sin \alpha + i k \cos \alpha) W = \zeta (D^2 - a^2) \mathcal{P}, \quad (3.2.23)$$

$$[\sigma + i k U(z)] \mathcal{T} - (i l \sin \alpha + i k \cos \alpha) Z + i l D U \mathcal{P} = \zeta (D^2 - a^2) \mathcal{T}. \quad (3.2.24)$$

### 3.2.3 Boundary conditions

The boundary conditions given by (3.2.6) need transforming into a form compatible with the above notation. The conditions on the vertical velocity component and the temperature conditions become respectively,

$$w = 0 \Rightarrow W = 0 \quad \text{on } z = 0, 1, \quad (3.2.25)$$

$$\theta = 0 \Rightarrow \Theta = 0 \quad \text{on } z = 0, 1. \quad (3.2.26)$$

For stress free boundaries we also have

$$\frac{\partial^2 w}{\partial z^2} = 0 \Rightarrow D^2 W = 0 \quad \text{on } z = 0, 1, \quad (3.2.27)$$

$$\frac{\partial \varphi}{\partial z} = 0 \Rightarrow D Z = 0 \quad \text{on } z = 0, 1. \quad (3.2.28)$$

The magnetic boundary conditions transform as

$$B_3 = 0 \Rightarrow \mathcal{P} = 0 \quad \text{on } z = 0, 1, \quad (3.2.29)$$

$$\frac{\partial B_1}{\partial z} = 0 \Rightarrow D \mathcal{T} = 0 \quad \text{on } z = 0, 1. \quad (3.2.30)$$

Equations (3.2.20)-(3.2.24) form a 12th order linear system of ODEs. Together with boundary conditions (3.2.25)-(3.2.30) they form a complex eigenvalue problem. For a small number of parameter regimes, this system can be solved analytically. For example, when  $Ta = 0$ ,  $\mathbf{B} = 0$ , we reduce to the simplest case considered in Chandrasekhar (1961), and the values of the Rayleigh number and wavenumber at the onset of convection can be determined exactly as

$$Ra_{\text{crit}} = \frac{27\pi^4}{4}, \quad a_{\text{crit}} = \frac{\pi}{\sqrt{2}}. \quad (3.2.31)$$

However, in general, we are required to solve the equations (3.2.20)-(3.2.24) numerically.

### 3.3 Numerical method

To solve our eigenvalue problem numerically we use a routine in MATLAB known as `bvp4c`, developed by Shampine *et al.* (2000). Almost any boundary value problem (BVP) can be formulated for solution with `bvp4c`. The first step is to write the equations to be solved as a system of first order ODEs. To do this we introduce new variables, one for each variable in the original problem plus one for each of its derivatives up to one less than the highest derivative appearing.

In order to use this method to solve equations (3.2.20)-(3.2.24), subject to the boundary conditions given by (3.2.25)-(3.2.30), we first split the equations into their real and imaginary parts. To do this we write each of the variables as a sum of its real and imaginary parts, i.e., write

$$W = W_R + iW_I, \quad Z = Z_R + iZ_I, \quad \Theta = \Theta_R + i\Theta_I, \quad (3.3.32)$$

$$\mathcal{P} = \mathcal{P}_R + i\mathcal{P}_I, \quad \mathcal{T} = \mathcal{T}_R + i\mathcal{T}_I, \quad \sigma = \sigma_R + i\sigma_I, \quad (3.3.33)$$

and substitute into each of the five equations (3.2.20)-(3.2.24). Taking the real and imaginary parts of these equations gives us ten equations, which we then write as a system of 24 first order differential equations. Since this is a linear eigenvalue problem, the amplitude is arbitrary, and so, in order to fix this amplitude, we require extra boundary conditions, one for each of the eigenvalues. Typically, we take either  $D\Theta_R = D\Theta_I = 1$  or  $DW_R = DW_I = 1$ .

We have developed two main variations of our linear code that use `bvp4c`. The first of these imposes  $\sigma_R = 0$  and solves for  $Ra_c \equiv Ra$  and  $\omega_c \equiv \sigma_I$ , for a given  $k$  and  $l$ . In other words, it finds the modes which are marginally stable (they are neither growing ( $\sigma_R > 0$ ) nor decaying ( $\sigma_R < 0$ )) and the frequency at which they occur. By minimising  $Ra_c$  over all wavenumbers, we obtain the critical Rayleigh number,  $Ra_{\text{crit}}$ . The wavenumbers at which this critical value occurs

are the critical wavenumbers, denoted  $k_{\text{crit}}$  and  $l_{\text{crit}}$ , the total critical wavenumber is then given by  $a_{\text{crit}} = \sqrt{k_{\text{crit}}^2 + l_{\text{crit}}^2}$ . The corresponding critical frequency of this mode is denoted  $\omega_{\text{crit}}$ . We refer to the critical Rayleigh number, critical wavenumber and critical frequency collectively as the critical values. Note, a larger critical wavenumber corresponds to a smaller length scale and vice versa. Similarly, a larger critical frequency corresponds to a solution with a shorter time period and vice versa.

$\sigma_R = 0$  determines the Rayleigh number required for the onset of instability. The instability can occur either as a direct bifurcation, where  $\sigma_R = \omega_c = 0$  or as a Hopf bifurcation, where  $\sigma_R = 0$  but  $\omega_c \neq 0$ . The first of these situations is referred to as stationary instability and the second as oscillatory instability (or overstability). For regular Rayleigh-Bénard convection, it has been shown that overstability is preferred if  $Pr \lesssim 0.6766$  and if  $Ta > Ta^*$ , where  $Ta^*$  is a function of wavenumber and  $Pr$ . The exact values and proof of this can be found in Chandrasekhar (1961).

The second variation of our code solves for  $\sigma_R$  and  $\sigma_I$ , for a given  $Ra$ ,  $k$  and  $l$ . This allows us to determine the growth rate of a mode, for a particular set of parameters. Maximising the calculated  $\sigma_R$  over the wavenumbers determines the fastest growing mode, and the wavenumber at which this mode occurs, and therefore establishing the wavelength of the mode we would expect to see in an experiment.

### 3.3.1 Eigenfunctions

After solving our 24 first order ODEs, MATLAB `bvp4c` allows us to retrieve any of our 24 variables. In particular, we are able to find the real and imaginary parts of  $W$ ,  $Z$ ,  $\Theta$ ,  $DW$ ,  $\mathcal{P}$ ,  $\mathcal{T}$  and  $D\mathcal{P}$ , evaluated at a series of points in  $z$ . We are then able to reconstruct  $\theta$ ,  $\mathbf{u}$ , and  $\mathbf{B}$  using equations (3.2.7), (3.2.8) and (3.2.10). Equation (3.2.8) gives the velocity field perturbations as

$$u = \text{Re} \left\{ \left( \frac{ik}{a^2} DW + \frac{il}{a^2} Z \right) e^{ikx+ily+\sigma t} \right\}, \quad (3.3.34)$$

$$v = \text{Re} \left\{ \left( \frac{il}{a^2} DW - \frac{ik}{a^2} Z \right) e^{ikx+ily+\sigma t} \right\}, \quad (3.3.35)$$

$$w = \text{Re} \left\{ W e^{ikx+ily+\sigma t} \right\}. \quad (3.3.36)$$

The temperature perturbation from (3.2.7) is given by

$$\theta = \text{Re} \left\{ \Theta e^{ikx+ily+\sigma t} \right\} \quad (3.3.37)$$

and the magnetic field perturbation components from (3.2.10) are similarly given by

$$B_1 = \text{Re} \left\{ \left( \frac{ik}{a^2} D\mathcal{P} + \frac{il}{a^2} \mathcal{T} \right) e^{ikx+ily+\sigma t} \right\}, \quad (3.3.38)$$

$$B_2 = \text{Re} \left\{ \left( \frac{il}{a^2} D\mathcal{P} - \frac{ik}{a^2} \mathcal{T} \right) e^{ikx+ily+\sigma t} \right\}, \quad (3.3.39)$$

$$B_3 = \text{Re}[\mathcal{P}e^{ikx+ily+\sigma t}]. \quad (3.3.40)$$

### 3.4 Numerical results

In this section we present the linear results; they can be categorised into three parts. We begin by considering the purely hydrodynamic case (see section 3.5), i.e., we set  $\mathbf{B} = 0$  (and so  $\mathcal{P} = \mathcal{T} = 0$ ) and neglect the equations given by (3.2.23) and (3.2.24). As a result, we reduce to the system of equations solved by Hathaway *et al.* (1980) (hereafter HTG), however, we shall enforce stress free boundary conditions whereas HTG imposed no slip boundary conditions. We will consider two cases within this hydrodynamic regime: initially, the basic state temperature will be taken to vary only in  $z$  and therefore there will be no thermal wind, i.e.,  $T_y = U = 0$ . A horizontal temperature gradient will be included in the second part of the hydrodynamic section though, and the effects of a thermal wind considered. The final part of the chapter (see section 3.6) will take  $\mathbf{B} \neq 0$  and so the effects of a horizontal magnetic field on rotating convection can be examined, but no thermal wind effects will be present.

### 3.5 Hydrodynamic results ( $\mathbf{B} = 0$ )

As mentioned above, when  $\mathbf{B} = 0$ , our system of equations reduces to the same system of equations as those used by HTG, and therefore we use their results as a test for our numerical code. However, HTG have rigid boundaries and so for the purposes of the test we have to change from stress free to no slip boundary conditions. This involves invoking  $DW = Z = 0$  on the boundaries instead of  $D^2W = DZ = 0$ . Our first test involves a case where  $T_y = 0$ . We calculate the critical Rayleigh number and critical wavenumber as a function of  $Ta$  for north-south (NS) and east-west (EW) convection rolls in a layer with  $\phi = \frac{\pi}{4}$  (see figure 3.1). NS rolls are defined as convection rolls whose axes are aligned in the  $y$ -direction (NS direction) and similarly EW convection rolls are those whose axes are aligned in the  $x$ -direction (EW direction). When  $\phi = \frac{\pi}{2}$ , NS and EW rolls are equivalent because of the symmetry about the  $z$  axis, however, when  $\phi \neq \frac{\pi}{2}$ , there is a distinction to be made between NS and EW rolls. Figure 3.1 is identical

to figure 2 of HTG and provides good support for the validity of our numerical code. We also successfully verified the code against a number of other cases, including ones where  $T_y \neq 0$ .

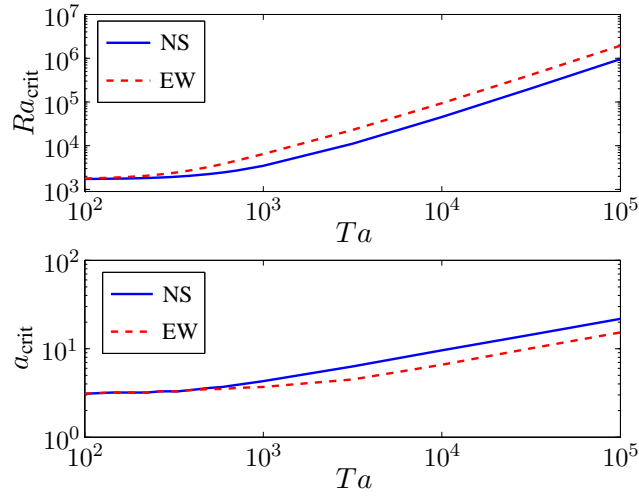


Figure 3.1: Critical Rayleigh number ( $Ra_{\text{crit}}$ ) and critical wavenumber ( $a_{\text{crit}}$ ) against Taylor number ( $Ta$ ) for NS (solid line) and EW (dashed line) convection rolls, in a layer with  $\phi = \frac{\pi}{4}$ . This figure exactly replicates figure 2 of HTG and provides good support for the accuracy of our numerical code.

### 3.5.1 Prandtl number effects

In many astrophysical situations, such as stellar interiors, the fluid Prandtl number is much smaller than unity and so the small  $Pr$  regime is one we wish to investigate further. The majority of work by HTG fixes  $Pr = 1$ , with a small amount of time given to  $Pr = 0.1$ . In this section, we examine the effects of small  $Pr$  in more detail. As mentioned in section 3.3, for small  $Pr$ , convection can set in as oscillatory modes and so we must consider the possibility of both direct and overstable convection.

$$T_y = 0$$

Initially, we consider the effects of small  $Pr$  on the onset of convection in a system with a tilted rotation vector, but no thermal wind ( $T_y = 0$ ). We study the dependence on  $Ta$  of the critical Rayleigh number, wavenumber and frequency given by  $Ra_{\text{crit}}$ ,  $a_{\text{crit}}$  and  $\omega_{\text{crit}}$  respectively. Figures 3.2 and 3.3 show separately the critical values as a function of  $Ta$ , for the cases of NS and EW convection rolls respectively, for a layer at  $\phi = \frac{\pi}{4}$ . The Rayleigh number at onset is

independent of  $Pr$  for direct modes, however, the Rayleigh number required for the onset of oscillatory convection depends on  $Pr$ . For NS rolls,  $Ra_{\text{crit}}$  decreases with decreasing  $Pr$  for fixed  $Ta$ , as do  $k_{\text{crit}}$  and  $\omega_{\text{crit}}$ , as shown in figure 3.2. As discussed in Chandrasekhar (1961), the tilted rotation vector has the effect of reducing the rotation rate by a factor of  $\sin \phi$  on convection in the  $x$ - $z$  plane. This results in the NS rolls having the same qualitative behaviour as for vertical rotation but with reduced critical values.

In contrast, the tilted rotation vector has a larger impact on the convection in the  $y$ - $z$  plane (EW rolls) as seen in figure 3.3. For smaller  $Pr$ , the growth of  $Ra_{\text{crit}}$  with  $Ta$  does not immediately settle to a power law and the critical wavenumber decreases with increasing  $Ta$ , before increasing again. Also, in this case, it is not always true that  $Ra_{\text{crit}}$  decreases with decreasing  $Pr$  for fixed  $Ta$ . For example, at  $Ta = 5 \times 10^5$ ,  $Ra_{\text{crit}} = 8413.2$  when  $Pr = 0.0125$  but  $Ra_{\text{crit}} = 8521.7$  when  $Pr = 0.00625$ . As was reported by HTG, for fixed  $Ta$  and  $Pr$  a lower  $Ra$  is required to destabilise NS rolls than EW rolls, we see this in our case too, i.e., for stress free boundary conditions at small  $Pr$ . Note also, for convection to onset as oscillatory modes, the rotation rate has to be high enough, and that this transition rotation rate is lower for EW rolls than it is for NS rolls.

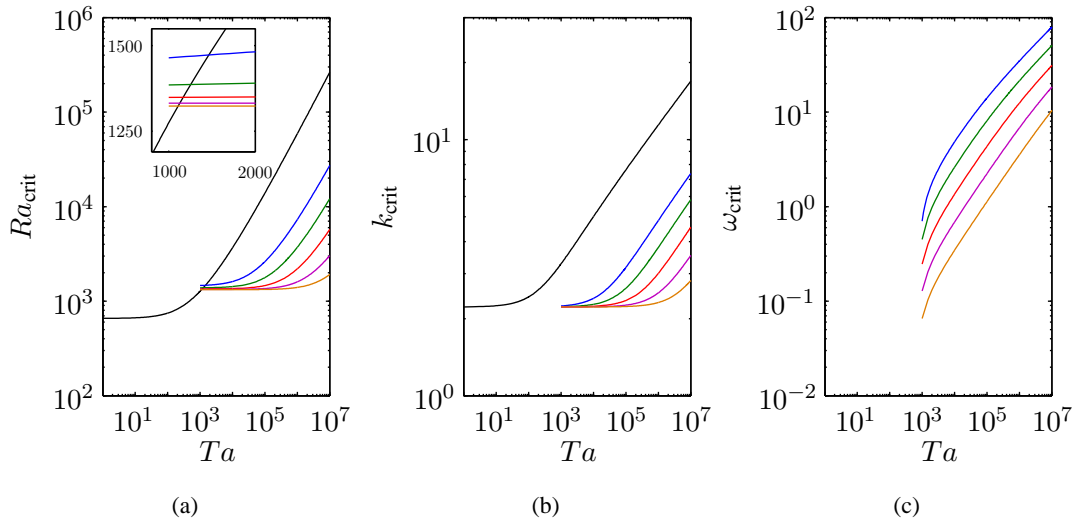


Figure 3.2: Critical values for NS rolls. (a) Critical Rayleigh number,  $Ra_{\text{crit}}$ , (b) critical wavenumber,  $k_{\text{crit}}$ , and (c) critical frequency,  $\omega_{\text{crit}}$ , of NS rolls against Taylor number,  $Ta$ , for different  $Pr$  in a layer at  $\phi = \frac{\pi}{4}$ . The black line represents direct modes and all other lines represent oscillatory modes. In black  $Pr = 1$ , blue  $Pr = 0.1$ , green  $Pr = 0.05$ , red  $Pr = 0.025$ , purple  $Pr = 0.0125$  and orange  $Pr = 0.00625$ .

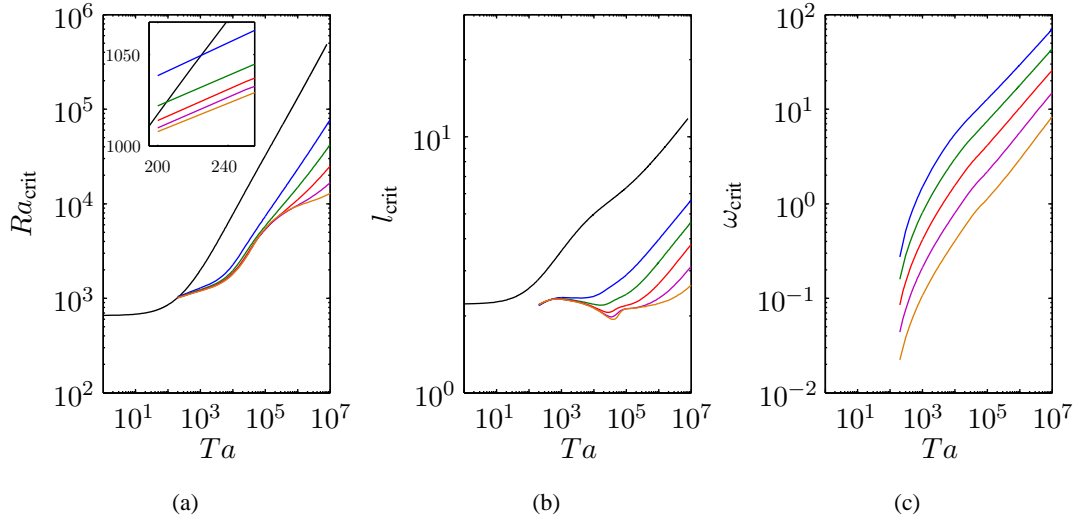


Figure 3.3: Critical values for EW rolls. (a) Critical Rayleigh number,  $Ra_{\text{crit}}$ , (b) critical wavenumber,  $l_{\text{crit}}$ , and (c) critical frequency,  $\omega_{\text{crit}}$ , of EW rolls against Taylor number,  $Ta$ , for different  $Pr$  in a layer at  $\phi = \frac{\pi}{4}$ . The black line represents direct modes and all other lines represent oscillatory modes. In black  $Pr = 1$ , blue  $Pr = 0.1$ , green  $Pr = 0.05$ , red  $Pr = 0.025$ , purple  $Pr = 0.0125$  and orange  $Pr = 0.00625$ .

### $T_y \neq 0$

This section considers the case when  $T_y \neq 0$  and so a horizontal temperature gradient is present in the basic state, resulting in a thermal wind, as discussed in section 2.3.2. HTG found that for Prandtl numbers  $\mathcal{O}(1)$ , if the shear is strong enough, NS rolls are stabilised by the thermal wind, whilst EW rolls can extract energy from the shear and grow. This leads to EW rolls becoming preferred over NS rolls. We found this to be true even when  $Pr$  was decreased to small values, therefore, this section will be restricted to examining EW rolls only.

It is informative to examine the effect of the tilted rotation vector and thermal wind on the orientation of the eigenfunctions. Figure 3.4 shows plots of  $w(y, z)$  (top row),  $\theta(y, z)$  (middle row) and  $\zeta(y, z)$  (bottom row) at  $Ra = Ra_{\text{crit}}$ ,  $l = l_{\text{crit}}$  and  $\omega = \omega_{\text{crit}}$  at a snapshot in time. In (a), there is no tilting of the convection cells and a reflectional symmetry is present. This symmetry can be seen to exist from equations (3.2.20)-(3.2.22), as when  $Q = 0$  and  $\phi = \frac{\pi}{2}$ , all the terms in these equations have the same parity, e.g., when  $W$  and  $\Theta$  are even and  $Z$  is odd. In (b), the rotation vector is tilted from the vertical to  $\phi = \frac{\pi}{4}$  and the convection cells align themselves with the axis of rotation. Furthermore, the reflectional symmetry present in (a) no longer exists.

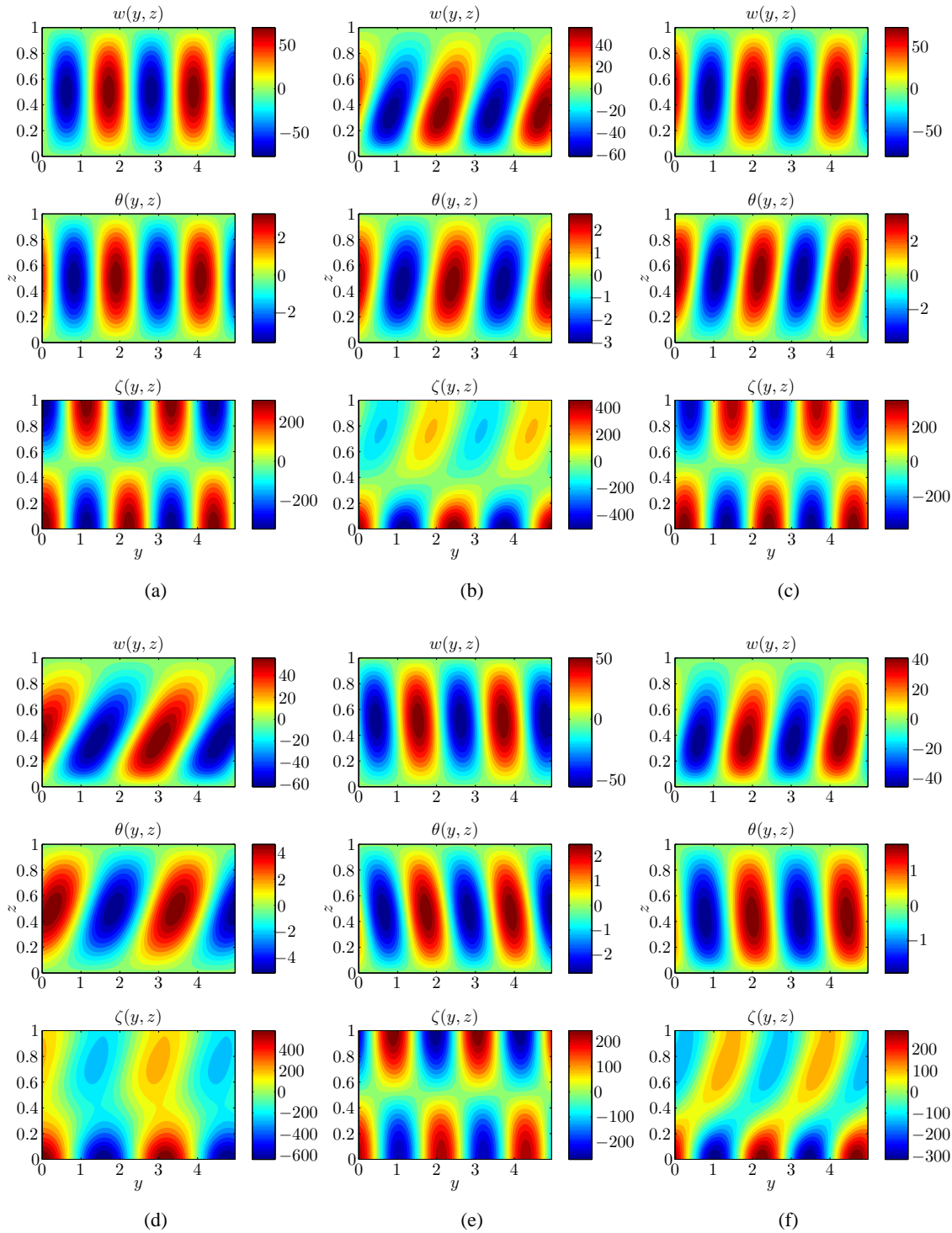


Figure 3.4: Eigenfunctions  $w(y, z)$ ,  $\theta(y, z)$  and  $\zeta(y, z)$  at  $Ra_{\text{crit}}$ ,  $l_{\text{crit}}$  and  $\omega_{\text{crit}}$  for  $Pr = 0.05$ ,  $Ta = 10^5$  and (a)  $T_y = 0$ ,  $\phi = \frac{\pi}{2}$ , (b)  $T_y = 0$ ,  $\phi = \frac{\pi}{4}$ , (c)  $T_y = -0.5$ ,  $\phi = \frac{\pi}{2}$ , (d)  $T_y = -0.5$ ,  $\phi = \frac{\pi}{4}$ , (e)  $T_y = 0.5$ ,  $\phi = \frac{\pi}{2}$ , (f)  $T_y = 0.5$ ,  $\phi = \frac{\pi}{4}$ .

This is because, in this case, the  $il \cos \phi Z$  and  $il \cos \phi W$  terms in equations (3.2.20) and (3.2.21) respectively are non-zero, and therefore break the symmetry. In figure 3.4 (a)-(f), the solutions are oscillatory, i.e.,  $\omega \neq 0$ . However, we comment that, if we consider steady solutions ( $\omega = 0$ ), then it is possible to find a rotational symmetry that is not present when ( $\omega \neq 0$ ). Tilting of the convection cells can be achieved for vertical rotation if a horizontal temperature gradient is applied, see (c), (e). For  $T_y > 0$ , the tilt is towards the equator, for  $T_y < 0$  the tilt is towards the pole. Note, in (c) and (e), a symmetry is not in fact present although this is not necessarily obvious from the plots, this is because of the size of  $T_y$ ; we comment that the asymmetry does become clearer the larger  $|T_y|$  is. When both a horizontal temperature gradient and a tilted rotation vector are present, the poleward tilt is either exaggerated (when  $T_y < 0$ ) or reduced (when  $T_y > 0$ ). This can be seen in subfigures (d) and (f) respectively.

### 3.5.2 Effect of $T_y$ on the onset of convection

To see how the addition of a thermal wind affects the onset of convection of EW rolls, we plot the critical Rayleigh number, wavenumber and frequency as a function of  $T_y$  for  $Ta$  fixed at  $10^5$  (see figure 3.5). We show the case for  $Pr = 1$  (black) and  $Pr = 0.1$  (blue).

We see that, for  $Pr = 1$ , the maximum  $Ra_{\text{crit}}$  is achieved for very small, positive  $T_y$  and for negative  $T_y$ , the presence of a thermal wind lowers the critical Rayleigh number, meaning that convection will onset for a smaller thermal forcing. From plot (b), for  $Pr = 1$ , a negative  $T_y$  results in a smaller preferred wavenumber than for positive  $T_y$ , with a smooth transition between the two. In other words, the rolls we would observe are of a larger size for negative  $T_y$  than they are for positive  $T_y$ . As for  $T_y = 0$ , the solutions for  $Pr = 1$  are direct modes and hence the critical frequency is zero for these solutions; we do not display this line on the plot of  $\omega_{\text{crit}}$ .

In figure 3.5, we also show the critical values for  $Pr = 0.1$ , a more realistic regime, as discussed previously. In this case, the maximum critical Rayleigh number occurs for  $T_y$  slightly negative, but for any significant horizontal temperature gradient,  $Ra_{\text{crit}}$  is less than for  $T_y = 0$ . As expected, the  $Pr = 0.1$  modes onset at a lower value of  $Ra$  than the  $Pr = 1$  modes, meaning that convection is more easily excited in the lower  $Pr$  case. The critical wavenumber,  $l_{\text{crit}}$ , is also smaller for  $Pr = 0.1$  than it is for  $Pr = 1$ . Also in contrast to the  $Pr = 1$  case,  $l_{\text{crit}}$  is similar for similar values of  $|T_y|$ ; instead, the difference between the solution for positive  $T_y$  and the solution for negative  $T_y$  appears in the frequency of the marginal mode, rather than in the wavenumber. For  $Pr = 0.1$ , the preferred modes are oscillatory, their associated critical frequency is shown in (c). In this case, as  $T_y$  increases the critical frequency also increases. We also notice that the

increase is more rapid in the negative  $T_y$  regime than it is in the positive  $T_y$  regime and that the solutions with positive  $T_y$  oscillate over a shorter period than the solutions with negative  $T_y$  do.

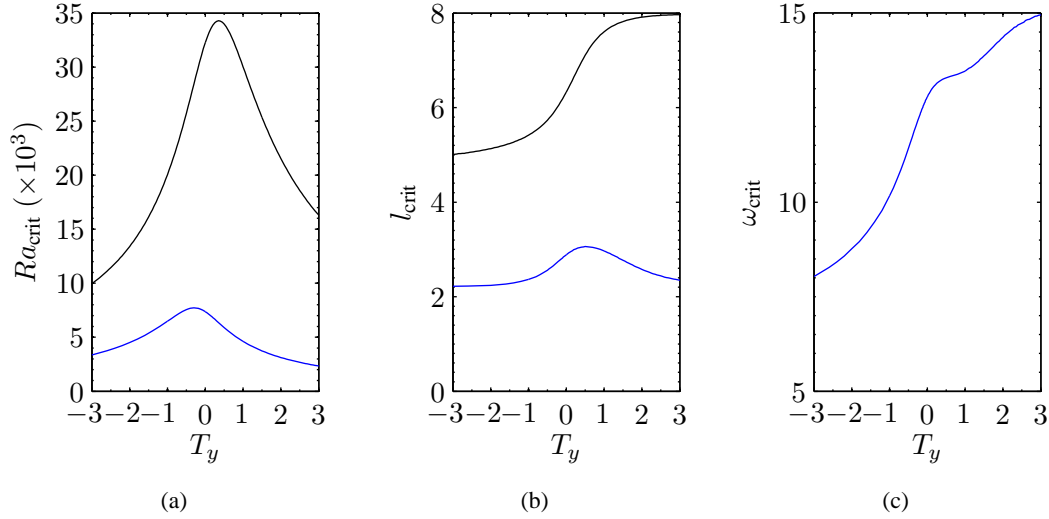


Figure 3.5: (a) Critical Rayleigh number ( $Ra_{crit}$ ), (b) critical wavenumber ( $l_{crit}$ ) and (c) critical frequency ( $\omega_{crit}$ ), as a function of  $T_y$ , for  $Pr = 1$  (black) and  $Pr = 0.1$  (blue) with  $Ta$  fixed at  $10^5$ . The  $Pr = 1$  solutions are steady and the  $Pr = 0.1$  solutions are oscillatory.

## 3.6 Effects of a horizontal magnetic field

Having studied the hydrodynamic problem in the previous section, we now include a horizontal magnetic field to investigate its effect. We set  $T_y = 0$  so that there is no horizontal temperature gradient and hence no thermal wind. To gain some insight into this problem, it is worth considering a simple case that can be studied analytically, before using the knowledge gained to assist with a more general numerical study.

### 3.6.1 Analytical results

We can make some progress analytically if we consider the case of vertical rotation ( $\phi = \frac{\pi}{2}$ ), magnetic field in the  $y$ -direction ( $\alpha = \frac{\pi}{2}$ ) and set  $k = 0$ , so that we become two-dimensional in

the  $y$ - $z$  plane. In this limit, and taking  $T_y = U = 0$ , the equations (3.2.20)-(3.2.24) become

$$\sigma(D^2 - l^2)W + PrTa^{\frac{1}{2}}DZ = -l^2PrRa\Theta + Pr(D^2 - l^2)^2W + Q\zeta Pril(D^2 - l^2)\mathcal{P}, \quad (3.6.41)$$

$$\sigma Z - PrTa^{\frac{1}{2}}DW = Pr(D^2 - l^2)Z + Q\zeta Pril\mathcal{T}, \quad (3.6.42)$$

$$\sigma\Theta - W = (D^2 - l^2)\Theta, \quad (3.6.43)$$

$$\sigma\mathcal{P} - ilW = \zeta(D^2 - l^2)\mathcal{P}, \quad (3.6.44)$$

$$\sigma\mathcal{T} - ilZ = -\zeta(D^2 - l^2)\mathcal{T}. \quad (3.6.45)$$

For the boundary conditions given by (3.2.25)-(3.2.30), the eigenmode solutions of the system given by (3.6.41)-(3.6.45) take a simple form, in particular we can let

$$\begin{aligned} W &= W_0 \sin(n\pi z), & Z &= Z_0 \cos(n\pi z), & \Theta &= \Theta_0 \sin(n\pi z), \\ \mathcal{P} &= \mathcal{P}_0 \sin(n\pi z), & \mathcal{T} &= \mathcal{T}_0 \cos(n\pi z), \end{aligned} \quad (3.6.46)$$

for  $n = 1, 2, \dots$ . Substituting these into equations (3.6.41)-(3.6.45), allows us to write

$$[\sigma A + PrA^2] W_0 = l^2 Ra Pr \Theta_0 + Q\zeta Pril A \mathcal{P}_0 - n\pi PrTa^{\frac{1}{2}} Z_0, \quad (3.6.47)$$

$$[\sigma + PrA] Z_0 = n\pi PrTa^{\frac{1}{2}} W_0 + Q\zeta Pril \mathcal{T}_0, \quad (3.6.48)$$

$$[\sigma + A] \Theta_0 = W_0, \quad (3.6.49)$$

$$[\sigma + \zeta A] \mathcal{P}_0 = ilW_0, \quad (3.6.50)$$

$$[\sigma + \zeta A] \mathcal{T}_0 = ilZ_0, \quad (3.6.51)$$

where we have defined  $A = n^2\pi^2 + l^2$ , in order to simplify the notation. We can combine these five equations into a single equation for the growth rate  $\sigma$ . To do this we first eliminate  $\mathcal{T}_0$  from equation (3.6.48) using equation (3.6.51) and then we eliminate  $\Theta_0$ ,  $\mathcal{P}_0$  and  $Z_0$  (in that order) from equation (3.6.47) to give a quintic equation for  $\sigma$ . The equation can be written as

$$a_1\sigma^5 + a_2\sigma^4 + a_3\sigma^3 + a_4\sigma^2 + a_5\sigma + a_6 = 0, \quad (3.6.52)$$

where

$$\begin{aligned}
a_1 &= A, \\
a_2 &= 2PrA^2 + 2\zeta A^2 + A^2, \\
a_3 &= 2Pr\zeta A^3 + PrA^3 + \zeta A^3 + (PrA + \zeta A)(PrA^2 + \zeta A^2 + A^2) \\
&\quad + 2Q\zeta Prl^2 A - l^2 PrRa + Pr^2 n^2 \pi^2 Ta, \\
a_4 &= \zeta PrA^4 + (\zeta A + PrA)(\zeta PrA^3 + PrA^3 + \zeta A^3) \\
&\quad + (Pr\zeta A^2 + Q\zeta Prl^2)(PrA^2 + \zeta A^2 + A^2) - \zeta Al^2 PrRa + Q\zeta Prl^2 A^2 \\
&\quad - (PrA + \zeta A)(l^2 PrRa - Q\zeta Prl^2 A) + Pr^2 n^2 \pi^2 Ta\zeta A + Pr^2 n^2 \pi^2 Ta(\zeta A + A), \\
a_5 &= (PrA + \zeta A)\zeta PrA^4 + (Pr\zeta A^2 + Q\zeta Prl^2)(\zeta PrA^3 + PrA^3 + \zeta A^3) \\
&\quad - (PrA + \zeta A)(\zeta Al^2 PrRa - Q\zeta Prl^2 A^2) - (Pr\zeta A^2 + Q\zeta Prl^2)(l^2 PrRa - Q\zeta Prl^2 A) \\
&\quad + Pr^2 n^2 \pi^2 Ta(\zeta A + A)\zeta A + Pr^2 n^2 \pi^2 Ta\zeta A^2, \\
a_6 &= (Pr\zeta A^2 + Q\zeta Prl^2)\zeta PrA^4 - (Pr\zeta A^2 + Q\zeta Prl^2)(\zeta Al^2 PrRa - Q\zeta Prl^2 A^2) \\
&\quad + Pr^2 n^2 \pi^2 Ta\zeta^2 A^3. \tag{3.6.53}
\end{aligned}$$

This dispersion relation allows us to find the eigenvalues, in particular, the Rayleigh number at which the marginal state ( $\sigma_R = 0$ ) occurs, along with the frequency of oscillation in the case when  $\omega \neq 0$  (overstable convection).

### Steady solutions

Convection sets in as steady rolls when  $\sigma_R = \omega = 0$ , i.e.,  $\sigma = 0$ . From (3.6.52), we see this occurs when  $a_6 = 0$ , that is, when

$$\begin{aligned}
&(Pr\zeta A^2 + Q\zeta Prl^2)\zeta PrA^4 - (Pr\zeta A^2 + Q\zeta Prl^2)(\zeta Al^2 PrRa - Q\zeta Prl^2 A^2) \\
&+ Pr^2 n^2 \pi^2 Ta\zeta^2 A^3 = 0. \tag{3.6.54}
\end{aligned}$$

Dividing by  $Pr^2 \zeta^2$  and rearranging, leads to the following condition on the Rayleigh number

$$Ra l^2 (A^3 + QAl^2) = A^3 (A^3 + QAl^2) + Ql^2 A (A^3 + Ql^2 A) + n^2 \pi^2 Ta A^3, \tag{3.6.55}$$

which gives us that, when  $\sigma = 0$ ,  $Ra$  is given by the following expression

$$\begin{aligned}
Ra &= \frac{A^3}{l^2} + QA + \frac{n^2 \pi^2 Ta A^3}{l^2 (A^3 + QAl^2)} \\
&= \frac{(n^2 \pi^2 + l^2)^3}{l^2} + Q(n^2 \pi^2 + l^2) + \frac{n^2 \pi^2 Ta (n^2 \pi^2 + l^2)^2}{l^2 ((n^2 \pi^2 + l^2)^2 + Ql^2)}, \tag{3.6.56}
\end{aligned}$$

see Roberts & Jones (2000).

We are interested in the first mode that goes unstable, i.e., the fastest growing mode that occurs for the smallest  $Ra$ . Clearly, from equation (3.6.56), this occurs when  $n = 1$ . Note that, in the absence of rotation ( $Ta = 0$ ) and with  $n = 1$ , equation (3.6.56) reduces to the expression found in Chandrasekhar (1961) and Arter (1983)

$$Ra = \frac{(\pi^2 + l^2)^3}{l^2} + Q(\pi^2 + l^2) \quad (3.6.57)$$

and in the absence of a magnetic field ( $Q = 0$ ), equation (3.6.56) reduces to the expression found in Chandrasekhar (1961)

$$Ra = \frac{Ta\pi^2}{l^2} + \frac{(\pi^2 + l^2)^3}{l^2}. \quad (3.6.58)$$

### Oscillatory solutions

For marginal overstable modes,  $\sigma = i\omega$  and so (3.6.52) gives us that

$$a_1 i\omega^5 + a_2 \omega^4 - a_3 i\omega^3 - a_4 \omega^2 + a_5 i\omega + a_6 = 0, \quad (3.6.59)$$

which, by taking the real and imaginary parts gives us two equations:

$$a_2 \omega^4 - a_4 \omega^2 + a_6 = 0, \quad (3.6.60)$$

$$a_1 \omega^5 - a_3 \omega^3 + a_5 \omega = 0. \quad (3.6.61)$$

To find the roots of these equations, a code in Maple was used to solve for  $\omega$  and  $Ra$  at the onset of convection when  $\phi = \frac{\pi}{2}$ . These solutions can then be used as an initial estimate for the  $\phi = \frac{\pi}{4}$  solutions in our `bvp4c` code. By using the  $\phi = \frac{\pi}{2}$  solutions as an initial estimate, it is hoped that the code will converge faster to the  $\phi = \frac{\pi}{4}$  solutions. As an example, in table 3.1, we include the values of  $Ra$  and  $\omega$  at onset for different wavenumbers in a case where  $\phi = \frac{\pi}{2}$ . In the complex plane, equations (3.6.60) and (3.6.61) have seven  $(Ra, \omega)$  pairs of solutions, but we are only interested in the cases where  $Ra$  and  $\omega$  are both real. One of the seven pairs of solutions is always real and corresponds to the direct mode at onset, i.e.,  $\omega = 0$ , this solution is denoted with a subscript zero in the table. The other six solutions consist of three pairs of solutions given by  $(Ra_i, \pm\omega_i)$  for  $i = 1, 2, 3$ . These oscillatory solutions, may or may not, be real, depending upon the parameters of the system. Table 3.1 shows a selection of results to highlight each of these different scenarios. For example, at  $l = 0.1$ , only five of the seven solutions are real, but for  $l = 1, 2, 3$ , all seven solutions are real and for very large  $l$ , only the direct mode exists. To obtain the critical Rayleigh number, we would need to minimise these results over  $l$ , but we are not

$l$	Direct		Overstable					
	$\mathbf{Ra}_0$	$\omega_0$	$\mathbf{Ra}_1$	$\omega_1$	$\mathbf{Ra}_2$	$\omega_2$	$\mathbf{Ra}_3$	$\omega_3$
0.1	$4.89 \times 10^7$	0	$2.01 \times 10^6$	$\pm 28.60$	$5.45 \times 10^7$	$\pm 0.50$	–	–
1	$1.22 \times 10^5$	0	$2.79 \times 10^4$	$\pm 29.88$	$5.39 \times 10^5$	$\pm 11.02$	$3.35 \times 10^4$	$\pm 2.57$
2	$1.41 \times 10^5$	0	$1.56 \times 10^4$	$\pm 33.39$	$1.28 \times 10^5$	$\pm 22.23$	$8.81 \times 10^3$	$\pm 9.72$
3	$1.90 \times 10^5$	0	$2.19 \times 10^4$	$\pm 37.68$	$4.39 \times 10^4$	$\pm 34.30$	$8.47 \times 10^3$	$\pm 18.90$
4	$2.60 \times 10^5$	0	$1.07 \times 10^4$	$\pm 28.85$	–	–	–	–
5	$3.51 \times 10^5$	0	$1.42 \times 10^4$	$\pm 39.00$	–	–	–	–
100	$2.00 \times 10^8$	0	–	–	–	–	–	–

Table 3.1: A table of solutions to the equations (3.6.60) and (3.6.61) for  $Pr = 0.1$ ,  $\zeta = 0.1$ ,  $Q = 10000$  and  $\phi = \frac{\pi}{2}$ . These are an example of the solutions used as an initial estimate in the numerical code that solves for the solution when  $\phi = \frac{\pi}{4}$ .

interested in calculating the critical values for the  $\phi = \frac{\pi}{2}$  case, our aim is to establish a sensible initial estimate to use in the code, to find the  $\phi = \frac{\pi}{4}$  solutions.

### 3.6.2 Numerical solutions

We wish to consider the effect of a tilted rotation vector on the magnetoconvection. As mentioned before, this can not be done analytically because  $\phi \neq \frac{\pi}{2}$  introduces extra terms into the equations (3.6.41)-(3.6.45), which mean that the expansions given in (3.6.46) can not be assumed. We therefore use our numerical code to derive results when  $\phi \neq \frac{\pi}{2}$ . As explained in the previous section, using the solutions found when  $\phi = \frac{\pi}{2}$  as an initial estimate for the solution when  $\phi = \frac{\pi}{4}$ , helps the bvp4c algorithm to converge faster to the  $\phi = \frac{\pi}{4}$  solution.

#### Testing the code

Before we proceed with investigating the  $\phi = \frac{\pi}{4}$  case, we test our numerical code where possible. If we set the Chandrasekhar number,  $Q$ , to zero we should recover the behaviour of the purely hydrodynamic case. This was the first check for the magnetic code and we successfully reproduced a number of purely hydrodynamic results.

Secondly, setting  $Ta = 0$  allows us to test the code against known results for magnetoconvection in a horizontal field, e.g., Arter (1983). From Arter, we have a theoretical expression for the Rayleigh number as a function of the wavenumber and  $Q$ , see equation (3.6.57). Plotting  $Ra$

against  $k$  (see figure 3.6) for this expression and for  $Ra$  from our code, we see that the two exactly coincide. The blue symbols represent the numerical results generated by the code and the red symbols the theoretical expression as given by Arter. The upper lines are the results for the steady solution and the lower lines for the oscillatory solution. We choose to display the Rayleigh number as a function of wavenumber when  $Pr = 1$ ,  $\zeta = 0.1$  and  $Q = 1000$ .

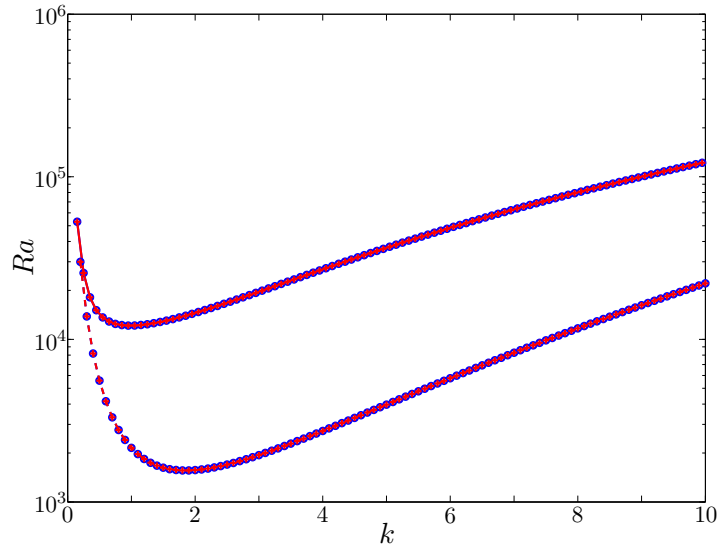


Figure 3.6: Rayleigh number against wavenumber for a layer with  $Q = 1000$ ,  $Pr = 1$  and  $\zeta = 0.1$ . The blue symbols represent the numerical results generated by the code and the red symbols the theoretical expression as given by Arter (1983). The two coincide. The upper lines are the results for the steady solution and the lower lines are for the oscillatory solution.

We now investigate the effect of a tilted rotation vector in the presence of a horizontal magnetic field on the onset of convection.

### 3.6.3 Two-dimensional solutions

In Chapter 8, we consider nonlinear convection in the presence of a horizontal magnetic field in a layer that is rotating about an axis that is oblique to gravity. We consider only axisymmetric two-dimensional solutions in the  $y$ - $z$  plane, i.e., we set  $\frac{\partial}{\partial x} \equiv 0$ . Therefore, we first study the linear problem in this same two-dimensional plane. This involves setting  $k = 0$  and hence we focus on EW rolls only.

We study a number of different parameter regimes: (i)  $Pr = 1$ ,  $\zeta < 1$ , (ii)  $Pr < 1$ ,  $\zeta = 1.1$ , (iii)  $Pr < 1$ ,  $\zeta < 1$  and we briefly comment on (iv)  $Pr = 1$ ,  $\zeta = 1.1$ . We note that in

magnetoconvection, oscillatory modes only exist for  $\zeta < 1$  and  $Q > Q^*$  (see Arter (1983)); and in rotating hydrodynamic convection, oscillatory modes only exist for  $Pr < 1$  and  $Ta > Ta^*$  (see Chandrasekhar (1961)). In all cases throughout this section we fix  $Ta = 10^5$ ,  $\phi = \frac{\pi}{4}$  and  $\alpha = \frac{\pi}{2}$ . This means the field is in the  $y$ -direction and so it will have an effect on the EW rolls. For EW rolls, it is known that a field in the  $x$ -direction will have no effect (see e.g., Proctor & Weiss (1982)).

**Case (i):**  $Pr = 1, \zeta = 0.1$

We begin by investigating the dependence on  $Q$  of the critical Rayleigh number, critical wavenumber and critical frequency given by  $Ra_{\text{crit}}$ ,  $l_{\text{crit}}$  and  $\omega_{\text{crit}}$  respectively. We find that, as expected, the Rayleigh number at onset is independent of  $Pr$  and  $\zeta$  for direct modes and, as was the case in section 3.5.1, the oscillatory mode depends on  $Pr$ , here it also depends on  $\zeta$ . Plots of the critical values against  $Q$  are shown in figure 3.7 for  $Pr = 1, \zeta = 0.1$ . The blue lines represent the direct mode and the red lines represent the oscillatory mode. Note that the oscillatory mode does not exist until  $Q$  is large enough, but once it does it is the preferred mode. We will refer to this oscillatory mode as the magnetic mode as it results when  $\zeta < 1$ . In both the steady and oscillatory cases, once  $Q$  has reached a sufficiently large value, there is a power law relating  $Ra_{\text{crit}}$  and  $Q$ .

For both modes, the minimum  $Ra_{\text{crit}}$  occurs for a non-minimal  $Q$  for which the solution exists, i.e.,  $Ra_{\text{crit}}$  is not monotonically increasing with  $Q$ . For both modes, the critical wavenumber decreases with increasing  $Q$  meaning that the marginal convection rolls have a larger length scale at higher  $Q$ . In addition, up until the largest  $Q$  considered, the oscillatory solutions have a smaller preferred length scale than the direct solutions. By definition, the critical frequency of the direct mode is zero but the oscillatory solution has a critical frequency that increases with increasing  $Q$ .

**Case (ii):**  $Pr = 0.1, \zeta = 1.1$

If we now take  $Pr < 1$  but  $\zeta > 1$ , in particular, if we take  $Pr = 0.1$  and  $\zeta = 1.1$ , we get the results shown in figure 3.8. This time the oscillatory solution is shown in green to distinguish it from the (magnetic) oscillatory solution in the previous case. We call this new oscillatory mode the rotating oscillatory mode as it results when  $Pr$  is small. Now the oscillatory solution is only preferred up until  $Q \sim 200$  and then the direct mode becomes preferred. Again, the wavenumber decreases with increasing  $Q$  but it is the oscillatory solutions that have the largest length scale (in

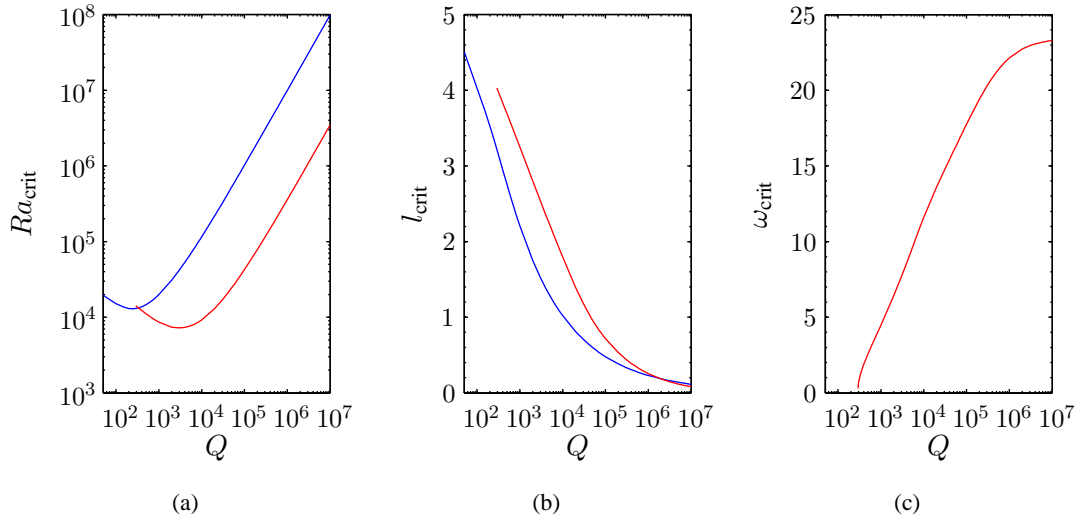


Figure 3.7: Critical values for case (i). Critical Rayleigh number (a), wavenumber (b) and frequency (c) as a function of  $Q$  for  $Pr = 1$  and  $\zeta = 0.1$  with  $Ta = 10^5$ . The direct mode is shown in blue and the oscillatory mode in red. In this case only the magnetic oscillatory mode exists.

contrast to case (i)). The critical frequency increases with  $Q$  but at larger  $Q$ , the growth slows and the increase is only slight.

**Case (iii):**  $Pr = 0.1$ ,  $\zeta = 0.1$

Taking the case when both  $Pr$  and  $\zeta$  are small, specifically  $Pr = \zeta = 0.1$ , we expect there to exist two overstable modes, the magnetic and the rotating oscillatory modes. Indeed, this is what we find (see figure 3.9). At small  $Q$ , the rotating mode (green) is preferred, then at  $Q \sim 1500$ , the magnetic mode (red) becomes preferred. Whilst the direct mode exists for all  $Q$  shown, it is never the preferred one. For large enough  $Q$ , the magnetic overstable mode has a larger preferred wavenumber than the preferred wavenumber of the direct mode, i.e., they have a smaller preferred length scale. The frequency increases with  $Q$  for both overstable branches.

**Case (iv):**  $Pr = 1$ ,  $\zeta = 1.1$

As might be expected, no overstable modes could be found when both  $Pr$  and  $\zeta$  are greater than or equal to one. In this case, the direct mode is the only solution and it has the same critical values as the direct mode in cases (i)-(iii), and so we do not display the results again here.

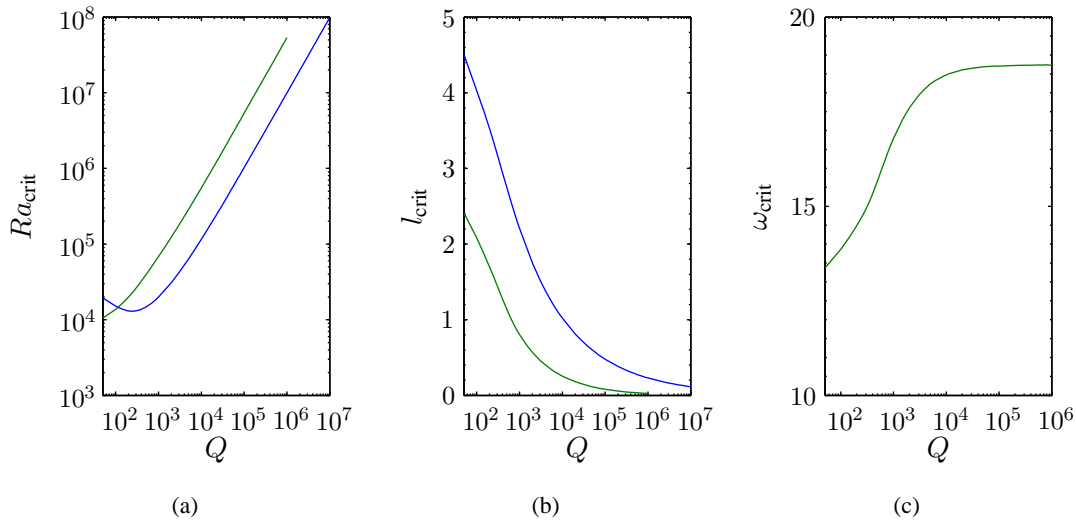


Figure 3.8: Critical values for case (ii). Critical Rayleigh number (a), wavenumber (b) and frequency (c) as a function of  $Q$  for  $Pr = 0.1$  and  $\zeta = 1.1$  with  $Ta = 10^5$ . The direct mode is shown in blue and the oscillatory mode in green. In this case only the rotating oscillatory mode exists.

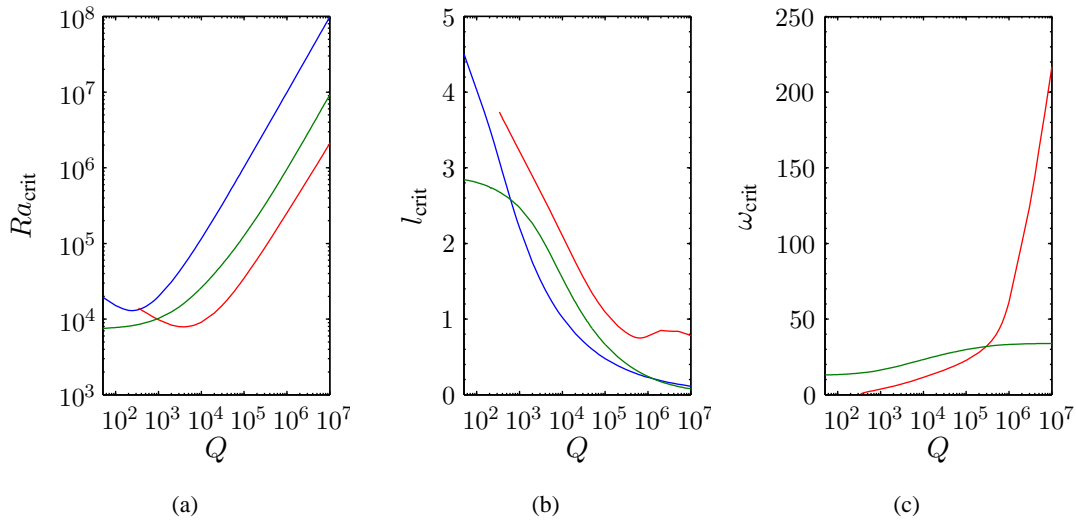


Figure 3.9: Critical values for case (iii). Critical Rayleigh number (a), wavenumber (b) and frequency (c) as a function of  $Q$  for  $Pr = 0.1$  and  $\zeta = 0.1$  with  $Ta = 10^5$ . The direct mode is shown in blue, the (magnetic) oscillatory mode in red and the (rotating) oscillatory mode in green.

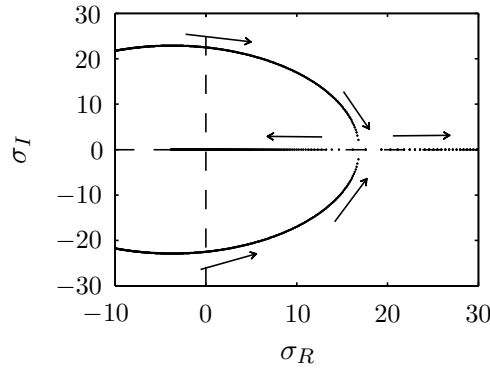


Figure 3.10: Eigenvalue diagram for  $l = 10$ ,  $Q = 500$ ,  $Ta = 10^5$ ,  $Pr = 1$  and  $\zeta = 0.1$ . The arrows indicate the direction of increasing Rayleigh number.

### 3.6.4 Eigenvalue diagrams

To analyse more closely the behaviour of the eigenvalues  $\sigma_R$  and  $\sigma_I$ , and therefore the bifurcations, we plot them against each other for increasing  $Ra$  (at fixed wavenumber). Figure 3.10 tracks the eigenvalues as we increase  $Ra$ , in the case when  $Pr = 1$ ,  $\zeta = 0.1$ ,  $Q = 500$  and  $l = 10$ . The direction of increasing  $Ra$  is indicated by the arrows shown. In this case, the quintic dispersion relation has only three solutions with real  $\sigma_I$ . Of these solutions one is always real and negative (and therefore stable). Below a particular value of Rayleigh number, the other two eigenvalues form a complex conjugate pair with negative real part (stable). As  $Ra$  is increased, we reach a value for which this eigenvalue pair become purely imaginary, i.e.,  $\sigma_R = 0$  and the system undergoes a Hopf bifurcation (as described in section 3.3). Increasing  $Ra$  further leads to this pair having positive real parts (unstable) but their imaginary parts decrease until we have a repeated eigenvalue. For  $Ra$  greater than this, both eigenvalues are real, and whilst the real part of one continues to increase in magnitude, the other decreases and passes through the origin in a direct bifurcation.

We have just described the case for a particular  $l$  and  $Q$  but, for the region of parameter space where one pair of oscillatory solutions exists, we would observe the same qualitative behaviour of the eigenvalues for any  $l$  and  $Q$ . The difference would occur in the values of the Rayleigh number and frequency at which the bifurcations occur.

The eigenvalue diagram corresponding to case (ii), is shown in fig 3.11 for two key examples. In (a)  $Q = 930$ ,  $l = 0.7$  and we see that as  $Ra$  is increased, we have that a complex conjugate pair of eigenvalues with negative real part move towards the imaginary axis ( $\sigma_R = 0$ ) and

pass over it, thereby undergoing a Hopf bifurcation. Continuing further along this path, the imaginary parts of the pair decrease in magnitude until they reach zero and we have two positive, real eigenvalues. On reaching this point, one eigenvalue increases in magnitude and the other decreases. Meanwhile, another eigenvalue moves from the stable region ( $\sigma_R < 0$ ) to the unstable region ( $\sigma_R > 0$ ), via a direct bifurcation. Eventually, for some value of  $Ra$ , this eigenvalue and the one from the previously complex conjugate pair with decreasing real part meet, and become once again a complex conjugate pair. When  $Ra$  is increased further, this complex conjugate pair moves back over the line  $\sigma_R = 0$  in another Hopf bifurcation and the eigenvalues become stable again. So there are two overstable branches appearing in this description but we only see the preferred one in the plots of the critical values in figure 3.8.

In (b)  $Q = 1000$  and  $l = 0.7$ . Now the eigenvalues for the different bifurcations do not interact. As  $Ra$  is increased the real, negative eigenvalue increases towards zero and continues passing through the origin in a direct bifurcation and then continues to grow. Separately from this, a complex conjugate pair with negative real part moves towards the line  $\sigma_R = 0$  and as  $Ra$  continues to increase, they undergo a Hopf bifurcation to become unstable. At even higher  $Ra$ , their real parts start to decrease as they move back towards the imaginary axis, eventually undergoing another Hopf bifurcation.

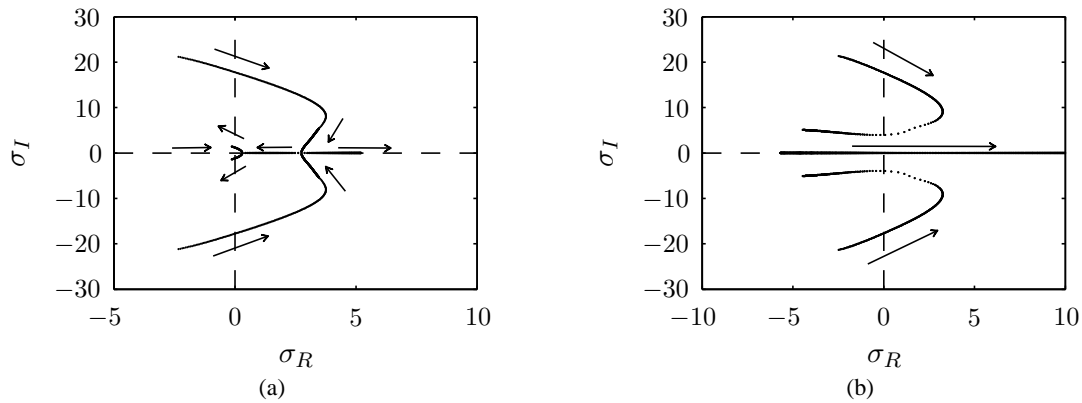


Figure 3.11: Eigenvalue diagram for a layer with  $Ta = 10^5$ ,  $Pr = 0.1$  and  $\zeta = 1.1$ . In a)  $Q = 930$  and  $l = 0.7$ ; in b)  $Q = 1000$  and  $l = 0.7$ . The arrows indicate the direction of increasing Rayleigh number.

In case (iii), it is possible for the dispersion relation to have seven roots with real  $\sigma_I$  (depending on  $l$ ). To study the bifurcations involved in this case more carefully, we plot the eigenvalues for a series of different  $l$  in figure 3.12. We fix  $Q = 900$  and consider different wavenumbers. In

(a),  $l = 0.9$  and the only oscillatory solutions present are those from the rotation modes. It is no surprise therefore, that the eigenvalue diagram takes the same form as figure 3.11 (a) and as such the description of the evolution of the eigenvalues with increasing Rayleigh number is the same as described in the accompanying paragraph to figure 3.11. In (b),  $l = 1.7$ , now the eigenvalues have progressed as in figure 3.11 (b) but in addition, two extra branches have appeared, although these have yet to reach the line  $\sigma_R = 0$ . In (c),  $l$  has been increased to  $l = 2$ , the two extra branches have now crossed the line  $\sigma_R = 0$  and undergone a bifurcation. This bifurcation is of the same form as in figure 3.10, the magnetic dominated case. Therefore the eigenvalues in this part of the eigenvalue diagram behave in a similar way to that of case (i). By  $l = 3.5$  (subfigure (d)), we can see the three bifurcations corresponding to the three overstable solutions and their eigenvalue branches are well established. The diagram is a combination of the solutions from the rotational modes (case (ii)) and the magnetic mode (case (i)). This is to be expected since we have small  $Pr$  and  $\zeta$ , and as a result all oscillatory solutions should be possible. In (e),  $l = 4.6$ , this is roughly the wavenumber at which the branches corresponding to the rotation modes cease to exist and we see that the branches have moved back over the line  $\sigma_R = 0$ . After this point there are no oscillatory solutions coming from the rotational branch. This is seen in (f), where  $l = 6$ , and we only have the one oscillatory branch. The form of the eigenvalues are now as in case (i), where the magnetic field dominated and indeed we see the eigenvalue diagrams are qualitatively the same.

### 3.6.5 Three-dimensional solutions

Our motivation for examining two-dimensional (EW) solutions in detail was as preparation for the nonlinear work that will follow in Chapter 8. It is still, however, worth considering three-dimensional perturbations, i.e., allowing  $k$  and  $l$  to both be non-zero. In the previous section, the small  $Pr$  and  $\zeta$  regimes led to the largest variety of behaviour, and so we choose to consider  $Pr = \zeta = 0.1$  in this section. This also allows for both magnetic and rotating overstable modes as we saw in the investigation of two-dimensional solutions.

Figure 3.13 shows the critical values as a function of  $Q$ . Now we have both  $l_{\text{crit}}$  and  $k_{\text{crit}}$  and the critical total horizontal wavenumber is given by  $a_{\text{crit}}^2 = k_{\text{crit}}^2 + l_{\text{crit}}^2$ . Again, the rotating mode is shown in green, the magnetic mode in red and the direct mode in blue. We recall that the magnetic and rotating modes are oscillatory and so have a non-zero frequency, whereas the direct mode is steady and so its critical frequency is zero. The first noticeable difference between the two-dimensional and three-dimensional solutions is that for the rotating mode,  $l_{\text{crit}} = 0$ , and so

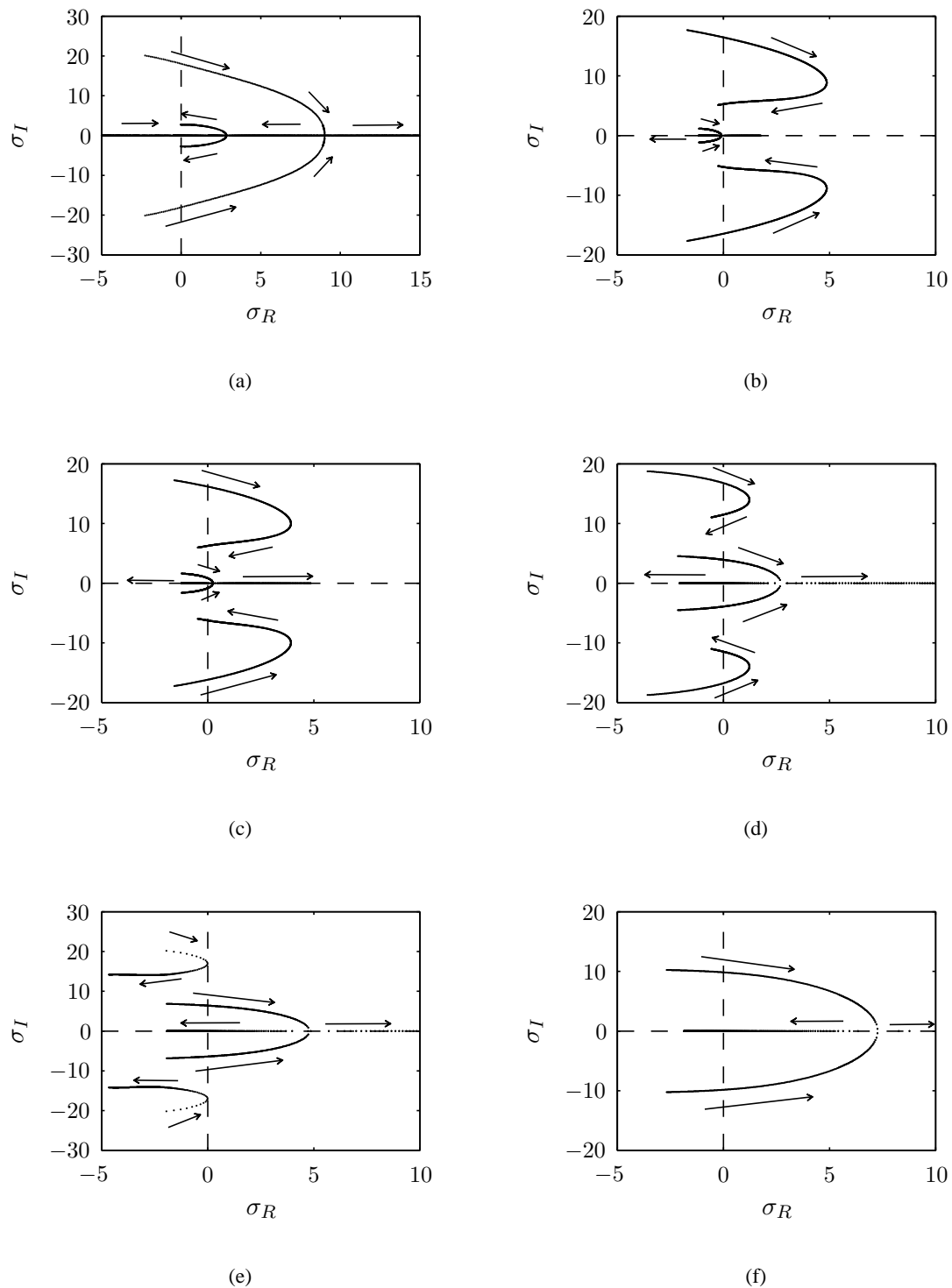


Figure 3.12: Eigenvalue diagram for a layer with  $Ta = 10^5$ ,  $Pr = 0.1$ ,  $\zeta = 0.1$ , and  $Q = 900$ . In a)  $k = 0.9$ , in b)  $k = 1.7$ , in c)  $k = 2$ , in d)  $k = 3.5$ , in e)  $k = 4.6$ , and in f)  $l = 6$ . The arrows indicate the direction of increasing Rayleigh number.

NS rolls are actually the preferred ones. Then, since  $\alpha = \frac{\pi}{2}$  (the field is in the  $y$ -direction) the field has no effect on the critical values, i.e., they are independent of  $Q$ . The magnetic mode behaves differently, for the smallest  $Q$  for which it exists, it has  $k_{\text{crit}} = 0$  and so EW rolls are preferred on this branch, but as  $Q$  is increased,  $k_{\text{crit}}$  increases and three-dimensional solutions become the preferred ones (for this branch). The direct solution appears to take on two different states. Firstly, for small  $Q$ ,  $l_{\text{crit}} = 0$  and so NS rolls are preferred and therefore, as described in the rotating mode case,  $Ra_{\text{crit}}$  is independent of  $Q$ . Then, at  $Q \sim 400$ , there is a transition to a three-dimensional solution and a decrease in  $Ra_{\text{crit}}$ . In this second regime, the critical Rayleigh number changes only slightly, whilst  $k_{\text{crit}}$  increases and  $l_{\text{crit}}$  decreases. Overall, the rotating oscillatory mode is the preferred mode, it has the lowest  $Ra_{\text{crit}}$  of all the branches, for all  $Q$ .

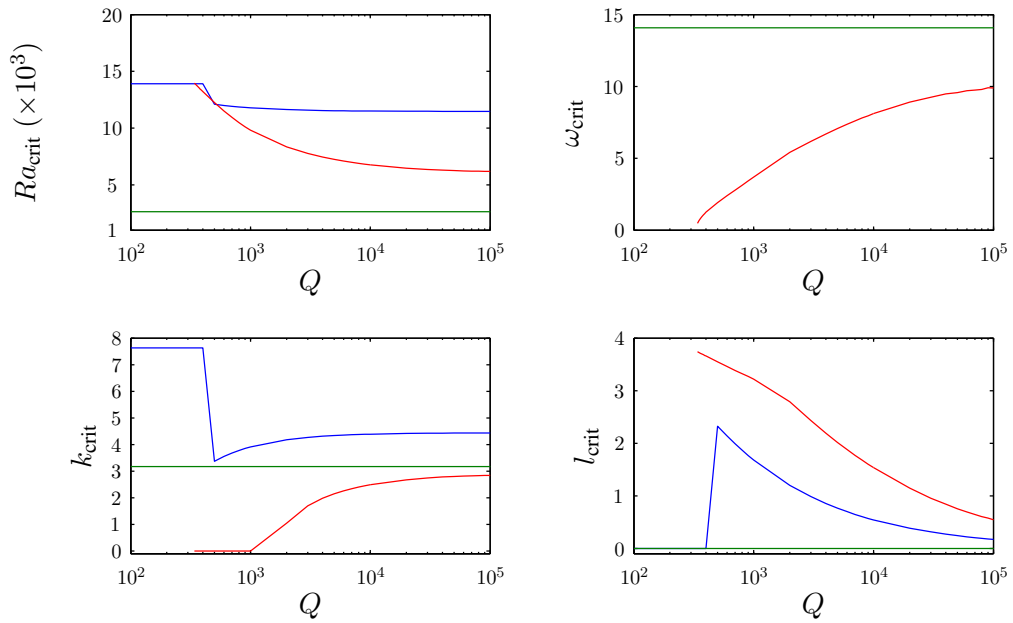


Figure 3.13: Critical Rayleigh number, ( $Ra_{\text{crit}}$ , top left), critical wavenumber ( $k_{\text{crit}}$ , bottom left,  $l_{\text{crit}}$ , bottom right) and critical frequency ( $\omega_{\text{crit}}$ , top right) as a function of  $Q$  for  $Pr = 0.1$  and  $\zeta = 0.1$  with  $Ta = 10^5$  for three-dimensional perturbations. The direct mode is shown in blue, the (magnetic) oscillatory mode in red and the (rotating) oscillatory mode in green.

### 3.7 Summary

We began the chapter with a derivation of the linear equations for rotating magnetoconvection with a tilted rotation vector and horizontal magnetic field (section 3.2). In some cases, we were

able to solve the linear equations analytically, but to solve them in the most general cases, we required a numerical code. This code was described in section 3.3 and was based around a boundary value problem solver in MATLAB known as `bvp4c`. The code was used to study the linear stability in a number of regimes that were not analytically tractable. In section 3.5, we examined the small Prandtl number regime as this is the regime into which many astrophysical flows fit. In the case of no thermal wind, the eigenfunctions were tilted when EW rolls were considered and this tilting was exaggerated by a negative horizontal temperature gradient. We also noted that the thermal wind, in general, acts to destabilise EW rolls and stabilise NS rolls.

The second part of the chapter was concerned with the case when the magnetic field strength was non-zero (section 3.6). Here, we used analytical results of a study of two-dimensional modes in vertically rotating magnetoconvection to help locate solutions when  $\phi = \frac{\pi}{4}$ . We found that different solutions existed, dependent on whether  $Pr$  and  $\zeta$  were greater or less than unity. We studied in more detail the behaviour of the eigenvalues in each of these cases to identify when each of the solutions exists.

To finish the chapter, we considered three-dimensional perturbations and found, in some cases, oblique rolls are actually the preferred ones.

The linear work in this chapter was undertaken to aid with a nonlinear study of convection under the Boussinesq approximation. A nonlinear study for the purely hydrodynamic case is carried out in Chapter 6, and for the MHD case in Chapter 8.

## Chapter 4

# Linear Anelastic Convection

### 4.1 Introduction

As explained in section 2.4, for systems where there are a large number of scale heights involved but that remain close to being adiabatic, the anelastic equations are an improvement on the Boussinesq equations. The anelastic equations allow for density stratification across the layer whilst still filtering out fast sound waves. This makes studying a compressible layer more computationally accessible. In much the same way as the Boussinesq case, the linear theory of the anelastic system is worth studying to firstly tell us about the stability of the fluid layer and secondly it can act as a useful test for the anelastic nonlinear study that follows in Chapter 7.

The onset of compressible convection using the anelastic approximation has been studied in a number of papers. Jones *et al.* (1990) considered a Cartesian geometry and took rotation, magnetic field and gravity to be mutually perpendicular. The linear theory of convection in a spherical shell geometry, using the anelastic approximation, was presented by Drew *et al.* (1995) and Jones *et al.* (2009) built upon this, by developing an asymptotic theory for the onset of compressible convection in rapidly rotating spherical shells.

More recently, Mizerski & Tobias (2011) investigated the effect of compressibility and stratification on convection, using the anelastic approximation, in a rotating plane layer model. As discussed in section 2.4 we use this model as the basis for our investigation but we adapt it to allow for a tilted rotation vector.

## 4.2 Linear equations

In Chapter 2, we derived the nonlinear equations for rotating convection under the anelastic approximation. For ease of reference, we restate the equations here. From equations (2.4.142)-(2.4.144) we have

$$\begin{aligned} \frac{\partial \mathbf{u}}{\partial t} + (\mathbf{u} \cdot \nabla) \mathbf{u} = & -\nabla \left( \frac{p}{\rho} \right) + RaPrs \hat{\mathbf{e}}_z - Ta^{\frac{1}{2}} Pr (\boldsymbol{\Omega} \times \mathbf{u}) + Pr \nabla^2 \mathbf{u} \\ & + \frac{Prm\theta}{1+\theta z} \left[ \frac{\partial \mathbf{u}}{\partial z} + \frac{2}{3} \nabla w + \frac{1}{3} (1+2m)\theta \frac{w}{1+\theta z} \hat{\mathbf{e}}_z \right], \end{aligned} \quad (4.2.1)$$

$$\nabla \cdot \mathbf{u} = -\frac{m\theta}{1+\theta z} w, \quad (4.2.2)$$

$$\begin{aligned} \frac{\partial s}{\partial t} + \mathbf{u} \cdot \nabla s = & \frac{w}{1+\theta z} + \frac{1}{\rho} \nabla^2 s + \frac{\theta}{(1+\theta z)^{m+1}} \frac{\partial s}{\partial z} \\ & - \frac{\theta}{Ra(1+\theta z)} \left[ 2 \sum_{i=1}^3 \left( \frac{\partial u_i}{\partial x_i} \right)^2 + \sum_{i<j} \left( \frac{\partial u_i}{\partial x_j} + \frac{\partial u_j}{\partial x_i} \right)^2 - \frac{2}{3} (\nabla \cdot \mathbf{u})^2 \right]. \end{aligned} \quad (4.2.3)$$

In this chapter, we are interested in the linear theory, and so we perturb equations (4.2.1)-(4.2.3) about the simple basic state given by (2.4.150) then, as in the Boussinesq case, we neglect all terms quadratic in the perturbations to give the linear anelastic equations

$$\begin{aligned} \frac{\partial \mathbf{u}'}{\partial t} = & -\nabla \left( \frac{p'}{\rho} \right) + RaPrs' \hat{\mathbf{e}}_z - Ta^{\frac{1}{2}} Pr (\boldsymbol{\Omega} \times \mathbf{u}') + Pr \nabla^2 \mathbf{u}' \\ & + \frac{Prm\theta}{1+\theta z} \left[ \frac{\partial \mathbf{u}'}{\partial z} + \frac{2}{3} \nabla w' + \frac{1}{3} (1+2m)\theta \frac{w'}{1+\theta z} \hat{\mathbf{e}}_z \right], \end{aligned} \quad (4.2.4)$$

$$\nabla \cdot \mathbf{u}' = -\frac{m\theta}{1+\theta z} w', \quad (4.2.5)$$

$$\frac{\partial s'}{\partial t} = \frac{w'}{1+\theta z} + \frac{1}{(1+\theta z)^m} \nabla^2 s' + \frac{\theta}{(1+\theta z)^{m+1}} \frac{\partial s'}{\partial z}. \quad (4.2.6)$$

Now, if we take the  $z$ -component of the curl of equation (4.2.4), we obtain

$$\frac{\partial \zeta}{\partial t} = Ta^{\frac{1}{2}} Pr \left[ \sin \phi \left( \frac{\partial w}{\partial z} + \frac{m\theta}{1+\theta z} w \right) + \cos \phi \frac{\partial w}{\partial y} \right] + Pr \nabla^2 \zeta + \frac{Prm\theta}{1+\theta z} \frac{\partial \zeta}{\partial z}, \quad (4.2.7)$$

where we have defined  $\zeta = \frac{\partial v}{\partial x} - \frac{\partial u}{\partial y}$  to be the  $z$ -component of vorticity and we have removed the primes from the perturbations. By taking the  $z$ -component of the double curl of (4.2.4), we obtain

$$\begin{aligned} -\frac{\partial}{\partial t} \left[ \nabla^2 w + \frac{\partial}{\partial z} \left( \frac{m\theta}{1+\theta z} w \right) \right] = & Ta^{\frac{1}{2}} Pr \left[ \sin \phi \frac{\partial \zeta}{\partial z} + \frac{m\theta}{1+\theta z} \cos \phi \frac{\partial w}{\partial x} + \cos \phi \frac{\partial \zeta}{\partial y} \right] \\ & - RaPr \nabla_H^2 s - Pr \nabla^4 w + \frac{3Prm(2-m)\theta^4}{(1+\theta z)^4} w - \frac{2Prm\theta}{1+\theta z} \frac{\partial}{\partial z} \nabla_H^2 w \\ & - \frac{2Prm^2\theta^2}{3(1+\theta z)^2} \nabla_H^2 w - \frac{2Prm\theta}{1+\theta z} \frac{\partial^3 w}{\partial z^3} + \frac{Prm(4-m)\theta^2}{(1+\theta z)^2} \frac{\partial^2 w}{\partial z^2} - \frac{3Prm(2-m)\theta^3}{(1+\theta z)^3} \frac{\partial w}{\partial z}. \end{aligned} \quad (4.2.8)$$

The energy equation (4.2.6) gives

$$\frac{\partial s}{\partial t} - \frac{w}{1 + \theta z} = \frac{1}{(1 + \theta z)^m} \nabla^2 s + \frac{\theta}{(1 + \theta z)^{m+1}} \frac{\partial s}{\partial z}, \quad (4.2.9)$$

and the divergence of the velocity field from equation (4.2.5) is given by

$$\nabla \cdot \mathbf{u} = -\frac{m\theta}{1 + \theta z} w. \quad (4.2.10)$$

In the standard way, we seek solutions proportional to  $e^{i(kx+ly)+\sigma t}$ , i.e., we look for solutions of the form

$$w = \text{Re} \left\{ W(z) e^{i(kx+ly)+\sigma t} \right\}, \quad (4.2.11)$$

$$\zeta = \text{Re} \left\{ Z(z) e^{i(kx+ly)+\sigma t} \right\}, \quad (4.2.12)$$

$$s = \text{Re} \left\{ S(z) e^{i(kx+ly)+\sigma t} \right\}, \quad (4.2.13)$$

where  $k$  and  $l$  are the wavenumbers in the  $x$  and  $y$  directions respectively and  $\sigma = \sigma_R + i\omega$  is the complex growth rate. With this, equations (4.2.7)-(4.2.9) become

$$\begin{aligned} \sigma Z = & Ta^{\frac{1}{2}} Pr \left[ \sin \phi \left( DW + \frac{m\theta}{1 + \theta z} W \right) + \cos \phi i l W \right] \\ & + Pr(D^2 - a^2)Z + \frac{Prm\theta}{1 + \theta z} DZ, \end{aligned} \quad (4.2.14)$$

$$\begin{aligned} -\sigma [D^2 W - a^2 W + \frac{m\theta}{1 + \theta z} DW - \frac{m\theta^2}{(1 + \theta z)^2} W] = & RaPra^2 S \\ + Ta^{\frac{1}{2}} Pr [ \sin \phi DZ + \frac{m\theta}{1 + \theta z} \cos \phi i k W + \cos \phi i l Z ] - & PrD^4 W + 2Pra^2 D^2 W \\ - Pra^4 W + \frac{3Prm(2-m)\theta^4}{(1 + \theta z)^4} W + \frac{2Prm\theta}{1 + \theta z} a^2 DW + \frac{2Prm^2\theta^2}{3(1 + \theta z)^2} a^2 W \\ - \frac{2Prm\theta}{1 + \theta z} D^3 W + \frac{Prm(4-m)\theta^2}{(1 + \theta z)^2} D^2 W - \frac{3Prm(2-m)\theta^3}{(1 + \theta z)^3} DW, \end{aligned} \quad (4.2.15)$$

$$\sigma S - \frac{W}{1 + \theta z} = \frac{1}{(1 + \theta z)^m} (D^2 - a^2)S + \frac{\theta}{(1 + \theta z)^{m+1}} DS \quad (4.2.16)$$

respectively, where  $a^2 = k^2 + l^2$  and  $D \equiv \frac{d}{dz}$ . We solve this linear eigenvalue problem using the `bvp4c` solver of MATLAB, with the method described in section 3.3. The boundary conditions we enforce are stress free and isentropic, as described in section 2.4.7. For the notation used in this section, the conditions (2.4.145)-(2.4.149) become

$$S = 0, \quad W = 0, \quad DZ = 0 \quad \text{and} \quad D^2 W + \frac{m\theta DW}{(1 + \theta z)} = 0 \quad \text{on } z = 0, 1. \quad (4.2.17)$$

Since we are close to adiabaticity, we use  $m = 1.495$  in all calculations. Berkoff *et al.* (2010) demonstrated that the anelastic approximation gives a good approximation to fully compressible

calculations even when the reference state is super-adiabatic, finding a 2% error even when  $\epsilon \sim 10$ . But as mentioned above, we prefer to remain close to the adiabatic state and set  $m \sim 1.5$ .

Note, we can check our code in the Boussinesq limit by setting  $\theta = 0$ .  $\theta$  is a measure of the degree of compressibility. Therefore, we will vary  $\theta$  to investigate the effect of a number of different stratifications. Since  $\bar{\rho} = (1 + \theta z)^m$ , we define

$$\bar{\rho}_{\text{bot}} = \bar{\rho}(z = 0) = 1 \quad \text{and} \quad \bar{\rho}_{\text{top}} = \bar{\rho}(z = 1) = (1 + \theta)^m. \quad (4.2.18)$$

Then, if we let  $r = \frac{\bar{\rho}_{\text{top}}}{\bar{\rho}_{\text{bot}}}$ , we have

$$\begin{aligned} r &= (1 + \theta)^m \Rightarrow m \ln(1 + \theta) = \ln r \\ &\Rightarrow (1 + \theta) = r^{\frac{1}{m}} \\ &\Rightarrow \theta = r^{\frac{1}{m}} - 1. \end{aligned} \quad (4.2.19)$$

We choose to focus on stratifications where  $r = 0.5, 0.1$  and  $0.01$  which correspond to  $\theta = -0.37101, -0.78566$  and  $-0.95406$  respectively. We have calculated values of  $\theta$  to five decimal places and these are the values we work with throughout, however, for clarity, hereafter we only give  $\theta$  to two decimal places when referring to it in the text.

## 4.3 Numerical results

### 4.3.1 Effect of $Ta$ on the onset of convection

In this section, we present results obtained by solving the linear system (4.2.14)-(4.2.16). To begin with, we set  $\sigma_R = 0$  and solve for the values of  $Ra$ ,  $a$  and  $\omega$  at onset, i.e., the critical Rayleigh number ( $Ra_{\text{crit}}$ ), critical wavenumber ( $a_{\text{crit}}$ ) and critical frequency ( $\omega_{\text{crit}}$ ). We are interested in how these vary with  $\theta$ ,  $\phi$  and  $Pr$ . Figure 4.1 shows  $Ra_{\text{crit}}$  (top),  $k_{\text{crit}}$  (middle) and  $\omega_{\text{crit}}$  (bottom) for NS rolls ( $l = 0$ ) when  $Pr = 0.1$  and  $\phi = \frac{\pi}{4}$ , for a number of different stratifications. As  $Pr < 1$ , all the solutions displayed are oscillatory. The black lines correspond to  $\theta = 0$ , red to  $\theta = -0.37$ , green to  $\theta = -0.79$  and blue to  $\theta = -0.95$ . We note that, for  $\theta \neq 0$  and  $l = 0$ , there is a distinction to be made between solutions with a positive critical frequency and those with a negative critical frequency. We consider this symmetry breaking in more depth in section 4.4. We denote by '+' those solutions that have a positive critical frequency and by 'o' those that have a negative critical frequency. For some parameters only marginal solutions with a negative frequency exist, these solutions are marked with a '.'.

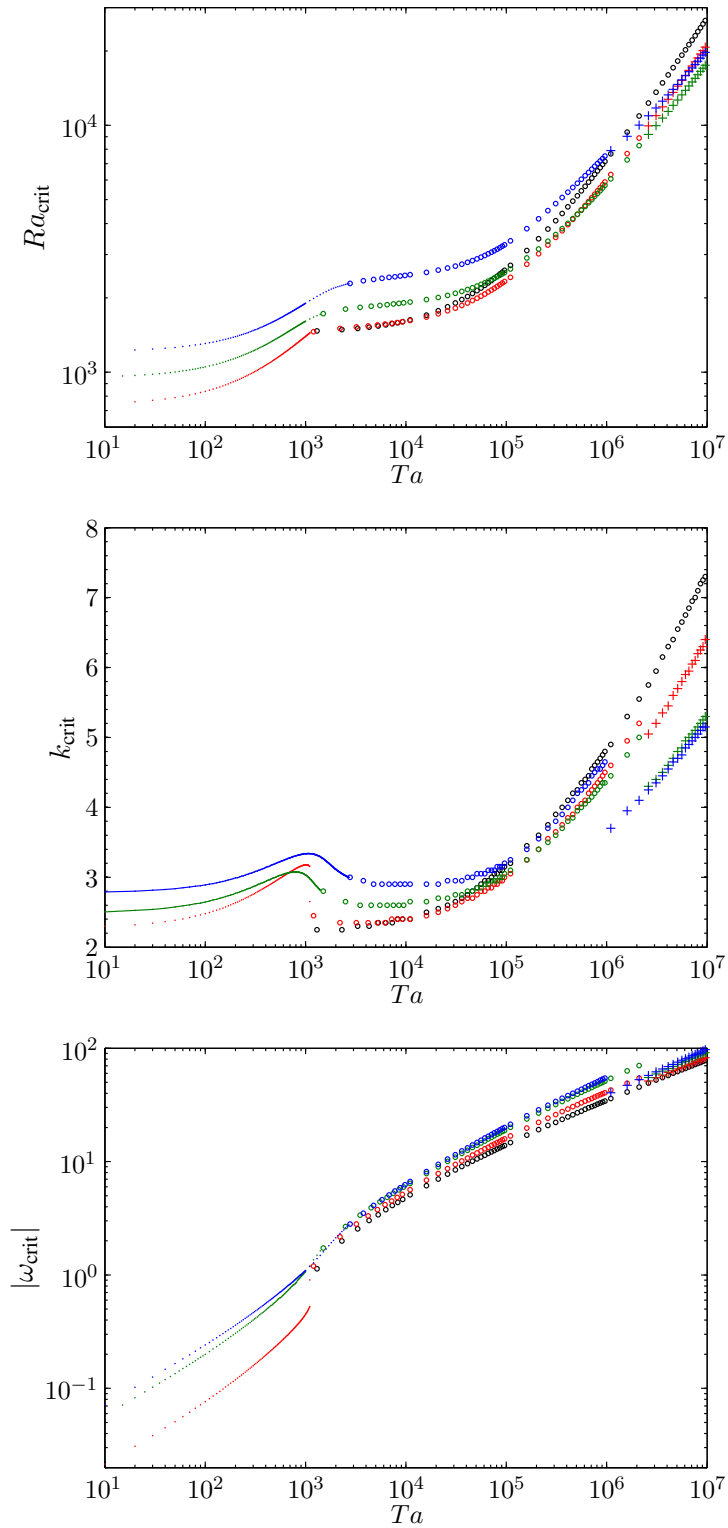


Figure 4.1:  $Ra_{\text{crit}}$  (top),  $k_{\text{crit}}$  (centre) and  $\omega_{\text{crit}}$  (bottom) against  $Ta$  for NS rolls when  $Pr = 0.1$  and  $\phi = \frac{\pi}{4}$ . In black  $\theta = 0$ , in red  $\theta = -0.37$ , in green  $\theta = -0.79$  and in blue  $\theta = -0.95$ . Solutions with positive preferred frequency are denoted with a '+' , solutions with negative preferred frequency are denoted with a 'o' and the cases where only marginal solutions with a negative frequency exist are denoted by a '.'.

Before we analyse the plots in figure 4.1 further, we comment that the solutions with positive and negative frequency are, in fact, left and right travelling waves, respectively. In figure 4.2, we show an eigenfunction at six different times over one period for an example of a left travelling wave (a) and a right travelling wave (b). The time period is given by  $\frac{2\pi}{\omega_{\text{crit}}}$ , so that the left travelling wave has a longer time period associated with it. A feature of travelling waves is that their amplitude remains fixed in time but they propagate in space, this can clearly be seen from the plots. The lack of symmetry of the solutions about  $z = 0.5$  arises because of the layer stratification, i.e., because  $\theta$  is non-zero. We will comment further on this asymmetry and the form of the eigenfunctions more generally in section 4.3.2.

We now return to considering the plots of the critical values given in figure 4.1. We note that although the  $\theta = 0$  solutions are marked as having a negative critical frequency,  $Ra_{\text{crit}}$  is in fact the same for both solutions with a positive frequency and solutions with a negative frequency. It can also be seen that, until  $Ta$  is large enough, the solutions with a negative frequency are the preferred ones for all the values of  $\theta$  shown, and then the solutions with positive frequency become the preferred ones. The value of  $Ta$  at which this transition occurs appears to decrease as  $|\theta|$  is increased. For  $\theta = 0$ , oscillatory solutions do not exist for  $Ta < Ta^*$  (see, e.g., Chandrasekhar (1961)), but as  $|\theta|$  is increased the negative branch exists for all  $Ta$ , however, the positive branch does not (we will see an explanation of this shortly). At moderate  $Ta$  ( $Ta \approx 2000$ ), it appears that the stronger the stratification is, the more stable the system, but as  $Ta$  is increased the weakest stratification (no stratification) becomes the most stable. Also, there is a small kink in the  $Ra_{\text{crit}}$  curve around the point the positive branch comes into existence for the  $\theta \neq 0$  solutions (at approximately  $Ta = 1$  to  $2 \times 10^3$ ). If we consider the plot of  $k_{\text{crit}}$ , then we see there is a kink in the critical wavenumber at the  $Ta$  just before the kink in the critical Rayleigh number. From the critical wavenumber plot, we see that there is a discontinuity when the solution changes from the negative frequency regime to the positive one, and that the critical wavenumber is typically larger when the critical frequency is positive, meaning that the eigenfunctions of the negative solutions have a smaller length scale. The difference between the length scales of the solutions with positive and negative frequency gets larger with increasing  $|\theta|$ . At moderate  $Ta$ , that is  $Ta \approx 2000$ ,  $k_{\text{crit}}$  is largest for  $|\theta|$  largest and decreases with  $|\theta|$ . But, as  $Ta$  is increased, the preferred length scale changes and, in the region of  $Ta$  where the solutions with positive frequency are preferred ( $Ta \approx 10^6 - 10^7$ ), the stronger the stratification, the smaller  $k_{\text{crit}}$ . From the plot of  $|\omega_{\text{crit}}|$  against  $Ta$  (figure 4.1 (c)) we see that, in general, the solutions with the strongest stratifications have the largest  $|\omega_{\text{crit}}|$ . This is true in both the regime where  $\omega_{\text{crit}}$  is positive and the one where  $\omega_{\text{crit}}$  is negative. The only region where this is not always true is around the  $Ta$  where the transition

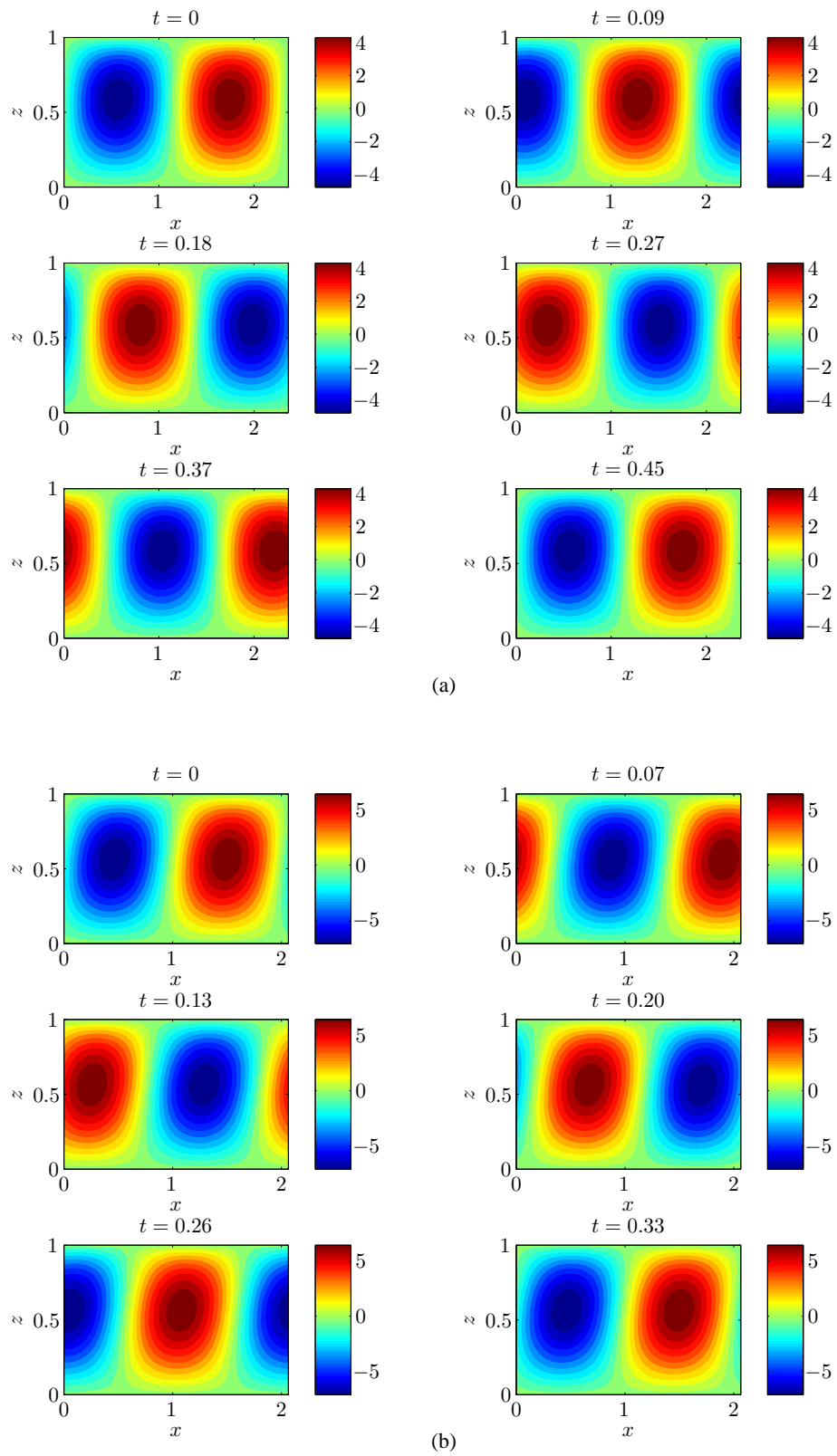


Figure 4.2:  $w(x, z, t)$  at onset over one time period for NS rolls when  $Pr = 0.1$ ,  $\phi = \frac{\pi}{4}$ ,  $\theta = -0.79$  and (a)  $\omega_{\text{crit}} > 0$  (left travelling wave), (b)  $\omega_{\text{crit}} < 0$  (right travelling wave).

from negative to positive solution occurs, because there, some of the solutions have  $\omega_{\text{crit}} > 0$  and some have  $\omega_{\text{crit}} < 0$ , depending on  $\theta$ .

As noted before, the solutions with positive frequency do not exist for small  $Ta$ , but the solutions with negative frequency do. To investigate this further, we plot  $\sigma_R$  against  $\sigma_I$  for different  $Ta$ , as  $Ra$  is increased. The results are shown in figure 4.3. In (a)  $\theta = 0$  and  $Ta = 10^2$ . Here we see that the eigenvalues do not pass through the line  $\sigma_R = 0$  for  $\sigma_I \neq 0$  and hence there are no oscillatory solutions at this  $Ta$ . But, if we increase  $Ta$  to  $10^3$  (see subfigure (b)), then the eigenvalues do pass through  $\sigma_R = 0$  for some non-zero frequency. Therefore, both the positive and negative branches exist at this  $Ta$ . Note for (a) and (b),  $\theta = 0$  and so the eigenvalue spectrum is symmetric, and hence at a particular  $Ta$ , marginal oscillatory modes either exist with both positive and negative frequency, or they do not exist at all. If we now consider what happens when  $\theta = -0.95$ , we get the eigenvalue spectrum as given in (c) where  $Ta = 2000$  and in (d) where  $Ta = 5000$ . In (c), the eigenvalues with a positive frequency always have  $\sigma_R < 0$  and so this explains why the marginal oscillatory modes with positive frequency do not exist for small  $Ta$ . For large enough  $Ta$ , the eigenvalues do eventually have  $\sigma_R > 0$  (see subfigure (d)) and so the positive frequency branch does become unstable and we have marginal oscillatory modes with both the positive and negative frequencies existing at this  $Ta$ .

Figure 4.4 shows the critical values for EW rolls ( $k = 0$ ). This time, surprisingly, there is no distinction to be made between solutions with positive and negative frequency (this is investigated further in section 4.4) and so the top plot is a plot of  $Ra_{\text{crit}}$  against  $Ta$ , the middle plot is a plot of  $l_{\text{crit}}$  against  $Ta$  and the bottom plot is the corresponding plot of  $\omega_{\text{crit}}$  against  $Ta$  for the positive branch only (the only difference between positive and negative branches here is the sign of the frequency). We see that for small  $Ta$ ,  $\theta = 0$  is the most unstable, but this changes as  $Ta$  is increased. For small  $Ta$ , the smallest critical wavenumbers occur for the smallest stratifications, but as  $Ta$  is increased, the smallest stratifications have the largest critical wavenumbers. The critical frequency works in the opposite way to this, i.e., for small  $Ta$  the smallest critical frequencies occur for the largest stratifications, but as  $Ta$  is increased, the largest stratifications have the largest critical frequencies. Comparing the magnitude of  $Ra_{\text{crit}}$  in the EW and NS cases shows that NS rolls are preferred for all  $\theta$ .

We notice that, unlike in the NS case, oscillatory solutions do not exist for small  $Ta$ . By plotting the real and imaginary parts of the growth rate against each other, for different  $Ta$ , we can see why. For example, in figure 4.5 (a), we plot the growth rates as  $Ra$  is increased for  $Pr = 0.1$ ,  $\theta = -0.79$ ,  $l = 3$ ,  $k = 0$  and  $Ta = 50$ . The arrows indicate the direction of increasing  $Ra$ .

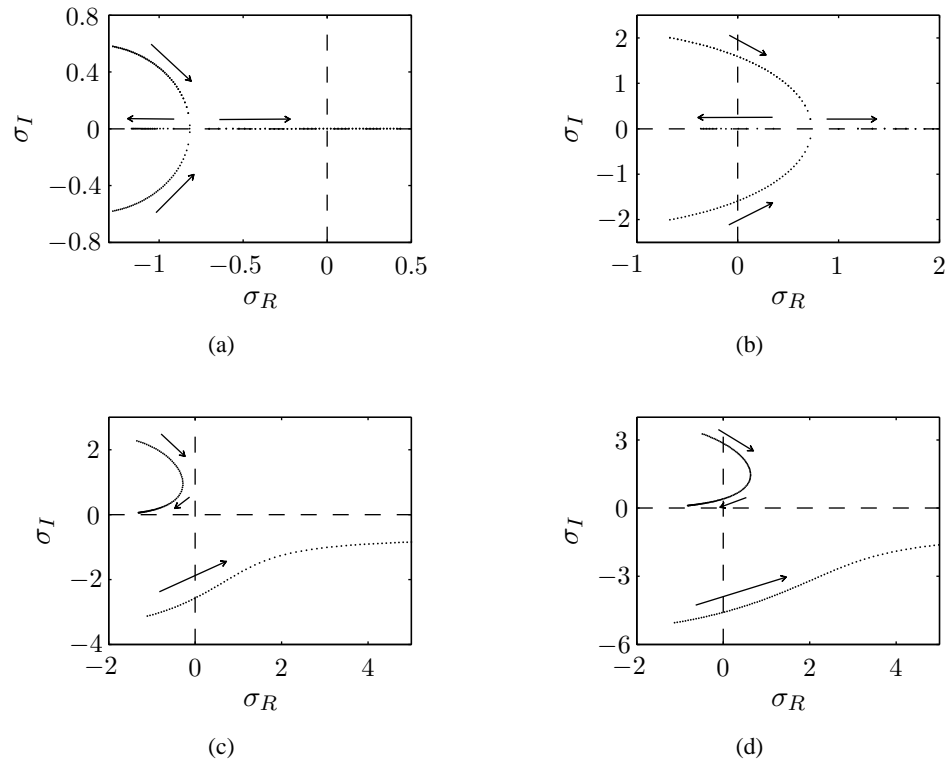


Figure 4.3:  $\sigma_R$  plotted against  $\sigma_I$  for (a)  $k = 2$ ,  $Ta = 10^2$  and  $\theta = 0$ , (b)  $k = 1$ ,  $Ta = 10^3$  and  $\theta = 0$ , (c)  $k = 2$ ,  $T = 2000$  and  $\theta = -0.95$  and (d)  $k = 2$ ,  $T = 5000$  and  $\theta = -0.95$ . Oscillatory bifurcations occur when  $\sigma_R = 0$  for  $\sigma_I \neq 0$ .

We see that for small  $Ra$ , the eigenvalues exist in complex conjugate pairs but with a negative real part so that the system is stable. Then, as  $Ra$  is increased, the complex conjugate pairs move towards the real axis ( $\sigma_I = 0$ ) where one of the pair moves to smaller  $\sigma_R$  and remains stable whilst the other moves towards  $\sigma_R > 0$ . For large enough  $Ra$ , this eigenvalue passes through  $(\sigma_R, \sigma_I) = (0, 0)$  in a direct bifurcation. The origin is the only point at which the line  $\sigma_R = 0$  is crossed and so, in this case, there are no Hopf bifurcations and hence no unstable oscillatory modes exist (see section 3.3 for a description of direct and Hopf bifurcations). This explains why, in figure 4.4, critical values do not exist for small  $Ta$ . In figure 4.5 (b),  $Ta$  is increased to  $10^5$  but other parameters remain the same. Now the line  $\sigma_R = 0$  is crossed for  $\sigma_I \neq 0$  and so oscillatory modes do exist at this  $Ta$ , as expected from figure 4.4. In addition, we remark on the symmetric nature of these eigenvalue diagrams; in particular, the eigenvalues arise in complex conjugate pairs, so that modes with positive frequency are not preferred over those with negative frequency, or vice versa. A further investigation of this symmetry is carried out in section 4.4.

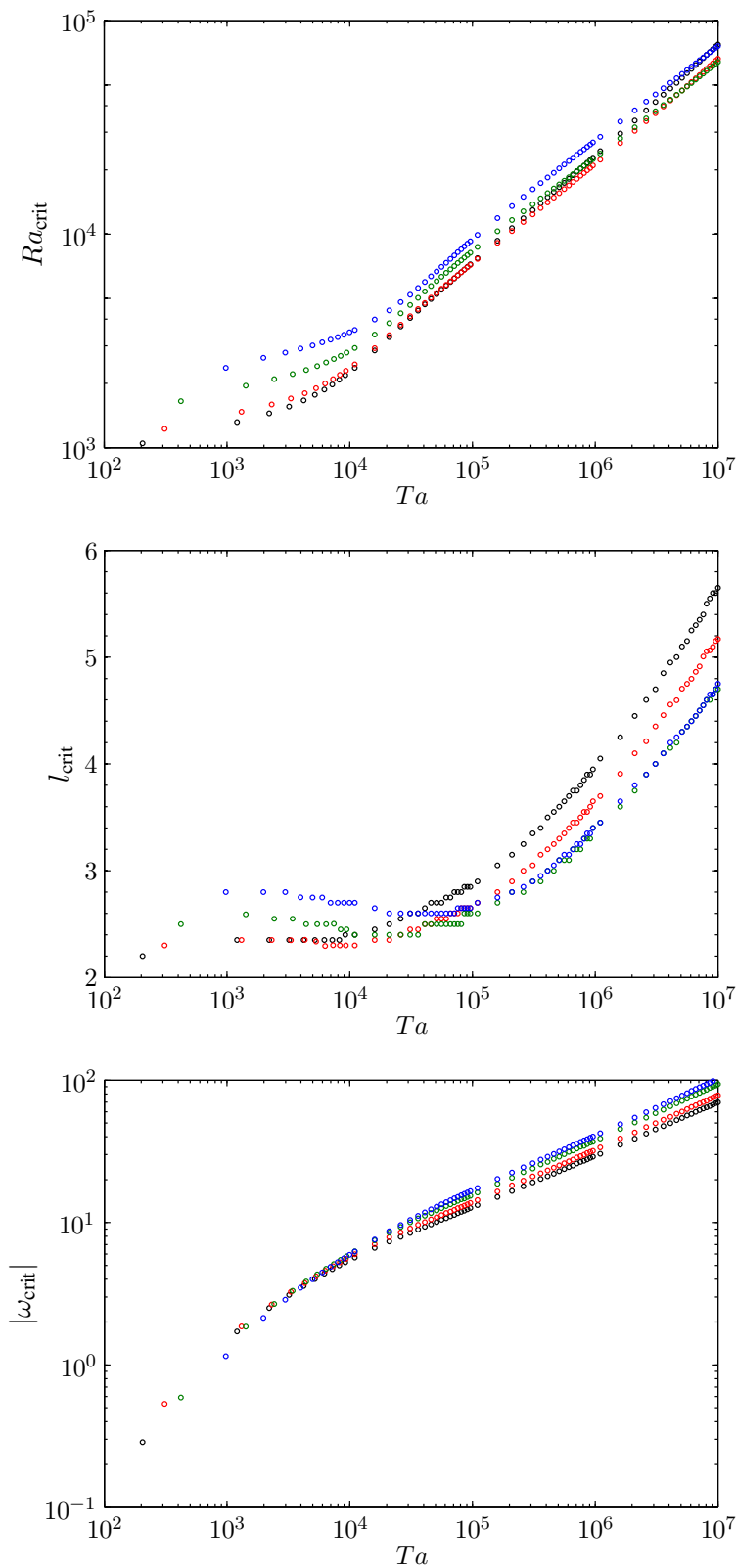


Figure 4.4:  $Ra_{\text{crit}}$  (top),  $l_{\text{crit}}$  (centre) and  $\omega_{\text{crit}}$  (bottom) against  $Ta$  for EW rolls when  $Pr = 0.1$  and  $\phi = \frac{\pi}{4}$ . In black  $\theta = 0$ , in red  $\theta = -0.37$ , in green  $\theta = -0.79$  and in blue  $\theta = -0.95$ . For EW rolls, the solutions with positive and negative frequency have the same  $Ra_{\text{crit}}$ , so both are preferred modes at onset.

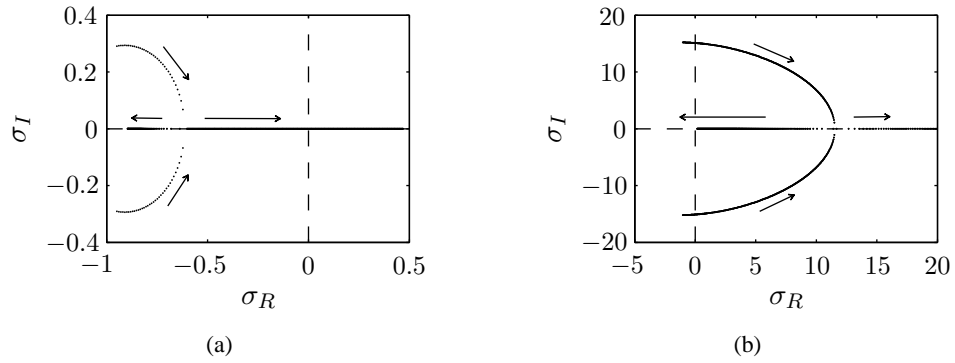


Figure 4.5:  $\sigma_R$  plotted against  $\sigma_I$  for  $\theta = -0.79$ ,  $k = 0$ ,  $l = 3$ , and (a)  $Ta = 50$ , (b)  $Ta = 10^5$ . Oscillatory bifurcations occur when  $\sigma_R = 0$  for  $\sigma_I \neq 0$ .

### 4.3.2 Eigenfunctions

It is informative to consider the differences to the eigenfunctions caused by stratification, in both the NS and EW cases. Figure 4.6 shows contour plots of  $w(y, z)$ ,  $s(y, z)$  and  $\zeta(y, z)$  at critical values for  $Pr = 0.1$ ,  $Ta = 10^7$ , and in (a),  $\theta = 0$ ,  $\phi = \frac{\pi}{2}$ ,  $l = 0$ , in (b),  $\theta = 0$ ,  $\phi = \frac{\pi}{4}$ ,  $l = 0$ , in (c),  $\theta = 0$ ,  $\phi = \frac{\pi}{4}$ ,  $k = 0$ , in (d),  $\theta = -0.95$ ,  $\phi = \frac{\pi}{2}$ ,  $l = 0$ , in (e),  $\theta = -0.95$ ,  $\phi = \frac{\pi}{4}$ ,  $l = 0$ , and in (f),  $\theta = -0.95$ ,  $\phi = \frac{\pi}{4}$ ,  $k = 0$ . We have included the cases when there is no stratification or no tilt to the rotation vector in order to make comparisons. As we have seen in Chapter 3, the tilt of the rotation vector only affects the orientation of the convection rolls in the  $y - z$  plane (EW rolls) and so the cells with the most tilt are in subfigures (c) and (f). Comparing (a) and (d), where the only difference is that (d) has a density stratification across the layer, we see that (d) has an asymmetry across the layer whereas (a) has a symmetry about  $z = 0.5$ . The stratification also appears to introduce a slight westward tilt in  $s$ . Comparing (b) and (e), where the rotation is now at an angle to the direction of gravity we see a similar breaking of symmetry and westward tilt of  $s$ . Comparing (c) and (f), allows us to see the difference when a stratification is added and EW rolls are considered. There is not a large change in  $w(y, z)$ , but a much bigger difference can be seen in  $s(y, z)$  where the equatorial tilt caused by the stratification has combined with the poleward tilt due to the rotation vector to give less poleward tilted cells than in the  $\theta = 0$  case.

To see the effect of  $\theta$  on the vertical structure of the eigenfunctions, we plot  $|W(z)|$  against  $z$  for NS rolls with  $\phi = \frac{\pi}{4}$ ,  $Pr = 0.1$ ,  $\theta = 0$  (blue),  $\theta = -0.37$  (red),  $\theta = -0.79$  (green) and  $\theta = -0.95$  (black) for (a)  $Ta = 10^3$  and (b)  $Ta = 10^7$ . The results are shown in figure 4.7. As  $|\theta|$  is increased, the asymmetry of the vertical structure increases, this effect is perhaps most obvious

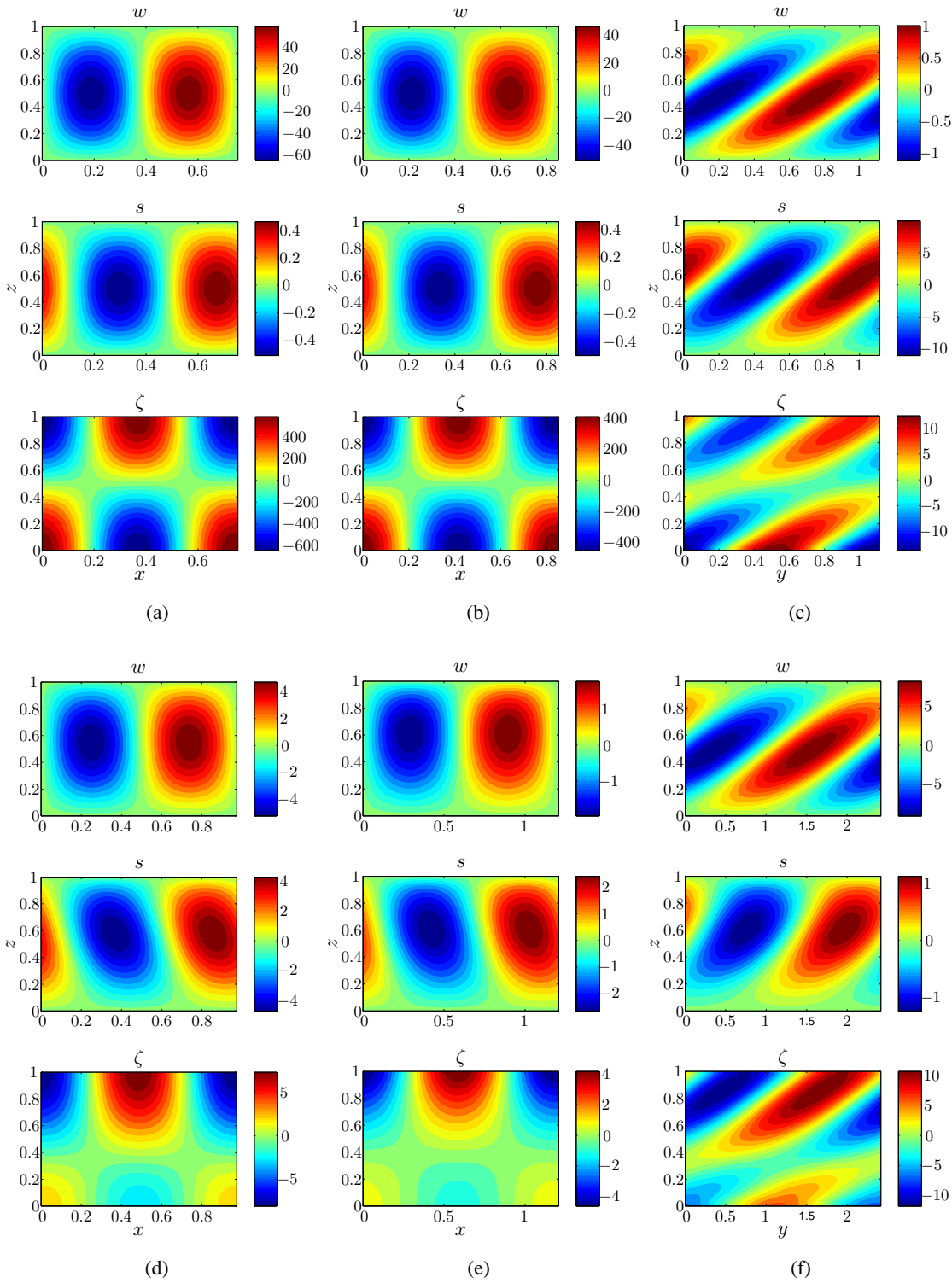


Figure 4.6: Eigenfunctions  $w$ ,  $s$  and  $\zeta$  at  $Ra_{\text{crit}}$  and  $a_{\text{crit}}$  for  $Pr = 0.1, Ta = 10^7$  and (a)  $\theta = 0, \phi = \frac{\pi}{2}, l = 0$ , (b)  $\theta = 0, \phi = \frac{\pi}{4}, l = 0$ , (c)  $\theta = 0, \phi = \frac{\pi}{4}, k = 0$ , (d)  $\theta = -0.95, \phi = \frac{\pi}{2}, l = 0$ , (e)  $\theta = -0.95, \phi = \frac{\pi}{4}, l = 0$ , and (f)  $\theta = -0.95, \phi = \frac{\pi}{4}, k = 0$ .

at the smaller of the two  $Ta$ . Mizerski & Tobias (2011) showed that, at high  $Ta$ , stratification did not have a great effect on the form of the eigenfunctions.

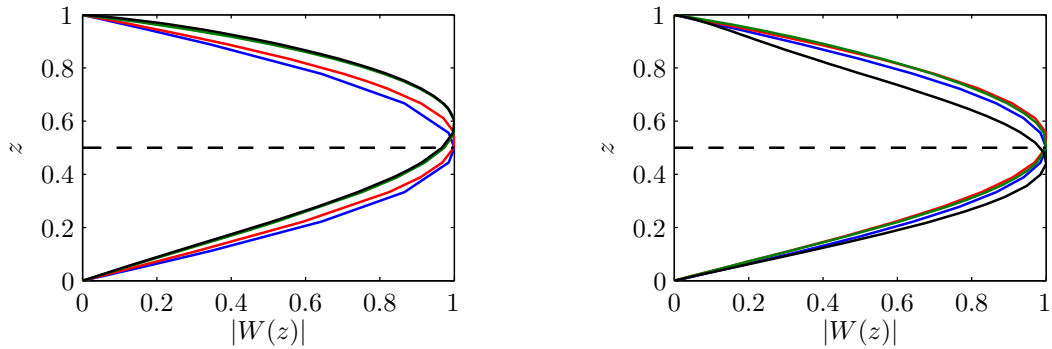


Figure 4.7: Amplitude function  $|W(z)|$  as a function of  $z$  for NS rolls,  $\phi = \frac{\pi}{4}$ ,  $Pr = 0.1$  and  $\theta = 0$  (blue),  $\theta = -0.37$  (red),  $\theta = -0.79$  (green) and  $\theta = -0.95$  (black) for (a)  $Ta = 10^3$  and (b)  $Ta = 10^7$ .

### 4.3.3 Three-dimensional solutions

We have seen that, when considering two-dimensional perturbations only, NS rolls are preferred over EW rolls, for all  $Ta$  and  $\theta$  considered. However, it might be that oblique rolls are the preferred ones, i.e., the convection rolls at onset have both wavenumber  $k$  and  $l$  non-zero. We considered three-dimensional perturbations and found that, in the majority of cases, the NS rolls were still found to be the preferred ones. However, for a small region of parameter space, oblique rolls were preferred. For example, when  $\theta = -0.37$  and  $Ta = 1200$ , the critical Rayleigh number is achieved at non-zero  $k$  and  $l$ , as shown in figure 4.8 (a). In this case,  $Ra_{\text{crit}} = 1427$ ,  $k_{\text{crit}} = 1.5900$ ,  $l_{\text{crit}} = 1.8250$  and  $\omega_{\text{crit}} = -1.6105$ . The three-dimensional mode is only slightly preferred over the NS mode though, where  $Ra_{\text{crit}} = 1459$ .

An example of a three-dimensional simulation, where a two-dimensional, NS mode is preferred is shown in figure 4.8 (b), we see that the critical wavenumber lies on the  $l = 0$  axis. Since in many of the cases we studied, the preferred modes also took the form of NS rolls, especially for large  $Ta$ , we will focus mainly on the case when  $l = 0$ . In addition, the earlier analysis (cf. figure 4.3) showed there is an interesting symmetry breaking in the NS case that is not present in the EW case (see section 4.3.1) and we would like to examine this further.

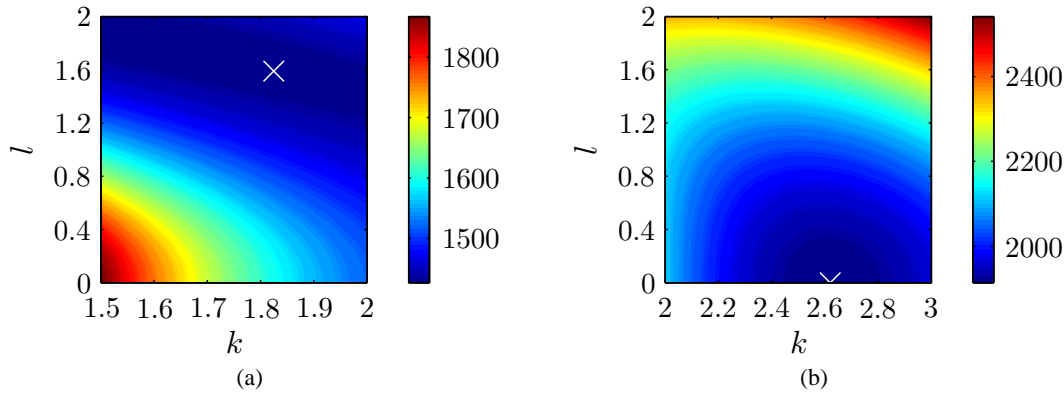


Figure 4.8: Contours of Rayleigh number against  $k$  and  $l$  for (a)  $Ta = 1200$ ,  $\theta = -0.37$  and (b)  $Ta = 10000$ ,  $\theta = -0.79$ . In (a) the preferred mode (white cross) is oblique and  $Ra_{\text{crit}} = 1427$ ,  $k_{\text{crit}} = 1.8250$ ,  $l_{\text{crit}} = 1.5900$  and  $\omega_{\text{crit}} = -1.6105$ , whereas in (b), the preferred mode (white cross) is oriented NS and  $Ra_{\text{crit}} = 1915$ ,  $k_{\text{crit}} = 2.6200$ ,  $l_{\text{crit}} = 0$  and  $\omega_{\text{crit}} = -6.1293$ .

#### 4.3.4 NS rolls - effect of $\phi$ and $Pr$

As we have just explained, in this section we choose to focus on NS rolls. Specifically, we study the effect of  $\phi$  and small  $Pr$  on the values of  $Ra$ ,  $k$  and  $\omega$  at onset, for different rotation rates and stratifications.

##### Effect of $\phi$

In order to make a direct comparison between solutions for different  $\phi$ , we plot their corresponding values of  $Ra_{\text{crit}}$ ,  $k_{\text{crit}}$  and  $\omega_{\text{crit}}$  on the same axes. We plot the cases when  $\phi = \frac{\pi}{2}$ ,  $\phi = \frac{\pi}{4}$  and  $\phi = \frac{\pi}{6}$  for the Boussinesq case ( $\theta = 0$ ) and a strongly stratified case ( $\theta = -0.95$ ). The results are shown in figure 4.9. The top plot is of  $Ra_{\text{crit}}$  against  $Ta$ , the middle plot is of  $k_{\text{crit}}$  against  $Ta$  and the bottom plot is of  $\omega_{\text{crit}}$  against  $Ta$ . The  $\theta = 0$  solutions are shown in black, blue and green for the  $\phi = \frac{\pi}{2}$ ,  $\phi = \frac{\pi}{4}$  and  $\phi = \frac{\pi}{6}$  cases respectively and the  $\theta = -0.95$  solutions are shown in red, orange and turquoise for the  $\phi = \frac{\pi}{2}$ ,  $\phi = \frac{\pi}{4}$  and  $\phi = \frac{\pi}{6}$  cases respectively. Again, 'o' represents solutions where the preferred frequency is negative, '+' where the preferred frequency is positive and '.' when only the solution with negative frequency exists.

Note that, the  $\phi = \frac{\pi}{2}$  solution does not have a broken symmetry (even when  $\theta \neq 0$ ), neither does the  $\theta = 0$  case (for all  $\phi$ ), and so the positive and negative branches have the same critical values in these cases. Therefore, both a tilted rotation vector and a stratification are required to break the

symmetry between the solutions with positive and negative critical frequency. Also in the  $\phi = \frac{\pi}{2}$  case, a high enough value of  $Ta$  has to be reached in order for oscillatory solutions to exist. For  $\theta = 0$ , there is a clear hierarchy of preferred solutions:  $\phi = \frac{\pi}{6}$  is the most unstable, followed by  $\phi = \frac{\pi}{4}$  and then  $\phi = \frac{\pi}{2}$  (this is in agreement with the Boussinesq analysis of Hathaway *et al.* (1980)). If we decrease  $\theta$  to  $-0.95$ , then the behaviour is changed slightly. Firstly, we note that, in this case, from figure 4.9 (a), the  $\phi = \frac{\pi}{6}$  solution has a second kink in it; in addition to the kink that occurs when the positive solution exists, there is a kink around the value of  $Ta$  at which the positive solution becomes preferred, and this coincides with a sharp rise in  $k_{\text{crit}}$ . This behaviour means that, in contrast to the  $\theta = 0$  case, the  $\phi = \frac{\pi}{6}$  solutions can be more stable than the  $\phi = \frac{\pi}{4}$  solutions, depending on  $Ta$  when  $\theta = -0.95$ . At small  $Ta$ , the  $\theta = 0$  solutions are less stable (have a lower  $Ra_{\text{crit}}$ ) than the  $\theta = -0.95$  solutions, but as  $Ta$  is increased, we reach a transition  $Ta$  at which the  $\theta = -0.95$  solutions become more stable than the  $\theta = 0$  solutions. This transition  $Ta$  happens at a larger  $Ta$  for smaller  $\phi$ , which since in this case,  $l = 0$ , and we are considering NS rolls, we would expect, because the component of the rotation vector affecting the  $x$ - $z$  plane is given by  $Ta \sin \phi$  (Chandrasekhar (1961)).

For  $\theta = 0$ ,  $k_{\text{crit}}$  is largest for  $\phi = \frac{\pi}{2}$ , then  $\phi = \frac{\pi}{4}$  and then  $\phi = \frac{\pi}{6}$ , for all  $Ta$ . At small  $Ta$ , there is little difference between the three cases but this difference increases with  $Ta$ . Again, adding a stratification makes a noticeable difference; at small  $Ta$  where both positive and negative frequency marginal solutions exist, but where the negative ones are preferred, the  $\phi = \frac{\pi}{2}$  solutions have the smallest  $k_{\text{crit}}$ , followed by  $\phi = \frac{\pi}{4}$  and then  $\phi = \frac{\pi}{6}$ . As  $Ta$  is increased, the solutions change their preferred length scale until, at large enough  $Ta$ , when the solutions with  $\omega_{\text{crit}} > 0$  are preferred, the  $\phi = \frac{\pi}{2}$  solutions have the largest  $k_{\text{crit}}$ , followed by  $\phi = \frac{\pi}{4}$  and then  $\phi = \frac{\pi}{6}$ . For  $\theta = 0$ ,  $\phi = \frac{\pi}{2}$  has the largest  $|\omega_{\text{crit}}|$ , followed by  $\phi = \frac{\pi}{4}$  and then  $\phi = \frac{\pi}{6}$ . Once  $Ta$  is large enough, so that all solutions exist, this ordering is also true for  $\theta = -0.95$ . Notice the difference when only negative solutions exist: there,  $\phi = \frac{\pi}{4}$  has a smaller  $|\omega_{\text{crit}}|$  than  $\phi = \frac{\pi}{6}$ .

### Effect of $Pr$

To see the effect of decreasing  $Pr$  for a fixed  $\theta$  we plot  $Ra_{\text{crit}}$ ,  $k_{\text{crit}}$  and  $\omega_{\text{crit}}$  against  $Ta$  for  $\theta = 0$  and  $\theta = -0.95$  for a number of different  $Pr$ . The results are shown in figure 4.10. The  $\theta = 0$  solutions are shown in black, blue, green and purple for  $Pr = 1$ ,  $Pr = 0.1$ ,  $Pr = 0.01$  and  $Pr = 0.001$  respectively and the  $\theta = -0.95$  solutions are shown in red, orange, turquoise and grey for  $Pr = 1$ ,  $Pr = 0.1$ ,  $Pr = 0.01$  and  $Pr = 0.001$  respectively. As in previous figures, the symbol type represents whether solutions with a positive or negative frequency are preferred.

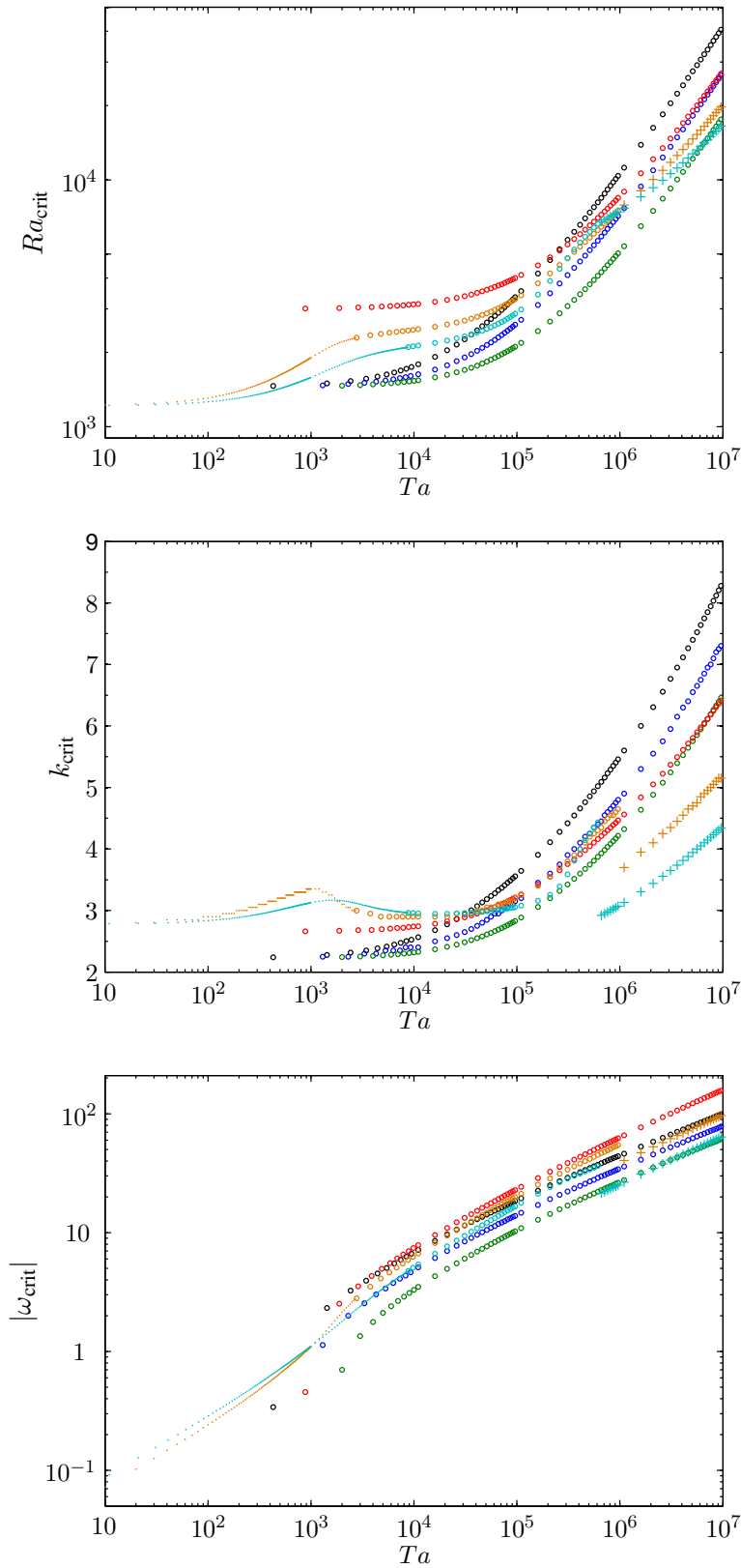


Figure 4.9:  $Ra_{\text{crit}}$  (top)  $k_{\text{crit}}$  (centre) and  $\omega_{\text{crit}}$  (bottom) against  $Ta$  for NS rolls when  $Pr = 0.1$ . Black (red, blue (orange) and green (turquoise) symbols denote  $\phi = \frac{\pi}{2}$ ,  $\phi = \frac{\pi}{4}$  and  $\phi = \frac{\pi}{6}$  respectively for  $\theta = 0$  ( $\theta = -0.95$ ). The symbol shape has the same interpretation as in figure 4.1.

A key difference between the stratified and unstratified cases, when  $Pr = 1$ , is that for  $\theta = 0$  the preferred solution is a steady mode, i.e.,  $\omega_{\text{crit}} = 0$ , but for  $\theta \neq 0$ , the preferred solution is an oscillatory mode, hence the  $\theta = 0$  case is not seen in figure 4.10 (c). For both values of  $\theta$  considered here, and for fixed  $Ta$ ,  $Ra_{\text{crit}}$ ,  $k_{\text{crit}}$  and  $\omega_{\text{crit}}$  decrease with  $Pr$ . For all of the  $Pr < 1$  cases considered, the  $\theta = 0$  solution has a smaller  $Ra_{\text{crit}}$  than the  $\theta = -0.95$  solution, until a large enough  $Ta$  is reached, at which point the stratified solution becomes the less stable. The  $Ta$  at which this change occurs increases with decreasing  $Pr$ . Another difference that occurs as  $Pr$  is decreased is that a second kink in the  $Ra_{\text{crit}}$  curve for  $\theta = -0.95$  becomes more prominent. In the  $Pr = 0.01$  and  $Pr = 0.001$  curves there is a large kink as the solutions with positive frequency become preferred, these kinks are not visible in the larger  $Pr$  curves. As in the case when  $\phi$  was changed, these kinks coincide with a sharp rise in  $k_{\text{crit}}$ . We also note that, in order to obtain power law growth of  $Ra_{\text{crit}}$  with  $Ta$ , a higher  $Ta$  is required for smaller  $Pr$ . Once  $Ta$  is large enough so that power law growth is observed, the stratified solutions then have a smaller  $k_{\text{crit}}$  and hence a larger length scale. When the solutions have a negative critical frequency,  $|\omega_{\text{crit}}|$  is larger for the stratified cases. If the stratified solutions have a positive critical frequency, then, for  $Pr = 0.1$ , the stratified solutions have the larger  $|\omega_{\text{crit}}|$ . For  $Pr = 0.01$  and  $Pr = 0.001$ , if the stratified solutions have a positive critical frequency, then the  $\theta = 0$  solutions have the larger  $|\omega_{\text{crit}}|$  until  $Ta$  is large enough and then the stratified cases have the larger  $|\omega_{\text{crit}}|$ .

### 4.3.5 Effect of $\theta$ on the onset of convection

We can also consider what happens to the critical values as we vary  $\theta$ , for fixed  $Ta$ .

Figure 4.11 shows the critical values against  $|\theta|$  for NS rolls with  $Pr = 0.1$  and  $\phi = \frac{\pi}{4}$ . The red lines represent solutions with  $Ta = 10^4$ , the blue lines represent solutions with  $Ta = 10^5$ , the black lines represent solutions with  $Ta = 10^6$  and the purple lines represent solutions with  $Ta = 10^7$ . Unlike previously, we now represent solutions with a positive critical frequency with a solid line and solutions with a negative critical frequency with a dashed line (we plot the absolute values of the critical frequencies). For small  $Ta$ , the negative branch is preferred but this changes to the positive branch as  $Ta$  is increased, as expected from the previous work in section 4.3. The positive solution always has the smaller critical wavenumber and critical frequency compared with the negative branch. The  $Ta = 10^4$  solution becomes more stable with increasing  $|\theta|$  but for higher  $Ta$  the minimum  $Ra_{\text{crit}}$  occurs at  $|\theta| > 0$ , with the minimum increasing with  $Ta$ . There is also a much larger variation in  $k_{\text{crit}}$  with increasing  $|\theta|$  for the positive case.

Figure 4.12 shows the equivalent to figure 4.11 but for EW rolls. As noted before, for  $k = 0$ ,

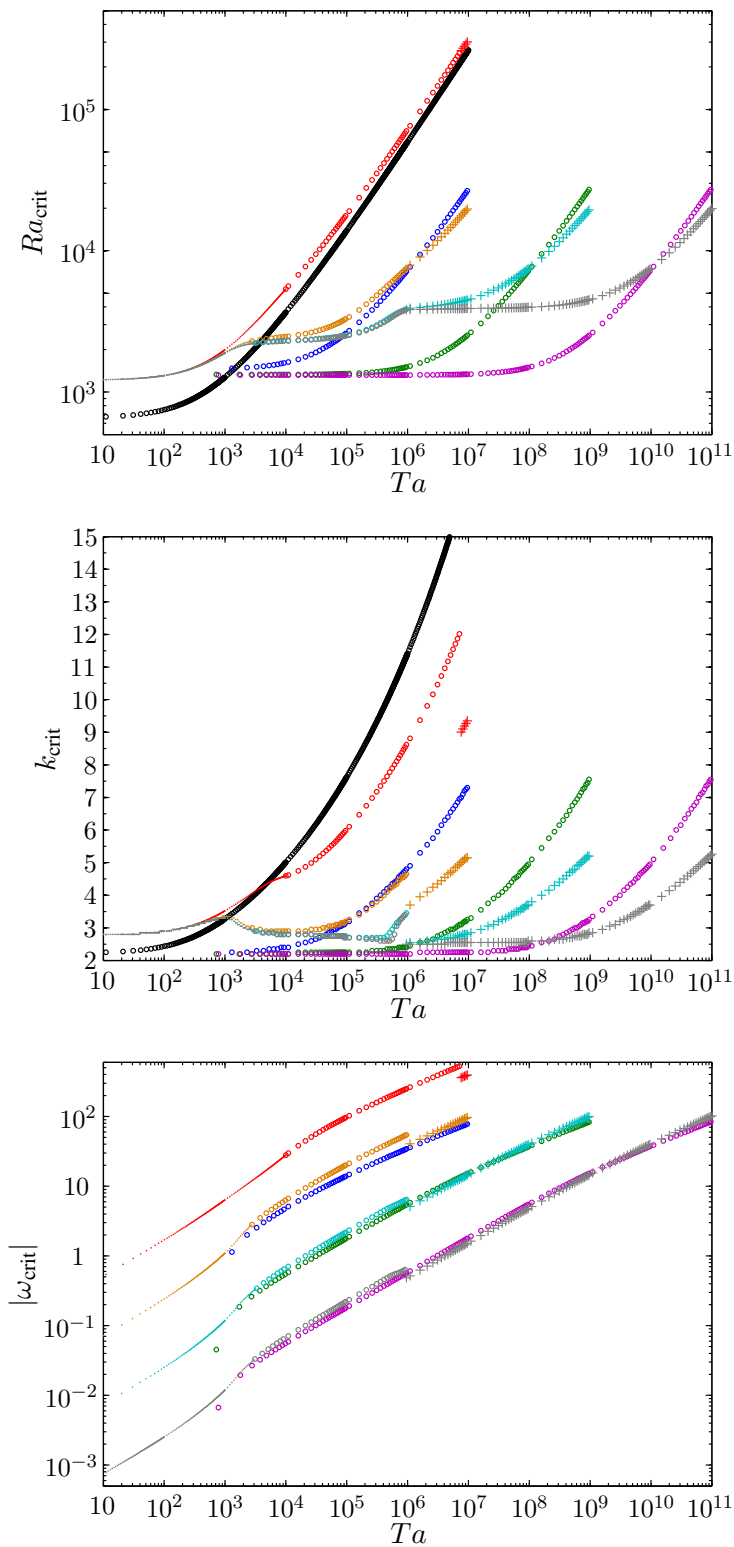


Figure 4.10:  $Ra_{\text{crit}}$  (top)  $k_{\text{crit}}$  (centre) and  $\omega_{\text{crit}}$  (bottom) against  $Ta$  for NS rolls when  $\phi = \frac{\pi}{4}$ . Black (red), blue (orange), green (turquoise) and purple (grey) symbols denote  $Pr = 1$ ,  $Pr = 0.1$ ,  $Pr = 0.01$ ,  $Pr = 0.001$  respectively for  $\theta = 0$  ( $\theta = -0.95$ ). The symbol shape has the same interpretation as in figure 4.1.

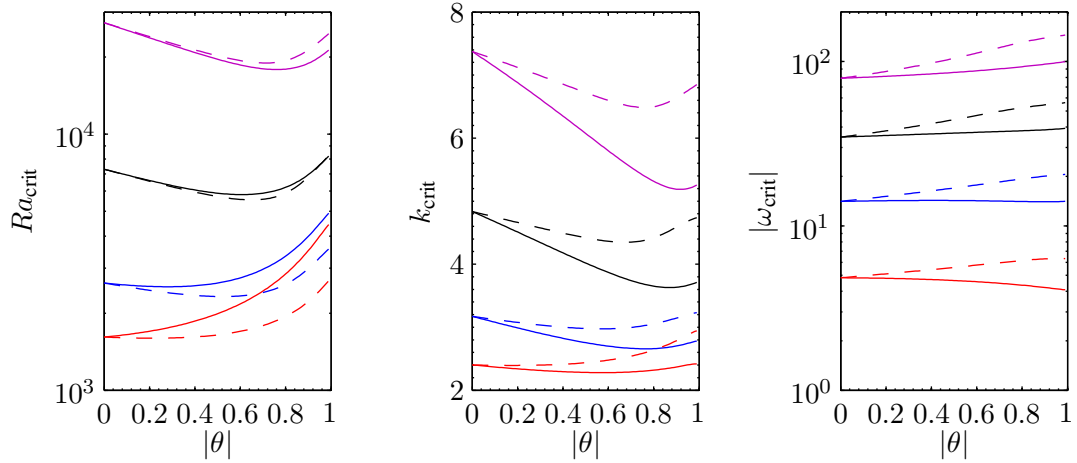


Figure 4.11:  $Ra_{\text{crit}}$  (left)  $k_{\text{crit}}$  (centre) and  $\omega_{\text{crit}}$  (right) against  $|\theta|$  for NS rolls when  $Pr = 0.1$ ,  $\phi = \frac{\pi}{4}$ . Solid lines represent solutions with  $\omega_{\text{crit}} > 0$  and dashed lines represent solutions with  $\omega_{\text{crit}} < 0$ . In red  $Ta = 10^4$ , in blue  $Ta = 10^5$ , in black  $Ta = 10^6$  and in purple  $Ta = 10^7$

there is not a distinction to be made between the solutions with positive and negative frequency as they have the same critical values, hence we only plot the positive frequency solutions. The behaviour is very similar to that in the NS case, but  $Ra_{\text{crit}}$  is higher in the EW case, so that NS rolls are preferred.

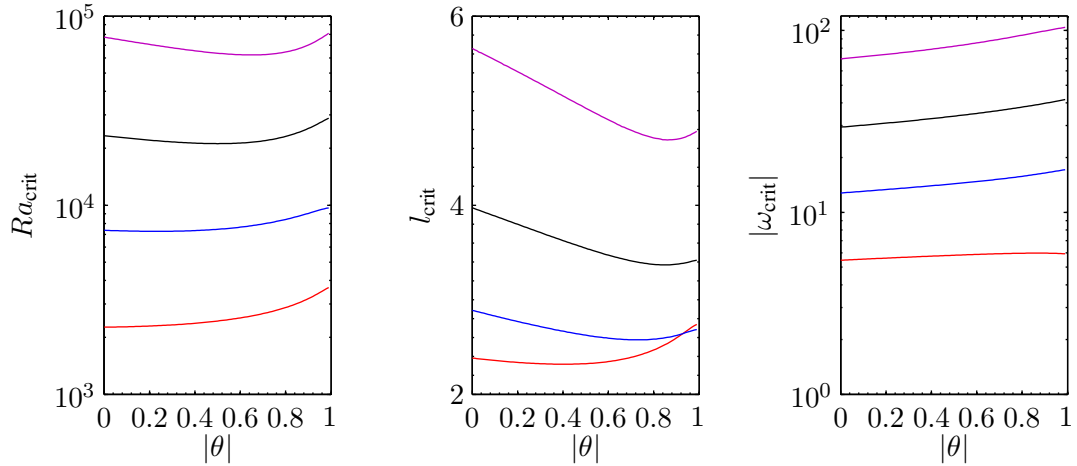


Figure 4.12:  $Ra_{\text{crit}}$  (left)  $l_{\text{crit}}$  (centre) and  $\omega_{\text{crit}}$  (right) against  $|\theta|$  for EW rolls when  $Pr = 0.1$ ,  $\phi = \frac{\pi}{4}$ . In red  $Ta = 10^4$ , in blue  $Ta = 10^5$ , in black  $Ta = 10^6$  and in purple  $Ta = 10^7$

Figure 4.13 allows us to compare three cases with three different tilt angles, (i)  $\phi = \frac{\pi}{2}$ , (ii)  $\phi = \frac{\pi}{4}$  and (iii)  $\phi = \frac{\pi}{6}$ . We have plotted the critical values against  $|\theta|$  for NS rolls with  $Pr = 0.1$  for two different  $Ta$ . The  $Ta = 10^4$  solutions are shown in black, blue and green for the  $\phi = \frac{\pi}{2}$ ,

$\phi = \frac{\pi}{4}$  and  $\phi = \frac{\pi}{6}$  cases respectively, and the  $Ta = 10^7$  solutions are shown in red, orange and turquoise for the  $\phi = \frac{\pi}{2}$ ,  $\phi = \frac{\pi}{4}$  and  $\phi = \frac{\pi}{6}$  cases respectively. For both  $Ta$  shown, and for all  $\theta$ ,  $\phi = \frac{\pi}{2}$  is the most stable followed by  $\phi = \frac{\pi}{4}$  and then  $\phi = \frac{\pi}{6}$ . For  $\phi = \frac{\pi}{2}$ , as we have seen previously, the solutions with positive and negative frequency correspond to the same critical Rayleigh number and same critical wavenumber, but for  $\phi \neq \frac{\pi}{2}$ , there is a distinction to be made between solutions with positive frequency and those with negative frequency. The difference between the positive and negative critical values increases with  $|\theta|$  and also with decreasing  $\phi$ . A key difference between the two  $Ta$  considered is that, for  $Ta = 10^4$ , the solutions with negative critical frequency are preferred over solutions with positive frequency but for  $Ta = 10^7$ , the solutions with positive critical frequency are the preferred ones. Since for  $Ta = 10^4$ , the negative solutions are the preferred ones, we see from the plot of  $k_{\text{crit}}$  that for small  $|\theta|$  the preferred  $k_{\text{crit}}$  is largest for  $\phi = \frac{\pi}{2}$ , followed by  $\phi = \frac{\pi}{4}$  and then  $\phi = \frac{\pi}{6}$  but, as  $|\theta|$  is increased, the preferred  $k_{\text{crit}}$  is largest for  $\phi = \frac{\pi}{6}$  followed by  $\phi = \frac{\pi}{4}$  and then  $\phi = \frac{\pi}{2}$ . For  $Ta = 10^7$ , the positive solutions are the preferred ones, and  $\phi = \frac{\pi}{2}$  has the largest preferred  $k_{\text{crit}}$  for all  $|\theta|$ . Notice also, that until the very largest  $|\theta|$ , for  $Ta = 10^7$ ,  $k_{\text{crit}}$  decreases with increasing  $|\theta|$  so that the length scale of the solutions at onset increases with  $|\theta|$ . For both  $Ta$ , the largest critical frequencies occur for  $\phi = \frac{\pi}{2}$  and decrease with  $\phi$ , for all  $|\theta|$ .

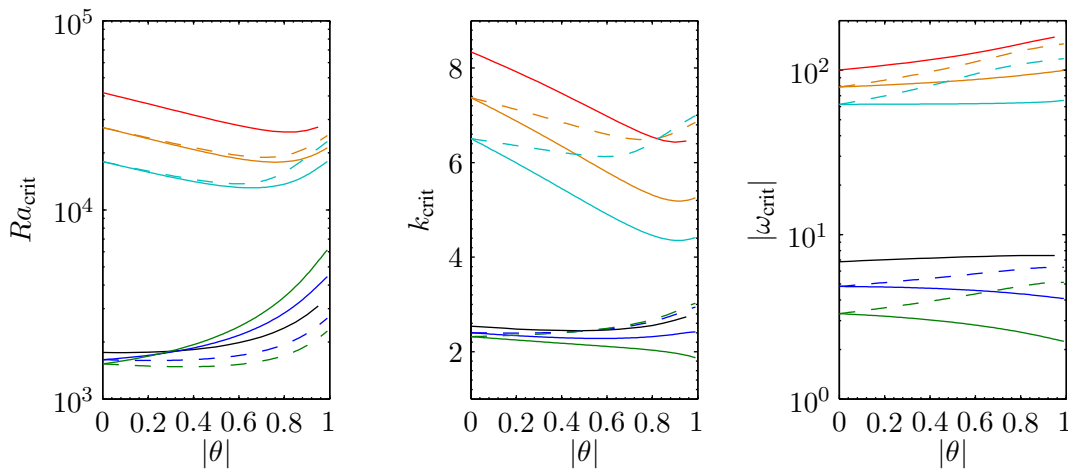


Figure 4.13:  $Ra_{\text{crit}}$  (left),  $k_{\text{crit}}$  (centre) and  $\omega_{\text{crit}}$  (right) against  $|\theta|$  for NS rolls when  $Pr = 0.1$ . Black (red), blue (orange) and green (turquoise) symbols correspond to  $\phi = \frac{\pi}{2}$ ,  $\phi = \frac{\pi}{4}$  and  $\phi = \frac{\pi}{6}$  respectively for  $Ta = 10^4$  ( $Ta = 10^7$ ). Solid lines correspond to solutions with  $\omega_{\text{crit}} > 0$  and dashed lines to solutions with  $\omega_{\text{crit}} < 0$ .

In figure 4.14, we show how the critical values are changed with  $\theta$  when  $Pr$  is decreased. We consider the case when  $Pr = 0.01$ , it is shown in black and red for  $Ta = 10^7$  and  $Ta = 10^9$

respectively, and the case when  $Pr = 0.001$ , it is shown in blue, orange and grey for  $Ta = 10^7$ ,  $Ta = 10^9$  and  $Ta = 10^{11}$  respectively. The solutions with positive frequency are displayed with a solid line whilst the solutions with a negative frequency are displayed with a dashed line. For both  $Pr$ , at the smaller  $Ta$ , the solution with negative critical frequency is preferred for most  $|\theta|$ , although at the largest stratifications the solutions with the positive critical frequency are preferred. Then, as  $Ta$  is increased, the solution with the positive frequency becomes the preferred one for all  $|\theta|$ . It is clear from the plots that the black and orange lines almost coincide. In other words, the critical values for  $Pr = 0.01$ ,  $Ta = 10^7$  and the critical values for  $Pr = 0.001$ ,  $Ta = 10^9$  are almost identical. For these parameters, we note that the product  $PrTa^{\frac{1}{2}}$  is the same in both cases, and so, this perhaps provides an explanation for this agreement between the two solutions (since  $PrTa^{\frac{1}{2}}$  is the form in which the Coriolis term appears in the governing equations, and for small  $Pr$ , large  $Ta$ , we expect this term to dominate, see equations (4.2.14)-(4.2.16)). This product is also the same for the solutions with  $Pr = 0.01$ ,  $Ta = 10^9$  solution and the  $Pr = 0.001$ ,  $Ta = 10^{11}$  and indeed the red and grey lines are also nearly identical.

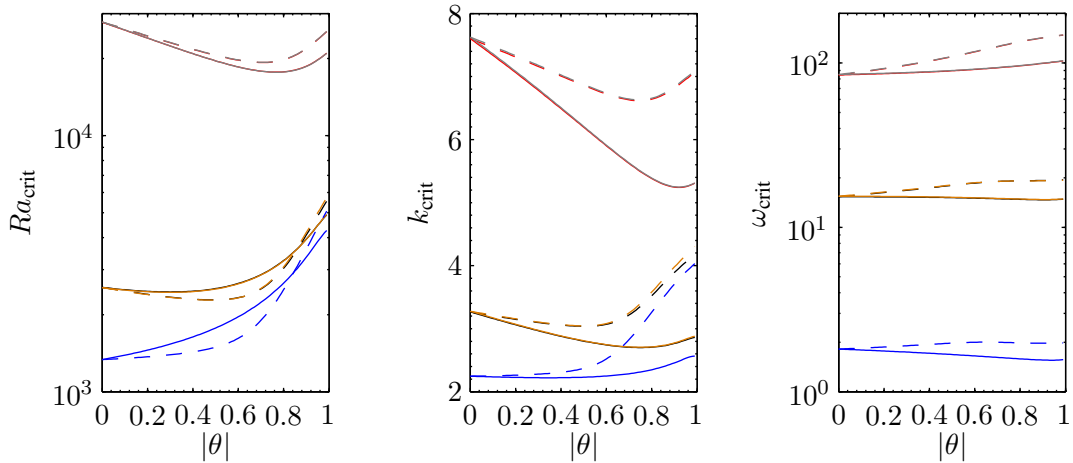


Figure 4.14:  $Ra_{\text{crit}}$  (left),  $k_{\text{crit}}$  (centre) and  $\omega_{\text{crit}}$  (right) against  $|\theta|$  for NS rolls when  $\phi = \frac{\pi}{4}$ . Black (blue), red (orange) and (grey) symbols correspond to  $Ta = 10^7$ ,  $Ta = 10^9$  and  $Ta = 10^{11}$  respectively for  $Pr = 0.01$  ( $Pr = 0.001$ ). Solid lines correspond to solutions with  $\omega_{\text{crit}} > 0$  and dashed lines to solutions with  $\omega_{\text{crit}} < 0$ .

#### 4.4 Symmetry considerations

As touched upon in section 4.3, when  $\theta \neq 0$  and  $l = 0$  (NS rolls), there is a distinction to be made between solutions with a positive critical frequency and those with a negative critical

frequency. However, when  $\theta \neq 0$  and  $k = 0$  (EW rolls) there is still a symmetry and the positive and negative branches have the same  $|\omega_{\text{crit}}|$ . This is a surprising result. Naively, we might expect that breaking the up-down symmetry of the system, via the introduction of a vertical density stratification, would cause a break in symmetry of the eigenvalue spectrum, and hence result in different frequencies for the positive and negative branches. Instead, when  $k = 0$ , the eigenvalues remain in complex conjugate pairs. To see this we plot the real and imaginary parts of the growth rate  $\sigma$  against each other, for a range of  $Ra$  but holding all other parameters fixed. For example, figure 4.15 shows the cases when (a)  $l = 0, k = 3$ , (b)  $k = 0, l = 3$  and (c)  $k = 3, l = 3$ . We see that in (a) and (c), the introduction of a vertical stratification across the layer has, as expected, broken the symmetry of the eigenvalue spectrum - they no longer appear in complex conjugate pairs. However, counter-intuitively, when  $k = 0$  (subfigure (b)), the symmetry is not broken and the eigenvalues remain in complex conjugate pairs, in an analogous way to the Boussinesq case ( $\theta = 0$ ). Evonuk (2008) and Glatzmaier *et al.* (2009) describe a mechanism that is perhaps responsible for this difference between NS and EW rolls. The crux of their argument is that the vorticity equation (curl of equation (4.2.4)) contains a term proportional to  $\mathbf{\Omega}(\nabla \cdot \mathbf{u})$ , which is in general, non-zero for anelastic convection. However, in our system, the  $x$ -component of this term is zero and so it does not have an effect on EW rolls, whereas, the  $y$ -component of this term is non-zero and so it does have an effect on NS rolls.

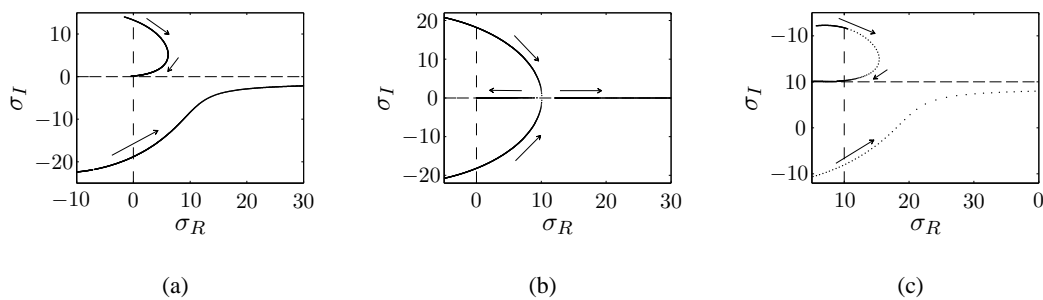


Figure 4.15: Real and imaginary parts of growth rate plotted against each other for different  $Ra$  whilst  $Ta = 10^5$ ,  $Pr = 0.1$ ,  $\phi = \frac{\pi}{4}$ ,  $\theta = -0.9$ . In (a)  $l = 0, k = 3$ , in (b)  $k = 0, l = 3$  and in (c)  $k = 3, l = 3$ . When  $k = 0$  the symmetry is not broken.

### 4.4.1 Eigenfunctions

To investigate the symmetry of the EW solutions further, we look at the eigenfunctions,  $|W(z)|$ ,  $|Z(z)|$  and  $|S(z)|$  as a function of vertical depth. Figure 4.16 displays the eigenfunctions as a function of layer depth for  $k = 0$ ,  $l = 2$ ,  $Ta = 10^5$ ,  $Pr = 0.1$ ,  $\phi = \frac{\pi}{4}$ ,  $Ra = 2 \times 10^5$  and (a)  $\theta = 0$ , (b)  $\theta = -0.95$ . The solid lines are the eigenfunctions corresponding to solutions with  $\omega > 0$  and the dotted lines are the eigenfunctions corresponding to solutions with  $\omega < 0$ . The eigenvalues, as explained before, are a complex conjugate pair for both  $\theta$ ; in (a)  $\sigma = 8.0489 \pm 11.3672i$  and in (b)  $\sigma = 4.8626 \pm 17.1070i$ . It is clear from the plots that, in the Boussinesq case, (a), the eigenfunctions are symmetric about  $z = 0.5$ , whereas when a stratification is added, (b), the corresponding eigenfunctions possess no obvious symmetry, despite the fact the eigenvalues are a complex conjugate pair.

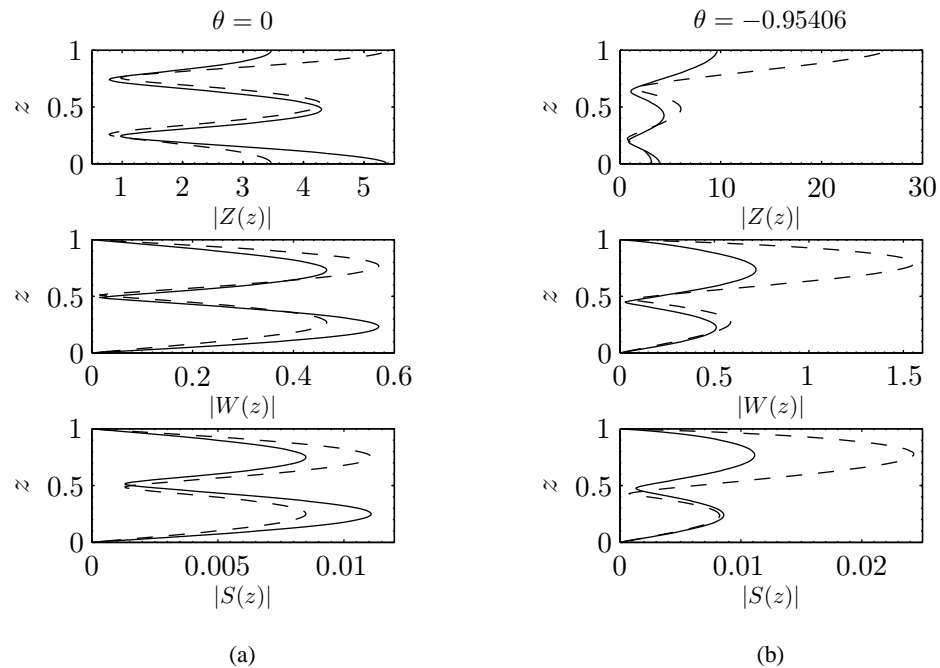


Figure 4.16: Eigenfunctions. The solutions  $|W(z)|$ ,  $|Z(z)|$  and  $|S(z)|$  as a function of  $z$  for  $k = 0$ ,  $l = 2$ ,  $Ta = 10^5$ ,  $Pr = 0.1$ ,  $\phi = \frac{\pi}{4}$ ,  $Ra = 2 \times 10^5$  and (a)  $\theta = 0$ , (b)  $\theta = -0.95$ . The solid line corresponds to the solutions with  $\omega > 0$  and the dotted lines to solutions with  $\omega < 0$ .

#### 4.4.2 Proof of symmetry when $k = 0$

The following is a proof of the symmetry of the spectrum of eigenvalues that exists when  $k = 0$ . The proof not only holds for the stress free boundary conditions considered above but is a more general result and holds for all natural boundary conditions. The proof is similar in nature to that of Proctor *et al.* (2011) who prove a similar result. However, they consider a system with symmetric equations but break the symmetry through asymmetric boundary conditions. This is in contrast to this work, where we have asymmetric equations to begin with, and typically our boundary conditions are symmetric.

To begin the proof, we make a change of variables. Let

$$\tilde{Z} = (1 + \theta z)^{\frac{m}{2}} Z, \quad (4.4.20)$$

$$\tilde{W} = (1 + \theta z)^{\frac{m}{2}} W, \quad (4.4.21)$$

$$\tilde{S} = (1 + \theta z)^{\frac{1}{2}} S, \quad (4.4.22)$$

then multiply (4.2.14) and (4.2.15) by  $(1 + \theta z)^{\frac{m}{2}}$ , (4.2.16) by  $(1 + \theta z)^{m + \frac{1}{2}} RaPra^2$  and substitute in (4.4.20) - (4.4.22), to give

$$\begin{aligned} \sigma \tilde{Z} = & Ta^{\frac{1}{2}} Pr \left[ \sin \phi \left( D\tilde{W} + \frac{m\theta}{2(1 + \theta z)} \tilde{W} \right) + \cos \phi i l \tilde{W} \right] + \\ & Pr(D^2 - a^2)\tilde{Z} - \frac{Prm\theta^2(\frac{m}{2} - 1)}{2(1 + \theta z)^2} \tilde{Z}, \end{aligned} \quad (4.4.23)$$

$$\begin{aligned} -\sigma[(D^2 - a^2)\tilde{W} - \frac{m\theta^2(1 + \frac{m}{2})}{2(1 + \theta z)^2} \tilde{W}] = & RaPra^2(1 + \theta z)^{\frac{m-1}{2}} \tilde{S} \\ + Ta^{\frac{1}{2}} Pr \sin \phi [D\tilde{Z} - \frac{m\theta}{2(1 + \theta z)} \tilde{Z}] + & Ta^{\frac{1}{2}} Pr \cos \phi \left[ \frac{m\theta}{1 + \theta z} i \mathbf{k} \tilde{W} + i l \tilde{Z} \right] \\ - PrD^4 \tilde{W} + 2Pra^2 D^2 \tilde{W} - Pra^4 \tilde{W} + \frac{Prm\theta^2(\frac{m}{2} + 1)}{(1 + \theta z)^2} D^2 \tilde{W} \\ - \frac{Pr\theta^3 m(m + 2)}{(1 + \theta z)^3} D\tilde{W} + \mathcal{F} \tilde{W}, \end{aligned} \quad (4.4.24)$$

where

$$\mathcal{F} = \frac{Prm\theta^4(3 + \frac{5m}{4} - \frac{m^2}{4} - \frac{m^3}{16})}{(1 + \theta z)^4} + \frac{Prma^2\theta^2(1 + \frac{m}{6})}{(1 + \theta z)^2}, \quad (4.4.25)$$

and

$$\sigma RaPra^2(1 + \theta z)^m \tilde{S} = RaPra^2(1 + \theta z)^{\frac{m-1}{2}} \tilde{W} + RaPra^2(D^2 - a^2)\tilde{S} + \frac{RaPra^2\theta^2}{4(1 + \theta z)^2} \tilde{S}. \quad (4.4.26)$$

When  $k = 0$ ,  $a = l$  and we can write this system as

$$\sigma \mathbf{A} \tilde{\mathbf{X}} = \mathbf{B} \tilde{\mathbf{X}} \quad (4.4.27)$$

$$\text{where } \tilde{\mathbf{X}} = \begin{bmatrix} \tilde{Z} \\ \tilde{W} \\ \tilde{S} \end{bmatrix}, \mathbf{A} = \begin{bmatrix} 1 & 0 & 0 \\ 0 & -(D^2 - l^2) + \frac{m\theta^2(\frac{m}{2}+1)}{2(1+\theta z)^2} & 0 \\ 0 & 0 & RaPra^2(1+\theta z)^m \end{bmatrix} \text{ and}$$

$$\mathbf{B} = \begin{bmatrix} Pr(D^2 - l^2) - \frac{Prm\theta^2(\frac{m}{2}-1)}{2(1+\theta z)^2} & Ta^{\frac{1}{2}}Pr[\sin \phi(D + \frac{m\theta}{2(1+\theta z)}) + \cos \phi il] & 0 \\ Ta^{\frac{1}{2}}Pr[\sin \phi(D - \frac{m\theta}{2(1+\theta z)}) + \cos \phi il] & -Pr(D^2 - l^2)^2 + \frac{Prm\theta^2(\frac{m}{2}+1)}{2(1+\theta z)^2}D^2 - \frac{Pr\theta^3 m(m+2)}{(1+\theta z)^3}D + \mathcal{F} & RaPr l^2(1+\theta z)^{\frac{m-1}{2}} \\ 0 & RaPra^2(1+\theta z)^{\frac{m-1}{2}} & RaPr l^2[(D^2 - l^2) + \frac{\theta^2}{4(1+\theta z)^2}] \end{bmatrix}.$$

Next, we define the inner product

$$\langle \tilde{\mathbf{X}}_1, \tilde{\mathbf{X}}_2 \rangle = \int_0^1 \tilde{\mathbf{X}}_1^{*T} \tilde{\mathbf{X}}_2 dz = \int_0^1 (\tilde{\mathbf{X}}_2^{*T} \tilde{\mathbf{X}}_1)^* dz = \langle \tilde{\mathbf{X}}_2, \tilde{\mathbf{X}}_1 \rangle^* \quad (4.4.28)$$

where

$$\tilde{\mathbf{X}}_1 = \begin{bmatrix} \tilde{Z}_1 \\ \tilde{W}_1 \\ \tilde{S}_1 \end{bmatrix}, \quad \tilde{\mathbf{X}}_2 = \begin{bmatrix} \tilde{Z}_2 \\ \tilde{W}_2 \\ \tilde{S}_2 \end{bmatrix}, \quad (4.4.29)$$

and  $\tilde{\mathbf{X}}_1$  satisfies the same boundary conditions as  $\tilde{\mathbf{X}}_2$ . Then, since  $\mathbf{A}$  is real and symmetric,

$$\begin{aligned} \langle \tilde{\mathbf{X}}_1, (\sigma \mathbf{A} \tilde{\mathbf{X}}_2 - \mathbf{B} \tilde{\mathbf{X}}_2) \rangle &= \int_0^1 \tilde{\mathbf{X}}_1^{*T} (\sigma \mathbf{A} \tilde{\mathbf{X}}_2 - \mathbf{B} \tilde{\mathbf{X}}_2) dz \\ &= \int_0^1 \tilde{\mathbf{X}}_2^T (\sigma^* \mathbf{A} \tilde{\mathbf{X}}_1 - \mathbf{B}^\dagger \tilde{\mathbf{X}}_1)^* dz = \langle (\sigma^* \mathbf{A} \tilde{\mathbf{X}}_1 - \mathbf{B}^\dagger \tilde{\mathbf{X}}_1), \tilde{\mathbf{X}}_2 \rangle. \end{aligned} \quad (4.4.30)$$

Note, equation (4.4.30) only holds if the boundary conditions on  $\tilde{\mathbf{X}}_i$  and  $\tilde{\mathbf{X}}_i^*$  ( $i = 1, 2$ ) are the same. So  $\mathbf{B}^\dagger$  is the formal adjoint of  $\mathbf{B}$ , i.e.,  $\langle \mathbf{u}, \mathbf{B} \mathbf{v} \rangle = \langle \mathbf{B}^\dagger \mathbf{u}, \mathbf{v} \rangle$  for vectors  $\mathbf{u}$  and  $\mathbf{v}$  and it is given by  $\mathbf{B}^\dagger =$

$$\begin{bmatrix} Pr(D^2 - l^2) - \frac{Prm\theta^2(\frac{m}{2}-1)}{2(1+\theta z)^2} & -Ta^{\frac{1}{2}}Pr[\sin \phi(D + \frac{m\theta}{2(1+\theta z)}) + \cos \phi il] & 0 \\ -Ta^{\frac{1}{2}}Pr[\sin \phi(D - \frac{m\theta}{2(1+\theta z)}) + \cos \phi il] & -Pr(D^2 - l^2)^2 + \frac{Prm\theta^2(\frac{m}{2}+1)}{2(1+\theta z)^2}D^2 - \frac{Pr\theta^3 m(m+2)}{(1+\theta z)^3}D + \mathcal{F} & RaPra^2(1+\theta z)^{\frac{m-1}{2}} \\ 0 & RaPr l^2(1+\theta z)^{\frac{m-1}{2}} & RaPr l^2[(D^2 - l^2) + \frac{\theta^2}{4(1+\theta z)^2}] \end{bmatrix}.$$

Since  $\mathbf{B}^\dagger$  is the formal adjoint of  $\mathbf{B}$ , its spectrum is the complex conjugate of the spectrum of  $\mathbf{B}$ . Now, if we let

$$\tilde{\mathbf{Y}}_1 = \begin{bmatrix} -\tilde{Z}_1 \\ \tilde{W}_1 \\ \tilde{S}_1 \end{bmatrix}, \quad (4.4.31)$$

then the adjoint equation

$$\sigma^* \mathbf{A} \tilde{\mathbf{X}}_1 = \mathbf{B}^\dagger \tilde{\mathbf{X}}_1 \quad \text{can be written as} \quad (4.4.32)$$

$$\sigma^* \mathbf{A} \tilde{\mathbf{Y}}_1 = \mathbf{B} \tilde{\mathbf{Y}}_1 \quad \text{when } k = 0. \quad (4.4.33)$$

So, if  $(\sigma, \tilde{\mathbf{X}}_1)$  is an eigenvalue, eigenfunction pair for the system then so is  $(\sigma^*, \tilde{\mathbf{Y}}_1)$ .

Hence, we have shown that, as long as the boundary conditions on  $\tilde{\mathbf{X}}$  and  $\tilde{\mathbf{X}}^*$  are the same, then when  $k = 0$ , the eigenvalue spectrum is symmetric. This is in agreement with the numerical results we found in section 4.3.

If  $k \neq 0$ , then the imaginary tilted anelastic term, highlighted in bold in equation (4.4.24), must be added to the central entry of the matrices  $\mathbf{B}$  and  $\mathbf{B}^\dagger$ , and this results in a breakdown of the proof, as the last step (from equation (4.4.32) to equation (4.4.33)) can not be carried out. Therefore, when  $k \neq 0$ , the eigenvalue spectrum is not symmetric, again in agreement with the numerical results obtained in 4.3.

## 4.5 Summary

This chapter analysed the effect of stratification and compressibility on the linear behaviour of rotating convection, where the rotation vector is oblique to gravity, using the anelastic approximation. This was a novel investigation as previous studies of rotating plane layer convection under the anelastic approximation have considered the case of vertical rotation only, e.g., Mizerski & Tobias (2011).

In section 4.2, we derived the linear equations under the anelastic approximation and noted that the addition of stratification to this system acts to add extra terms to the equations studied under the Boussinesq approximation. As a result, the anelastic system can only be solved numerically. Using an extension of the MATLAB code detailed in section 3.3, we studied the effect of the stratification on the onset of convection in a number of different regimes. A key discovery was that, in the presence of stratification, there is a difference between solutions with positive and negative frequencies when NS rolls are considered but not when EW rolls are considered. In

section 4.4, we examined the symmetry that occurs in the EW case further and proved that the symmetry exists for all parameters when any natural boundary conditions are imposed.

As a consequence of the unexpected symmetry-breaking in the NS case, we chose to focus on the two-dimensional case of NS rolls. We found that at small  $Ta$ , the solutions with negative frequency are preferred, i.e., the solutions are right travelling waves, but at  $Ta$  large enough (the value of which depends on other parameters) the solutions with positive frequency are preferred, i.e., the solutions are left travelling waves. We also noted that, the effect of  $|\theta|$  on the critical values is less dramatic for large  $Ta$ . In this chapter, we only gave a small consideration to three-dimensional modes, further analysis of these would improve this work.

We remark here also that, as we are interested in the driving of mean flows, it might be intriguing to consider the Reynolds stresses as calculated using the eigenfunctions outputted from a linear calculation. We will revisit this idea in Chapter 7, where we will consider nonlinear anelastic convection. In that chapter, we will define Reynolds stresses and make comparisons between the fully nonlinear Reynolds stresses and those calculated from the linear eigenfunctions.



## Chapter 5

# Nonlinear Numerical Method

In Chapters 3 and 4, we considered the linear system of rotating convection under the Boussinesq and anelastic approximations respectively. In order to investigate the behaviour of the system beyond the initial onset of convection, we are required to solve the nonlinear equations numerically. This chapter details the numerical method used to solve the nonlinear governing equations derived in Chapter 2. Details are given for the method used to solve the equations of the Boussinesq hydrodynamic system, with a discussion on how to extend to the Boussinesq MHD and anelastic cases towards the end of the chapter, in sections 5.6 and 5.7 respectively.

### 5.1 Introduction to pseudospectral methods

The method we utilise is of the Fourier-Chebyshev pseudospectral class. Such methods, and the techniques involved in the methods, are discussed in a plethora of literature. For example, see Canuto *et al.* (1993), Trefethen (2000), Boyd (2001), Peyret (2002), Canuto *et al.* (2006) and Glatzmaier (2013). These sources are the ones that were consulted when developing the numerical code described in this chapter.

Spectral methods can be very useful as they are often able to achieve accurate results, at relatively low computational cost. The development of efficient Fast Fourier Transform (FFT) algorithms on which spectral methods are built are key to this efficiency. We will employ an algorithm known as FFTW, developed by Frigo & Johnson (2005), to compute our transforms.

A spectral method consists of expressing the variables we wish to solve for, as a combination of time-independent, spatially varying basis functions. The time-dependent coefficients defining such an expression are unknown and we can write the equations to solve for these spectral

coefficients instead. A transform, built around the FFT, is used to translate between physical variables evaluated at grid points and spectral coefficients. Expressing variables in their spectral form makes for relative ease of computation of derivatives. However, the formation of nonlinear terms is computationally expensive in spectral space, as convolutions are required. Instead, multiplications to form the nonlinear terms are carried out in physical space before the resulting product is transformed back to spectral space to continue with the time marching. It is for this reason that the method is termed pseudospectral, as opposed to fully spectral, where nonlinear terms are calculated in spectral space.

## 5.2 Governing equations

In Chapter 2, we gave a derivation of the nonlinear equations that describe convection in a rotating plane layer. In this section we recast the equations into a form suitable for solving numerically, though we first restate the original equations, for ease of reference. From equations (2.3.51)-(2.3.53), with  $\mathbf{B} = 0$ , they are

$$\begin{aligned} \frac{\partial \mathbf{u}}{\partial t} + (U + u) \frac{\partial \mathbf{u}}{\partial x} + v \frac{\partial \mathbf{u}}{\partial y} + w \frac{\partial \mathbf{u}}{\partial z} (\mathbf{u}_{BS} + \mathbf{u}) = \\ - Pr \nabla p + Ra Pr \theta \hat{\mathbf{e}}_z - Ta^{\frac{1}{2}} Pr \boldsymbol{\Omega} \times \mathbf{u} + Pr \nabla^2 \mathbf{u}, \end{aligned} \quad (5.2.1)$$

$$\nabla \cdot \mathbf{u} = 0, \quad (5.2.2)$$

$$\frac{\partial \theta}{\partial t} + (U + u) \frac{\partial \theta}{\partial x} + v \frac{\partial \theta}{\partial y} (T_{BS} + \theta) + w \frac{\partial \theta}{\partial z} (T_{BS} + \theta) = \nabla^2 \theta, \quad (5.2.3)$$

and from section 2.3.3, the boundary conditions we impose are as follows:

$$w = 0, \quad \frac{\partial u}{\partial z} = \frac{\partial v}{\partial z} = 0, \quad \theta = 0, \quad \text{on } z = 0, 1. \quad (5.2.4)$$

For all the nonlinear work in this thesis, we restrict ourselves to the two-dimensional system with the rotation vector in the  $y$ - $z$  plane, so that we assume all variations with respect to  $x$  vanish, i.e.,  $\frac{\partial}{\partial x} \equiv 0$ . Under this assumption, the incompressibility condition (5.2.2) becomes  $\frac{\partial v}{\partial y} + \frac{\partial w}{\partial z} = 0$ , this suggests the introduction of a streamfunction  $\psi(y, z)$ , defined by

$$\frac{\partial \psi}{\partial z} = v, \quad \frac{\partial \psi}{\partial y} = -w, \quad (5.2.5)$$

so that  $\nabla^2 \psi = \frac{\partial v}{\partial z} - \frac{\partial w}{\partial y}$  and  $\mathbf{u} = (u, \frac{\partial \psi}{\partial z}, \frac{\partial \psi}{\partial y})$ . The vorticity  $\boldsymbol{\omega}$  is defined by

$$\boldsymbol{\omega} = \nabla \times \mathbf{u} = (\omega, u_z, -u_y), \quad (5.2.6)$$

where  $\omega = w_y - v_z$  is the  $x$ -component of the vorticity. Note our use of a subscript to denote differentiation with respect to that variable. We will interchange this notation with the previously used  $\partial$  notation throughout this chapter. With this definition of  $\omega$ , we have

$$\nabla^2 \psi = -\omega. \quad (5.2.7)$$

Now, consider the  $x$ -component of the curl of (5.2.1)

$$\frac{\partial \omega}{\partial t} + (\mathbf{u} \cdot \nabla) \omega - PrTa^{\frac{1}{2}}(u_y \cos \phi + u_z \sin \phi) = RaPr \frac{\partial \theta}{\partial y} + Pr \nabla^2 \omega, \quad (5.2.8)$$

where we have used

$$\begin{aligned} (\nabla \times (\mathbf{u} \cdot \nabla) \mathbf{u}) \cdot \hat{\mathbf{e}}_x &= (\nabla \times (\nabla(\frac{1}{2} \mathbf{u}^2) - \mathbf{u} \times \boldsymbol{\omega})) \cdot \hat{\mathbf{e}}_x \\ &= -(\nabla \times (\mathbf{u} \times \boldsymbol{\omega})) \cdot \hat{\mathbf{e}}_x \\ &= (-\mathbf{u}(\nabla \cdot \boldsymbol{\omega}) + \boldsymbol{\omega}(\nabla \cdot \mathbf{u}) - (\boldsymbol{\omega} \cdot \nabla) \mathbf{u} + (\mathbf{u} \cdot \nabla) \boldsymbol{\omega}) \cdot \hat{\mathbf{e}}_x \\ &= (\mathbf{u} \cdot \nabla) \omega, \end{aligned} \quad (5.2.9)$$

where the first term on the right-hand side of equation (5.2.9) vanishes by definition of  $\boldsymbol{\omega} = \nabla \times \mathbf{u}$ , the second term on the right-hand side vanishes because of the incompressibility condition, (5.2.2), and the third term on the right-hand side vanishes since we are restricting ourselves to the case when  $\frac{\partial}{\partial x} \equiv 0$ . In deriving equation (5.2.8), we have also used

$$(\nabla \times (\boldsymbol{\Omega} \times \mathbf{u})) \cdot \hat{\mathbf{e}}_x = -u_y \cos \phi - u_z \sin \phi \quad (5.2.10)$$

and

$$(\nabla \times \theta \hat{\mathbf{z}}) \cdot \hat{\mathbf{e}}_x = \frac{\partial \theta}{\partial y}. \quad (5.2.11)$$

For convenience, we write equation (5.2.8) as

$$\frac{\partial \omega}{\partial t} - Pr \nabla^2 \omega = PrTa^{\frac{1}{2}}(\cos \phi u_y + \sin \phi u_z) + RaPr \frac{\partial \theta}{\partial y} + J(\psi, \omega), \quad (5.2.12)$$

where the Jacobian  $J(\psi, \omega)$  is given by

$$J(\psi, \omega) = \left( \frac{\partial \psi}{\partial y} \frac{\partial \omega}{\partial z} - \frac{\partial \psi}{\partial z} \frac{\partial \omega}{\partial y} \right). \quad (5.2.13)$$

Similarly, we can write equation (5.2.3) as

$$\begin{aligned} \frac{\partial \theta}{\partial t} - \nabla^2 \theta &= -(\mathbf{u} \cdot \nabla) \theta + w - vT_y \\ &= J(\psi, \theta) - \frac{\partial \psi}{\partial y} - T_y \frac{\partial \psi}{\partial z}, \end{aligned} \quad (5.2.14)$$

where  $J(\psi, \theta) = \left( \frac{\partial \psi}{\partial y} \frac{\partial \theta}{\partial z} - \frac{\partial \psi}{\partial z} \frac{\partial \theta}{\partial y} \right)$ .

Finally, the  $x$ -component of (5.2.1) gives an equation for  $u$

$$\frac{\partial u}{\partial t} + v \frac{\partial u}{\partial y} + w \frac{dU}{dz} + w \frac{\partial u}{\partial z} + PrTa^{\frac{1}{2}}(\cos \phi w - \sin \phi v) = Pr\nabla^2 u, \quad (5.2.15)$$

which, on substitution for  $v$  and  $w$  in terms of  $\psi$  (from equation (5.2.5)), after rearranging, gives

$$\frac{\partial u}{\partial t} - Pr\nabla^2 u = PrTa^{\frac{1}{2}}(\cos \phi \frac{\partial \psi}{\partial y} + \sin \phi \frac{\partial \psi}{\partial z}) + J(\psi, u) - w \frac{dU}{dz}, \quad (5.2.16)$$

where we recall from equation (2.3.59),  $U = -\frac{T_y Ra}{Ta^{\frac{1}{2}} \sin \phi}$  and  $J(\psi, u)$  is defined in an analogous way to equation (5.2.13). Note that the pressure term is absent as we assume  $\frac{\partial}{\partial x} \equiv 0$ .

So, in summary, the system of equations for nonlinear hydrodynamic convection we wish to solve are

$$\frac{\partial \omega}{\partial t} - Pr\nabla^2 \omega = PrTa^{\frac{1}{2}}(\cos \phi u_y + \sin \phi u_z) + RaPr \frac{\partial \theta}{\partial y} + J(\psi, \omega), \quad (5.2.17)$$

$$\frac{\partial \theta}{\partial t} - \nabla^2 \theta = J(\psi, \theta) - \frac{\partial \psi}{\partial y} - T_y \frac{\partial \psi}{\partial z}, \quad (5.2.18)$$

$$\frac{\partial u}{\partial t} - Pr\nabla^2 u = PrTa^{\frac{1}{2}}(\cos \phi \frac{\partial \psi}{\partial y} + \sin \phi \frac{\partial \psi}{\partial z}) + J(\psi, u) - \frac{\partial \psi}{\partial y} \frac{dU}{dz}, \quad (5.2.19)$$

$$\nabla^2 \psi = -\omega. \quad (5.2.20)$$

### 5.2.1 Boundary conditions

We need to express our boundary conditions, given by (5.2.4), in a form compatible with our vorticity-streamfunction formulation. The first condition,  $w = 0$  on  $z = 0, 1$ , gives us that  $\frac{\partial \psi}{\partial y} = 0$  on  $z = 0, 1$  (using (5.2.5)) and so  $\psi$  is constant along the boundaries, we can choose this constant to be zero. If we now consider a condition for the vorticity,  $\omega = \frac{\partial w}{\partial y} - \frac{\partial v}{\partial z}$ , on the boundaries, then, from (5.2.4), we have  $w = 0$  and  $\frac{\partial v}{\partial z} = 0$  on the boundaries and so  $\omega = 0$  on  $z = 0, 1$ . The condition on  $\theta$  remains the same. Therefore, the boundary conditions in the vorticity-streamfunction formulation are given by

$$\psi = 0, \quad \frac{\partial u}{\partial z} = \frac{\partial v}{\partial z} = 0, \quad \omega = 0, \quad \theta = 0 \quad \text{on } z = 0, 1. \quad (5.2.21)$$

## 5.3 Method of solution

### 5.3.1 Coordinate transformation

To solve our nonlinear governing equations, we use a Fourier-Chebyshev pseudospectral method, as described in section 5.1. This method requires the equations to be defined on  $y' \in [0, 2\pi]$ ,  $z' \in$

$[-1, 1]$ . Currently, as written in dimensionless form, the equations are defined on  $y \in [0, L]$ ,  $z \in [0, 1]$ , where  $L$  is the width of our computational domain in the  $y$ -direction. Therefore, we make linear transformations to map the equations onto the computational domain. These transformations are given by

$$y' = \frac{2\pi}{L}y, \quad z' = 2z - 1.$$

With this, equations (5.2.17)-(5.2.20) become

$$\frac{\partial \omega}{\partial t} - Pr \left( a^2 \frac{\partial^2}{\partial y'^2} + 4 \frac{\partial^2}{\partial z'^2} \right) \omega = F \quad (5.3.22)$$

$$\frac{\partial \theta}{\partial t} - \left( a^2 \frac{\partial^2}{\partial y'^2} + 4 \frac{\partial^2}{\partial z'^2} \right) \theta = G \quad (5.3.23)$$

$$\frac{\partial u}{\partial t} - Pr \left( a^2 \frac{\partial^2}{\partial y'^2} + 4 \frac{\partial^2}{\partial z'^2} \right) u = H \quad (5.3.24)$$

$$\left( a^2 \frac{\partial^2}{\partial y'^2} + 4 \frac{\partial^2}{\partial z'^2} \right) \psi = -\omega \quad (5.3.25)$$

where  $a = \frac{2\pi}{L}$  and

$$F = PrTa^{\frac{1}{2}}(a \cos \phi u_{y'} + 2 \sin \phi u_{z'}) + aRaPr \frac{\partial \theta}{\partial y'} + J'(\psi, \omega), \quad (5.3.26)$$

$$G = J'(\psi, \omega) - a \frac{\partial \psi}{\partial y'} - 2 \frac{\partial \psi}{\partial z'} T_y, \quad (5.3.27)$$

$$H = PrTa^{\frac{1}{2}}(a \cos \phi \psi_{y'} + 2 \sin \phi \psi_{z'}) + J'(\psi, u) - a \frac{\partial \psi}{\partial y'} \frac{T_y Ra}{Ta^{\frac{1}{2}} \sin \phi}, \quad (5.3.28)$$

and we have introduced  $J'(\psi, \xi) = 2a \frac{\partial \psi}{\partial y'} \frac{\partial \xi}{\partial z'} - 2a \frac{\partial \psi}{\partial z'} \frac{\partial \xi}{\partial y'}$ .

### 5.3.2 Fourier Expansion

To solve these equations numerically we use a method that assumes periodicity in the  $y$ -direction and approximates variables as truncated Fourier series in  $y'$ , that is,

$$\omega(y', z', t) = \sum_{m=0}^{N_y-1} \hat{\omega}_m(z', t) e^{imy'} \quad (5.3.29)$$

$$u(y', z', t) = \sum_{m=0}^{N_y-1} \hat{u}_m(z', t) e^{imy'} \quad (5.3.30)$$

$$\theta(y', z', t) = \sum_{m=0}^{N_y-1} \hat{\theta}_m(z', t) e^{imy'} \quad (5.3.31)$$

$$\psi(y', z', t) = \sum_{m=0}^{N_y-1} \hat{\psi}_m(z', t) e^{imy'} \quad (5.3.32)$$

where  $N_y$  is the number of modes we choose in the  $y$ -direction. Note that, whilst  $\omega$ ,  $u$ ,  $\theta$  and  $\psi$  are real,  $\hat{\omega}_m$ ,  $\hat{u}_m$ ,  $\hat{\theta}_m$  and  $\hat{\psi}_m$  may be complex. The numerical grid on which we discretise and solve our equations is uniformly spaced in  $y$ , the nodes are given by

$$y'_k = 2\pi k/N_y, \quad k = 0, 1, \dots, N_y - 1. \quad (5.3.33)$$

On substitution of these Fourier expansions equations (5.3.22)-(5.3.25) become

$$\frac{\partial \hat{\omega}_m}{\partial t} - Pr(4\partial_{zz} - m^2 a^2)\hat{\omega}_m = \hat{F}_m, \quad (5.3.34)$$

$$\frac{\partial \hat{\theta}_m}{\partial t} - (4\partial_{zz} - m^2 a^2)\hat{\theta}_m = \hat{G}_m, \quad (5.3.35)$$

$$\frac{\partial \hat{u}_m}{\partial t} - Pr(4\partial_{zz} - m^2 a^2)\hat{u}_m = \hat{H}_m, \quad (5.3.36)$$

$$(4\partial_{zz} - m^2 a^2)\hat{\psi}_m = -\hat{\omega}_m, \quad (5.3.37)$$

where the exponential terms have cancelled. Note that, for convenience, we have removed the summation over  $m = 0, 1, \dots, N_y - 1$  and also the primes from our computational variables.  $\hat{F}_m$ ,  $\hat{G}_m$  and  $\hat{H}_m$  are the Fourier coefficients of the functions  $F(y, z, t)$ ,  $G(y, z, t)$  and  $H(y, z, t)$  respectively.

The boundary conditions given by equations (5.2.21) become

$$\hat{\omega}_m(\pm 1, t) = \hat{\theta}_m(\pm 1, t) = \frac{\partial \hat{u}_m(\pm 1, t)}{\partial z} = \hat{\psi}_m(\pm 1, t) = 0. \quad (5.3.38)$$

Notice in equations (5.3.34)-(5.3.37),  $y$ -derivatives are simply calculated in Fourier space by multiplying by  $im$  for each derivative. We can see this from

$$\begin{aligned} \frac{\partial \omega}{\partial y}(y, z, t) &= \sum_{m=0}^{N_y-1} \hat{\omega}_m(z, t) \frac{\partial}{\partial y}(e^{imy}) \\ &= \sum_{m=0}^{N_y-1} im\hat{\omega}_m(z, t)(e^{imy}) \\ &= im\omega \end{aligned} \quad (5.3.39)$$

i.e., the Fourier coefficients of  $\frac{\partial \omega}{\partial y}$  are  $im\hat{\omega}_m$ , where  $\hat{\omega}_m$  are the Fourier coefficients of  $\omega$ . It follows that  $\frac{\partial^2 \omega}{\partial y^2} = -m^2\omega$ .

### 5.3.3 Chebyshev expansion

Next, we choose to evaluate the  $z$ -dependence by a Chebyshev series. The Chebyshev polynomials,  $T_n(z)$ , are defined on  $z \in [-1, 1]$  and can be obtained from the following recurrence

relation (see, e.g., Boyd (2001)):

$$T_0(z) = 1, \quad T_1(z) = z, \quad T_{n+1}(z) = 2zT_n(z) - T_{n-1}(z) \quad \text{for } n = 1, 2, \dots \quad (5.3.40)$$

We choose to expand in Chebyshev polynomials in  $z$  because, unlike Fourier series, Chebyshev series avoid the parity mixing in the rotation term of equations (5.2.17) and (5.2.19). In addition, the uneven grid spacing in  $z$  is such that there are more points near the boundaries, which aids with boundary layer resolution.

Assuming a Chebyshev expansion for the  $z$ -dependence of our spectral coefficients, leads to the following:

$$\hat{\omega}_m(z, t) = \sum_{l=1}^{N_z+2} \hat{\omega}_{ml}(t) T_{l-1}(z), \quad (5.3.41)$$

$$\hat{\theta}_m(z, t) = \sum_{l=1}^{N_z+2} \hat{\theta}_{ml}(t) T_{l-1}(z), \quad (5.3.42)$$

$$\hat{u}_m(z, t) = \sum_{l=1}^{N_z+2} \hat{u}_{ml}(t) T_{l-1}(z), \quad (5.3.43)$$

$$\hat{\psi}_m(z, t) = \sum_{l=1}^{N_z+2} \hat{\psi}_{ml}(t) T_{l-1}(z), \quad (5.3.44)$$

for each  $m = 0, 1, \dots, N_y - 1$ .

We sample the expansions (5.3.41)-(5.3.44) at  $N_z$  Chebyshev points given by

$$z_j = \cos \frac{(2j-1)\pi}{2N_z}, \quad j = 1(1)N_z. \quad (5.3.45)$$

In addition to these  $N_z$  interior points, we have our boundary points  $z = \pm 1$ , giving  $N_z + 2$  points in total. This is why our expansions (5.3.41)-(5.3.44) run from  $l = 1$  to  $l = N_z + 2$ .

### **$z$ -derivatives**

Before we proceed with substituting the Chebyshev expansions (5.3.41)-(5.3.44) into the governing equations, we describe how we calculate  $z$ -derivatives. For example, if we need to know

$$\frac{\partial^2}{\partial z^2} \hat{f}_m(z, t) = \frac{\partial^2}{\partial z^2} \sum_{l=1}^{N_z+2} \hat{f}_{ml}(t) T_{l-1}(z),$$

then instead of computing the second derivative of Chebyshev polynomials we could employ a recurrence relation for calculating the coefficients of the derivative expanded in Chebyshev polynomials, i.e.,

$$\frac{\partial^2 \hat{f}_m(z, t)}{\partial z^2} = \sum_{l=1}^{N_z+2} \hat{f}_{ml}^{(2)}(t) T_{l-1}(z). \quad (5.3.46)$$

Such a recurrence relation is described in Boyd (2001) and Peyret (2002) and we outline it now.

If we want the  $q^{th}$  derivative of  $\hat{f}_m$ , then we write

$$\frac{\partial^q \hat{f}_m(z, t)}{\partial z^q} = \sum_{l=1}^{N_z+2} \hat{f}_{ml}^{(q)}(t) T_{l-1}(z)$$

and determine the coefficients  $\hat{f}_{ml}^{(q)}$ , in descending order, using

$$c_{l-2} \hat{f}_{m(l-1)}^{(q)} = e_{l+q} \hat{f}_{m(l+1)}^{(q)} + 2(l-1) \hat{f}_{ml}^{(q-1)} \quad l = N_z + 2, N_z + 1, \dots, 2 \quad (5.3.47)$$

with initial conditions  $\hat{f}_{ml}^{(q)} = 0$  if  $l > N_z + 2 - q$  and

$$c_l = \begin{cases} 2 & \text{if } l = 0 \\ 1 & \text{if } l > 0 \end{cases} \quad e_l = \begin{cases} 1 & \text{if } l \leq N_z + 2 \\ 0 & \text{if } l > N_z + 2. \end{cases} \quad (5.3.48)$$

This method will be useful when calculating derivatives in  $z$ , though we treat 2nd-order derivatives in  $z$  in a different way, as we shall describe now.

There is an alternative way in which we can express the second order  $z$ -derivatives in equations (5.3.34)-(5.3.37). Peyret (2002) details another recurrence relation which connects the coefficients of the second derivative directly to those of the zeroth derivative. Following the derivation given in Peyret, we take the recurrence relation given by (5.3.47) and write it for  $q = 1$  and  $q = 2$ . This gives

$$c_{(l-2)} \hat{f}_{m(l-1)}^{(1)} = e_{l+1} \hat{f}_{m(l+1)}^{(1)} + 2(l-1) \hat{f}_{ml}^{(0)} \quad (5.3.49)$$

$$c_{(l-2)} \hat{f}_{m(l-1)}^{(2)} = e_{l+2} \hat{f}_{m(l+1)}^{(2)} + 2(l-1) \hat{f}_{ml}^{(1)}. \quad (5.3.50)$$

By writing equation (5.3.50) with  $l+1$  and  $l-1$  in place of  $l$ , we can eliminate the first derivative terms from equation (5.3.49), to leave an equation in terms of the coefficients of the zeroth and second derivatives only. To this end, putting  $l+1$  in place of  $l$  in equation (5.3.50) and rearranging gives

$$\hat{f}_{m(l+1)}^{(1)} = \frac{c_{l-1} \hat{f}_{ml}^{(2)} - e_{l+3} \hat{f}_{m(l+2)}^{(2)}}{2l}. \quad (5.3.51)$$

Similarly, equation (5.3.50) with  $l-1$  in place of  $l$  gives

$$\hat{f}_{m(l-1)}^{(1)} = \frac{c_{l-3} \hat{f}_{m(l-2)}^{(2)} - e_{l+1} \hat{f}_{ml}^{(2)}}{2(l-2)}. \quad (5.3.52)$$

Then, substituting equations (5.3.51) and (5.3.52) into (5.3.49) gives

$$c_{l-2} \left( \frac{c_{l-3} \hat{f}_{m(l-2)}^{(2)} - e_{l+1} \hat{f}_{ml}^{(2)}}{2(l-2)} \right) = e_{l+1} \left( \frac{c_{l-1} \hat{f}_{ml}^{(2)} - e_{l+3} \hat{f}_{m(l+2)}^{(2)}}{2l} \right) + 2(l-1) \hat{f}_{ml}^{(0)} \quad (5.3.53)$$

for  $l = 3, 4, \dots, N_z + 2$ . Since (5.3.53) is only valid for  $l \geq 3$ , we have  $c_{l-1} = c_{l-2} = 1$  and  $e_{l+1}e_{l+3} = e_{l+3}$  (from (5.3.48)), for all  $l$ . Using these facts, and expanding (5.3.53), leads to

$$2(l-1)\hat{f}_{ml}^{(0)} = \frac{c_{l-3}\hat{f}_{m(l-2)}^{(2)}}{2(l-2)} - \frac{e_{l+1}\hat{f}_{ml}^{(2)}}{2(l-2)} - \frac{e_{l+1}\hat{f}_{ml}^{(2)}}{2l} + \frac{e_{l+3}\hat{f}_{m(l+2)}^{(2)}}{2l}. \quad (5.3.54)$$

Dividing by  $2(l-2)$  gives an expression for  $\hat{f}_{ml}^{(0)}$

$$\hat{f}_{ml}^{(0)} = \frac{c_{l-3}\hat{f}_{m(l-2)}^{(2)}}{4(l-1)(l-2)} - \frac{e_{l+1}\hat{f}_{ml}^{(2)}(4l-4)}{8l(l-1)(l-2)} + \frac{e_{l+3}\hat{f}_{m(l+2)}^{(2)}}{4l(l-1)}, \quad (5.3.55)$$

which can be written

$$\hat{f}_{ml}^{(0)} = P_l\hat{f}_{m(l-2)}^{(2)} + Q_l\hat{f}_{ml}^{(2)} + R_l\hat{f}_{m(l+2)}^{(2)} \quad \text{for } l = 3, 4, \dots, N_z + 2 \quad (5.3.56)$$

where,

$$P_l = \frac{c_{l-3}}{4(l-1)(l-2)}, \quad Q_l = -\frac{e_{l+1}}{2l(l-2)}, \quad R_l = \frac{e_{l+3}}{4l(l-1)}. \quad (5.3.57)$$

We will use the method just described to express the coefficients of the second derivatives in our equations in terms of coefficients of zeroth derivatives.

### 5.3.4 Application to the problem

Now that we have developed the method we will use, we apply it to our system of equations. First, substitute the Chebyshev expansions (5.3.41)-(5.3.44) into equations (5.3.34)-(5.3.37) to give

$$\frac{\partial \hat{\omega}_{ml}}{\partial t} - Pr(4\hat{\omega}_{ml}^{(2)} - m^2 a^2 \hat{\omega}_{ml}) = \hat{F}_{ml} \equiv E_{ml}^\omega \quad (5.3.58)$$

$$\frac{\partial \hat{\theta}_{ml}}{\partial t} - (4\hat{\theta}_{ml}^{(2)} - m^2 a^2 \hat{\theta}_{ml}) = \hat{G}_{ml} \equiv E_{ml}^\theta \quad (5.3.59)$$

$$\frac{\partial \hat{u}_{ml}}{\partial t} - Pr(4\hat{u}_{ml}^{(2)} - m^2 a^2 \hat{u}_{ml}) = \hat{H}_{ml} \equiv E_{ml}^u \quad (5.3.60)$$

$$4\hat{\psi}_{ml}^{(2)} - m^2 a^2 \hat{\psi}_{ml} = -\hat{\omega}_{ml} \equiv E_{ml}^\psi \quad (5.3.61)$$

where, as described previously,  $\hat{\omega}_{ml}^{(2)}$  etc., are the coefficients of the second derivative of  $\hat{\omega}_m$  when expressed as a Chebyshev series (cf. equation (5.3.46)). Equations (5.3.58)-(5.3.61) are to be solved for  $l = 1, 2, \dots, N_z + 2$  and  $m = 0, 1, \dots, N_y - 1$ .

In order to eliminate the second order derivative coefficients from the equation for  $\omega$  (5.3.58), we form the combination  $P_l E_{m(l-2)}^\omega + Q_l E_{ml}^\omega + R_l E_{m(l+2)}^\omega$  with  $P_l, Q_l, R_l$  as in (5.3.57). This gives,

$$\begin{aligned} & \frac{\partial}{\partial t} [P_l \hat{\omega}_{m(l-2)} + Q_l \hat{\omega}_{ml} + R_l \hat{\omega}_{m(l+2)}] - \\ & Pr \left[ 4(P_l \hat{\omega}_{m(l-2)}^{(2)} + Q_l \hat{\omega}_{ml}^{(2)} + R_l \hat{\omega}_{m(l+2)}^{(2)}) - m^2 a^2 (P_l \hat{\omega}_{m(l-2)} + Q_l \hat{\omega}_{ml} + R_l \hat{\omega}_{m(l+2)}) \right] = \\ & P_l \hat{F}_{m(l-2)} + Q_l \hat{F}_{ml} + R_l \hat{F}_{m(l+2)}. \end{aligned} \quad (5.3.62)$$

Now, equation (5.3.56) gives  $P_l \hat{\omega}_{m(l-2)}^{(2)} + Q_l \hat{\omega}_{ml}^{(2)} + R_l \hat{\omega}_{m(l+2)}^{(2)} = \hat{\omega}_{ml}$ , which we use to eliminate any second derivative coefficients to obtain

$$\begin{aligned} & \frac{\partial}{\partial t} [P_l \hat{\omega}_{m(l-2)} + Q_l \hat{\omega}_{ml} + R_l \hat{\omega}_{m(l+2)}] - \\ & Pr [4\hat{\omega}_{ml} - m^2 a^2 (P_l \hat{\omega}_{m(l-2)} + Q_l \hat{\omega}_{ml} + R_l \hat{\omega}_{m(l+2)})] = P_l \hat{F}_{m(l-2)} + Q_l \hat{F}_{ml} + R_l \hat{F}_{m(l+2)}. \end{aligned} \quad (5.3.63)$$

In an analogous way, we form the appropriate combinations to remove the second derivative coefficients from the equations for  $\hat{\theta}$ ,  $\hat{u}$  and  $\hat{\psi}$ , (5.3.59)-(5.3.61). This gives for  $\hat{\theta}_{ml}$ ,

$$\begin{aligned} & \frac{\partial}{\partial t} [P_l \hat{\theta}_{m(l-2)} + Q_l \hat{\theta}_{ml} + R_l \hat{\theta}_{m(l+2)}] - \\ & [4\hat{\theta}_{ml} - m^2 a^2 (P_l \hat{\theta}_{m(l-2)} + Q_l \hat{\theta}_{ml} + R_l \hat{\theta}_{m(l+2)})] = P_l \hat{G}_{m(l-2)} + Q_l \hat{G}_{ml} + R_l \hat{G}_{m(l+2)}, \end{aligned} \quad (5.3.64)$$

for  $\hat{u}_{ml}$ ,

$$\begin{aligned} & \frac{\partial}{\partial t} [P_l \hat{u}_{m(l-2)} + Q_l \hat{u}_{ml} + R_l \hat{u}_{m(l+2)}] - \\ & Pr [4\hat{u}_{ml} - m^2 a^2 (P_l \hat{u}_{m(l-2)} + Q_l \hat{u}_{ml} + R_l \hat{u}_{m(l+2)})] = P_l \hat{H}_{m(l-2)} + Q_l \hat{H}_{ml} + R_l \hat{H}_{m(l+2)}, \end{aligned} \quad (5.3.65)$$

and for  $\hat{\psi}_{ml}$ ,

$$- [4\hat{\psi}_{ml} - m^2 a^2 (P_l \hat{\psi}_{m(l-2)} + Q_l \hat{\psi}_{ml} + R_l \hat{\psi}_{m(l+2)})] = P_l \hat{\omega}_{m(l-2)} + Q_l \hat{\omega}_{ml} + R_l \hat{\omega}_{m(l+2)}. \quad (5.3.66)$$

### Boundary conditions

Expanding in Chebyshev polynomials means our boundary conditions (5.3.38) become

$$\hat{\omega}_m(\pm 1, t) = \sum_{l=1}^{N_z+2} \hat{\omega}_{ml}(t) T_{l-1}(\pm 1) = \sum_{l=1}^{N_z+2} (\pm 1)^{l-1} \hat{\omega}_{ml}(t) = 0, \quad (5.3.67)$$

$$\hat{\theta}_m = \sum_{l=1}^{N_z+2} (\pm 1)^{l-1} \hat{\theta}_{ml}(t) = 0, \quad (5.3.68)$$

$$\frac{\partial \hat{u}_m}{\partial z} = \sum_{l=1}^{N_z+2} (\pm 1)^{l-1} \hat{u}_{ml}^{(1)}(t) = \sum_{l=1}^{N_z+2} 2(\pm 1)^l (l-1)^2 \hat{u}_{ml}(t) = 0, \quad (5.3.69)$$

$$\hat{\psi}_m = \sum_{l=1}^{N_z+2} (\pm 1)^{l-1} \hat{\psi}_{ml}(t) = 0. \quad (5.3.70)$$

where we have used  $T_n(\pm 1) = (\pm 1)^n$  for all  $n$ , and  $\frac{dT_n}{dz}(\pm 1) = (\pm 1)^l n^2$  for all  $n$  (Boyd (2001)).

### 5.3.5 A note on calculating spectral coefficients

As discussed, we compute derivatives in spectral space, but little has been said on the transform that takes the variables to spectral space. The transform uses a Discrete Fourier Transform (DFT) in the  $y$  direction and a Discrete Cosine Transform (DCT) in the  $z$  direction (see Peyret (2002)). To perform this transform, we take the variable in question, for example,

$$\omega(y, z, t) = \sum_{l=1}^{N_z} \sum_{m=0}^{N_y-1} \hat{\omega}_{ml}(t) T_{l-1}(z) e^{imy} \quad (5.3.71)$$

and sample this variable on our discrete grid given by (5.3.33) and (5.3.45) to give

$$\omega(y_k, z_j, t) = \sum_{l=1}^{N_z+2} \sum_{m=0}^{N_y-1} \hat{\omega}_{ml}(t) T_{l-1}(z_j) e^{\frac{2\pi imk}{N_y}} \quad (5.3.72)$$

or

$$\omega(y_k, z_j, t) = \sum_{l=1}^{N_z} \sum_{m=0}^{N_y-1} \hat{\omega}_{ml}(t) \cos\left(\frac{(2j-1)(l-1)\pi}{2N_z}\right) e^{\frac{2\pi imk}{N_y}}, \quad (5.3.73)$$

where we have used the relation  $T_{l-1}(\cos \alpha) = \cos[(l-1)\alpha]$ . The spectral coefficients  $\hat{\omega}_{ml}$  can then be obtained by taking an DFT in  $y$  and a DCT in  $z$ . This last representation highlights why we use a cosine transform; Canuto *et al.* (1993), Brachet *et al.* (1983), Boyd (2001) detail how an efficient DCT can be computed using FFTs. This is the approach we implement in our numerical code but we use efficient DFT and DCT routines available in FFTW library (see Frigo & Johnson (2012)).

### 5.3.6 Nonlinear terms

Our governing equations, (5.3.22)-(5.3.25), and method of solution require us to compute the spectral coefficients of functions  $F, G, H$ , which contain the nonlinear terms. The general method for calculating these is outlined here: we first transform the variables to spectral space, where we perform differentiation in  $y$  or  $z$  as required. We then use an inverse transform to move the spectral coefficients back to real space and it is in real space where we perform the multiplication of terms to form the nonlinear products. Once we have the nonlinear products, we once again transform to spectral space and then solve the appropriate equation. This has to be done at every time step, it is therefore the most computationally demanding part of our routine.

### 5.3.7 Dealiasing

On a finite grid when the spacing between grid points is  $\Delta x$ , the shortest wavelength resolved is  $\lambda = 2\Delta x$  and therefore the maximum wavenumber is  $k_{\max} = \frac{\pi}{\Delta x}$ . Thus, high frequencies

become too small to be resolved and instead they are aliased to a smaller frequency. High frequencies are generated by nonlinear terms and aliasing causes energy transfer from high frequencies to low frequencies which can lead to instability in the numerical scheme. Orszag (1971) showed that removing the upper third of wavenumbers solved the problem of aliasing when the nonlinearities are quadratic. This is the approach we take to avoid the aliasing instability, it is easily implemented by setting the coefficients corresponding to the highest one third of frequencies to zero in Fourier space, before transforming to physical space.

### 5.3.8 Time stepping

To advance the solution in time we use a semi-implicit, predictor-corrector time stepping scheme. This involves using the Crank-Nicolson (CN) scheme on the left hand side and the second-order Adams-Bashforth (AB2) scheme for the right hand side, we will refer to this combination as the CN-AB2 scheme. These schemes are detailed in e.g., Boyd (2001). For an ODE,  $\frac{du}{dt} = F(u, t)$ , the Crank-Nicolson scheme is given by

$$\frac{u^{n+1} - u^n}{\Delta t} = \frac{F^{n+1} + F^n}{2}, \quad (5.3.74)$$

where  $\Delta t$  is the size of the time step and  $u^n = u(n\Delta t)$ . This is an implicit scheme as it requires the value of  $u^{n+1}$  to be used in the calculation of  $F^{n+1}$ , whereas the Adam-Bashforth scheme is explicit and is given by

$$\frac{u^{n+1} - u^n}{\Delta t} = \frac{3F^n - F^{n-1}}{2}. \quad (5.3.75)$$

It is computationally expensive to treat nonlinear terms implicitly and so this explicit scheme is suited to the right hand sides of our equations (as they contain the nonlinear terms). Our equations take the form

$$\frac{\partial V}{\partial t} + f = F, \quad (5.3.76)$$

where  $V$  represents either  $\omega$ ,  $\theta$  or  $u$ ,  $f$  contains the diffusive terms and all nonlinear terms are contained in  $F$ . So, implementing a scheme that uses CN for the left-hand side and AB2 for the right-hand side, we have

$$\frac{V^{n+1} - V^n}{\Delta t} + \frac{f^{n+1} + f^n}{2} = \frac{3F^n - F^{n-1}}{2}. \quad (5.3.77)$$

Note, for the first time step, we do not know  $F$  at an earlier time step and so to initialise the scheme we take  $F^{n-1} = F^n$  when  $n = 1$ ; this amounts to doing a forward Euler step for the first time step, and AB2 thereafter. The predictor-corrector process works by forming a 'predicted'

value for the solution,  $V_p^{n+1}$ , by solving

$$\frac{V_p^{n+1} - V^n}{\Delta t} + \frac{f_p^{n+1} + f^n}{2} = \frac{3F^n - F^{n-1}}{2}. \quad (5.3.78)$$

The predicted value is then used to calculate  $F_p^{n+1}$ , i.e., the right-hand side of (5.3.76) evaluated at the predicted values. An average of this and the original  $F^n$  is then taken, in a trapezoidal rule, to give  $F_c^{n+1} = \frac{F^n + F_p^{n+1}}{2}$ .  $F_c^{n+1}$  is then used as the right-hand side for the corrector step

$$\frac{V_c^{n+1} - V^n}{\Delta t} + \frac{f_c^{n+1} + f^n}{2} = F_c^{n+1}, \quad (5.3.79)$$

where  $V_c^{n+1}$  is the corrected solution at the  $n + 1$ st level.

The predicted and corrected values are compared and if

$$\frac{|V_p^{n+1} - V_c^{n+1}|}{|V_c^{n+1}|} \leq \epsilon \text{ then we take } V^{n+1} = V_c^{n+1}, \quad (5.3.80)$$

where  $\epsilon$  is a specified tolerance. If the condition is not satisfied, the original values are restored and the time step is decreased (typically halved), and the process starts again. When  $V^{n+1} = V_c^{n+1}$  then we can proceed to the next time step. If solutions are within a specified value then the time step is increased (typically by a factor of  $\sqrt{2}$ ) for the next iteration.

### 5.3.9 Application of the time stepping method

Applying the CN-AB2 method described in section 5.3.8 to our equations (5.3.63)-(5.3.65) gives the following system of equations. Note, we give details for the equation for  $\omega$  and just state the others as they arise in an analogous way. The CN-AB2 scheme for the equation for  $\omega$ , (5.3.63), is given by

$$\begin{aligned} & P_l \hat{\omega}_{m(l-2)}^{n+1} + Q_l \hat{\omega}_{ml}^{n+1} + R_l \hat{\omega}_{m(l+2)}^{n+1} \\ & - (P_l \hat{\omega}_{m(l-2)}^n + Q_l \hat{\omega}_{ml}^n + R_l \hat{\omega}_{m(l+2)}^n) - \frac{Pr \Delta t}{2} (4\hat{\omega}_{ml}^{n+1} + 4\hat{\omega}_{ml}^n) \\ & + \frac{Pr \Delta t m^2 a^2}{2} \left[ P_l \hat{\omega}_{m(l-2)}^{n+1} + Q_l \hat{\omega}_{ml}^{n+1} + R_l \hat{\omega}_{m(l+2)}^{n+1} + P_l \hat{\omega}_{m(l-2)}^n + Q_l \hat{\omega}_{ml}^n + R_l \hat{\omega}_{m(l+2)}^n \right] \\ & = \frac{\Delta t}{2} \left[ 3P_l \hat{F}_{m(l-2)}^n + 3Q_l \hat{F}_{ml}^n + 3R_l \hat{F}_{m(l+2)}^n - (P_l \hat{F}_{m(l-2)}^{n-1} + Q_l \hat{F}_{ml}^{n-1} + R_l \hat{F}_{m(l+2)}^{n-1}) \right], \end{aligned} \quad (5.3.81)$$

which, on collecting terms at the  $n + 1$ st level on the left-hand side and terms at the  $n$ th level on the right-hand side, gives

$$\begin{aligned}
& P_l \hat{\omega}_{m(l-2)}^{n+1} \left(1 + \frac{Pr \Delta t m^2 a^2}{2}\right) + [Q_l \left(1 + \frac{Pr \Delta t m^2 a^2}{2}\right) - 2Pr \Delta t] \hat{\omega}_{ml}^{n+1} + \\
& R_l \left(1 + \frac{Pr \Delta t m^2 a^2}{2}\right) \hat{\omega}_{m(l+2)}^{n+1} = P_l \left(1 - \frac{Pr \Delta t m^2 a^2}{2}\right) \hat{\omega}_{m(l-2)}^n + \\
& [Q_l \left(1 - \frac{Pr \Delta t m^2 a^2}{2}\right) + 2Pr \Delta t] \hat{\omega}_{ml}^n + R_l \left(1 - \frac{Pr \Delta t m^2 a^2}{2}\right) \hat{\omega}_{m(l+2)}^n \\
& + \frac{3\Delta t}{2} \left[ P_l \hat{F}_{m(l-2)}^n + Q_l \hat{F}_{ml}^n + R_l \hat{F}_{m(l+2)}^n \right] - \frac{\Delta t}{2} \left( P_l \hat{F}_{m(l-2)}^{n-1} + Q_l \hat{F}_{ml}^{n-1} + R_l \hat{F}_{m(l+2)}^{n-1} \right),
\end{aligned} \tag{5.3.82}$$

which has to be solved for  $m = 0, 1, \dots, N_y - 1$  and  $l = 3, 4, \dots, N_z + 2$ .

The equations for  $\hat{\theta}$  is similar

$$\begin{aligned}
& P_l \hat{\theta}_{m(l-2)}^{n+1} \left(1 + \frac{\Delta t m^2 a^2}{2}\right) + [Q_l \left(1 + \frac{\Delta t m^2 a^2}{2}\right) - 2\Delta t] \hat{\theta}_{ml}^{n+1} + R_l \left(1 + \frac{\Delta t m^2 a^2}{2}\right) \hat{\theta}_{m(l+2)}^{n+1} = \\
& P_l \left(1 - \frac{\Delta t m^2 a^2}{2}\right) \hat{\theta}_{m(l-2)}^n + [Q_l \left(1 - \frac{\Delta t m^2 a^2}{2}\right) + 2\Delta t] \hat{\theta}_{ml}^n + R_l \left(1 - \frac{\Delta t m^2 a^2}{2}\right) \hat{\theta}_{m(l+2)}^n + \\
& \frac{3\Delta t}{2} \left[ P_l \hat{G}_{m(l-2)}^n + Q_l \hat{G}_{ml}^n + R_l \hat{G}_{m(l+2)}^n \right] - \frac{\Delta t}{2} \left( P_l \hat{G}_{m(l-2)}^{n-1} + Q_l \hat{G}_{ml}^{n-1} + R_l \hat{G}_{m(l+2)}^{n-1} \right),
\end{aligned} \tag{5.3.83}$$

as is the equation for  $\hat{u}$

$$\begin{aligned}
& P_l \hat{u}_{m(l-2)}^{n+1} \left(1 + \frac{Pr \Delta t m^2 a^2}{2}\right) + [Q_l \left(1 + \frac{Pr \Delta t m^2 a^2}{2}\right) - 2Pr \Delta t] \hat{u}_{ml}^{n+1} + \\
& R_l \left(1 + \frac{Pr \Delta t m^2 a^2}{2}\right) \hat{u}_{m(l+2)}^{n+1} = P_l \left(1 - \frac{Pr \Delta t m^2 a^2}{2}\right) \hat{u}_{m(l-2)}^n + \\
& [Q_l \left(1 - \frac{Pr \Delta t m^2 a^2}{2}\right) + 2Pr \Delta t] \hat{u}_{ml}^n + R_l \left(1 - \frac{Pr \Delta t m^2 a^2}{2}\right) \hat{u}_{m(l+2)}^n + \\
& \frac{3\Delta t}{2} \left[ P_l \hat{H}_{m(l-2)}^n + Q_l \hat{H}_{ml}^n + R_l \hat{H}_{m(l+2)}^n \right] - \frac{\Delta t}{2} \left( P_l \hat{H}_{m(l-2)}^{n-1} + Q_l \hat{H}_{ml}^{n-1} + R_l \hat{H}_{m(l+2)}^{n-1} \right).
\end{aligned} \tag{5.3.84}$$

We obtain  $\hat{\psi}_{ml}$  at the  $n + 1$ st step by solving  $\hat{\omega}_{ml}^{n+1} = -\nabla^2 \hat{\psi}_{ml}^{n+1}$ . From equation (5.3.66), at the  $n + 1$ st step, we have

$$\begin{aligned}
& P_l \hat{\omega}_{m(l-2)}^{n+1} + Q_l \hat{\omega}_{ml}^{n+1} + R_l \hat{\omega}_{m(l+2)}^{n+1} = \\
& -4\hat{\psi}_{ml}^{n+1} + m^2 a^2 \left( P_l \hat{\psi}_{m(l-2)}^{n+1} + Q_l \hat{\psi}_{ml}^{n+1} + R_l \hat{\psi}_{m(l+2)}^{n+1} \right).
\end{aligned} \tag{5.3.85}$$

It is clear from equations (5.3.82)-(5.3.85) that we have two uncoupled systems, one for the odd coefficients and one for the even coefficients.

In order to find the corresponding boundary conditions we take the current two conditions (from equations (5.3.67))

$$\sum_{l=1}^{N_z+2} \hat{\omega}_{ml}(t) = 0 \text{ at } z = 1, \tag{5.3.86}$$

$$\sum_{l=1}^{N_z+2} (-1)^{l-1} \hat{\omega}_{ml}(t) = 0 \text{ at } z = -1 \quad (5.3.87)$$

and add them together to obtain an equation involving the odd coefficients only. Similarly, subtracting one from the other provides an equation for the even coefficients. We now have two systems complete with boundary conditions which we can represent in matrix form, i.e.,

$$CL_{odd}^{\omega} \hat{\omega}_{m,odd}^{n+1} = CR_{odd}^{\omega} \hat{\omega}_{m,odd}^n + \frac{\Delta t}{2} C_{odd} (3\hat{\mathbf{F}}_{m,odd}^n - \hat{\mathbf{F}}_{m,odd}^{n-1}) \quad (5.3.88)$$

$$CL_{even}^{\omega} \hat{\omega}_{m,even}^{n+1} = CR_{even}^{\omega} \hat{\omega}_{m,even}^n + \frac{\Delta t}{2} C_{even} (3\hat{\mathbf{F}}_{m,even}^n - \hat{\mathbf{F}}_{m,even}^{n-1}) \quad (5.3.89)$$

where  $\omega_{m,odd}^{n+1}$  represents the odd entries of  $\omega$ ,  $\omega_{m,even}^{n+1}$  represents the even entries of  $\omega$  and we have used a similar notation for  $F$ . We also have that  $CL_{odd}^{\omega}, CR_{odd}^{\omega}, CL_{even}^{\omega}, CR_{even}^{\omega}, C_{odd}$  and  $C_{even}$  are all of the form

$$\begin{pmatrix} a & a & a & \cdots & \cdots & a \\ \ddots & \ddots & \ddots & 0 & \cdots & \vdots \\ 0 & \ddots & \ddots & \ddots & 0 & \vdots \\ \vdots & 0 & \tilde{P}_l & \tilde{Q}_l & \tilde{R}_l & 0 \\ \vdots & \vdots & 0 & \ddots & \ddots & \ddots \\ 0 & \cdots & \cdots & 0 & \ddots & \ddots \end{pmatrix} \quad (5.3.90)$$

where

$$a = \begin{cases} 1 & \text{for } CL_{odd}^{\omega} \\ -1 & \text{for } CL_{even}^{\omega} \\ 0 & \text{for } CR_{odd}^{\omega}, CR_{even}^{\omega}, C_{odd}, C_{even}, \end{cases}$$

with those matrices denoted  $_{odd}$ , formed when  $l = 3, 5, \dots, N_z + 1$ , and those denoted  $_{even}$

formed when  $l = 4, 6, \dots, N_z + 2$ . The diagonals  $\tilde{P}_l$ ,  $\tilde{Q}_l$  and  $\tilde{R}_l$  are given by

$$\tilde{P}_l = \begin{cases} (1 + \frac{Pr\Delta tm^2 a^2}{2})P_l & \text{for } CL_{odd}^\omega, CL_{even}^\omega \\ (1 - \frac{Pr\Delta tm^2 a^2}{2})P_l & \text{for } CR_{odd}^\omega, CR_{even}^\omega \\ P_l & \text{for } C_{odd}, C_{even} \end{cases} \quad (5.3.91)$$

$$\tilde{Q}_l = \begin{cases} (1 + \frac{Pr\Delta tm^2 a^2}{2})Q_l - 2Pr\Delta t & \text{for } CL_{odd}^\omega, CL_{even}^\omega \\ (1 - \frac{Pr\Delta tm^2 a^2}{2})Q_l + 2Pr\Delta t & \text{for } CR_{odd}^\omega, CR_{even}^\omega \\ Q_l & \text{for } C_{odd}, C_{even} \end{cases} \quad (5.3.92)$$

$$\tilde{R}_l = \begin{cases} (1 + \frac{Pr\Delta tm^2 a^2}{2})R_l & \text{for } CL_{odd}^\omega, CL_{even}^\omega \\ (1 - \frac{Pr\Delta tm^2 a^2}{2})R_l & \text{for } CR_{odd}^\omega, CR_{even}^\omega \\ R_l & \text{for } C_{odd}, C_{even}. \end{cases} \quad (5.3.93)$$

The corresponding matrix equations for the equations for  $\hat{\theta}$ ,  $\hat{u}$  and  $\hat{\psi}$ , (5.3.83)-(5.3.85), are given by:

$$CL^\theta \hat{\theta}_m^{n+1} = CR^\theta \hat{\theta}_m^n + \frac{\Delta t}{2} C(3\hat{G}_m^n - \hat{G}_m^{n-1}), \quad (5.3.94)$$

$$CL^u \hat{u}_m^{n+1} = CR^u \hat{u}_m^n + \frac{\Delta t}{2} C(3\hat{H}_m^n - \hat{H}_m^{n-1}), \quad (5.3.95)$$

$$CL^\psi \hat{\psi}_m^{n+1} = C\hat{\omega}_m^{n+1}, \quad (5.3.96)$$

for both the odd and the even coefficients.

For the equation for  $\hat{\theta}$ , (5.3.94), all matrices are the same as those in (5.3.88) and (5.3.89) except with any  $Pr$  factors set to one.

For the  $\hat{u}$  equation, (5.3.95), the only change from the matrices in (5.3.88) and (5.3.89) is the top row due to the boundary condition, it is now given by

$$a = \begin{cases} 2(l-1)^2 & l = 1, 3, \dots, N_z + 1 & \text{for } CL_{odd}^u \\ 2(l-1)^2 & l = 2, 4, \dots, N_z + 2 & \text{for } CL_{even}^u. \end{cases}$$

The equation for  $\hat{\psi}$ , (5.3.96), takes a slightly different form, in this case we have

$$a = \begin{cases} 1 & \text{for } CL_{odd}^{\psi} \\ -1 & \text{for } CL_{even}^{\psi} \end{cases} \quad (5.3.97)$$

$$\tilde{P}_l = m^2 a^2 P_l \quad \text{for } CL_{odd}^{\psi}, CL_{even}^{\psi} \quad (5.3.98)$$

$$\tilde{Q}_l = (-4 + m^2 a^2) Q_l \quad \text{for } CL_{odd}^{\psi}, CL_{even}^{\psi} \quad (5.3.99)$$

$$\tilde{R}_l = m^2 a^2 R_l \quad \text{for } CL_{odd}^{\psi}, CL_{even}^{\psi}. \quad (5.3.100)$$

We state again that, these matrix equations must be solved over all wavenumbers  $m = 0, 1, \dots, N_y - 1$ . The right-hand side of equations (5.3.88), (5.3.94)-(5.3.96) are known vectors of size  $N_z + 2$ . Notice all of matrices on the left-hand side of the equations are quasi-tridiagonal, that is, they consist of nonzero entries down the main diagonal and the sub and super diagonals and one nonzero row, the top row. The remaining entries of the matrices are filled with zeros, this is a fact that we should exploit for more efficient matrix inversion. Naive inversions of the matrices take typically  $O(N_z^3)$  operations for each inversion. Peyret (2002) details an algorithm, developed by Thual (1986), which leads to an operation count that is  $O(N_z)$ . This algorithm is an extension of LU decomposition, we describe it in the next section as it is the algorithm we use in our code.

### 5.3.10 Thual algorithm

We will detail how to solve the matrix system of equations involving the quasi-diagonal matrices, given by (5.3.88) and (5.3.89). The algorithm used was developed by Thual (1986) and is well documented in Peyret (2002). To demonstrate the algorithm we will consider the equation for  $\omega_{odd}$ , but the algorithm can be applied in an analogous way to the other equations. We have

$$CL_{odd}^{\omega} \hat{\omega}_{m,odd}^{n+1} = CR_{odd}^{\omega} \hat{\omega}_{m,odd}^n + \frac{\Delta t}{2} C_{odd} (3\hat{F}_{m,odd}^n - \hat{F}_{m,odd}^{n-1}). \quad (5.3.101)$$

As explained before, the right-hand side is known and amounts to a vector, which for simplicity we will denote by  $\mathcal{F}_{odd}$ , and so we have

$$CL_{odd}^{\omega} \hat{\omega}_{m,odd}^{n+1} = \mathcal{F}_{odd} \quad (5.3.102)$$

or, using (5.3.88) and (5.3.90),

$$\tilde{P}_l \hat{\omega}_{l-2} + \tilde{Q}_l \hat{\omega}_l + \tilde{R}_l \hat{\omega}_{l+2} = \mathcal{F}_l, \quad l = 3, 5, \dots, N_z - 1, \quad (5.3.103)$$

where, for brevity, we have removed the 'odd' label, the  $m$  label and the  $n + 1$  label. In addition, we have

$$\tilde{P}_l \hat{w}_{l-2} + \tilde{Q}_l \hat{w}_l = \mathcal{F}_l, \text{ when } l = N_z + 1. \quad (5.3.104)$$

To make the tridiagonal nature of this problem clear, we introduce notation consistent with that used in Peyret (2002):

$$(p_l, q_l, r_l, f_l) = (\tilde{P}_{2l-1}, \tilde{Q}_{2l-1}, \tilde{R}_{2l-1}, \tilde{F}_{2l-1}) \quad \text{for } l = 2, 3, \dots, \frac{N_z + 2}{2} \quad (5.3.105)$$

$$w_l = \hat{w}_{2l-1} \quad \text{for } l = 1, 2, \dots, \frac{N_z + 2}{2}. \quad (5.3.106)$$

This gives, on substitution into (5.3.103) and (5.3.104),

$$p_l w_{l-1} + q_l w_l + r_l w_{l+1} = f_l \quad \text{for } l = 2, 3, \dots, \frac{N_z}{2}, \quad (5.3.107)$$

$$p_l w_{l-1} + q_l w_l = f_l \quad \text{for } l = \frac{N_z + 2}{2} \quad (5.3.108)$$

and

$$\sum_{l=1}^{\frac{N_z+2}{2}} a_l w_l = g. \quad (5.3.109)$$

For the  $\omega_{odd}$  boundary condition, equation (5.3.86) gives,  $a_n = 1$  for all  $n$ , and  $g = 0$ , but for the purposes of demonstrating this algorithm we will leave them as  $a$  and  $g$  until the end. The solution uses the recurrence formula

$$w_{l+1} = X_l w_l + Y_l \quad \text{for } l = 1, 2, \dots, \frac{N_z}{2}. \quad (5.3.110)$$

Next, we eliminate  $w_{l+1}$  from (5.3.107) using (5.3.110) to give

$$p_l w_{l-1} + w_l (q_l + r_l X_l) = f_l - r_l Y_l \quad (5.3.111)$$

and hence

$$w_l = \frac{f_l - r_l Y_l}{q_l + r_l X_l} - \frac{p_l w_{l-1}}{q_l + r_l X_l}. \quad (5.3.112)$$

Now consider (5.3.110), written with  $l - 1$  in place of  $l$ :

$$w_l = X_{l-1} w_{l-1} + Y_{l-1}. \quad (5.3.113)$$

Comparing (5.3.111) and (5.3.113) gives

$$X_{l-1} = -\frac{p_l}{q_l + r_l X_l}, \quad l = \frac{N_z}{2}, \frac{N_z}{2} - 1, \dots, 2, \quad (5.3.114)$$

$$Y_{l-1} = \frac{f_l - r_l Y_l}{q_l + r_l X_l}, \quad l = \frac{N_z}{2}, \frac{N_z}{2} - 1, \dots, 2. \quad (5.3.115)$$

These are computed in reverse order, starting from  $l = \frac{N_z}{2}$ . Hence we require  $X_{\frac{N_z}{2}}$  and  $Y_{\frac{N_z}{2}}$  to start the iteration procedure. We obtain these starting values as follows: equation (5.3.108) gives

$$\begin{aligned} p_{\frac{N_z+2}{2}} w_{\frac{N_z}{2}} + q_{\frac{N_z+2}{2}} w_{\frac{N_z+2}{2}} &= f_{\frac{N_z+2}{2}} \\ \Rightarrow w_{\frac{N_z+2}{2}} &= \frac{f_{\frac{N_z+2}{2}} - p_{\frac{N_z+2}{2}} w_{\frac{N_z}{2}}}{q_{\frac{N_z+2}{2}}} \end{aligned} \quad (5.3.116)$$

and (5.3.110), with  $l = \frac{N_z}{2}$ , gives

$$w_{\frac{N_z+2}{2}} = X_{\frac{N_z}{2}} w_{\frac{N_z}{2}} + Y_{\frac{N_z}{2}}. \quad (5.3.117)$$

Comparing (5.3.116) and (5.3.117) yields

$$X_{\frac{N_z}{2}} = -\frac{p_{\frac{N_z+2}{2}}}{q_{\frac{N_z+2}{2}}}, \quad Y_{\frac{N_z}{2}} = \frac{f_{\frac{N_z+2}{2}}}{q_{\frac{N_z+2}{2}}}. \quad (5.3.118)$$

We now know  $X_l, Y_l$  for  $l = 1, 2, \dots, \frac{N_z}{2}$  and so (5.3.110) can be used to find  $w_l$  for  $l = 2, 3, \dots, \frac{N_z+2}{2}$  provided  $w_1$  is known. We calculate  $w_1$  from (5.3.109). (5.3.113) allows us to write  $w_2, \dots, w_{\frac{N_z+2}{2}}$  in terms of  $w_1$  by

$$w_l = \alpha_l w_1 + \beta_l \quad l = 1, 2, \dots, \frac{N_z+2}{2}. \quad (5.3.119)$$

When  $l = 1$ , we get  $w_1 = \alpha_1 w_1 + \beta_1$ , i.e.,  $\alpha_1 = 1, \beta_1 = 0$ .

Next, we formulate a recurrence relation for  $\alpha_l, \beta_l$ . This is done by considering (5.3.113) and (5.3.119) written for  $l - 1$ , i.e.,

$$w_{l-1} = \alpha_{l-1} w_1 + \beta_{l-1}.$$

This can be used to eliminate  $w_{l-1}$  from (5.3.113) to give

$$w_l = X_{l-1}(\alpha_{l-1} w_1 + \beta_{l-1}) + Y_{l-1}.$$

Comparing this with (5.3.119) yields

$$\alpha_l = X_{l-1} \alpha_{l-1} \quad l = 2, 3, \dots, \frac{N_z+2}{2}, \quad (5.3.120)$$

$$\beta_l = X_{l-1} \beta_{l-1} + Y_{l-1} \quad l = 2, 3, \dots, \frac{N_z+2}{2}. \quad (5.3.121)$$

Now, (5.3.109) and (5.3.119) combine to give

$$\begin{aligned} \sum_{l=1}^{\frac{N_z+2}{2}} a_l (\alpha_l w_1 + \beta_l) &= g \\ \Rightarrow w_1 &= \frac{g - \sum_{l=1}^{\frac{N_z+2}{2}} a_l \beta_l}{\sum_{l=1}^{\frac{N_z+2}{2}} a_l \alpha_l}. \end{aligned} \quad (5.3.122)$$

So, to summarise the algorithm:

- Calculate  $X_l, Y_l$  ( $l = 1, 2, \dots, \frac{N_z}{2}$ ) from (5.3.114) and (5.3.115)
- Calculate  $\alpha_l, \beta_l$  ( $l = 1, 2, \dots, \frac{N_z+2}{2}$ ) from (5.3.120) and (5.3.121)
- Calculate  $w_1$  from (5.3.122)
- Calculate  $w_l$  ( $l = 2, 3, \dots, \frac{N_z+2}{2}$ ) from (5.3.110)

This algorithm was detailed using the equation for  $\omega_{odd}$  as an example, but it is suitable for all our quasi-tridiagonal systems in section 5.3.9, and is our method of choice to solve our matrix equations.

## 5.4 Testing the code

Before applying our code to the particular problems we wish to solve, we tested it against the published results of Veronis (1968) and Moore & Weiss (1973). The former of these studies considered nonlinear convection rotating about a vertical axis, therefore, in order to test against their work, we set  $\phi = \frac{\pi}{2}$  and try to reproduce some of the results. The latter study concerns non-rotating convection and so could be used to check our code in the limit  $Ta \rightarrow 0$ . In both cases, for a range of  $Ra$  and  $Pr$ , the Nusselt number was calculated (see section 5.5 for a definition) and for the same input parameters, we were able to calculate the same Nusselt number. For the highest  $Ra$  tested we differed slightly from the published results but we believe this is due to the higher resolution we were able to achieve with our more modern code.

To test the terms resulting from the tilted rotation vector, we calculated the growth rate of solutions with  $\phi \neq \frac{\pi}{2}$  and compared it with the expected growth rate as calculated by our linear code described in Chapter 3. As the rotation terms (where  $\phi$  appears) are linear, this is enough to check the accuracy of the terms that result from the tilted rotation vector. We successfully verified a number of cases.

## 5.5 Useful diagnostics

A number of quantities will be used to analyse the data we obtain from our numerical code. This section defines some of them and, if necessary, how to calculate them.

### 5.5.1 Mean flows

We are interested in the mean flows driven by our system. Here, we define mean flows to be the horizontally averaged i.e., averaged in  $y$ , components of horizontal velocity,  $u$  and  $v$  (denoted by an overbar):

$$\bar{u}(z, t) = \frac{1}{L} \int_0^L u(y, z, t) dy, \quad (5.5.123)$$

$$\bar{v}(z, t) = \frac{1}{L} \int_0^L v(y, z, t) dy. \quad (5.5.124)$$

A convenient way to compute the mean flows is in spectral space. This is done by taking the Fourier transform of  $u$  or  $v$  and then  $\bar{u}$ ,  $\bar{v}$  is given by the  $m = 0$  mode.

The mean flows are largely time-dependent and so we will often work with long-time averages of them, any time averages will be denoted by angle brackets,  $\langle \cdot \rangle$ .

### 5.5.2 Nusselt number

As a measure of the effectiveness of heat transfer by thermal convection we use the Nusselt number, a nondimensional number defined as the following ratio

$$Nu = \frac{\text{convective heat flux} + \text{conductive heat flux}}{\text{conductive heat flux}}. \quad (5.5.125)$$

Note, when  $Nu = 1$ , there is no convection and heat transfer occurs purely through conduction. Also, the bigger  $Nu$ , the more effective convection is at transporting heat. We wish to write the Nusselt number in terms of our nondimensional temperature perturbation  $\theta$ , which we solve for in our numerical code. To do this, consider the nondimensional heat equation given by

$$\frac{\partial T}{\partial t} = \nabla^2 T - (\mathbf{u} \cdot \nabla)T = \nabla \cdot (\nabla T - \mathbf{u}T), \quad (5.5.126)$$

where the second equality is true because  $\nabla \cdot \mathbf{u} = 0$ .

Next, integrate over the fluid layer to give

$$\frac{1}{L} \int_0^1 \int_0^L \frac{\partial T}{\partial t} dy dz = \frac{1}{L} \int_0^1 \int_0^L \nabla \cdot (\nabla T - \mathbf{u}T) dy dz = \frac{1}{L} \int_0^L \frac{\partial T}{\partial z} - wT dy, \quad (5.5.127)$$

where we have used the divergence theorem, and taken the normal to be in the  $z$ -direction. Recall, from (2.3.39) with  $T_{BS} = 1 - z$ , we have  $T = 1 - z + \theta$ , and hence

$$\begin{aligned} \frac{1}{L} \int_0^1 \int_0^L \frac{\partial \theta}{\partial t} dy dz &= \frac{1}{L} \int_0^L -1 + \frac{\partial \theta}{\partial z} - w(1 - z + \theta) dy \\ &= -1 + \frac{\partial \theta}{\partial z} - w(1 - z + \theta). \end{aligned} \quad (5.5.128)$$

The total flux remains constant throughout the layer and so we can choose to evaluate it anywhere in the layer, for example at the bottom boundary ( $z = 0$ ). The right-hand side of (5.5.128) gives the convective heat flux plus the conductive heat flux in the layer, which evaluated at the bottom boundary ( $z = 0$ ) gives  $-1 + \frac{\partial \bar{\theta}}{\partial z}|_{z=0}$ , since  $w = 0$  on the boundary. The nondimensional flux due to conduction only is  $-1$  (derivative of basic state temperature) and hence,

$$Nu = \frac{-1 + \frac{\partial \bar{\theta}}{\partial z}|_{z=0}}{-1} = 1 - \frac{\partial \bar{\theta}}{\partial z}|_{z=0}. \quad (5.5.129)$$

### 5.5.3 Kinetic energies

As a measure of the strength of the mean flows produced in the system, we calculate the kinetic energy of  $\bar{u}$  and  $\bar{v}$  in two different ways, each one with a different interpretation. They are defined as follows:

1.  $KE_{\langle \bar{\xi} \rangle} = \frac{1}{2} \int_0^1 \langle \bar{\xi}(z, t) \rangle^2 dz$
2.  $\langle KE_{\bar{\xi}} \rangle = \langle \frac{1}{2} \int_0^1 \bar{\xi}(z, t)^2 dz \rangle$

where  $\xi$  is the variable  $u$  or  $v$  and again  $\langle \cdot \rangle$  denotes a time-average.

The first definition is a measure of the mean of  $\bar{\xi}$ ; positive and negative contributions will cancel, giving a guide to the systematic nature of the flow. The second definition gives a measure of the variability of  $\bar{\xi}$ ; since  $\bar{\xi}$  can be positive or negative, squaring first ensures there is no cancellation of  $\bar{\xi}$ . By comparing the sizes of  $KE_{\langle \bar{\xi} \rangle}$  and  $\langle KE_{\bar{\xi}} \rangle$ , we can assess how systematic the flow,  $\bar{\xi}$ , is. If a mean flow has a similar  $KE_{\langle \bar{\xi} \rangle}$  and  $\langle KE_{\bar{\xi}} \rangle$ , then it will be considered systematic. If, however,  $\langle KE_{\bar{\xi}} \rangle$  is much larger than  $KE_{\langle \bar{\xi} \rangle}$ , then  $\bar{\xi}$  will be considered to be highly fluctuating and not very systematic. In Chapters 6-8, we use the term systematic frequently, and its meaning should be taken to be as just described.

It is also informative to consider the total kinetic energy of the perturbations, this is given by

$$KE_{pert}(t) = \frac{1}{2L} \int_0^1 \int_0^L (u(y, z, t)^2 + v(y, z, t)^2 + w(y, z, t)^2) dy dz. \quad (5.5.130)$$

## 5.6 Extending the method to solve the MHD equations

We have detailed the numerical method we use in our nonlinear code for the purely hydrodynamic equations. To extend the method to solve for the MHD equations is straightforward. The

momentum equation (5.2.1) is augmented by the Lorentz force (see section 2.1), this is just an extra term in the equations and provides no problem for the numerical method. In addition, we have to solve the induction equation (2.3.54) subject to  $\nabla \cdot \mathbf{B} = 0$ . This can also be solved in a similar way to the equation solved in the purely hydrodynamic case, as we outline below.

Analogous to the way in which we introduced the streamfunction for the perturbation velocity field (cf. equations (5.2.5)), we introduce a flux function  $A(y, z)$  for the perturbation magnetic field so that

$$\mathbf{B} = \left( B_1, \frac{\partial A}{\partial z}, -\frac{\partial A}{\partial y} \right), \quad (5.6.131)$$

which allows us to define the current  $\mathbf{j} = \nabla \times \mathbf{B} = \left( j, \frac{\partial B_1}{\partial z}, -\frac{\partial B_1}{\partial y} \right)$ , where  $j = -\nabla^2 A$  is the  $x$ -component of the current.

With this, the  $x$ -component of the vorticity equation (5.2.17) when a horizontal magnetic field is present, becomes

$$\frac{\partial \omega}{\partial t} - Pr \nabla^2 \omega = Pr T a^{\frac{1}{2}} (\cos \phi u_y + \sin \phi u_z) + Ra Pr \frac{\partial \theta}{\partial y} + J(\psi, \omega) - Q \zeta Pr (J(A, j) - \frac{\partial j}{\partial y} \sin \alpha), \quad (5.6.132)$$

the temperature equation (5.2.18) remains the same, i.e.,

$$\frac{\partial \theta}{\partial t} - \nabla^2 \theta = J(\psi, \theta) - \frac{\partial \psi}{\partial y} - T_y \frac{\partial \psi}{\partial z}. \quad (5.6.133)$$

The  $x$ -component of the momentum equation (5.2.19) is augmented by the Lorentz force to give

$$\begin{aligned} \frac{\partial u}{\partial t} - Pr \nabla^2 u &= Pr T a^{\frac{1}{2}} (\cos \phi \frac{\partial \psi}{\partial y} + \sin \phi \frac{\partial \psi}{\partial z}) + J(\psi, u) - \\ &\frac{\partial \psi}{\partial y} \frac{dU}{dz} + Q \zeta Pr \left( \frac{\partial \tilde{B}_1}{\partial y} \sin \alpha - J(A, \tilde{B}_1) \right). \end{aligned} \quad (5.6.134)$$

$\psi$  is obtained from  $\omega$  by solving the same equation as in the hydrodynamic case, i.e.,

$$\nabla^2 \psi = -\omega. \quad (5.6.135)$$

The evolution of the magnetic field is given by equation (2.3.54), i.e.,

$$\frac{\partial \mathbf{B}}{\partial t} = \nabla \times [(\mathbf{U}_{BS} + \mathbf{u}) \times \mathbf{B} + (\mathbf{u} \times \mathbf{B}_{BS})] + \zeta \nabla^2 \mathbf{B}, \quad (5.6.136)$$

with  $\mathbf{B}$  as in equation (5.6.131). By taking the  $x$ -component of this equation, we obtain an equation for  $B_1$

$$\frac{\partial B_1}{\partial t} - \zeta \nabla^2 B_1 = \frac{\partial u}{\partial y} \sin \alpha - \frac{\partial A}{\partial y} \frac{dU}{dz} - J(A, u) + J(\psi, B_1), \quad (5.6.137)$$

and by taking the  $x$ -component of the uncurled induction equation (5.6.136), we obtain an equation for  $A$

$$\frac{\partial A}{\partial t} - \zeta \nabla^2 A = J(\psi, A) + \frac{\partial \psi}{\partial y} \sin \alpha. \quad (5.6.138)$$

Equation (5.6.132) can be written in the form

$$\frac{\partial \omega}{\partial t} - Pr \nabla^2 \omega = F_{mag} \quad (5.6.139)$$

where

$$F_{mag} = Pr T a^{\frac{1}{2}} (\cos \phi u_y + \sin \phi u_z) + Ra Pr \frac{\partial \theta}{\partial y} + J(\psi, \omega) - Q \zeta Pr (J(A, j) - \frac{\partial j}{\partial y} \sin \alpha),$$

and can therefore be solved in the same way as described in section 5.3.

Likewise, equation (5.6.134) can be written in the form

$$\frac{\partial u}{\partial t} - Pr \nabla^2 u = H_{mag} \quad (5.6.140)$$

where

$$H_{mag} = Pr T a^{\frac{1}{2}} (\cos \phi \frac{\partial \psi}{\partial y} + \sin \phi \frac{\partial \psi}{\partial z}) + J(\psi, u) - \frac{\partial \psi}{\partial y} \frac{dU}{dz} + Q \zeta Pr \left( \frac{\partial \tilde{B}_1}{\partial y} \sin \alpha - J(A, \tilde{B}_1) \right)$$

and is also solved by the same method.

Rewriting (5.6.137) and (5.6.138) as

$$\frac{\partial B_1}{\partial t} - \zeta \nabla^2 B_1 = L_{mag} \quad \text{where } L_{mag} = \frac{\partial u}{\partial y} \sin \alpha - \frac{\partial A}{\partial y} \frac{dU}{dz} - J(A, u) + J(\psi, \tilde{B}_1), \quad (5.6.141)$$

$$\frac{\partial A}{\partial t} - \zeta \nabla^2 A = K_{mag} \quad \text{where } K_{mag} = J(\psi, A) + \frac{\partial \psi}{\partial y} \sin \alpha, \quad (5.6.142)$$

we see that these equations are also of the appropriate form for implementing the numerical method of section 5.3.

Therefore, we have shown that the numerical method derived in section 5.3 for the purely hydrodynamic system can easily be extended to solve the equations of the MHD system.

### 5.6.1 Boundary conditions

In addition to the boundary conditions from the hydrodynamic system, we impose the following magnetic boundary conditions:

$$A = 0, \quad \frac{\partial B_1}{\partial z} = 0, \quad \text{on } z = 0, 1, \quad (5.6.143)$$

derived from requiring  $B_3 = 0$  and  $\frac{\partial B_1}{\partial z} = 0$  on the boundaries (see section 2.3.1).

### 5.6.2 Testing the MHD code

To check the accuracy of our MHD code, we first tested it against our hydrodynamic nonlinear code (introduced in sections 5.2 and 5.3). We set  $Q = 0$  and successfully reproduced a number of results. To test the linear magnetic terms, we checked the growth rate against the expected growth rate as calculated from our linear code and found good agreement. Finally, we tested the full code against some of the nonlinear results in Arter (1983) and reproduced them successfully.

### 5.6.3 Useful diagnostics

In addition to the useful diagnostics from section 5.5, we define the full magnetic energy as follows

$$ME = Q\zeta Pr \frac{1}{2L} \int_0^1 \int_0^L [(B_1(y, z, t) + \cos \alpha)^2 + (A_z(y, z, t) + \sin \alpha)^2 + A_y(y, z, t)^2] dy dz \quad (5.6.144)$$

and also the magnetic energy in the magnetic perturbations as

$$ME_{\text{pert}} = Q\zeta Pr \frac{1}{2L} \int_0^1 \int_0^L [B_1(y, z, t)^2 + A_z(y, z, t)^2 + A_y(y, z, t)^2] dy dz. \quad (5.6.145)$$

## 5.7 Extending the method to solve the anelastic equations

The nonlinear anelastic equations for our system as given by (2.4.142)-(2.4.144) contain  $z$ -dependent reference state quantities. As a consequence of this, the method for solving the nonlinear anelastic equations is more involved than the method described in sections 5.3-5.6, for the nonlinear Boussinesq equations. We outline the method used in the anelastic case here.

First, consider

$$\nabla \cdot (\bar{\rho} \mathbf{u}) = 0 \quad (5.7.146)$$

and so

$$\bar{\rho} \frac{\partial v}{\partial y} + \frac{\partial}{\partial z} (\bar{\rho} w) = 0, \quad (5.7.147)$$

where we are again assuming all variations with respect to  $x$  vanish. Now, let  $\bar{\rho} \mathbf{u} = \left( \bar{\rho} u, \frac{\partial \psi}{\partial z}, -\frac{\partial \psi}{\partial y} \right)$ , where  $\psi$  is our streamfunction and then (5.7.147) is automatically satisfied. This gives

$$v = \frac{1}{\bar{\rho}} \frac{\partial \psi}{\partial z} \quad \text{and} \quad w = -\frac{1}{\bar{\rho}} \frac{\partial \psi}{\partial y}. \quad (5.7.148)$$

The vorticity is then given by  $\boldsymbol{\omega} = \nabla \times \mathbf{u} = (\omega, u_z, -u_y)$ , where

$$\begin{aligned}\omega &= w_y - v_z \\ &= -\frac{1}{\bar{\rho}} \frac{\partial^2 \psi}{\partial y^2} - \frac{\partial}{\partial z} \left( \frac{1}{\bar{\rho}} \frac{\partial \psi}{\partial z} \right) \\ &= -\frac{1}{\bar{\rho}} \nabla^2 \psi - \frac{\partial}{\partial z} \left( \frac{1}{\bar{\rho}} \right) \frac{\partial \psi}{\partial z}.\end{aligned}\quad (5.7.149)$$

With this, the  $x$ -component of the vorticity equation (obtained by taking the curl of (2.4.142)) becomes

$$\begin{aligned}\frac{\partial \omega}{\partial t} - Pr \nabla^2 \omega &= \frac{1}{\bar{\rho}} J(\psi, \omega) - \omega(v_y + w_z) + Ra Pr s_y + Ta^{\frac{1}{2}} Pr (\cos \phi u_y + \sin \phi u_z) \\ &\quad + \frac{Pr}{\bar{\rho}} \frac{d\bar{\rho}}{dz} \left( \frac{4}{3}(v_{yy} + w_{yz}) - \frac{\partial \omega}{\partial z} - 2(v_{yy} + v_{zz}) \right) \\ &\quad - \left( \frac{Pr}{\bar{\rho}} \frac{d^2 \bar{\rho}}{dz^2} - \frac{Pr}{\bar{\rho}^2} \left( \frac{d\bar{\rho}}{dz} \right)^2 \right) (v_z + w_y) \\ &= \frac{1}{\bar{\rho}} J(\psi, \omega) - \omega(v_y + w_z) + Ra Pr s_y + Ta^{\frac{1}{2}} Pr (\cos \phi u_y + \sin \phi u_z) \\ &\quad + \frac{Pr}{\bar{\rho}} \frac{d\bar{\rho}}{dz} \left( \frac{1}{3} \omega_z - \frac{2}{3}(v_{yy} + v_{zz}) \right) - Pr \frac{d}{dz} \left( \frac{1}{\bar{\rho}} \frac{d\bar{\rho}}{dz} \right) (v_z + w_y).\end{aligned}\quad (5.7.150)$$

The  $x$ -component of the momentum equation (2.4.142) becomes

$$\frac{\partial u}{\partial t} - Pr \nabla^2 u = \frac{1}{\bar{\rho}} J(\psi, u) + \frac{Pr}{\bar{\rho}} \frac{d\bar{\rho}}{dz} \frac{\partial u}{\partial z} + \frac{Ta^{\frac{1}{2}} Pr}{\bar{\rho}} \left( \cos \phi \frac{\partial \psi}{\partial y} + \sin \phi \frac{\partial \psi}{\partial z} \right) \quad (5.7.151)$$

and the entropy equation (2.4.144) is written as

$$\begin{aligned}\frac{\partial s}{\partial t} - \frac{1}{\bar{\rho}} \nabla^2 s &= \frac{1}{\bar{\rho}} J(\psi, s) - w \frac{d\bar{s}}{dz} + \frac{1}{\bar{\rho} \bar{T}} \frac{d\bar{T}}{dz} \frac{\partial s}{\partial z} - \\ &\quad \frac{\theta}{Ra \bar{T}} \left( \left( \frac{\partial u}{\partial y} \right)^2 + \left( \frac{\partial u}{\partial z} \right)^2 + (w_y + v_z)^2 + \frac{4}{3} (w_z^2 - w_z v_y + v_y^2) \right) \equiv G,\end{aligned}\quad (5.7.152)$$

where all quantities with an overbar are taken to be the reference state quantities given by (2.4.140) and (2.4.141) in Chapter 2.

Equations (5.7.150) and (5.7.151) are of the same form as their Boussinesq counterparts, i.e., they are of the form  $\frac{\partial \xi}{\partial t} - Pr \nabla^2 \xi = \text{RHS}$ . Therefore, we can use the method described in section 5.3, to solve these equations. The only difference is that, here, we will discretise space in the  $z$ -direction by using Gauss-Lobatto (GL) points, i.e.,

$$z_j = \cos \left( \frac{(j-1)\pi}{N_z - 1} \right) \quad \text{for } j = 1, 2, \dots, N_z. \quad (5.7.153)$$

The reason for changing to GL points is that it makes solving the entropy equation (5.7.152) easier, as we shall see next. Equation (5.7.152) has a  $\frac{1}{\bar{\rho}}$  multiplying the second term on the left-hand side and since this factor is a function of  $z$ , we have to treat this equation in a different way

to the equation for  $\theta$  in the hydrodynamic case, (5.2.18). Inspired by DeRosa (2001), we solve equation (5.7.152) in 'semi-spectral' space, that is, spectral in  $y$  but physical in  $z$ . To do this, consider equation (5.7.152) written as

$$\frac{\partial \tilde{s}}{\partial t} - \tilde{L}\tilde{s} = \tilde{G}, \quad (5.7.154)$$

where a ' $\sim$ ' denotes an FFT, e.g.,  $\tilde{s} = \text{FFT}(s)$  and where  $\tilde{L} = \frac{1}{\rho}(\text{CDD} + m^2)$ . CDD is the scaled Chebyshev differentiation matrix used to calculate derivatives in real space. Trefethen (2000) gives a simple form for constructing such a matrix using GL points - it is for this reason we switch to GL points from the original collocation points. We note though, that CDD is a dense matrix and so, unlike the differentiation matrices resulting from the recurrence relation of spectral coefficients, inverting the matrix is a more computationally intensive task.

Once transformed into 'semi-spectral' space, we can apply the same Crank-Nicolson implicit scheme to the left hand side and the explicit Adams-Bashforth to the right hand side as we did before (see section 5.3.8), to give

$$\frac{\tilde{s}^{n+1} - \tilde{s}^n}{\Delta t} - \left( \frac{\tilde{L}\tilde{s}^{n+1} - \tilde{L}\tilde{s}^n}{2} \right) = \frac{3\tilde{G}^n - \tilde{G}^{n-1}}{2} \quad (5.7.155)$$

or

$$\left( 1 - \frac{\Delta t}{2}\tilde{L} \right) \tilde{s}^{n+1} = \left( 1 + \frac{\Delta t}{2}\tilde{L} \right) \tilde{s}^n + \frac{\Delta t}{2}(3\tilde{G}^n - \tilde{G}^{n-1}), \quad (5.7.156)$$

which can be written as  $A\tilde{s}^{n+1} = B$  where

$$A = 1 - \frac{\Delta t}{2}\tilde{L} \quad (5.7.157)$$

and

$$B = \left( 1 + \frac{\Delta t}{2}\tilde{L} \right) \tilde{s}^n + \frac{\Delta t}{2}(3\tilde{G}^n - \tilde{G}^{n-1}). \quad (5.7.158)$$

This matrix equation is then solved using a LAPACK routine for LU decomposition (see e.g., Anderson *et al.* (1999)).

In a similar way, equation (5.7.149) is also solved in 'semi-spectral' space owing to the  $\frac{1}{\rho}$  multiplying the  $\nabla^2\psi$ . Equation (5.7.149) can be written as

$$\tilde{\omega}^{n+1} = A_1\tilde{\psi}^{n+1}, \quad (5.7.159)$$

where

$$A_1 = -\frac{1}{\rho}(\text{CDD} + m^2) - \frac{d}{dz} \left( \frac{1}{\rho} \right) \text{CD}. \quad (5.7.160)$$

This matrix equation is solved using Schur decomposition, because, as Peyret (2002) explains, Schur decomposition leads to better conditioned matrices for equations of the form (5.7.149). Again, the Schur decomposition is performed using a routine from the LAPACK library (Anderson *et al.* (1999)).

### 5.7.1 Testing the anelastic code

As was done for the Boussinesq codes, we tested the linear growth rates of the nonlinear anelastic code against those predicted by the linear code developed for the work in Chapter 4 and found good agreement. We also performed some simulations to check that the anelastic code recovered the results of the Boussinesq code in the appropriate limit ( $\theta = 0$ ) and again found good agreement. The only terms which are not tested by the two checks mentioned so far, are the terms that appear in the equations only when  $\theta \neq 0$  and are nonlinear. On inspection of equations (2.4.142)-(2.4.144), we see that the only terms that fall into this category are the viscous heating terms in equation (2.4.144). One way to test these terms is to impose a shear flow. For example, we force the momentum equation, (2.4.142), and let  $\mathbf{u} = U(z)\mathbf{e}_x$  and  $s = S(z)$ . In this case, equations (2.4.142) and (2.4.144) reduce to

$$-Pr \frac{d^2 U}{dz^2} = \frac{Pr}{\bar{\rho}} \frac{d\bar{\rho}}{dz} \frac{dU}{dz} + F(z), \quad (5.7.161)$$

$$-\frac{1}{\bar{\rho}} \frac{d^2 S}{dz^2} = \frac{1}{\bar{\rho}\bar{T}} \frac{d\bar{T}}{dz} \frac{dS}{dz} - \frac{\theta}{Ra\bar{T}} \left( \frac{dU}{dz} \right)^2 \quad (5.7.162)$$

respectively, where  $F(z)$  is our imposed forcing term. We have also taken  $Ta = 0$  as the terms due to the rotation have already been tested. If we choose  $F = -\frac{Pr\pi \cos(\pi z)}{(1+\theta z)^m}$ , then equation (5.7.161) becomes

$$\frac{d^2 U}{dz^2} + \frac{m\theta}{(1+\theta z)} \frac{dU}{dz} = \frac{\pi \cos(\pi z)}{(1+\theta z)^m}, \quad (5.7.163)$$

which can be solved for the general solution  $\frac{dU}{dz} = \frac{\sin(\pi z)}{(1+\theta z)^m} + C$ . Imposing  $\frac{dU}{dz} = 0$  on  $z = 0, 1$  gives  $C = 0$ . With this expression for  $\frac{dU}{dz}$ , we can solve equation (5.7.162) for  $S$  in MATLAB and check it against  $s$  obtained when  $F$  is imposed in the nonlinear code. We successfully verified a number of cases.

### 5.7.2 Useful diagnostics

Mean flows are calculated in exactly the same way as described in section 5.5. But, in the anelastic equations,  $\bar{\rho}$  is a function of  $z$ , and so it must be explicitly included in the definition of the kinetic energies. For all cases studied in this thesis, we use the following definitions:

$$KE_{pert} = \frac{1}{2L} \int_0^1 \int_0^L \bar{\rho} [u(y, z, t)^2 + \psi_z(y, z, t)^2 + \psi_y(y, z, t)^2] dy dz, \quad (5.7.164)$$

$$KE_{\langle \bar{\xi} \rangle} = \frac{1}{2} \int_0^1 \bar{\rho} \langle \bar{\xi}(z, t) \rangle^2 dz, \quad (5.7.165)$$

$$\langle KE_{\bar{\xi}} \rangle = \left\langle \frac{1}{2} \int_0^1 \bar{\rho} \bar{\xi}(z, t)^2 dz, \right\rangle \quad (5.7.166)$$

where  $\xi$  is the variable  $u$  or  $v$ .  $KE_{\langle \bar{\xi} \rangle}$  and  $\langle KE_{\bar{\xi}} \rangle$  have the same interpretation as in the Boussinesq case, i.e., as described in section 5.5.3.

## 5.8 Summary

Following the guidance of Peyret (2002), amongst others, we have constructed and tested an efficient, nonlinear, pseudospectral numerical code to solve the equations derived in Chapter 2. In section 5.2, we reformulated the governing equations so that they involved a streamfunction and the vorticity. Using the purely hydrodynamic system as our example, we then detailed the numerical algorithm used to solve the equations. The method assumes periodicity in the  $y$ -direction and expands the variables as Fourier series' in this direction, whilst in the  $z$ -direction, the variables are expanded as Chebyshev series'. Derivatives are computed efficiently in spectral space and nonlinear products are formed by multiplying together the relevant quantities in physical space. Sampling the equations on a discrete grid allows them to be written as matrix equations. Furthermore, the matrices are of quasi-tridiagonal structure, meaning that they can be inverted efficiently using an algorithm courtesy of Thual (1986).

Whilst, the majority of this chapter dealt with the purely hydrodynamic system, section 5.6 gave details on how to extend the code to solve the equations of the MHD system. This was a relatively straightforward task as the extra terms and equations resulting from the presence of a magnetic field can be solved using the same method. However, applying this method to the nonlinear anelastic equations provided more complications, arising because of the dependence of the basic state on  $z$ . Section 5.7 detailed a solution to these complications by solving some of the equations in 'semi-spectral' space.

All three numerical codes were tested against other work, our linear codes and each other; good agreement was found in all cases. Successful construction and verification of our codes allows us to proceed with confidence and examine the systems in the nonlinear regime, in particular, we can now investigate mean flow generation in our different systems. The following three chapters present the numerical results obtained for the Boussinesq and anelastic systems using these codes.



## Chapter 6

# Nonlinear Hydrodynamic Convection

### 6.1 Introduction

This chapter considers the nonlinear evolution of the variables governed by equations (5.2.17)-(5.2.20). We emphasise that these equations are two-dimensional in the sense that they only depend on  $y$  and  $z$ , however, all three components of the flow are included. Since mean flows result from nonlinear interactions, by retaining the nonlinear terms in the governing equations we can investigate the mean flows driven by the system. As discussed in Chapter 1, section 1.4.3, there have been a number of studies of mean flow generation in convection. This chapter aims to add to these studies by focussing on the effect of a tilted rotation vector, the Prandtl number and a thermal wind on the mean flows driven. In this chapter, we consider solutions to the Boussinesq, hydrodynamic system, and later we extend the work to examine the anelastic and MHD systems (see Chapters 7 and 8 respectively). Owing to the complexity of the governing equations we are required to solve them numerically; to do this, we employ the algorithm described in Chapter 5.

### 6.2 Numerical results

Before considering the mean flows driven by the system, we investigate some more general properties of the convection. In this chapter, we consider two distinct cases, (i)  $T_y = 0$ , i.e., there is no thermal wind and (ii)  $T_y \neq 0$ , i.e., there is a thermal wind, and in both cases we investigate the effect of different parameters on the system but, unless otherwise stated, we fix the rotation rate by setting  $Ta = 10^5$  and the size of the computational box by setting  $L = 5$ .

### 6.2.1 No thermal wind

We begin by setting  $T_y = 0$  and hence there are no thermal wind effects to consider. To investigate the effect of a tilted rotation vector, i.e., the case where the rotation vector is oblique to gravity, we fix  $Pr = 1$  and increase  $Ra$  for three different  $\phi$ : (i)  $\phi = \frac{\pi}{2}$  (vertical rotation), (ii)  $\phi = \frac{\pi}{4}$  (a layer at  $45^\circ$ ), (iii)  $\phi = \frac{\pi}{6}$  (a layer at  $30^\circ$ ).

We find that as  $Ra$  is increased, the solutions progress through a series of different types of solution. This progression is best depicted by a regime diagram, as shown in figure 6.1, where each symbol represents a different type of solution. The red squares represent steady solutions, blue circles represent oscillatory or periodic solutions, green triangles represent quasi-periodic solutions (QP), and light blue stars represent chaotic solutions.

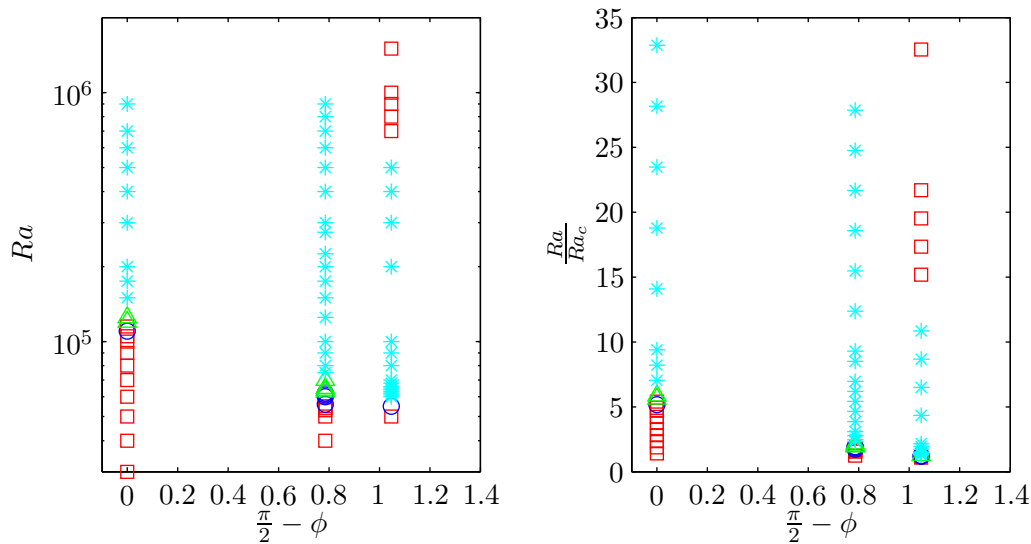


Figure 6.1: Regime diagram for solutions at fixed  $\phi$  and  $Ra$  for  $Pr = 1$ ,  $\phi = \frac{\pi}{2}$ ,  $\frac{\pi}{4}$  and  $\frac{\pi}{6}$ . Red squares represent steady solutions, blue circles represent periodic solutions, green triangles represent quasi-periodic solutions and light blue stars represent chaotic solutions. The results are plotted against (a)  $Ra$ , and (b)  $\frac{Ra}{Ra_c}$ .

Plot (a) shows the type of solution that is found for different values of  $Ra$ , and plot (b) shows the same but plotted against  $\frac{Ra}{Ra_c}$  where  $Ra_c$  is the value at which convection onsets in a box of length  $L = 5$ . For reference, here,  $Ra_c = 2.13 \times 10^4$  for  $\phi = \frac{\pi}{2}$ ,  $Ra_c = 3.23 \times 10^4$  for  $\phi = \frac{\pi}{4}$  and  $Ra_c = 4.61 \times 10^4$  for  $\phi = \frac{\pi}{6}$ . From the diagrams we see that, for all values of  $\phi$  studied, the solution is steady when it first goes unstable, then as  $Ra$  is increased, it undergoes a Hopf

bifurcation and becomes periodic. Further increase of  $Ra$  leads to another (secondary Hopf) bifurcation giving a QP solution before the solution becomes chaotic at even larger  $Ra$ . Notice when  $\phi = \frac{\pi}{6}$ , the solution returns to a steady state, at large enough  $Ra$ . This is examined in more detail in section 6.2.4. The regime diagram also highlights that, as the rotation vector is tilted from the vertical, a higher  $Ra$  is required for growth, i.e., decreasing  $\phi$  has a stabilising effect on the system. Also, the larger the tilt from the vertical, the smaller the range of  $Ra$  over which the bifurcations occur, that is, the solution becomes chaotic at lower  $Ra$ . For the untilted case, the solution remains steady until  $Ra \gtrsim 10^5$ .

### 6.2.2 Transition to chaos

To analyse the different types of solution that occur for a tilted rotation vector more closely, we choose to focus on the case where  $\phi = \frac{\pi}{4}$ . Figure 6.2 shows plots of the time series of the Nusselt number,  $Nu$ , and the kinetic energy in the perturbations,  $KE_{\text{pert}}$ , for different  $Ra$ .

In (a),  $Ra = 40000$  ( $1.24Ra_c$ ) and the solution has settled into a steady state; in (b)  $Ra = 50000$  ( $1.55Ra_c$ ) and the solution is oscillating with a distinct single period; in (c)  $Ra = 63000$  ( $1.95Ra_c$ ) and the solution is still oscillating but now there is more than one associated period - we call this solution quasi-periodic. In (d)  $Ra = 75000$  ( $2.33Ra_c$ ) and the solution has become chaotic. In other words, the system has undergone a number of bifurcations en route to chaos. This transition to chaos can be viewed in an alternative way by looking at phase space and so-called Poincaré sections (see Guckenheimer & Holmes (1983) for details). Figure 6.3 shows plots of the solutions in phase space,  $(KE_{\bar{u}}, KE_{\bar{v}}, Nu)$  for the same  $Ra$  as in figure 6.2, where  $KE_{\bar{u}}$  is the kinetic energy in  $\bar{u}$  and  $KE_{\bar{v}}$  is the kinetic energy in  $\bar{v}$ , as described in section 5.5. Alongside each phase space plot is a cut of the phase space, through a constant value of  $KE_{\bar{u}}$ . For the steady solution at  $Ra = 40000$ , the Poincaré section is a fixed point. In (b) we see the oscillatory solution cuts the plane in two places, indicating that the solution has undergone a Hopf bifurcation. As  $Ra$  is increased to approximately  $Ra = 63000$ , the solution undergoes a second bifurcation to a torus which is characterised in the Poincaré section by the two closed loops. Subfigure (d) displays the phase space for the case when  $Ra$  is increased to 75000, a chaotic solution, which results in a Poincaré section with no obvious pattern. This route to chaos is known as the Ruelle-Takens-Newhouse route to chaos, after the seminal work of Newhouse *et al.* (1978).

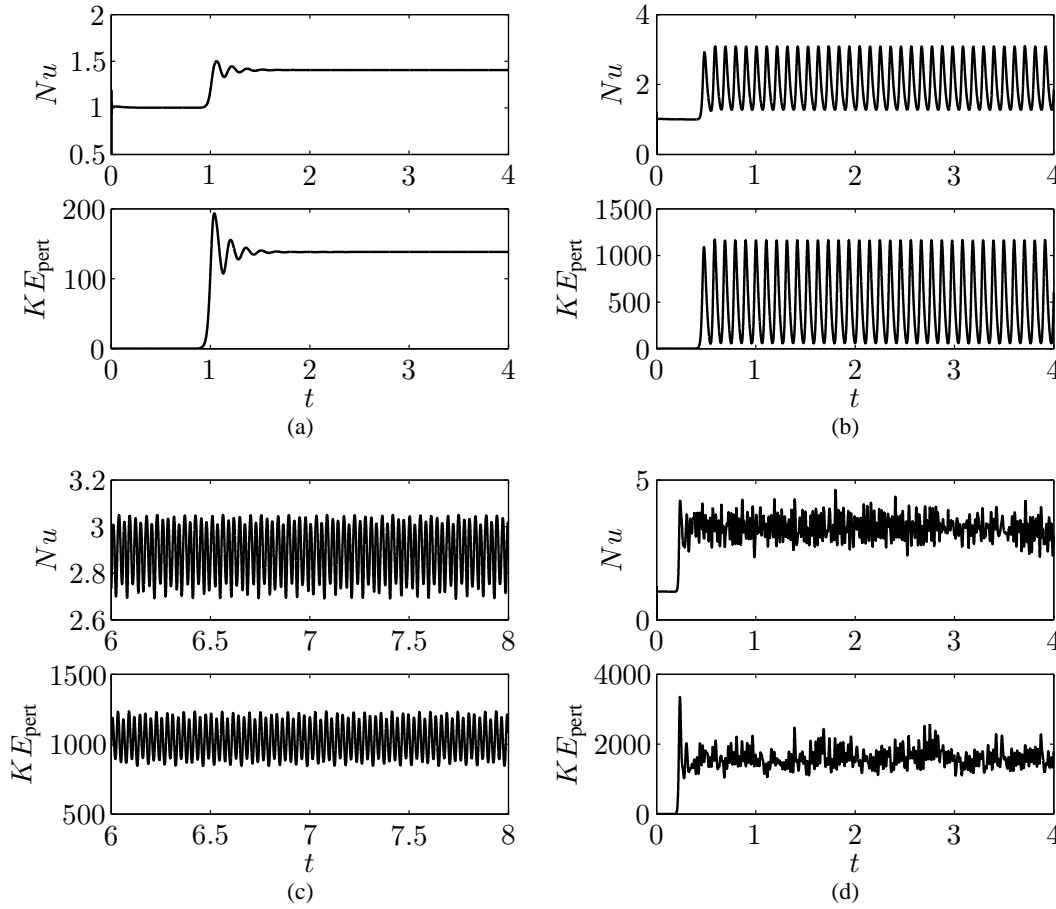


Figure 6.2: Time series of Nusselt number ( $Nu$ ) and kinetic energy ( $KE_{\text{pert}}$ ) for the case when  $Pr = 1$ ,  $\phi = \frac{\pi}{4}$  and in (a),  $Ra = 40000$ , in (b),  $Ra = 50000$ , in (c),  $Ra = 63000$ , and in (d),  $Ra = 75000$ .

### 6.2.3 Nonlinear solutions

It is informative to visualise the flow in each of the solution regimes seen in section 6.2.2. To do this, we plot contours of  $\psi(y, z)$  at a snapshot in time (see figure 6.4). In (a), we have the steady solution and the streamfunction appears as regular convection cells. Clearly evident is the tilted nature of the rolls, choosing to align with the rotation vector, as in the linear theory (see Hathaway *et al.* (1980)). In (b), we consider the QP case, now the streamfunction is less regular in shape and cells have merged to form larger structures, but the tilt is still apparent. By  $Ra = 75000$ , (c), we have reached the chaotic regime and this is reflected in the form of the solution. When  $Ra$  is increased further to  $Ra = 2 \times 10^5$ , the solutions become highly chaotic, see figure 6.4 (d). Again, we notice that larger scale structures are forming.

Figure 6.5 shows contours of the total temperature,  $T = 1 - z + \theta$ , corresponding to each of the

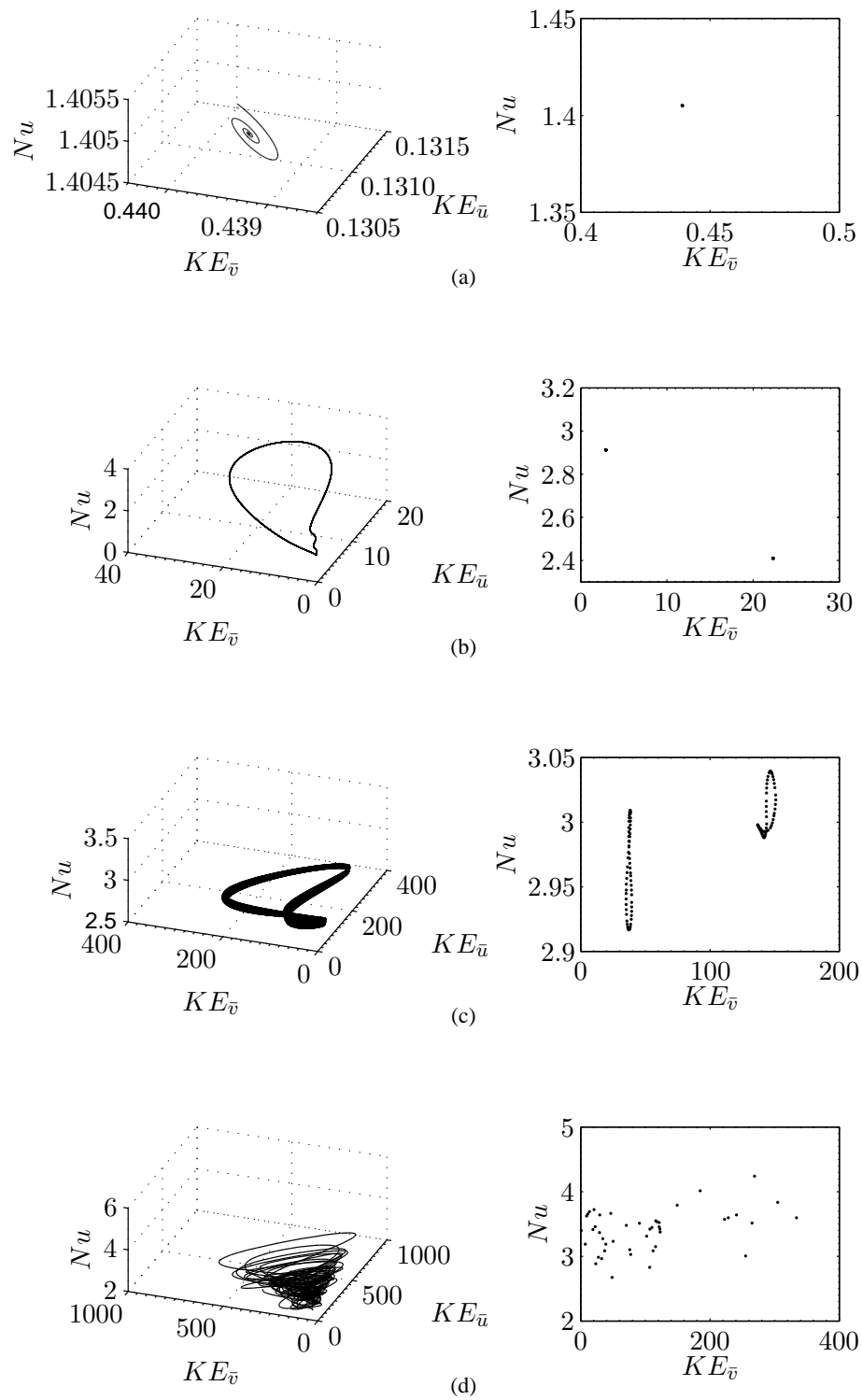


Figure 6.3: Phase space and alongside it a Poincaré section for each of the cases in figure 6.2. In (a),  $Ra = 40000$  and the section is taken at  $KE_{\bar{u}} = 0.1307$ , in (b),  $Ra = 50000$  and the section is taken at  $KE_{\bar{u}} = 6$ , in (c),  $Ra = 63000$  and the section is taken at  $KE_{\bar{u}} = 100$  and in (d),  $Ra = 75000$  and the section is taken at  $KE_{\bar{u}} = 200$ .

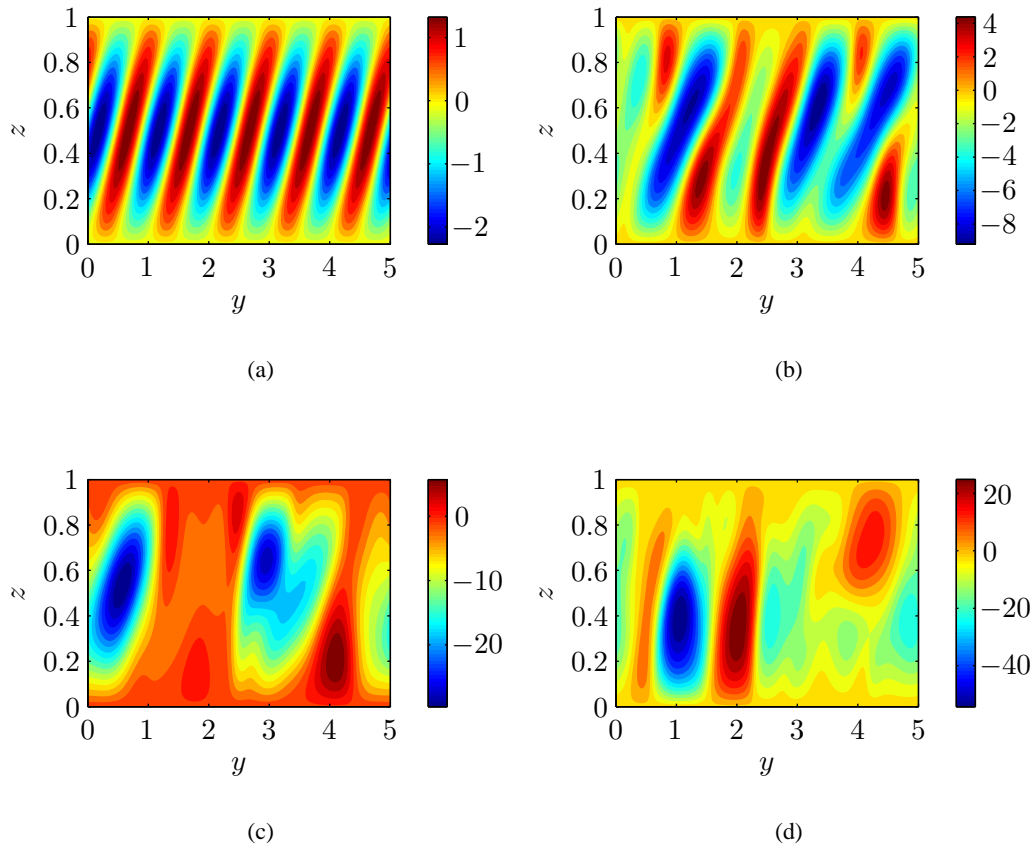


Figure 6.4: Contours of the streamfunction  $\psi(y, z)$  in a settled state, for the case with  $Pr = 1$  and  $\phi = \frac{\pi}{4}$ . In (a),  $Ra = 40000$ , in (b),  $Ra = 63000$ , in (c),  $Ra = 75000$  and in (d),  $Ra = 2 \times 10^5$ .

cases in figure 6.4. In (a), the fluid is largely hot at the bottom (red) and cooler at the top (blue) with little mixing between the boundaries. As  $Ra$  is increased, the hotter and cooler fluid start to mix to make the interior of the fluid layer more isothermal and thin thermal plumes are evident, as seen in figure 6.5 (b) through (d).

By considering  $\bar{T}$ , the horizontally averaged temperature (see figure 6.6), we see that as  $Ra$  is increased, the fluid motions are acting to make the interior of the fluid closer to being isothermal. In all cases, despite mixing, we still have a boundary layer at each boundary due to the fixed temperature conditions.

## 6.2.4 Large-scale solutions

As commented on in section 6.2.1, when  $\phi = \frac{\pi}{6}$ , the solution enters a second steady regime at large  $Ra$ . If we examine the dependency of  $Nu$  on  $Ra$  for one of these examples ( $Pr = 1$ ,

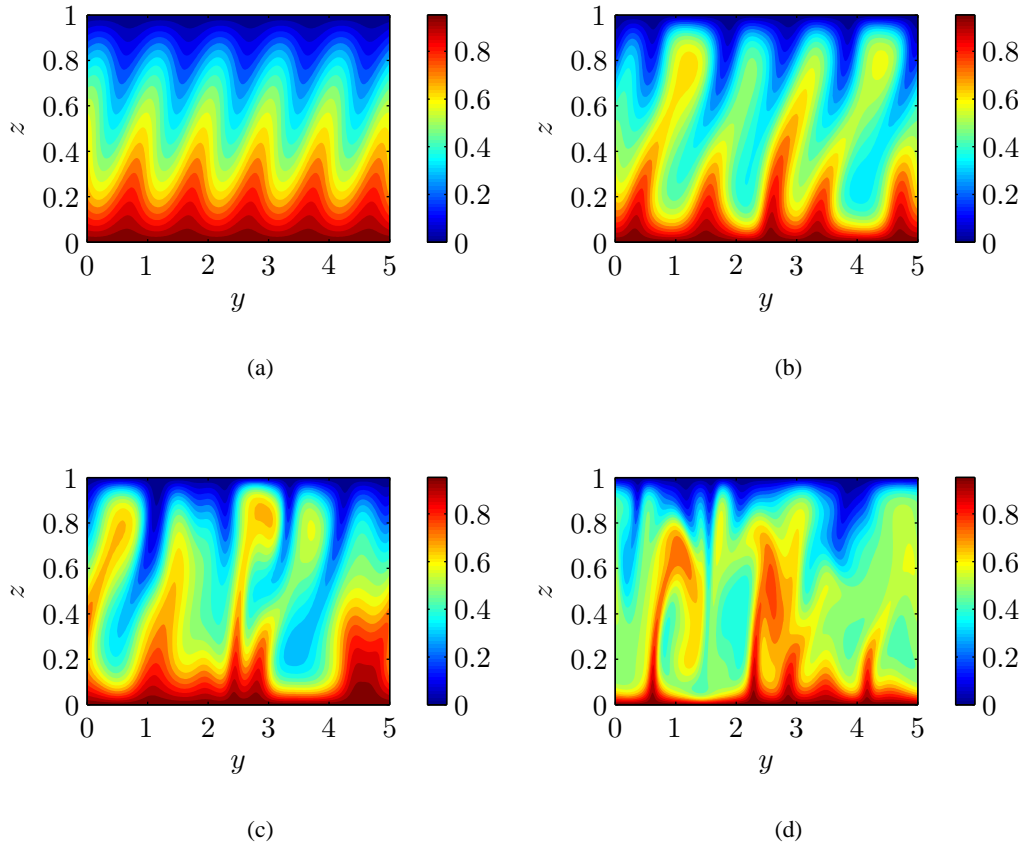


Figure 6.5: Contours of the temperature  $T(y, z)$  after the final time step for the case with  $Pr = 1$  and  $\phi = \frac{\pi}{4}$ . In (a),  $Ra = 40000$ , in (b),  $Ra = 63000$ , in (c),  $Ra = 75000$  and in (d),  $Ra = 2 \times 10^5$ .

$\phi = \frac{\pi}{6}$ ,  $Ta = 10^5$ ), see figure 6.7, then there are some significant points to note. First, for small  $Ra$ ,  $Nu$  increases with  $Ra$  before settling to a scaling law with less rapid increase. Secondly, between  $Ra = 6 \times 10^5$  and  $Ra = 7 \times 10^5$  there is a jump in  $Nu$ , this jump coincides with the change in regime from chaotic back to steady. It appears as though the system has found a more efficient mode of heat transfer (higher  $Nu$ ) in a steady regime.

Comparing contour plots of  $\psi$  from the two different steady regimes highlights a key difference - the scale of the solution (see figure 6.8). The length scale in the second steady regime is much larger, in fact, it is approximately the size of the domain, i.e, only one positive and one negative convection cell fit into the box. It is also noticeable that the tilt of the rotation vector is evident at lower  $Ra$ , where the convection rolls align themselves with the rotation vector, whereas, for the large-scale solutions this alignment has disappeared.

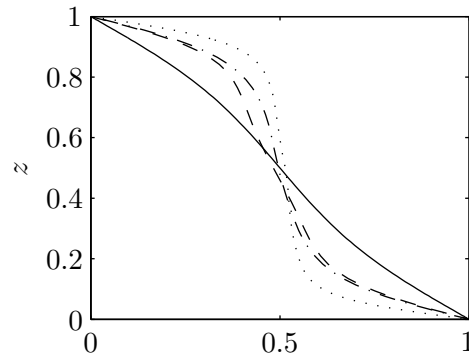


Figure 6.6: Time-averaged, mean temperature profiles  $\bar{T}$ , for the cases shown in figure 6.5. The solid line represents  $Ra = 40000$ , the dashed line represents  $Ra = 63000$ , the dot-dashed line represents  $Ra = 75000$  and the dotted line represents  $Ra = 2 \times 10^5$ . Increasing  $Ra$  acts to make the interior of the fluid layer more isothermal.

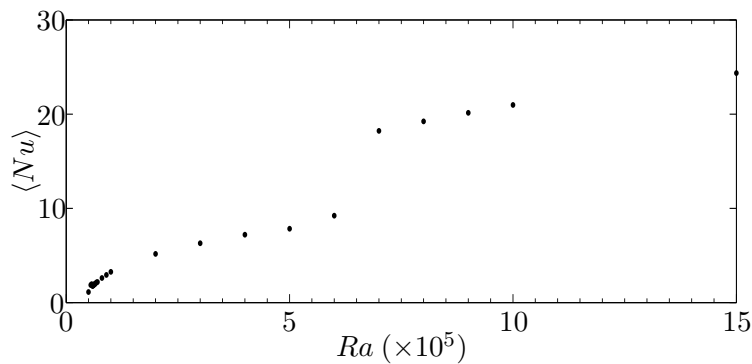


Figure 6.7: Nusselt number ( $Nu$ ) against Rayleigh number ( $Ra$ ) for  $Pr = 1$ ,  $\phi = \frac{\pi}{6}$ ,  $Ta = 10^5$ . As  $Ra$  is increased the solution changes regimes. In particular, at  $Ra = 6 \times 10^5$  the solution is chaotic but at  $Ra = 7 \times 10^5$  the solution is steady. This change in regime coincides with an increase in  $Nu$ .

The temperature,  $T = 1 - z + \theta$ , corresponding to one of these large-scale solutions is shown in figure 6.9 (a), alongside the profile of the horizontal average of the temperature in (b). We see that the system has reached an almost isothermal state, due to the highly efficient convecting state it has been able to achieve. One can see that the bulk of the fluid is isothermal but there exist two thin boundary layers. Chini & Cox (2009) and Hepworth (2014) found similar, steady, large-scale solutions in non-rotating, two-dimensional Rayleigh-Bénard convection at  $Pr = 1$ .

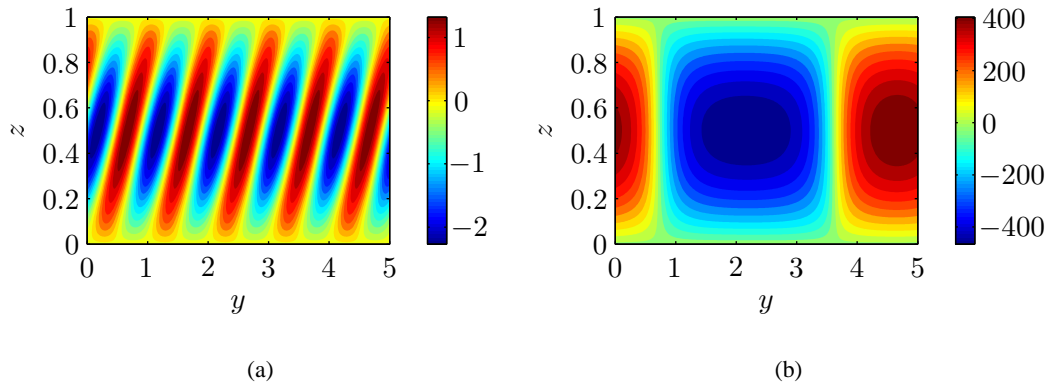


Figure 6.8: Contours of  $\psi(y, z)$  for steady solutions taken from two different steady regimes. In (a)  $Ra = 40000$  and in (b)  $Ra = 8 \times 10^5$ . The larger  $Ra$  solution exhibits a much larger length scale and the cells are not aligned with the rotation vector, as they are in (a).

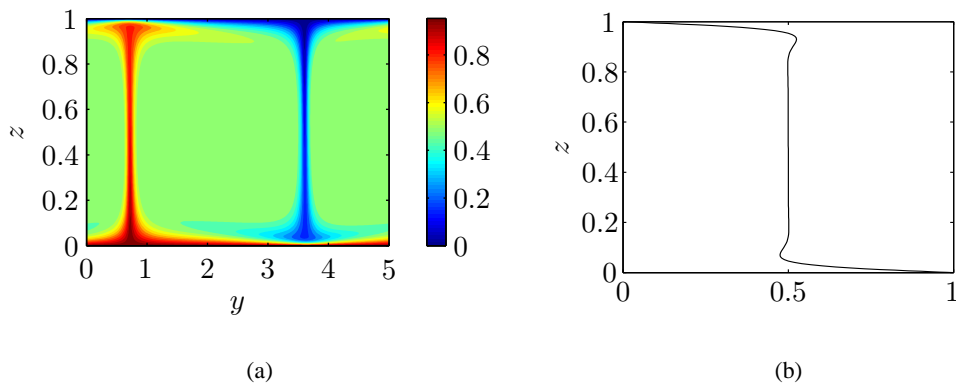


Figure 6.9: (a) Temperature as a function of  $y$  and  $z$ . (b) Horizontally averaged temperature as a function of  $z$ . In both cases,  $Ra = 8 \times 10^5$ ,  $Pr = 1$ ,  $\phi = \frac{\pi}{4}$ ,  $Ta = 10^5$ . The bulk of the fluid is isothermal except for the two thin boundary layers.

### 6.2.5 Decreasing $Pr$

We now decrease the Prandtl number, from  $Pr = 1$  to  $Pr = 0.1$ . In doing so, the critical Rayleigh number of the system is also decreased, i.e., instability sets in at a lower Rayleigh number. As with  $Pr = 1$ , we find the solutions progress through a series of states as we increase  $Ra$ , as indicated by the regime diagram in figure 6.10. As before, red squares represent steady solutions, blue circles represent periodic solutions, green triangles represent quasi-periodic solutions (QP), and light blue stars represent chaotic solutions. Here we have also characterised a different type of

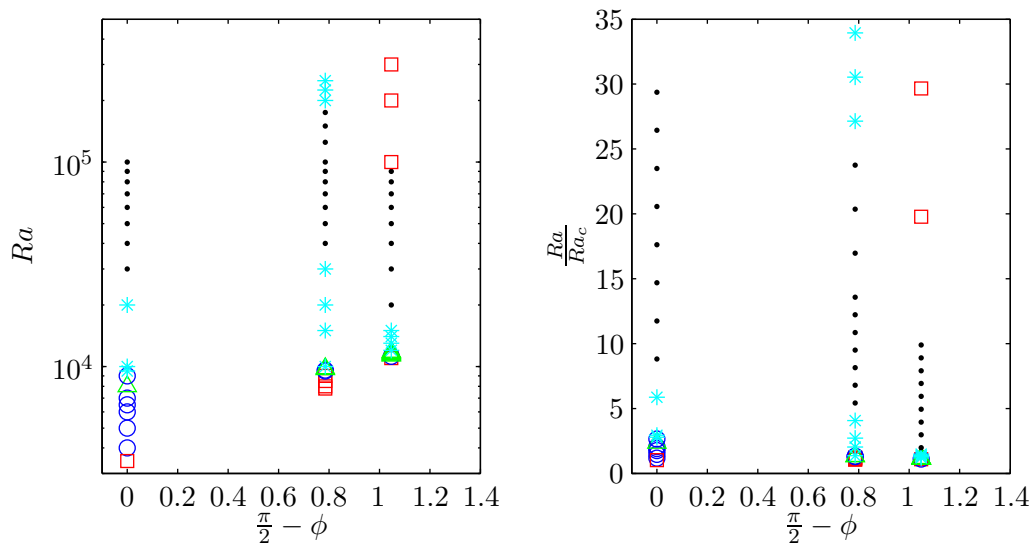


Figure 6.10: Regime diagram for solutions at fixed  $\phi$  and  $Ra$  for  $Pr = 0.1$ ,  $\phi = \frac{\pi}{2}$ ,  $\frac{\pi}{4}$  and  $\frac{\pi}{6}$ . Red squares represent steady solutions, blue circles represent periodic solutions, green triangles represent quasi-periodic solutions, black dots relaxation oscillations and light blue stars represent chaotic solutions. The results are plotted against (a)  $Ra$ , and (b)  $\frac{Ra}{Ra_c}$ .

solution which we describe as relaxation oscillations, these solutions are indicated on the regime diagram by black dots. Relaxation oscillations are chaotic type solutions but where bursts of energy occur intermittently. A time series of the Nusselt number and kinetic energy of one of these solutions is shown in figure 6.11 (a). In this relaxation oscillation state, as the convection gets more vigorous (higher  $Nu$ ) a larger mean flow is driven, this is seen in figure 6.11 (b). Here we have plotted the mean flows  $\bar{u}$  (blue) and  $\bar{v}$  (red), we see that the peaks in the energy of the mean flows correspond to dips in  $Nu$  (cf. figure 6.11(a)). So, as the convection gets more vigorous (higher  $Nu$ ) it leads to larger mean flows which act to inhibit the convection and this is matched by a decrease in  $Nu$ . The process repeats, each cycle resulting in the 'bursts' of energy we see. Such bursting solutions have been seen in studies of convection in other systems, for example, Brummell & Hart (1993), Rotvig & Jones (2006) and Teed *et al.* (2012) in annulus models, and Grote & Busse (2001) in a spherical shell geometry.

By plotting the phase space,  $(KE_{\bar{u}}, KE_{\bar{v}}, Nu)$ , and Poincaré sections for a relaxation oscillation solution (see figure 6.12) we see that the relaxation oscillation solution does not lead to a distinct pattern in phase space, it is just a chaotic solution but with other properties as described above.

Returning to figure 6.10 we see that, as  $Ra$  is increased, the solutions move from being steady to

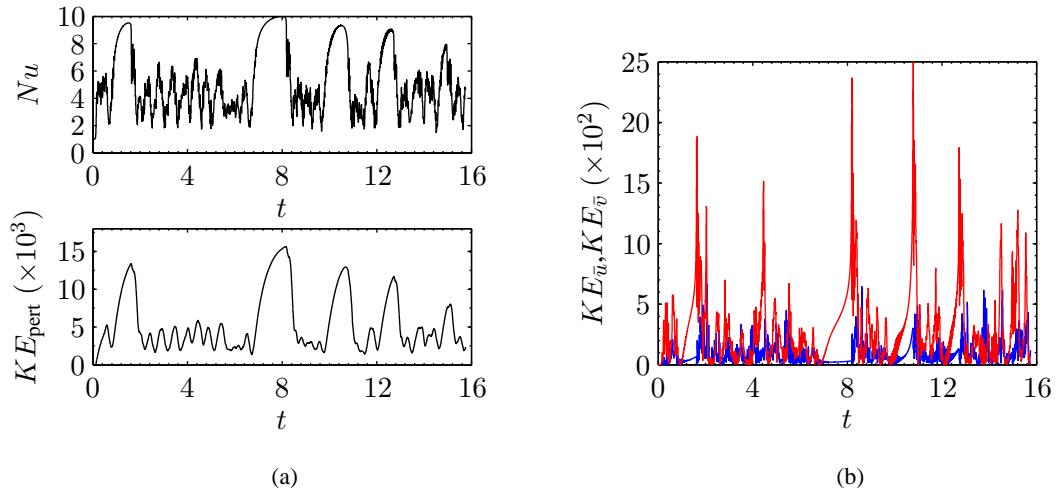


Figure 6.11: (a) Time series of Nusselt number ( $Nu$ ) and kinetic energy ( $KE_{\text{pert}}$ ) for the case when  $Pr = 0.1$ ,  $\phi = \frac{\pi}{4}$  and  $Ra = 70000$ . (b) shows plots of the kinetic energy in  $\bar{u}$  (blue) and  $\bar{v}$  (red) against time for the same case.

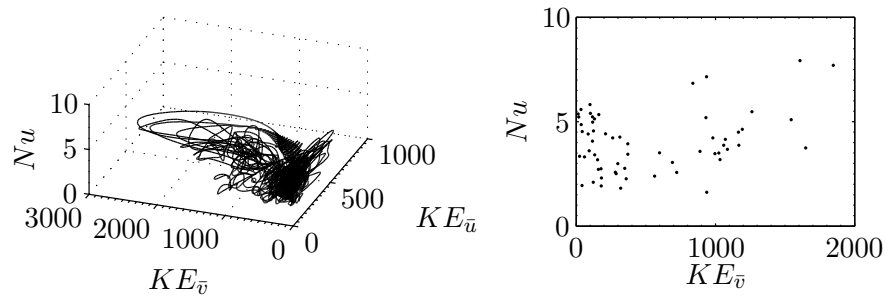


Figure 6.12: Phase space and alongside it a Poincaré section for the relaxation oscillation case shown in figure 6.11. The cut through phase space is taken at  $KE_{\bar{u}} = 300$ .

periodic to QP to chaotic to relaxation oscillations, but in addition, for large  $Ra$ , when  $\phi = \frac{\pi}{4}$ , the solution goes chaotic again, and when  $\phi = \frac{\pi}{6}$ , the solution goes steady again. As in the  $Pr = 1$  case, the large  $Ra$  steady solutions that occur when  $\phi = \frac{\pi}{6}$  appear as large-scale structures and analysis of  $Nu$  shows that the convection is more effective at transporting heat for these steady solutions. Also as in the  $Pr = 1$  case, the large-scale solutions occur when the solutions move from being chaotic to being steady, we do not present the analysis for  $Pr = 0.1$  here, as it is the same as in the  $Pr = 1$  case.

### Comparison of $Pr = 1$ with $Pr = 0.1$

The progression through a series of different types of solution is common to both  $Pr = 1$  and  $Pr = 0.1$ . However, when  $Pr = 0.1$ , we observed an extra type of solution in which relaxation oscillations are observed, these were not found when  $Pr = 1$ . When  $Pr = 0.1$ , the bifurcations and transitions occur at lower  $Ra$  than when  $Pr = 1$ , this is to be expected given that the critical  $Ra$  is lower for the smaller  $Pr$ . As the rotation vector is tilted from the vertical, the critical  $Ra$  is increased in both cases. Unlike in the  $Pr = 1$  case, when  $Pr = 0.1$  and  $\phi = \frac{\pi}{2}$  the solution becomes periodic at relatively low  $Ra$ . When  $\phi = \frac{\pi}{6}$ , both the  $Pr = 1$  and  $Pr = 0.1$  cases experience a regime where the solution returns to a steady state and large-scale flows are produced. These are met with an increased efficiency of heat transfer by convection, indicated by the large  $Nu$  that occurs with such solutions. The  $Pr = 1$  streamfunction close to onset is of a smaller length scale than the  $Pr = 0.1$  streamfunction close to onset. However, in both cases, as  $Ra$  increases, the scale of the solution also increases. As expected, the convection acts to make the layer more isothermal in the interior and near the boundaries two boundary layers form. This is seen in both the  $Pr = 1$  and  $Pr = 0.1$  cases.

### Robustness of large-scale solutions

We have seen that, when  $\phi = \frac{\pi}{6}$  and  $Ta = 10^5$ , the solution returns to a steady state (after being very time-dependent) and this has been found to occur when  $Pr = 1$  and when  $Pr = 0.1$ , albeit at different  $Ra$ . In addition to the parameters already discussed, we have investigated whether similar large-scale solutions exist for other parameters, as shown in table 6.1. Whilst it is difficult to draw definite conclusions from this data, it does appear that, the smaller  $Pr$  and  $\phi$  are, the more likely large-scale solutions are to exist, and persist, for higher  $Ta$ . For example, large-scale solutions are found for  $Pr = 1$ ,  $Ta = 10^5$ ,  $Ra = 7 \times 10^5$  and  $\phi = \frac{\pi}{6}$  (run 2), but if we increase  $\phi$  (run 12) then we are no longer able to find any large-scale solutions. Furthermore, if  $Ta$  is increased to  $10^6$ , then the only large-scale steady solutions that have been found occur when  $Pr = 0.1$ . For  $Pr = 1$ , the largest rotation rate at which large-scale solutions have been found is  $Ta = 1.5 \times 10^5$ .

Run	$Pr$	$Ta$	$Ra$	$\phi$	Steady? Y/N
1	0.1	$10^5$	$1.5 \times 10^5 - 3 \times 10^5$	$\frac{\pi}{6}$	Y
2	1	$10^5$	$7 \times 10^5 - 2 \times 10^6$	$\frac{\pi}{6}$	Y
3	0.1	$10^6$	$3 \times 10^5 - 5 \times 10^6$	$\frac{\pi}{12}$	Y
4	0.1	$1.2 \times 10^5$	$3 \times 10^5$	$\frac{\pi}{6}$	Y
5	0.1	$2 \times 10^5$	$3 \times 10^5$	$\frac{\pi}{6}$	N
6	1	$1.5 \times 10^5$	$1.5 \times 10^6$	$\frac{\pi}{6}$	Y
7	1	$2 \times 10^5$	$1.5 \times 10^6$	$\frac{\pi}{6}$	N
8	1	$1.5 \times 10^5$	$9 \times 10^5$	$\frac{\pi}{6}$	Y
9	1	$2 \times 10^5$	$9 \times 10^5$	$\frac{\pi}{6}$	N
10	1	$10^4$	$1 \times 10^6$	$\frac{\pi}{6}$	Y
11	1	$10^5$	$1 \times 10^6$	$\frac{\pi}{5}$	N
12	1	$10^5$	$7 \times 10^5$	$\frac{\pi}{5.5} - \frac{\pi}{2}$	N
13	1	$5 \times 10^5$	$9 \times 10^5$	$\frac{\pi}{12}$	N
14	1	$10^4$	$10^7$	$\frac{\pi}{6}$	Y

Table 6.1: A table to show in which runs large-scale steady solutions occur. Also shown, are runs with parameters close to those runs which have large-scale solutions but which are not found to reach the high  $Nu$ , steady states in which the large-scale structures are observed.

## 6.3 Mean flows

Having investigated some more general properties of convection, we now focus on the mean flows driven, as this is a primary aim of our study. As we saw in Chapter 1, convection is capable of driving mean flows. The strength and direction of these flows is governed by the parameters of the system. In particular, we are interested in the effects of small  $Pr$  and the tilted rotation vector on the driving of these flows. The mean flows in the  $x$  and  $y$  directions are denoted  $\bar{u}$  and  $\bar{v}$  respectively, and they are defined in section 5.5.1. One way to characterise the size of mean flows produced is from their energy. The kinetic energy in the mean flow can be described in two ways, as explained in section 5.5.3. The different measures of kinetic energy can be used as a measure of the “mean” of the flow or as a measure of the “variability”. We consider the ratio of kinetic energy in the mean flow to the total kinetic energy in the perturbations, this will give us a measure of whether the change in energy of the mean flow is a direct result of the change in energy in the perturbation. For example, does  $\bar{u}$  decrease only because  $u$  does or is there some other process affecting the mean?

### 6.3.1 Effect of $\phi$ on mean flows

This section considers the effect of  $\phi$  on the mean flows driven by the system. Figure 6.13 (a) shows plots of the ratio of the variability measure to total kinetic energy against  $Ra$  (top row) and  $\frac{Ra}{Ra_c}$  (bottom row) for  $Pr = 1$ . The left column shows plots relating to  $\bar{u}$  and the right column relates to  $\bar{v}$ . Figure 6.13 (b) contains the equivalent plots for the mean measure. From (a) and (b), for  $Ra$  sufficiently above its critical value and for  $Ra \leq 6 \times 10^5$ , we see that both measures of the kinetic energy in  $\bar{v}$  are largest when  $\phi = \frac{\pi}{6}$ , followed by  $\phi = \frac{\pi}{4}$  and then  $\phi = \frac{\pi}{2}$ . At  $Ra \approx 6 \times 10^5$ ,  $\phi = \frac{\pi}{6}$ , the energy in  $\bar{v}$  drops significantly, this corresponds to the value of  $Ra$  at which the solution changes regime from chaotic back to steady (cf. section 6.2.4) and after this point,  $\phi = \frac{\pi}{4}$  gives the largest mean flows. This hierarchy suggests that, when in the chaotic regime, the more the rotation vector is tilted from the vertical the bigger the flow driven in the plane of the rotation vector ( $\bar{v}$ ), but when not in the chaotic regime, only small mean flows are generated.

In general,  $\bar{u}$  is smaller than  $\bar{v}$ , this can be seen from figure 6.13; the kinetic energy in  $\langle \bar{u} \rangle$  is an order of magnitude less than the kinetic energy in  $\langle \bar{v} \rangle$ . We might expect  $\bar{u} < \bar{v}$ , as  $\bar{u}$  is the mean flow in a direction perpendicular to the plane in which the tilted rotation vector lies and so it is free to fluctuate in all directions. Despite being much smaller in magnitude, the mean

measure of  $\bar{u}$  still gives a larger mean flow for a tilted rotation vector compared to the  $\phi = \frac{\pi}{2}$  case. Comparing the size of the mean and the variability measures for  $\bar{v}$ , we see that they are similar, suggesting  $\bar{v}$  does not have too many fluctuations about zero and is a fairly systematic flow. However, comparing the size of the mean and variability measures for  $\bar{u}$  we find that the mean measure is an order of magnitude smaller than the variability measure, indicating that  $\bar{u}$  is highly varying in time. For  $\phi = \frac{\pi}{2}$ , the rotation vector is vertical, and there is no preferred direction for the mean flow. Therefore, we expect the mean measure in this case to be zero, as flows in all directions should cancel on time-averaging. This is in fact observed in figure 6.13 (b). However, in the variability measure all contributions are squared first and thus, for  $\phi = \frac{\pi}{2}$ , there is a nonzero energy in the mean flow.

The kinetic energies are calculated by considering averages taken over a long period of time, but it is interesting to analyse the time-dependent nature of the flows. Figure 6.14 fixes  $Ra = 2 \times 10^5$ ,  $Pr = 1$  and displays  $\bar{u}$  and  $\bar{v}$  as a function of  $z$  and  $t$  for  $\phi = \frac{\pi}{2}$ ,  $\phi = \frac{\pi}{4}$  and  $\phi = \frac{\pi}{6}$ . Plotted alongside the time-dependent plots are plots of the time-averaged  $z$ -structure of the mean flow. Clearly,  $\langle \bar{v} \rangle$  is largest for  $\phi = \frac{\pi}{6}$  and then  $\phi = \frac{\pi}{4}$ , as we expect from the previous energy analysis. We also see the more systematic nature of  $\bar{v}$  for  $\phi = \frac{\pi}{4}$  and  $\phi = \frac{\pi}{6}$ , it is mostly all of one sign in the lower half of the layer, and mostly all of the other sign in the top half of the layer, whereas,  $\bar{u}$  is more variable, leading to a smaller mean. This is all consistent with the energy plots in figure 6.13. For  $\phi = \frac{\pi}{2}$ , we see that there is a significant mean flow driven, up to 60 units, but the flow is in all directions and so averages to a small mean. If we average over a long enough time period then we would expect this mean to go to zero, as we saw in figure 6.13 (b). The vertical structure of  $\langle \bar{u} \rangle$  and  $\langle \bar{v} \rangle$  is very similar for  $\phi = \frac{\pi}{4}$  and  $\phi = \frac{\pi}{6}$ . We see that, the  $\phi = \frac{\pi}{6}$  mean flows are of the same form as the  $\phi = \frac{\pi}{4}$  flows but slightly larger in magnitude. When  $\phi = \frac{\pi}{2}$  the form is very different - but that is to be expected as we do not really expect there to be a mean flow at all when  $\phi = \frac{\pi}{2}$ .

### 6.3.2 Effect of $Pr$ on mean flows

To investigate the effect of  $Pr$  on the mean flows driven, we fix  $\phi = \frac{\pi}{4}$ . Plots of the ratios of the different measures of kinetic energy in the flow to the total kinetic energy are shown in figure 6.15. From the plots of the mean measure of kinetic energy with  $Pr = 0.1$  and  $Ra = 1.5 \times 10^5$  (see figure 6.15 (b), red lines), we notice a jump in the energy. This jump coincides with a change from a chaotic regime, where bursting is evident, to a chaotic regime where no bursting is observed, the flows are more systematic in the latter case and therefore this explains the jump. When comparing

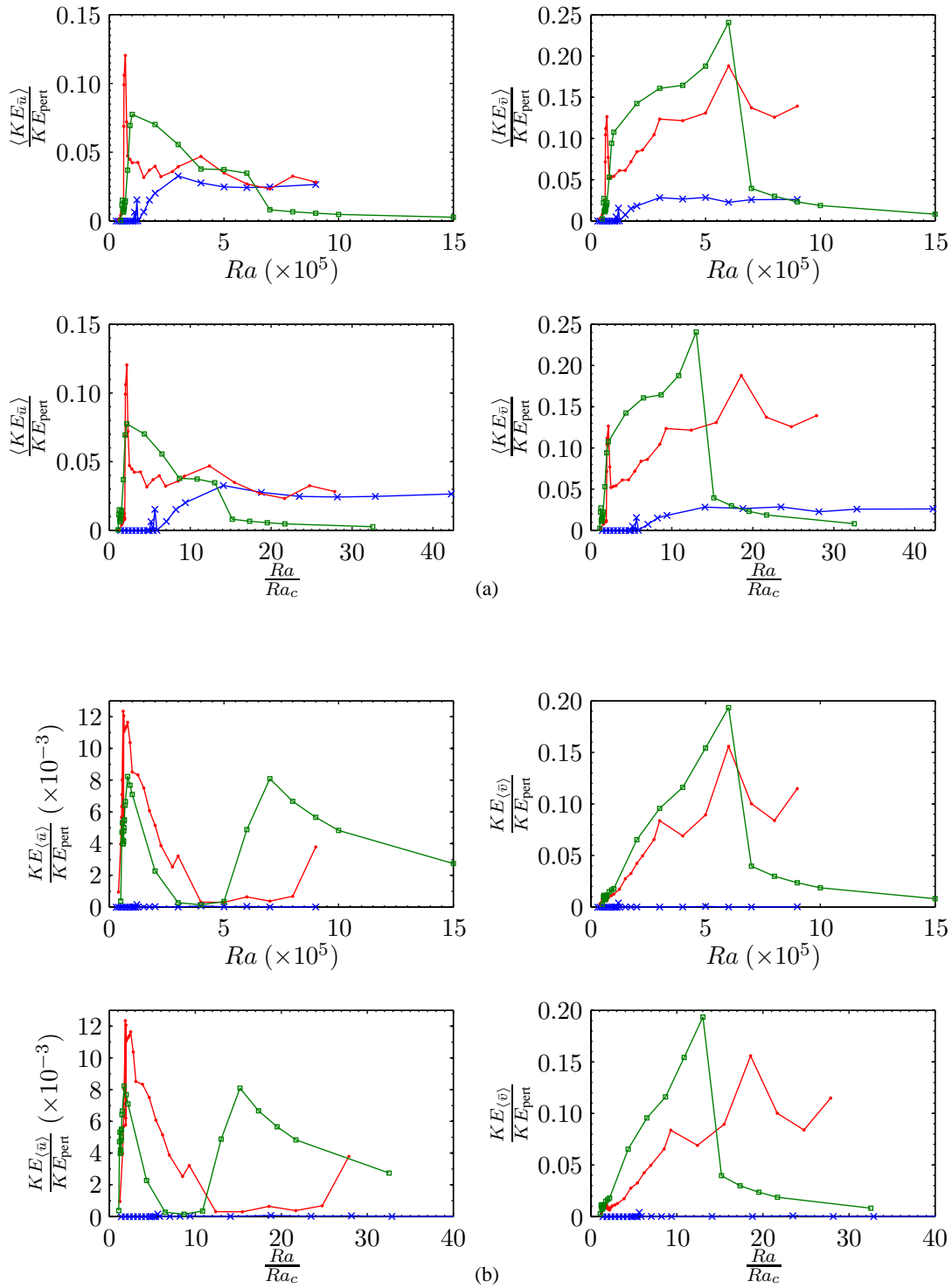


Figure 6.13: Ratios of the kinetic energy in  $\bar{u}$  and  $\bar{v}$  to the kinetic energy in the perturbations calculated using, in (a), the variability measure ( $\langle KE_{\bar{\xi}} \rangle$ ), and in (b), the mean measure ( $KE_{\langle \bar{\xi} \rangle}$ ), for  $Pr = 1$ ,  $\phi = \frac{\pi}{2}$  (blue, crosses),  $\phi = \frac{\pi}{4}$  (red, dots) and  $\phi = \frac{\pi}{6}$  (green, squares). In each case, the top row shows plots of the ratios against  $Ra$  and the bottom row against  $\frac{Ra}{Ra_c}$ .

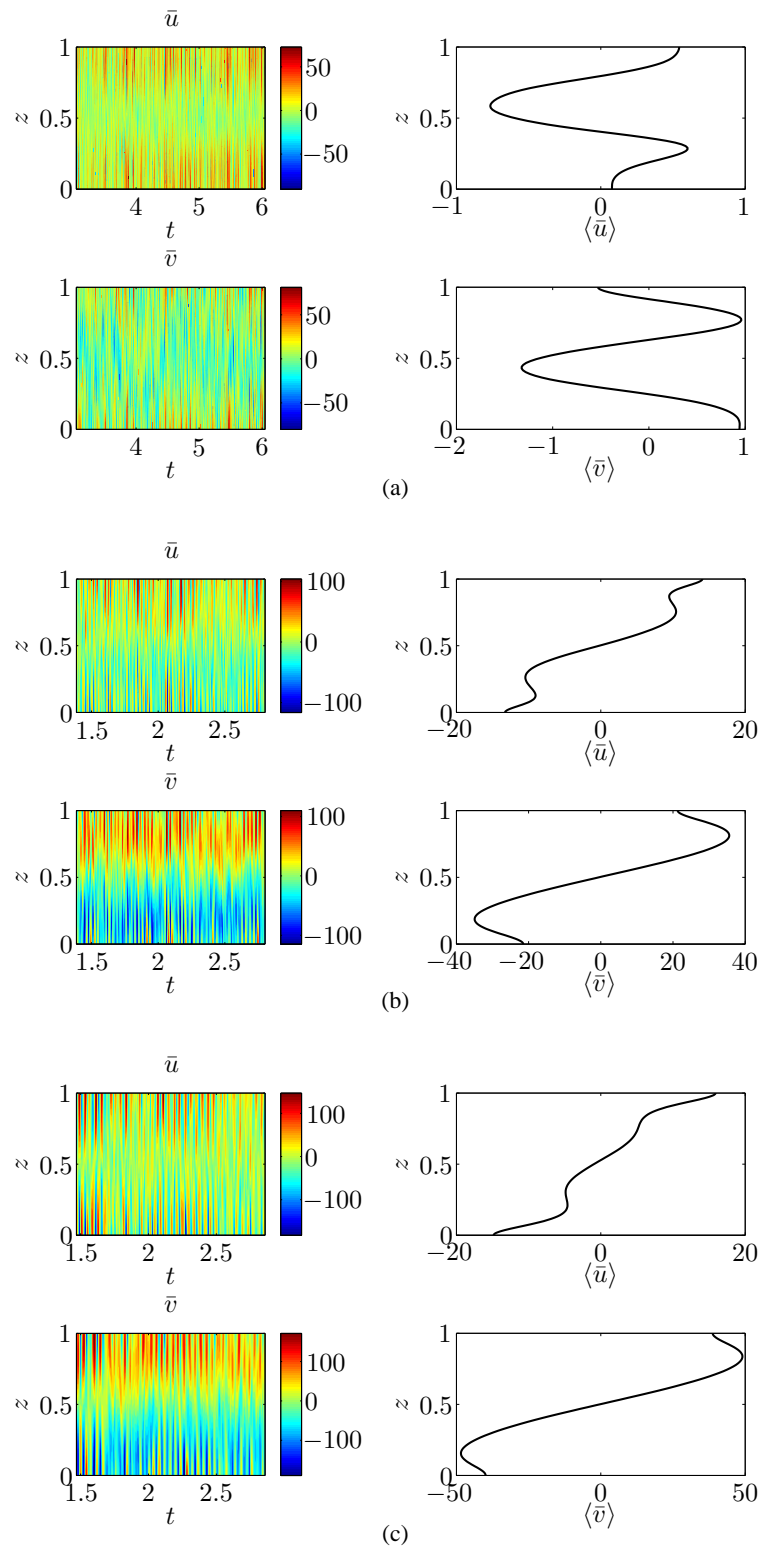


Figure 6.14: Contour plots of the mean flows  $\bar{u}(z, t)$ ,  $\bar{v}(z, t)$  and their corresponding time-average  $\langle \bar{u} \rangle$ ,  $\langle \bar{v} \rangle$  as a function of  $z$ . In all cases,  $Pr = 1$  and  $Ra = 2 \times 10^5$  but  $\phi$  is varied. In (a)  $\phi = \frac{\pi}{2}$ , in (b)  $\phi = \frac{\pi}{4}$ , and in (c)  $\phi = \frac{\pi}{6}$ .

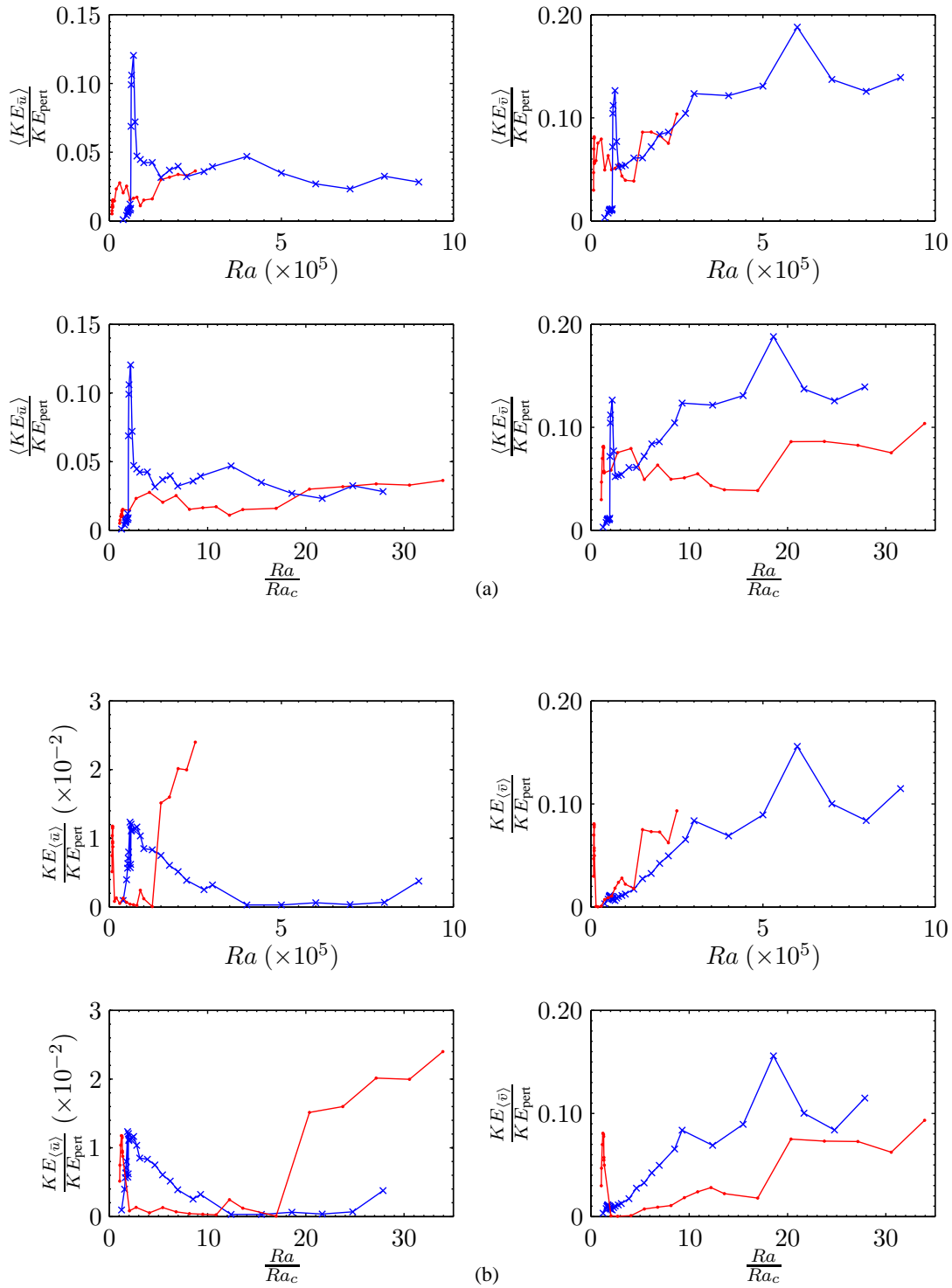


Figure 6.15: Ratios of the kinetic energy in  $\bar{u}$  and  $\bar{v}$  to the kinetic energy in the perturbations calculated using, in (a), the variability measure ( $\langle KE_{\bar{\xi}} \rangle$ ) and in (b), the mean measure ( $KE_{\langle \bar{\xi} \rangle}$ ), for  $\phi = \frac{\pi}{4}$ ,  $Pr = 1$  (blue, crosses) and  $Pr = 0.1$  (red, dots). The top row shows plots of the ratios against  $Ra$  and the bottom row against  $\frac{Ra}{Ra_c}$ .

the kinetic energies at different  $Pr$ , the conclusions depend on whether we compare them at fixed  $Ra$  or fixed  $\frac{Ra}{Ra_c}$ . This difference is more important here, than when changing  $\phi$  for example, since reducing  $Pr$  from one to 0.1 reduces  $Ra_c$  by approximately a factor of 10. For large enough  $Ra$ , the energy as given by the variability measure (figure 6.15 (a)) is approximately the same for both  $Pr$ . However, the mean measure is larger for  $Pr = 0.1$  and so the smaller  $Pr$  gives the more systematic mean flows. For fixed  $\frac{Ra}{Ra_c}$ , the variability energy in  $\bar{v}$  is much larger for  $Pr = 1$  than for  $Pr = 0.1$ , which results in  $Pr = 1$  also having the larger mean measure even though  $Pr = 0.1$  is more systematic. In contrast, for large enough  $\frac{Ra}{Ra_c}$ , the variability measure of  $\bar{u}$  is similar for both  $Pr$  and so the mean measure of  $\bar{u}$  is largest for  $Pr = 0.1$  because the  $Pr = 0.1$  flow is more systematic. As was seen in figure 6.13, by comparing the magnitude of the mean and variability measures, it is again clear that  $\bar{v}$  is much more systematic than  $\bar{u}$ .

In figure 6.16, we show some examples of mean flows as functions of  $z$  and  $t$ , and their time-averaged counterparts, for fixed  $Ra$  or  $\frac{Ra}{Ra_c}$ . In (a) and (b),  $Ra$  and  $\phi$  are fixed but  $Pr$  is varied. From the time-dependent plots, the  $Pr = 1$  flows appear to fluctuate more in time, this agrees with the energy plots in figure 6.15. The  $Pr = 0.1$  flows are more systematic, i.e., they have a larger mean size even though their maxima and minima are smaller than the  $Pr = 1$  case.

In figure 6.16 (c) and (d),  $\frac{Ra}{Ra_c} \approx 20$  and  $\phi = \frac{\pi}{4}$  whilst  $Pr$  is varied. Now  $\langle \bar{v} \rangle$  is much bigger when  $Pr = 1$ , than when  $Pr = 0.1$ , owing to the increased supercriticality.  $\bar{u}$  is also larger in magnitude when  $Pr = 1$ , but  $\bar{u}$  is highly varying in this case and so averages to a smaller mean when  $Pr = 1$ , than when  $Pr = 0.1$ .

### 6.3.3 Reynolds stresses

Reynolds stresses are known to drive mean flows (see e.g., Hathaway & Somerville (1983), Brummell *et al.* (1998)). To analyse their role in mean flow generation, we consider the mean equations. We obtain these equations by horizontally averaging the momentum equation. The  $y$ -average of the  $x$ -component of the momentum equation (5.2.1) gives

$$\frac{\partial \bar{u}}{\partial t} - Pr \frac{\partial^2 \bar{u}}{\partial z^2} = Pr T a^{\frac{1}{2}} \sin \phi \bar{v} - \frac{\partial}{\partial z} \overline{uw}, \quad (6.3.1)$$

where we have used the fact that we have periodic boundary conditions in  $y$ ,  $w = -\frac{\partial \psi}{\partial y}$  and  $v = \frac{\partial \psi}{\partial z}$ . In a similar way, we take the  $y$ -average of the  $y$ -component of the momentum equation (5.2.1) to give (as in Hathaway & Somerville (1986))

$$\frac{\partial \bar{v}}{\partial t} - Pr \frac{\partial^2 \bar{v}}{\partial z^2} = -Pr T a^{\frac{1}{2}} \sin \phi \bar{u} - \frac{\partial}{\partial z} \overline{vw}. \quad (6.3.2)$$

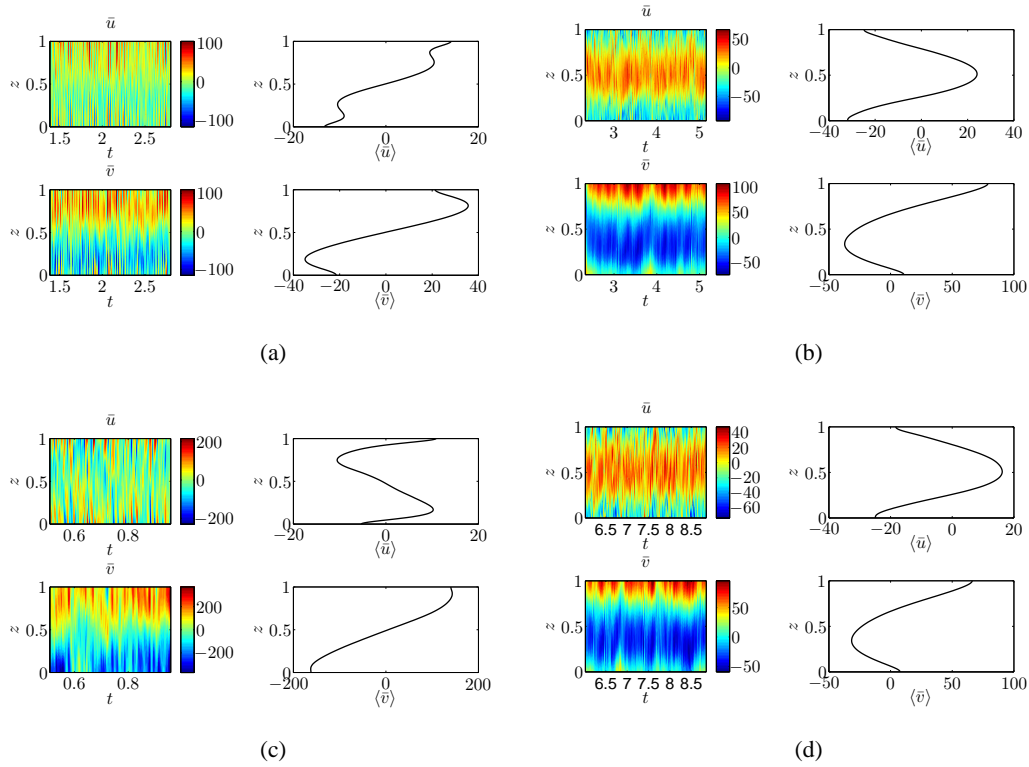


Figure 6.16: Contour plots of the mean flows  $\bar{u}(z, t)$ ,  $\bar{v}(z, t)$  and their corresponding time-average  $\langle \bar{u} \rangle$ ,  $\langle \bar{v} \rangle$  as a function of  $z$ . In (a),  $\phi = \frac{\pi}{4}$ ,  $Ra = 2 \times 10^5$  and  $Pr = 1$ , in (b),  $\phi = \frac{\pi}{4}$ ,  $Ra = 2 \times 10^5$  and  $Pr = 0.1$ , in (c),  $\phi = \frac{\pi}{4}$ ,  $Ra \approx 20Ra_c$ ,  $Ra = 7 \times 10^5$  and  $Pr = 1$ , and in (d),  $\phi = \frac{\pi}{4}$ ,  $Ra \approx 20Ra_c$ ,  $Ra = 1.5 \times 10^5$  and  $Pr = 0.1$ .

By integrating over a long enough time period to assume a steady state, the time derivative can be neglected, and this, after rearranging, gives

$$Pr \langle \bar{u} \rangle = \frac{Pr}{Ta^{\frac{1}{2}} \sin \phi} \frac{\partial^2 \langle \bar{v} \rangle}{\partial z^2} - \frac{1}{Ta^{\frac{1}{2}} \sin \phi} \frac{\partial}{\partial z} \langle \bar{v} \bar{w} \rangle, \quad (6.3.3)$$

$$Pr \langle \bar{v} \rangle = -\frac{Pr}{Ta^{\frac{1}{2}} \sin \phi} \frac{\partial^2 \langle \bar{u} \rangle}{\partial z^2} + \frac{1}{Ta^{\frac{1}{2}} \sin \phi} \frac{\partial}{\partial z} \langle \bar{u} \bar{w} \rangle. \quad (6.3.4)$$

The quantities  $\overline{uw}$ ,  $\overline{vw}$  are the Reynolds stresses, they measure the correlation between the horizontal and vertical velocity components. With a tilted rotation vector we might expect these correlations to be nonzero. We note, from equations (6.3.3) and (6.3.4), that it is the  $z$ -derivative of  $\langle \bar{v} \bar{w} \rangle$  that drives  $\langle \bar{u} \rangle$  and the  $z$ -derivative of  $\langle \bar{u} \bar{w} \rangle$  that drives  $\langle \bar{v} \rangle$ . Note also the dependence of the equations on  $Pr$  - we shall comment on this further shortly. In what follows, for both equations, we refer to the term on the left-hand side as the mean flow term, the first term on the right-hand side as the viscous term and the second term on the right-hand side as the Reynolds stress (RS) term.

We saw before, in section 6.3.1, that when  $\phi = \frac{\pi}{2}$ ,  $\langle \bar{u} \rangle$  and  $\langle \bar{v} \rangle$  are small. By considering the RS terms of equations (6.3.3) and (6.3.4) we see why. In figure 6.17 (a) and (b),  $\phi = \frac{\pi}{2}$ , and in (c) and (d),  $\phi = \frac{\pi}{4}$ , for  $Ra = 2 \times 10^5$  and  $Pr = 1$ . In (a) and (c), the RS term driving  $\bar{u}$  is plotted, i.e.,  $\frac{\partial(\overline{vw})}{\partial z}$ , and in (b) and (d), the RS term driving  $\bar{v}$  is plotted, i.e.,  $\frac{\partial(\overline{uw})}{\partial z}$ . The magnitude, as given by the colour bar, is only slightly higher in the  $\phi = \frac{\pi}{4}$  cases, yet, it is clear that in the  $\phi = \frac{\pi}{4}$  cases the correlations are much stronger, with a positive band evident in the upper half-plane and a negative band in the lower half-plane, resulting in the systematic mean flows observed in figure 6.14. In contrast, in the  $\phi = \frac{\pi}{2}$  cases the correlations are highly fluctuating in time such that they average to a small value and hence there are no systematic flows for vertical rotation.

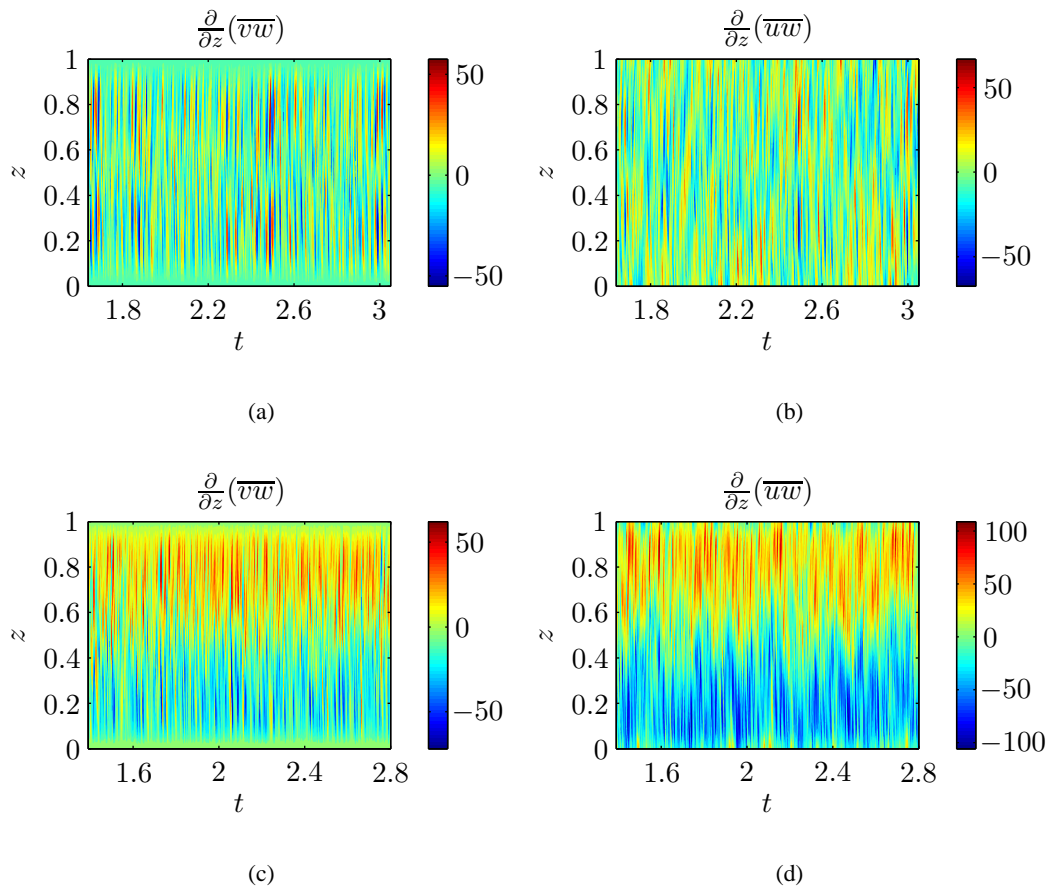


Figure 6.17: Contour plots of the Reynolds stresses terms given by  $\frac{\partial(\overline{vw})}{\partial z}$  in (a) and (c) and  $\frac{\partial(\overline{uw})}{\partial z}$  in (b) and (d). In all cases,  $Pr = 1$  and  $Ra = 2 \times 10^5$  but in (a) and (b),  $\phi = \frac{\pi}{2}$ , and in (c) and (d),  $\phi = \frac{\pi}{4}$ .

Next, we analyse the size of the terms that contribute to the size of the mean flows, given in (6.3.3) and (6.3.4), for different  $Pr$ . To do this, we plot each of the terms in equations (6.3.3) and (6.3.4)

as a function of  $z$ . From figure 6.18, we see that the dominant balance is between the mean flow term (blue) and the Reynolds stress term (red) with a less significant contribution from the viscous term (green). We note that, for  $Pr = 1$ , the mean flow terms and the mean flows themselves are identical, and so a solid blue line is not visible in figure 6.18 as it lies beneath the black line. We see that, the viscous term contributes to  $\bar{u}$  more than it does to  $\bar{v}$ , this is because the viscous term affecting  $\bar{u}$  depends on  $\bar{v}$  which tends to be larger than  $\bar{u}$ , whilst the viscous term affecting  $\bar{v}$  depends on  $\bar{u}$ .

Comparing the  $Pr = 1$  and  $Pr = 0.1$  cases, we observe that the  $Pr = 0.1$  flows are bigger, even though the correlations are smaller for  $Pr = 0.1$  than they are for  $Pr = 1$ . However, the factor of  $Pr$  in equations (6.3.3) and (6.3.4) means that for smaller  $Pr$ , a larger mean flow can be driven even for smaller Reynolds stresses. Similarly, the  $Pr$  factor in the viscous terms means that as  $Pr$  is decreased, the magnitude and vertical structure of the mean flows are increasingly dominated by the Reynolds stresses.

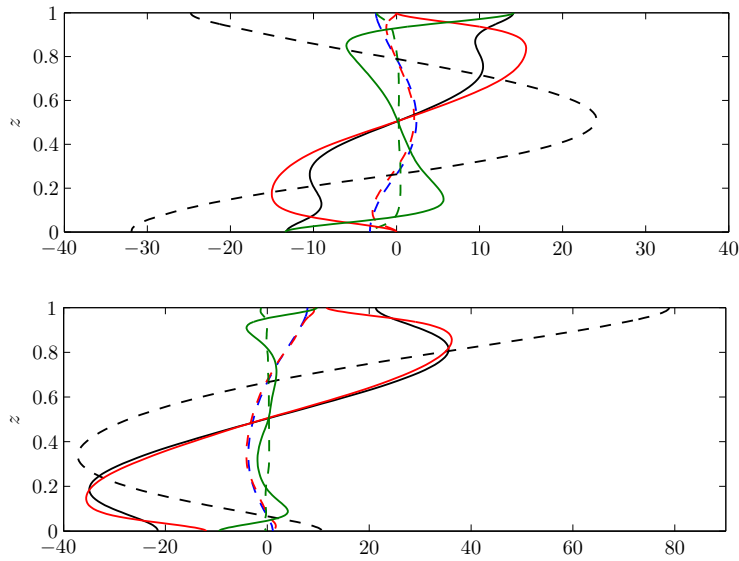


Figure 6.18: Top: each of the terms in equation (6.3.3) driving  $\bar{u}$ . Bottom: each of the terms in equation (6.3.4) driving  $\bar{v}$ . In both cases the terms are plotted as a function of  $z$  for  $Ra = 2 \times 10^5$ ,  $Ta = 10^5$  and  $\phi = \frac{\pi}{4}$ . The solid lines represent  $Pr = 1$  and the dashed lines represent  $Pr = 0.1$ . In blue are the mean flow terms, in red are the Reynolds stress terms and in green are the viscous terms. Also plotted are the mean flows (black) without the  $Pr$  factor.

Figure 6.19 shows plots of each of the terms in equations (6.3.3) and (6.3.4) but now  $\frac{Ra}{Ra_c}$  is held constant. As in figure 6.18,  $\bar{v}$  is dominated by the Reynolds stress term with a small contribution

from the viscous term. Again,  $\bar{u}$  is also dominated by the Reynolds stress term, but the viscous term for  $Pr = 1$  is also significant. As explained before, this is due to  $\bar{v}$  being much larger than  $\bar{u}$ . In this case, the Reynolds stress terms are much larger for  $Pr = 1$  than for  $Pr = 0.1$  and as a result the mean flows driven are larger, especially  $\bar{v}$ , even when the  $Pr$  factors in equations (6.3.3) and (6.3.4) are taken into account.

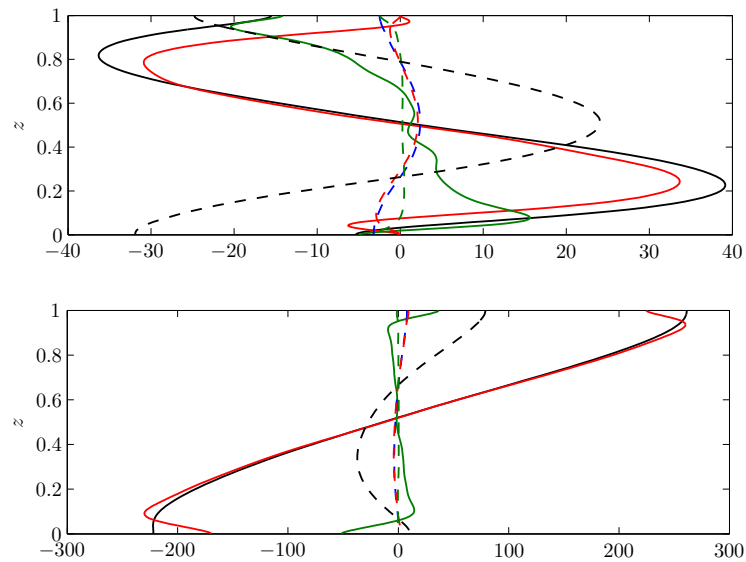


Figure 6.19: Top: each of the terms in equation (6.3.3) driving  $\bar{u}$ . Bottom: each of the terms in equation (6.3.4) driving  $\bar{v}$ . In both cases the terms are plotted as a function of  $z$  for  $Ra = 27Ra_c$ ,  $Ta = 10^5$  and  $\phi = \frac{\pi}{4}$ . The solid lines represent  $Pr = 1$  and the dashed lines represent  $Pr = 0.1$ . In blue are the mean flow terms, in red are the Reynolds stress terms and in green are the viscous terms. Also plotted are the mean flows (black) without the  $Pr$  factor.

## 6.4 Addition of a thermal wind

We now study our system with an imposed horizontal temperature gradient, i.e.,  $T_y \neq 0$ . As discussed previously (see section 2.3.2), this results in a thermal wind that has vertical shear. As mentioned in Chapter 1, specifically, section 1.4.3, there have been a number of studies involving the interaction of mean flow and shear. For example, see Hathaway & Somerville (1986, 1987) and Saito & Ishioka (2011), however, these studies impose the vertical shear rather than having the shear result from a latitudinal temperature gradient. Rashid *et al.* (2008), considered hydrodynamic instabilities in a system with a latitudinal temperature gradient, but they assume

a stable stratification and have baroclinic modes. As far as we are aware, there have been no published results of a nonlinear study of mean flows in a tilted plane layer with thermal wind shear.

Throughout this section, we fix  $T_y = -0.5$ , since, from Chapter 3, figure 3.4, the cells with a negative  $T_y$  have exaggerated poleward tilt and we might expect this to help drive mean flows. A negative  $T_y$  is representative of bodies with hotter equators and cooler poles.

We begin by considering the effect of  $T_y \neq 0$  on the nonlinear solutions. As we did for  $T_y = 0$  (section 6.2.1), we slowly increase  $Ra$  from its value at onset. Initially, we let  $Pr = 1$  and vary  $\phi$ , the results are shown in figure 6.20. In (a), we plot against  $Ra$  and in (b), we plot against  $\frac{Ra}{Ra_c}$ . As  $Ra$  is increased the solutions undergo a number of transitions and each type of solution is represented by a different symbol. Red squares represent steady solutions, blue circles represent periodic solutions, green triangles represent quasi-periodic solutions and light blue stars represent chaotic solutions.

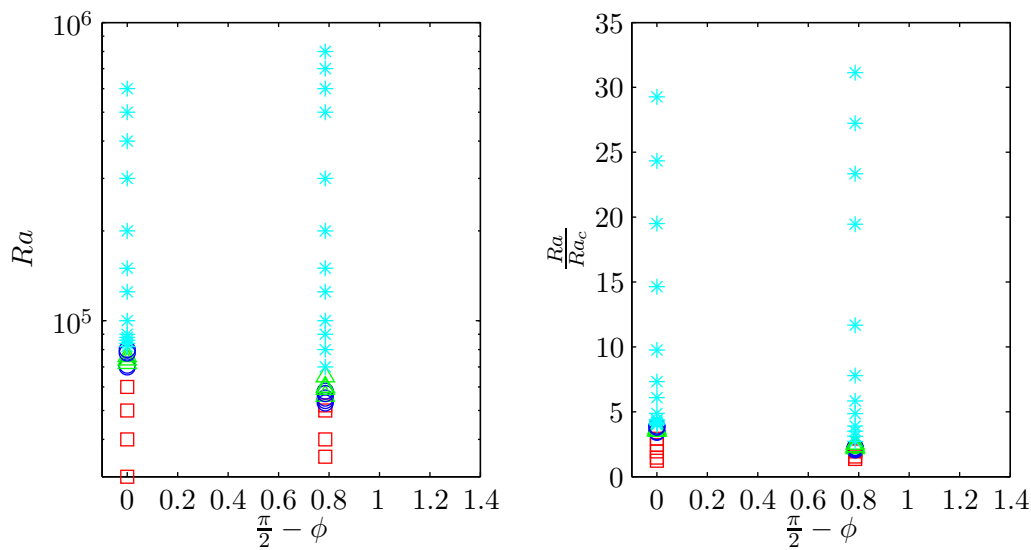


Figure 6.20: Regime diagram for solutions at fixed  $\phi$  and  $Ra$  for  $T_y = -0.5$ ,  $Pr = 1$ ,  $\phi = \frac{\pi}{2}$  and  $\phi = \frac{\pi}{4}$ . Red squares represent steady solutions, blue circles represent periodic solutions, green triangles represent quasi-periodic solutions and light blue stars represent chaotic solutions. The results are plotted against (a)  $Ra$ , and (b)  $\frac{Ra}{Ra_c}$ .

From Chapter 3, section 3.5.2, the critical Rayleigh number can be slightly altered when a thermal wind is introduced - for  $Pr = 1$  and  $T_y = -0.5$ , it is reduced. In this case,  $Ra_c = 2.05 \times 10^4$  for

$\phi = \frac{\pi}{2}$  and  $Ra_c = 2.57 \times 10^4$  for  $\phi = \frac{\pi}{4}$ . The regime diagram in figure 6.20 shows the solutions pass through the same sequence of bifurcations as when  $T_y = 0$  (see figure 6.1). However, with  $T_y = -0.5$ , the transition to chaos happens sooner (at a lower value of  $Ra$ ,  $\frac{Ra}{Ra_c}$ ) for both  $\phi = \frac{\pi}{2}$  and  $\phi = \frac{\pi}{4}$ .

### 6.4.1 Nonlinear solutions

To see the effect of the horizontal temperature gradient on the form of the nonlinear solutions, we plot contours of  $\psi(y, z)$  (see figure 6.21). In (a),  $Ra = 40000$  and we display a snapshot of a steady solution. The solution is similar in appearance to that when  $T_y = 0$ ; the convection cells are aligned with the tilt. In (b),  $Ra = 55000$  and the solution is oscillatory; in this case the cells are confined to the bulk of the layer, with little flow close to the boundaries. In (c),  $Ra = 60000$  and the neat convection cell pattern in (b) has been distorted. By  $Ra = 2 \times 10^5$ , the solution lies well within the chaotic regime, this is reflected in the more chaotic streamfunction we see in subfigure (d). Note as  $Ra$  has increased the length scale of the solutions has also increased, as was the case when  $T_y = 0$  (see figure 6.4).

Figure 6.22 shows the typical evolution of the temperature of a chaotic solution. In (a), contours of the basic state temperature,  $T_{BS} = 1 - z + T_y y$ , are shown as a function of  $y$  and  $z$ . Clearly evident is the temperature gradient in both the horizontal and vertical directions. In the basic state, the hottest fluid is at  $(y, z) = (0, 0)$  and the coolest fluid is at  $(y, z) = (L, 1)$ . Allowing the system to evolve, and correcting the basic state by the perturbation  $\theta(y, z)$ , to give the total temperature  $T(y, z) = 1 - z + T_y y + \theta(y, z)$ , gives the contours shown in (b), for one particular case. Whilst it is difficult to interpret exactly what has occurred physically, we can see that there has been a move to isothermalise the layer at fixed  $y$ . So, whilst the gradient in the  $y$ -direction still exists, the gradient in the  $z$ -direction has been diminished.

#### A note on large-scale solutions

In section 6.2.4, we remarked on large-scale solutions that were found when  $T_y = 0$  (see table 6.1), where in some cases, the solutions somewhat unexpectedly, returned to a steady state at large  $Ra$ . We have not found any such solutions when  $T_y = -0.5$ . Using the  $T_y = 0$  large-scale solution as an initial condition, and slowly increasing  $|T_y|$ , we were only able to find large-scale steady solutions at very small  $|T_y|$ , i.e.,  $|T_y| \leq 0.05$ . For larger  $|T_y|$ , the solutions remained chaotic.

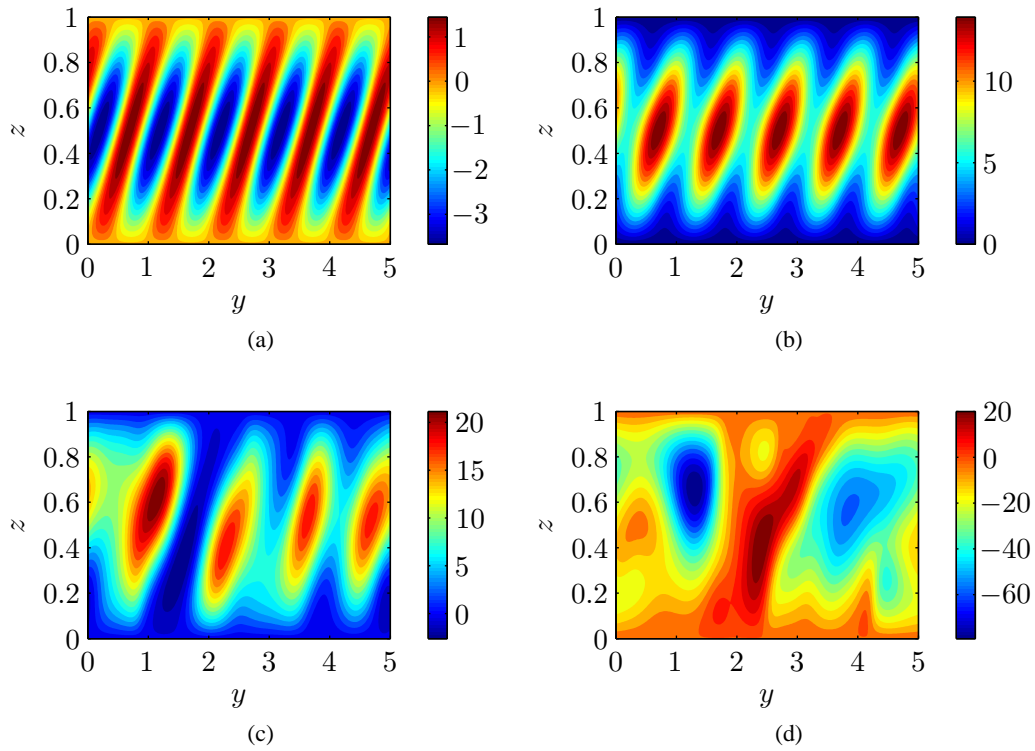


Figure 6.21: Contours of the streamfunction  $\psi(y, z)$  in a settled state for the case with  $Pr = 1$ ,  $\phi = \frac{\pi}{4}$  and  $T_y = -0.5$ . In (a),  $Ra = 40000$ , in (b),  $Ra = 55000$ , in (c),  $Ra = 60000$  and in (d),  $Ra = 2 \times 10^5$ .

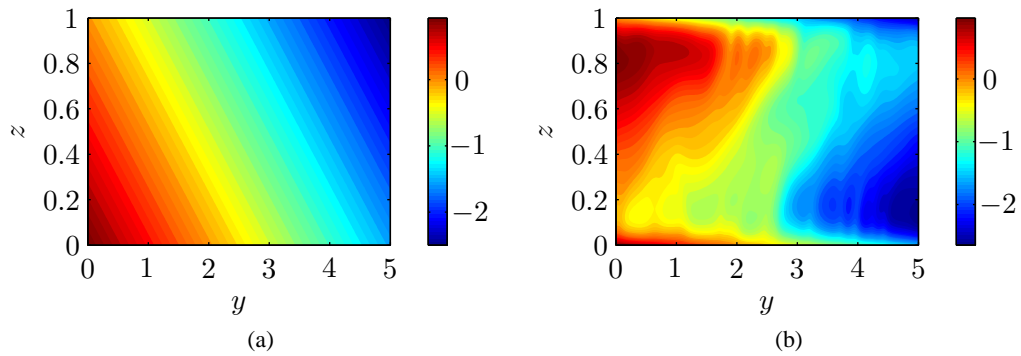


Figure 6.22: (a) Contours of the basic state temperature,  $T_{BS} = 1 - z + T_y y$ . (b) Contours of the total temperature  $T(y, z) = 1 - z + T_y y + \theta(y, z)$  after the system has been allowed to evolve in time, for the case with  $Pr = 1$ ,  $\phi = \frac{\pi}{4}$ ,  $T_y = -0.5$ , and  $Ra = 2 \times 10^5$ .

## 6.4.2 Interaction between convection and thermal wind shear

The thermal wind shear that balances the horizontal temperature gradient has an associated velocity which we use as our basic state velocity. The only non-zero component of this velocity

is in the  $x$ -direction and, from equation (2.3.59), is given by

$$U_{BS} = -\frac{T_y Ra \left(z - \frac{1}{2}\right)}{Ta^{\frac{1}{2}} \sin \phi}. \quad (6.4.5)$$

In our convecting system, as time evolves, two things can happen:

1. The convection can put energy into the shear and increase it.
2. The convection can extract energy from the shear and decrease it.

To assess which of these occurs, we define  $u_{total} = U_{BS} + u$  to be the total velocity in the  $x$ -direction. We are then interested in the kinetic energy in the total mean flow, i.e.,  $KE_{\bar{u}_{total}} = \frac{1}{2} \int_0^1 (\overline{U_{BS} + u})^2 dz$ . As before, we consider two measures of this, depending on how we take the time-average. The mean measure is given by

$$KE_{\langle \bar{u}_{total} \rangle} = \frac{1}{2} \int_0^1 (\langle \overline{U_{BS} + u} \rangle)^2 dz \quad (6.4.6)$$

and the variability measure is given by

$$\langle KE_{\bar{u}_{total}} \rangle = \frac{1}{2} \langle \int_0^1 \overline{(U_{BS} + u)^2} dz \rangle. \quad (6.4.7)$$

With these new quantities, (6.4.6) and (6.4.7), and the measures from section 5.5, we investigate the effect of a nonzero  $T_y$  on the mean flows driven.

Figure 6.23 (a) shows plots of the ratio of the variability measure to the total kinetic energy, for different  $\phi$ , against  $Ra$  (top row) and  $\frac{Ra}{Ra_c}$  (bottom row) for  $Pr = 1$  and  $T_y = -0.5$  and (b) shows plots of the ratio of the mean measure to the total kinetic energy against the same quantities. The left-hand columns of (a) and (b), show plots of  $\bar{u}$  and the right-hand columns, show plots of  $\bar{v}$ . The solid lines represent  $T_y = -0.5$  and the dotted lines are the  $T_y = 0$  results from before, for comparison. We see that the  $T_y = -0.5$  flows are generally more energetic than the  $T_y = 0$  flows (they have a higher variability measure of kinetic energy). In a similar way, we observe that the  $\phi = \frac{\pi}{4}$  cases are more energetic than the  $\phi = \frac{\pi}{2}$  cases. However, the larger  $\phi$  is, the larger the mean measure (at large enough  $Ra$ ) and so the larger  $\phi$  is, the more systematic the flow. Note that, as for  $T_y = 0$ ,  $\bar{v}$  is more systematic than  $\bar{u}$  when a thermal wind is present. Notice also that, unlike in the  $T_y = 0$  case, when  $\phi = \frac{\pi}{2}$ , a non-zero mean flow is driven. This is because of the basic state shear flow in the  $x$ -direction.

Figure 6.23 (c) plots the mean and variability measures of  $KE_{\bar{u}_{total}}$  as given by equations (6.4.6) and (6.4.7) against  $Ra$  (top row) and  $\frac{Ra}{Ra_c}$  (bottom row). The dashed lines represent the energy in  $U_{BS}$ , i.e., the energy in  $\bar{u}$  at  $t = 0$ , and so we can assess whether the shear is increased or

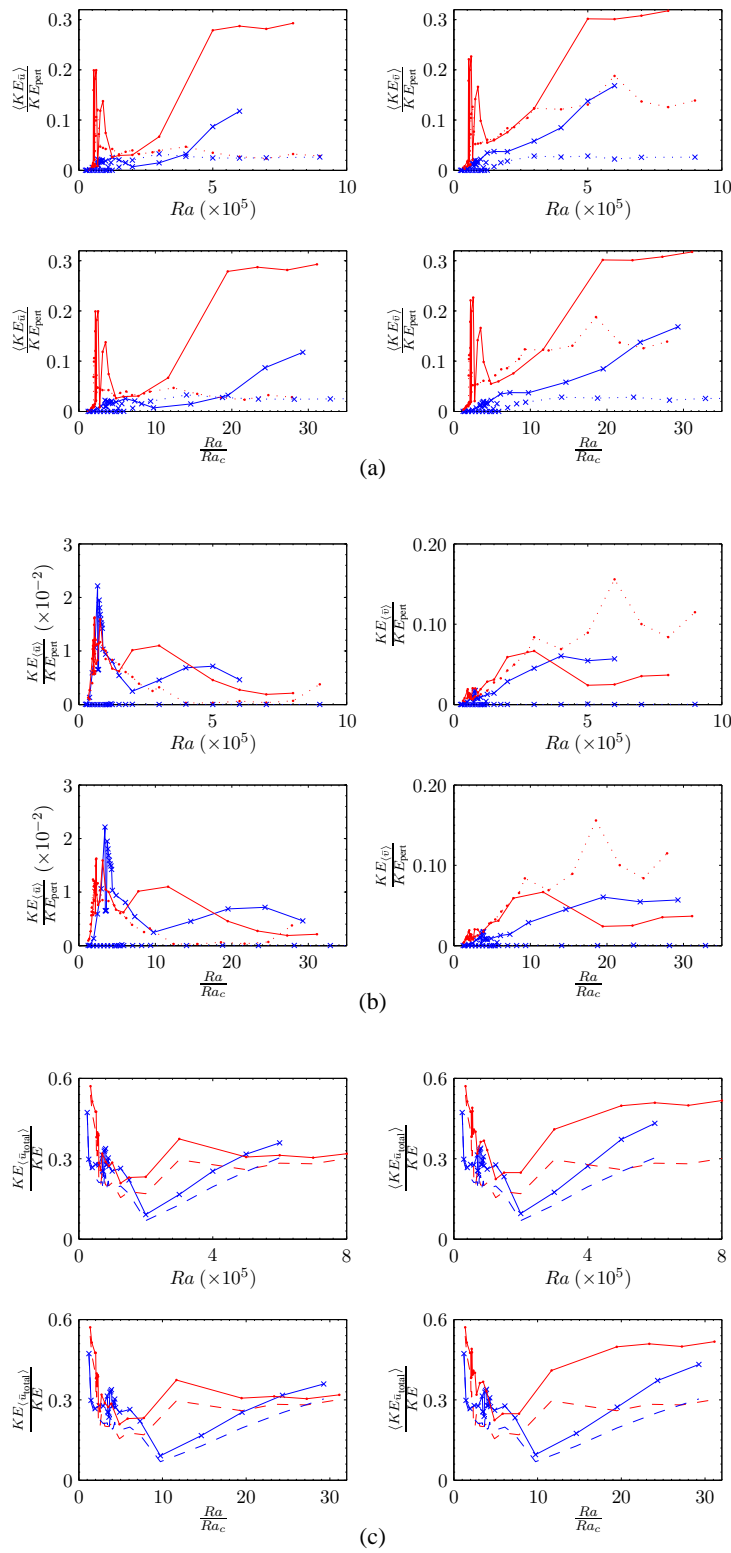


Figure 6.23: Ratio of the KE in the mean flows to KE in the perturbations calculated using (a) the variability measure and (b) the mean measure. The solid lines are for  $T_y = -0.5$  and the dotted lines are for  $T_y = 0$ . In (c), the ratio of the KE in  $\bar{u}_{total}$  to total KE is presented with dashed lines corresponding to the KE in  $U_{BS}$ . In all cases,  $Pr = 1$ , and the blue lines correspond to  $\phi = \frac{\pi}{2}$  and the red lines to  $\phi = \frac{\pi}{4}$ .

decreased over time. In this case, for both  $\phi$ , the mean measure gives an increase in the shear - this means there is less energy available to put into  $\bar{v}$  and hence could explain why, for  $\phi = \frac{\pi}{4}$ ,  $\bar{v}$  is smaller for  $T_y = -0.5$  than when  $T_y = 0$ .

Now let us consider the energy in the mean flows when  $\phi = \frac{\pi}{4}$  and the Prandtl number is varied, the results are shown in figure 6.24. In (a), is the variability measure of the energy in the flows and in (b), is the mean measure of the energy in the flows. Again, we see that the  $T_y = -0.5$  flows are generally more energetic than the  $T_y = 0$  flows (larger variability measure). To compare the different Prandtl numbers it is important to consider the difference between fixed  $Ra$  and fixed  $\frac{Ra}{Ra_c}$ , because of the difference in  $Ra_c$  between  $Pr = 1$  and  $Pr = 0.1$ . For fixed  $Ra$ , the  $Pr = 0.1$  flows are more energetic than for  $Pr = 1$ , and are more systematic. This results in  $\bar{v}$  having the largest mean when  $Pr = 0.1$ , which might be to be expected since  $Ra_c$  decreases with  $Pr$ , and so for fixed  $Ra$ , the system is more supercritical for  $Pr = 0.1$ . For small  $\frac{Ra}{Ra_c}$ , the behaviour is as for fixed  $Ra$ , but for large  $\frac{Ra}{Ra_c}$ , the energy, as given by the variability measure, is similar for  $Pr = 1$  and  $Pr = 0.1$ . However, for  $Pr = 0.1$  the flow in  $y$  is much more systematic, leading to a larger mean measure of  $\bar{v}$ .

Figure 6.24 (c), left-hand plots, give that the shear is increased for  $Pr = 1$  and decreased for  $Pr = 0.1$ . Therefore, for  $Pr = 1$ , there is less energy available for  $\bar{v}$  and we see that, for  $Pr = 1$ , the mean measure of  $\bar{v}$  for  $T_y = -0.5$  is smaller than for  $T_y = 0$ , but for  $Pr = 0.1$ , there is more energy available to put into  $\bar{v}$ , and this is consistent with the fact that  $\bar{v}$  is larger for  $T_y = -0.5$ , than it is for  $T_y = 0$ .

We can see examples of some of the characteristics described above by looking at the mean flows as a function of time and  $z$ . Figure 6.25 shows  $\bar{u}$  and  $\bar{v}$  as function of time and  $z$  and alongside the contour plots are the time-averaged mean flows for  $Ra = 2 \times 10^5$ ,  $Pr = 1$ ,  $T_y = -0.5$  and (a)  $\phi = \frac{\pi}{2}$  and (b)  $\phi = \frac{\pi}{4}$ . We see that the system with a tilted rotation vector drives a larger mean flow. This is what we expect from the plots of the mean kinetic energy in figure 6.23 (b), at  $Ra = 2 \times 10^5$ . Comparing with the equivalent plots when there is no thermal wind (figure 6.14 (a) and (b)), we see a difference between the  $\phi = \frac{\pi}{2}$  cases. When  $T_y = 0$ , the mean flow is small, but when  $T_y = -0.5$ , there is a significant mean flow with a preferred direction. When  $\phi = \frac{\pi}{4}$ , the mean flows are similar in that their structure in  $z$  appears to be qualitatively the same. But we do see that the mean flows are larger in the thermal wind case. This is in agreement with the energy plots in figure 6.23 (b), at  $Ra = 2 \times 10^5$ .

In figure 6.26 we vary  $Pr$  whilst keeping  $\phi = \frac{\pi}{4}$ ,  $Ra = 2 \times 10^5$  and  $T_y = -0.5$ . In this case,  $\langle \bar{u} \rangle$  is largest when  $Pr = 1$ , whereas  $\langle \bar{v} \rangle$  is largest when  $Pr = 0.1$ . This concurs with the energy

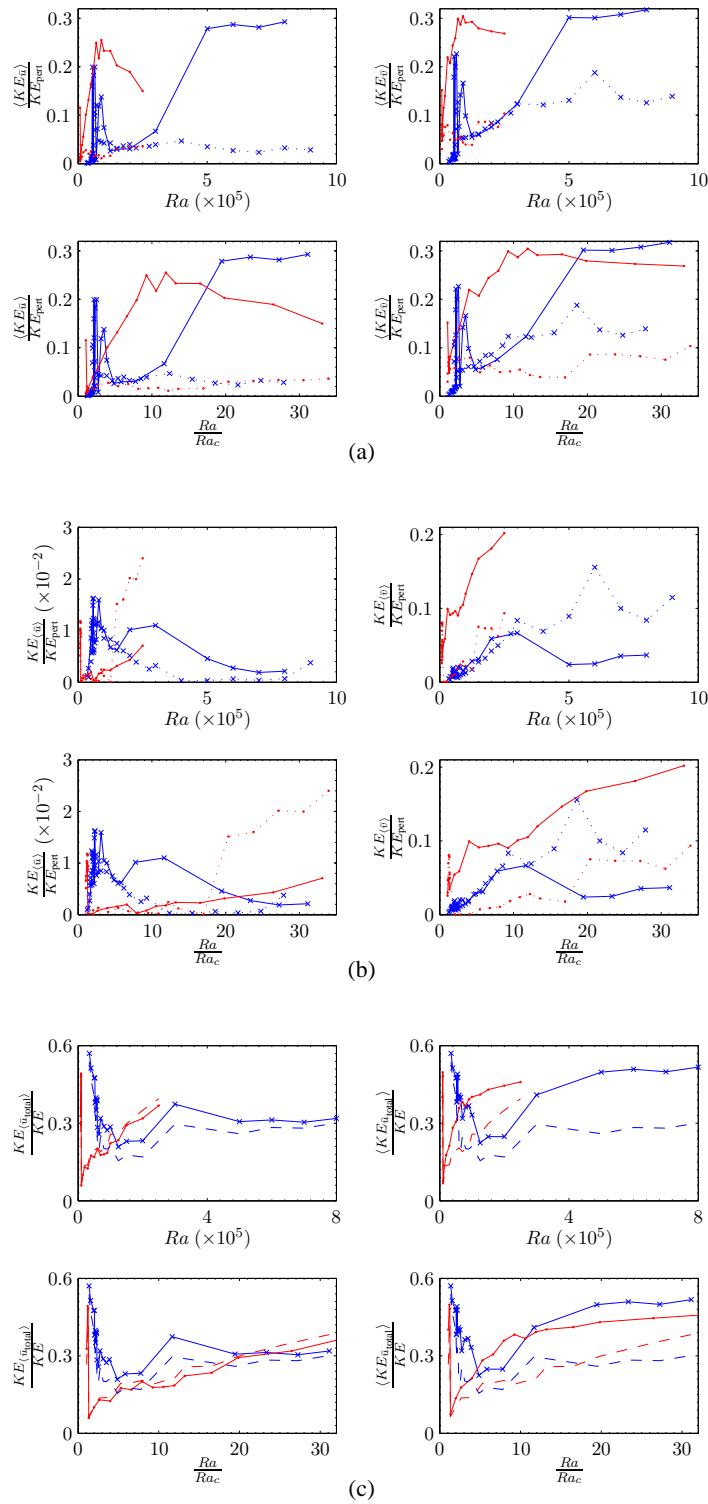


Figure 6.24: Ratio of the KE in the mean flows to KE in the perturbations calculated using (a) the variability measure and (b) the mean measure. The solid lines are for  $T_y = -0.5$  and the dotted lines are for  $T_y = 0$ . In (c), the ratio of the KE in  $\bar{u}_{total}$  to total KE is presented with dashed lines corresponding to the KE in  $U_{BS}$ . In all cases,  $\phi = \frac{\pi}{4}$ , and the blue lines correspond to  $Pr = 1$  and the red lines to  $Pr = 0.1$ .

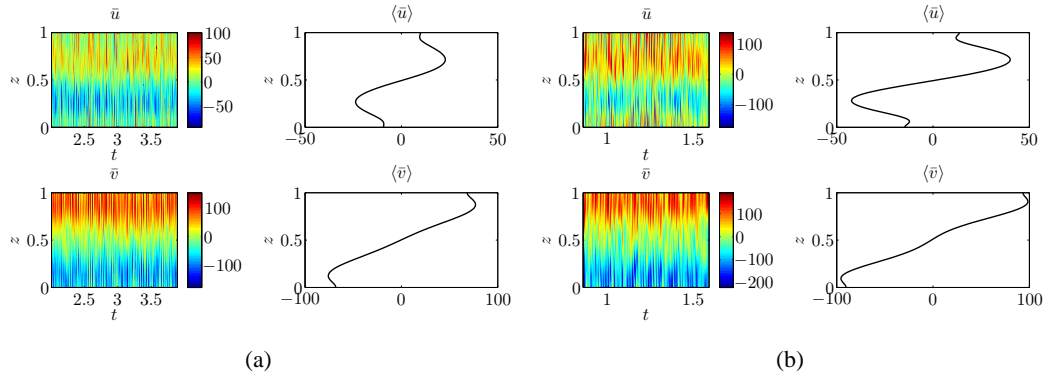


Figure 6.25: Contour plots of the mean flows  $\bar{u}(z, t)$ ,  $\bar{v}(z, t)$  and their corresponding time-average  $\langle \bar{u} \rangle$ ,  $\langle \bar{v} \rangle$  as a function of  $z$ . In (a) and (b),  $Pr = 1$ ,  $T_y = -0.5$  and  $Ra = 2 \times 10^5$  but  $\phi$  is varied. In (a)  $\phi = \frac{\pi}{2}$  and in (b)  $\phi = \frac{\pi}{4}$ .

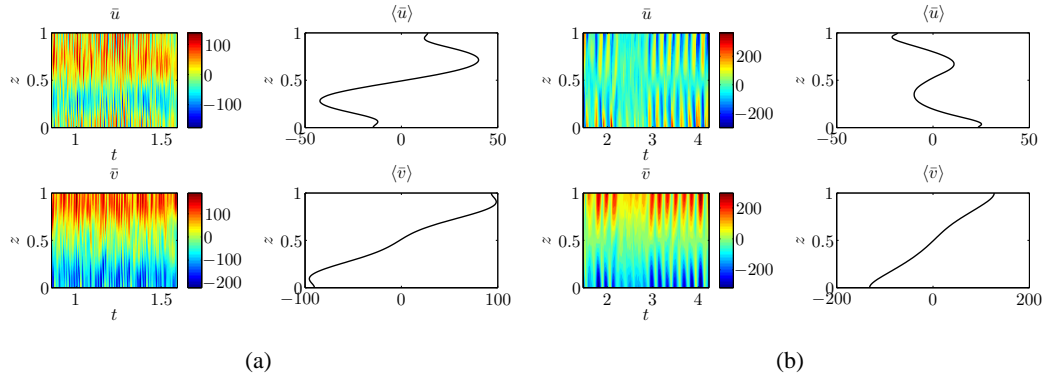


Figure 6.26: Contour plots of the mean flows  $\bar{u}(z, t)$ ,  $\bar{v}(z, t)$  and their corresponding time-average  $\langle \bar{u} \rangle$ ,  $\langle \bar{v} \rangle$  as a function of  $z$ . In both cases  $\phi = \frac{\pi}{4}$ ,  $T_y = -0.5$  and  $Ra = 2 \times 10^5$  but in (a)  $Pr = 1$  and in (b)  $Pr = 0.1$ .

plots of figure 6.24. In both (a) and (b), for  $\bar{v}$ , the maximum magnitude is similar to the amplitude of the mean flow suggesting  $\bar{v}$  is systematic. On comparison with the  $T_y = 0$  case (fig 6.16 (a) and (b)), we see that the thermal wind case gives more energetic flows, especially for  $\bar{v}$ .

To assess whether the steepness of the gradient of shear is increased or decreased for a range of parameters we use the mean measure of energy in  $\bar{u}_{total}$ . This is because we want a measure of the gradient of velocity and so the sign of the velocity is significant. In the examples so far, whether or not the shear is increased or decreased has depended on  $Pr$  and  $\phi$ . We now examine this parameter dependence. Using the mean measure only, we determine whether the shear is increased or decreased for a number of different parameter regimes. The results are shown in figure 6.27. We hold two of  $\phi$ ,  $Pr$ ,  $Ra$  and  $Ta$  constant and vary the other two, marking points

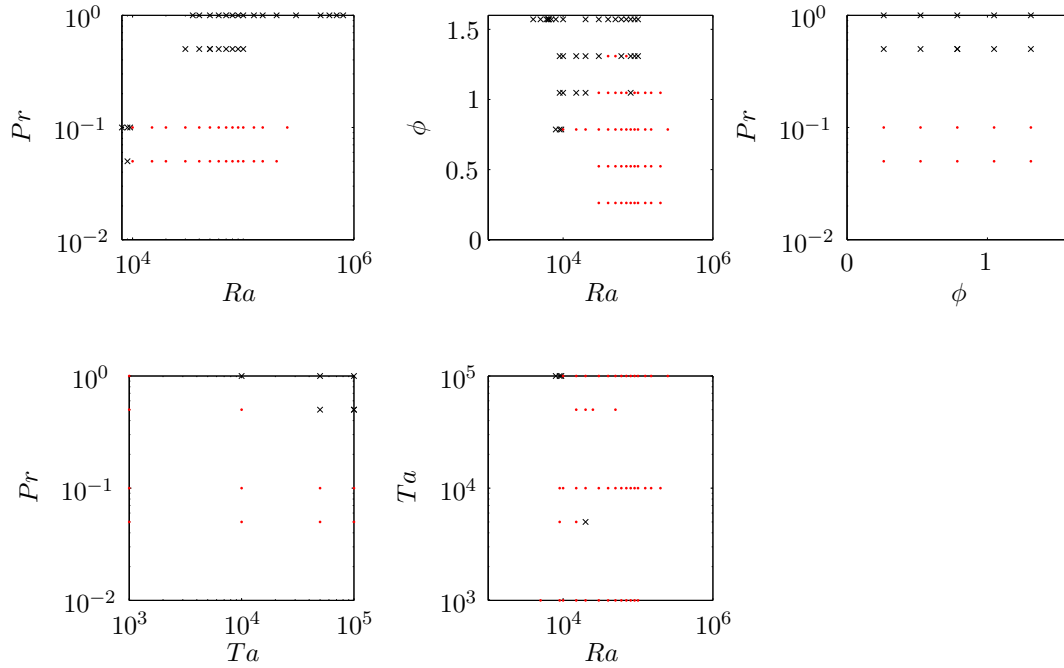


Figure 6.27: Regime diagram to show for which parameters the shear is increased, and for which the shear is reduced and energy extracted from the shear. Red dots indicate a decrease in shear and black crosses indicate an increase. In all cases  $T_y = -0.5$ .

in parameter space where  $KE_{\bar{u}_{total}} < KE_{UBS}$  (shear reduced) with a red dot and points where  $KE_{\bar{u}_{total}} > KE_{UBS}$  (shear increased) with a black cross. Although this is not a complete study of all possible parameters, we can still see some trends. In particular, as  $Pr$ ,  $Ta$  or  $\phi$  is decreased, or  $Ra$  is increased, the convection tends to extract energy from the shear. This can perhaps be explained if we consider the form of the shear. From equation (6.4.5), we have

$$\frac{dU_{BS}}{dz} = -\frac{T_y Ra}{Ta^{\frac{1}{2}} \sin \phi} \quad (6.4.8)$$

and so increasing  $Ra$ , or decreasing  $Ta$  or  $\phi$ , increases the basic state shear. If the basic state shear is strong, then we would expect the convection to act to reduce the shear by extracting energy from it, rather than increasing it further, this is in agreement with what we observe in our simulations.

### 6.4.3 Reynolds Stresses

Taking horizontal averages of the  $x$  and  $y$  components of the momentum equation, (5.2.1), gives the mean flow equations. Even if  $T_y \neq 0$ , we find the mean flow equations are exactly as in equations (6.3.1) and (6.3.2). That is, the mean flows do not explicitly depend on  $T_y$ . Changes

to the mean flows with  $T_y$  must occur due to the implicit dependence of the Reynolds stresses on  $T_y$ .

As before, we can consider contour plots of the Reynolds stresses as a function of time and  $z$ . Figure 6.28 has  $Ra = 2 \times 10^5$ ,  $Pr = 1$ ,  $T_y = -0.5$  and in (a) and (b),  $\phi = \frac{\pi}{2}$ , and in (c) and (d),  $\phi = \frac{\pi}{4}$ . In (a) and (c) are the RS terms responsible for driving  $\bar{u}$ , i.e.,  $\frac{\partial(\overline{vw})}{\partial z}$ , and in (b) and (d) are the RS terms responsible for driving  $\bar{v}$ , i.e.,  $\frac{\partial(\overline{uw})}{\partial z}$ . If we compare with figure 6.17, which has no thermal wind for the same parameter values, we see that the Reynolds stresses produced in the thermal wind case are larger in magnitude. We also notice that the RS terms in the  $\phi = \frac{\pi}{2}$  case are more systematic, leading to the significant mean flow we saw driven in the earlier example (see figure 6.25), this was not the case when  $T_y = 0$ .

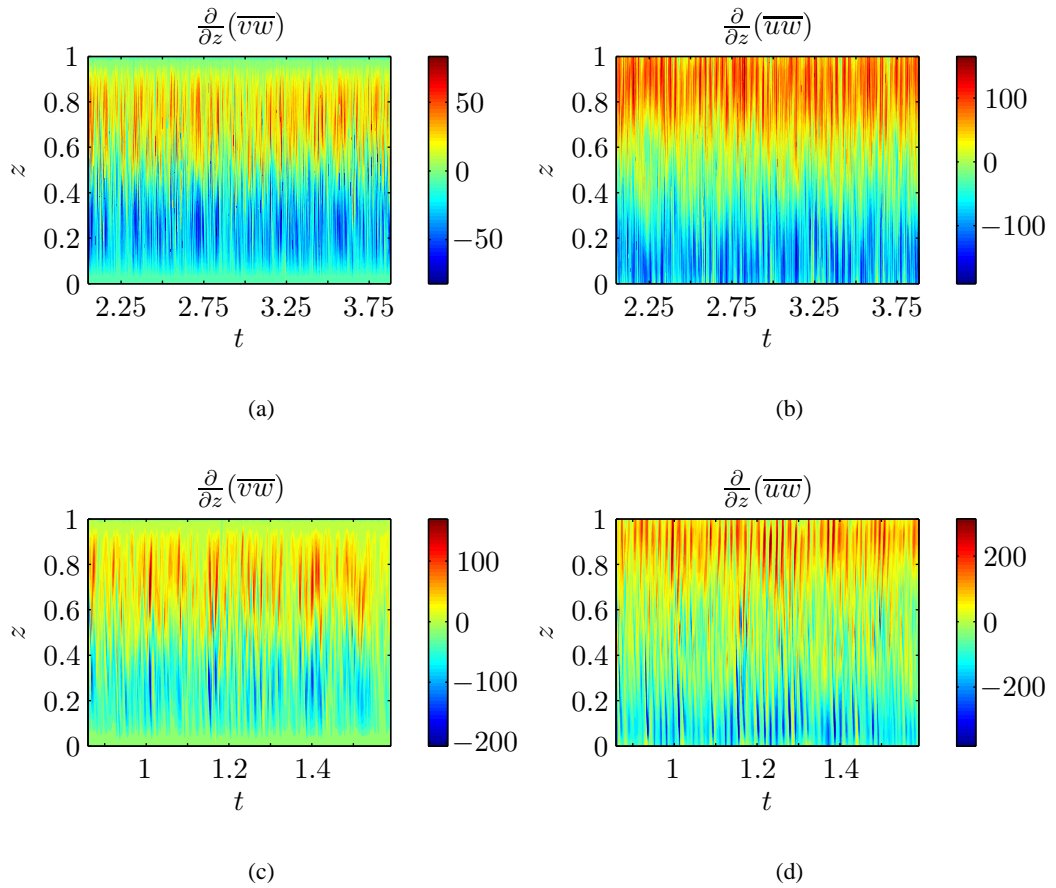


Figure 6.28: Contour plots of the Reynolds stresses terms given by  $\frac{\partial}{\partial z}(\overline{vw})$  in (a) and (c) and  $\frac{\partial}{\partial z}(\overline{uw})$  in (b) and (d). In all cases,  $Pr = 1$ ,  $Ra = 2 \times 10^5$  and  $T_y = -0.5$  but in (a) and (b),  $\phi = \frac{\pi}{2}$  and in (c) and (d),  $\phi = \frac{\pi}{4}$ .

We perform a similar analysis to the one in section 6.3.3, by plotting each of the terms in equation

(6.3.3) and (6.3.4) as a function of  $z$ . Figure 6.29 has  $Ra = 2 \times 10^5$ ,  $Ta = 10^5$ ,  $\phi = \frac{\pi}{4}$ ,  $T_y = -0.5$  and  $Pr = 1$  (solid) and  $Pr = 0.1$  (dashed). Again, it is noticeable that the Reynolds stresses in the  $Pr = 1$  case are significantly bigger than in the  $Pr = 0.1$  case, yet  $\bar{v}$  in the  $Pr = 0.1$  case is larger than in the  $Pr = 1$  case and  $\bar{u}$  is comparable for the two  $Pr$ . Comparing the thermal wind plots (figure 6.29) with the plots where  $T_y = 0$  (figure 6.18) we observe that  $\bar{v}$  is much larger when the thermal wind is present, this comes from the larger Reynolds stress driving that occurs when  $T_y \neq 0$ .

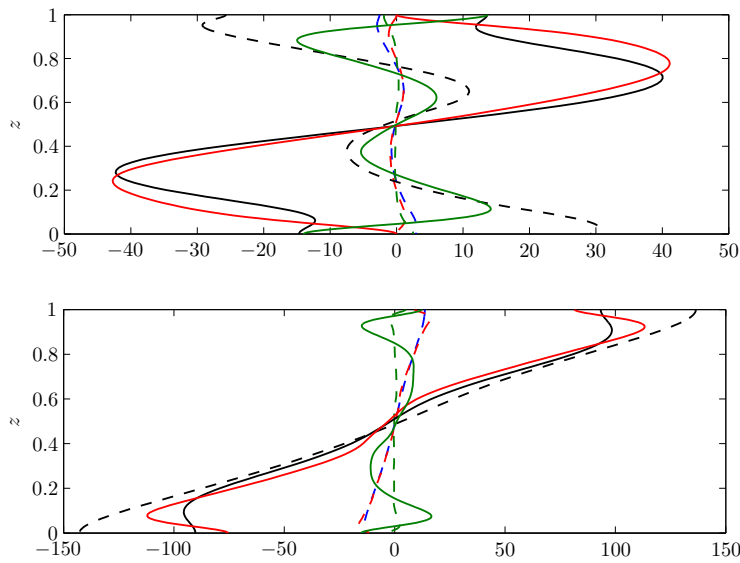


Figure 6.29: Top: each of the terms in equation (6.3.3) driving  $\bar{u}$ . Bottom: each of the terms in equation (6.3.4) driving  $\bar{v}$ . In both cases the terms are plotted as a function of  $z$  for  $Ra = 2 \times 10^5$ ,  $T_y = -0.5$ ,  $Ta = 10^5$  and  $\phi = \frac{\pi}{4}$ . The solid lines represent  $Pr = 1$  and the dashed lines represent  $Pr = 0.1$ . In blue are the mean flow terms, in red are the Reynolds stress terms and in green are the viscous terms. Also plotted are the mean flows (black) without the  $Pr$  factor.

Figure 6.30 shows the same terms as figure 6.29 but now  $\frac{Ra}{Ra_c}$  is held constant, rather than  $Ra$ . The dominant balance is still between the Reynolds stress term and the mean flow term, but  $\bar{u}$  has a significant contribution from the viscous term. As before, for fixed  $\frac{Ra}{Ra_c}$ , the Reynolds stress terms are much larger when  $Pr = 1$ , and even when considering the  $Pr$  factor in the equations, the mean flows are still larger for  $Pr = 1$ . Comparing with figure 6.19 (the equivalent plots for  $T_y = 0$ ) we see that the terms are of a similar size for  $\bar{v}$  when  $Pr = 1$ , but for  $Pr = 0.1$ ,  $\bar{v}$  is larger when a thermal wind is present as a result of increased Reynolds stresses.

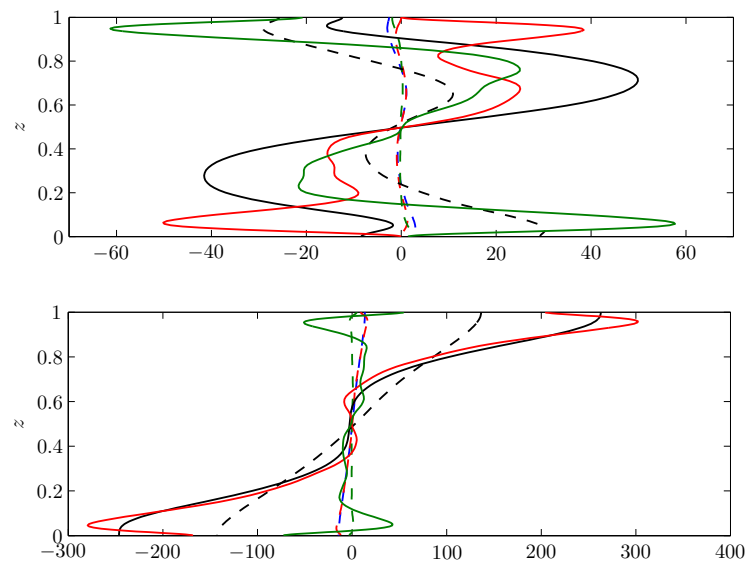


Figure 6.30: Top: each of the terms in equation (6.3.3) driving  $\bar{u}$ . Bottom: each of the terms in equation (6.3.4) driving  $\bar{v}$ . In both cases the terms are plotted as a function of  $z$  for  $Ra = 27Ra_c$ ,  $T_y = -0.5$ ,  $Ta = 10^5$  and  $\phi = \frac{\pi}{4}$ . The solid lines represent  $Pr = 1$  and the dashed lines represent  $Pr = 0.1$ . In blue are the mean flow terms, in red are the Reynolds stress terms and in green are the viscous terms. Also plotted are the mean flows (black) without the  $Pr$  factor.

## 6.5 Summary

The first part of the chapter considered nonlinear Boussinesq convection with a tilted rotation vector and a purely vertical temperature gradient (no thermal wind). We ran a number of simulations for a range of  $Ra$ , varying  $\phi$  and  $Pr$  (with  $Ta = 10^5$  in most cases). It was found that the solutions progressed through a series of different regimes as  $Ra$  was increased. The general pattern was to go from steady to oscillatory to quasi-periodic to chaotic, but when  $Pr = 0.1$  we found a slightly different regime which we referred to as the relaxation oscillation regime. In some cases, as  $Ra$  was increased, the solutions moved through the chaotic regime and steady solutions were again found. These were large-scale solutions which were found to be very efficient at transporting heat by convection. Although no strict relationship was found, it was noted that these solutions were more likely to persist at higher  $Ta$ , for smaller  $Pr$  and  $\phi$ . These large-scale solutions are perhaps a manifestation of the fact we have  $\frac{\partial}{\partial x} \equiv 0$ , and if we were to consider the full three-dimensional system, we may no longer find such large-scale, steady solutions. This is beyond the scope of this thesis but is discussed further in Chapter 9.

We are interested in the mean flows that can be driven by convection in our plane layer system. By tilting the rotation vector from the vertical we found non-trivial correlations which led to significant, systematic mean flows. With  $\phi = \frac{\pi}{2}$  (vertical rotation vector), all directions are equal and there is no preferred flow direction. The vertical structure of the mean flows was observed to be very similar between the tilted cases considered but very different between the tilted and untilted cases. Deriving the mean flow equations highlighted the Reynolds stress terms which are responsible for driving the mean flows. It was shown that for  $\phi = \frac{\pi}{2}$ , these terms are small on averaging, but for a tilted case, they form a systematic pattern on averaging. Smaller  $Pr$  does result in smaller RS terms but the  $Pr$  factor in the mean flow equations mean that, in fact, larger mean flows can result at smaller  $Pr$ .

The second part of the chapter considered the addition of a thermal wind (via a horizontal temperature gradient) to the above system. It was found that this caused the transition to chaos to occur over a smaller range of  $Ra$ . Large-scale solutions were only found at very small  $T_y$ , for larger  $|T_y|$ , the solutions remained chaotic. It was thought a thermal wind would aid the driving of mean flows and in general, adding a thermal wind did drive more energetic flows. We also demonstrated that even when the rotation vector is vertical, if  $T_y \neq 0$ , a nontrivial mean flow is driven. Derivation of the mean flow equations in the case when  $T_y \neq 0$ , gave no explicit dependence on  $T_y$  and so changes to the mean flows with  $T_y$  must occur due to the implicit

dependence of the Reynolds stresses on  $T_y$ . Generally, flows in the plane of the rotation vector ( $\bar{v}$ ) are more systematic than those that are not ( $\bar{u}$ ) but we save a discussion of the physical relevance of this for the concluding chapter (Chapter 9).

We studied the interaction of convection and thermal wind shear and showed it is possible for convection to put energy into, or extract energy from, the thermal wind shear. In particular, figure 6.24 showed that when  $Pr = 1$ , the shear is increased by the convection but when  $Pr = 0.1$ , the shear is decreased. More generally, we found that whether convection put energy into, or extracted energy from, the shear flow depended on the parameters  $Pr$ ,  $Ra$ ,  $Ta$  and  $\phi$ . We identified a general trend that decreasing  $Pr$ ,  $\phi$  or  $Ta$  tended to cause the convection to extract energy from the shear.

This study has been restricted to the two-dimensional case corresponding to the EW rolls of Chapter 3, i.e.,  $\frac{\partial}{\partial x} = 0$ . As predicted by the linear theory, NS rolls are stabilised upon addition of a strong enough thermal wind shear and we performed a number of nonlinear simulations to confirm this, but the results were not shown in this chapter.



## Chapter 7

# Nonlinear Anelastic Convection

### 7.1 Introduction

Until now, the nonlinear work we have presented has assumed the Boussinesq approximation (see section 2.3), but as discussed previously, it is more realistic to allow for density changes across the layer depth. To do this, we consider the system under the anelastic approximation, as derived in Chapter 2, section 2.4. The linear analysis of this anelastic system was carried out in Chapter 4. This chapter builds on that work to examine the nonlinear effects of stratification on the convection in our system. We first analyse the change the stratification makes to the dynamics, before assessing the impact on the mean flows driven. The numerical technique used to solve the nonlinear anelastic equations, (2.4.142)-(2.4.144), is similar to that used in the previous chapter, but there are some differences because of the  $z$ -dependence of the reference state. The details of the code used to solve the nonlinear anelastic equations were given in section 5.7.

### 7.2 Numerical results

To investigate the effect of stratification on our system, we vary  $\theta$ , as, from section 4.2,  $\theta$  can be thought of as a measure of compressibility. Throughout this chapter we fix the rotation rate at  $Ta = 10^5$ , the angle of the rotation vector at  $\phi = \frac{\pi}{4}$  and the size of the computational box at  $L = 5$ . We begin by examining the types of solution that occur for increasing  $|\theta|$ , whilst keeping  $Ra$  fixed. The results are shown in figure 7.1, where we have indicated the type of solution that occurs for a range of  $|\theta|$  and  $Ra$  values. We include the Boussinesq results (equivalent to setting  $\theta = 0$ ), in order to see directly, the difference between the stratified and non-stratified cases. For

$\theta = 0$ , apart from the solution at  $Ra = 50000$ , all the solutions shown are chaotic (denoted by a cross), but increasing  $|\theta|$  introduces another type of solution, the relaxation oscillation (denoted by a dot). This type of solution was described in detail in section 6.2.5 for Boussinesq convection. From the regime diagram, we see that once  $Ra$  is large enough, for all  $\theta \neq 0$  that we studied, the relaxation oscillation solution is the type of the solution we see. At  $Ra = 50000$  (the lowest  $Ra$  shown in figure 7.1), there also exist steady and quasi-periodic solutions, but we shall focus on the cases where the solutions are chaotic in this chapter.

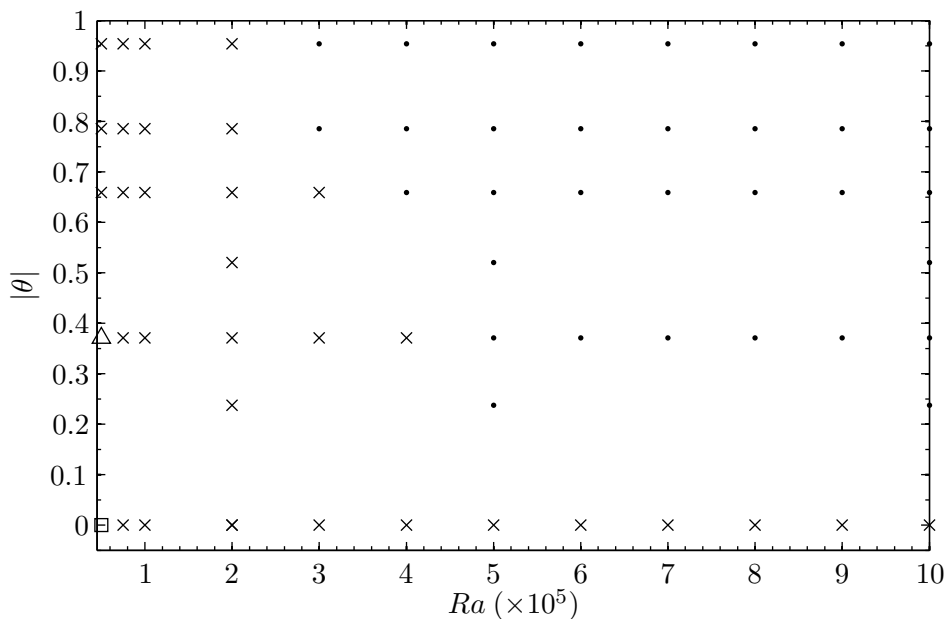


Figure 7.1: A regime diagram to show the types of solution that occur in our system, for different values of  $\theta$  and  $Ra$ . Steady solutions are denoted by a square, quasi-periodic solutions by a triangle, chaotic solutions by a cross and relaxation oscillation solutions by a dot. In all cases  $Pr = 1$ .

To see the difference between the chaotic and relaxation oscillation regimes, we show an example of the time series of the kinetic energy in the perturbations in each case, see figure 7.2. In (a), the solution is chaotic and this is characterised by the apparent random path of  $KE_{\text{pert}}$  in time. This is in contrast to (b), where the solution is in the relaxation oscillation regime, and we observe bursts of energy intermittently with chaotic behaviour present in between the bursts. We described the relaxation oscillation, or intermittent, regime in detail in section 6.2 where we were using the

Boussinesq approximation, but in that case we required  $Pr = 0.1$  to find any relaxation oscillation solutions.

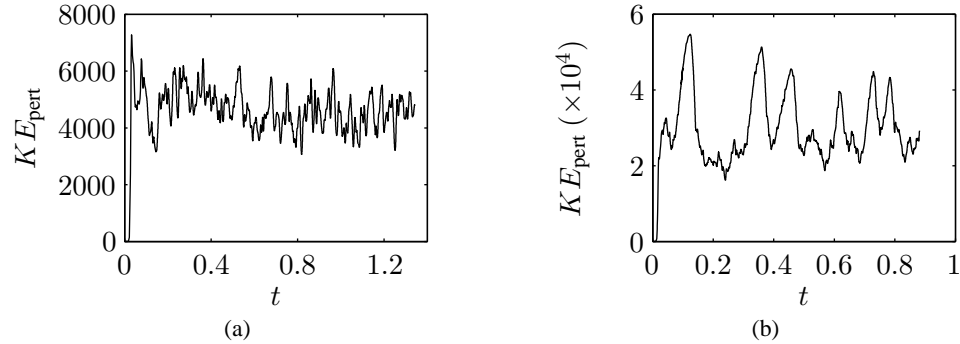


Figure 7.2: Time series of  $KE_{\text{pert}}$  for  $Pr = 1$ ,  $\theta = -0.79$  for a chaotic solution in (a) at  $Ra = 2 \times 10^5$  and a relaxation oscillation solution in (b) at  $Ra = 5 \times 10^5$ .

To analyse a large number of simulations more easily, we wish to be able to consider time-averages, but this needs to be done with caution. From figure 7.2 (a), we can see that averaging over a long enough time period will give reasonably steady statistics, independent of the time period we choose to average over, but from figure 7.2 (b), the statistics will depend on how many bursts are included in the time period over which the average is taken. In other words, the variance about a mean of the relaxation oscillation solution will be higher than that of a chaotic solution. This is demonstrated by considering the probability distribution of the kinetic energy in each case (see figure 7.3). In (a), there is a well defined peak of the distribution and much less power in the tails of the distribution. However, in (b), there is a much larger spread of the data. This information tells us that time-averaged data may not be the best measure for the intermittent solutions as there is a large variation of the flow in time, about the mean. To establish the effect of stratification on the system, we therefore focus on the chaotic solutions, as these are easier to characterise relatively accurately using time-averages.

To examine the effect of vertical stratification on the fluid velocity and entropy, we take a Boussinesq simulation and increase  $|\theta|$ . In doing so, we increase the contrast in density, pressure and temperature between the top and bottom of the layer. For ease of reference, we recall from section 4.2 that a contrast of 0.5 corresponds to  $\theta = -0.37$ , of 0.2 to  $\theta = -0.66$ , of 0.1 to  $\theta = -0.79$  and of 0.01 to  $\theta = -0.95$ . In figure 7.4, we show plots of the velocity for different  $\theta$ , we plot  $(v, w)$  as vectors in  $(y, z)$ . It is clear that as the stratification is increased, the asymmetry

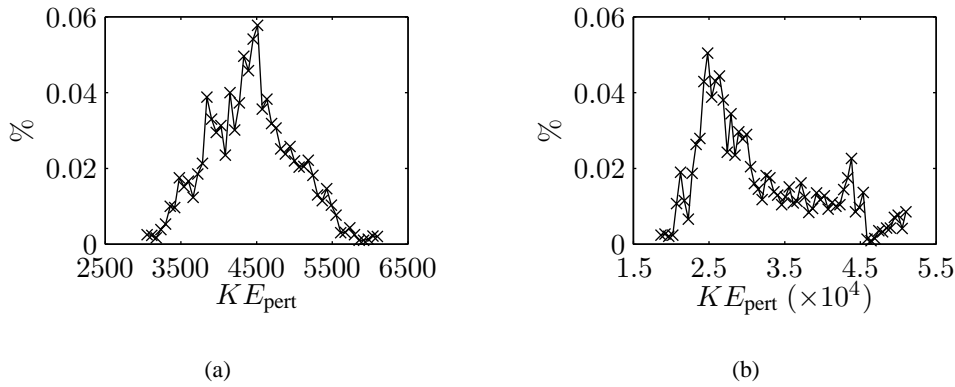


Figure 7.3: Relative distribution of  $KE_{\text{pert}}$  for the same parameters as used in figure 7.2. In (a) the mean is 4432.7951 and the standard deviation 566.7354. In (b), the mean is 31556.0515 and the standard deviation is 7743.3476

across the layer becomes stronger. For  $\theta = -0.37$ , this effect is small, but by  $\theta = -0.95$ , it has become very pronounced in that for each convection cell, the direction of flow at the top persists until much lower in the layer ( $z \sim 0.2$  for  $\theta = -0.95$  contrasted with  $z \sim 0.5$  for  $\theta \sim 0$ ).

In this anelastic model, it is the departure from adiabaticity that drives convection, i.e., we only get convection when there is a gradient of entropy across the layer. In this sense the entropy gradient can be thought of as analogous to the temperature gradient in Boussinesq convection. Figure 7.5 shows the total entropy, i.e.,

$$s_{\text{tot}} = \bar{s} + s = -\frac{1}{\theta} \ln(1 + \theta z) + s,$$

as a function of space at a snapshot in time for a number of different  $\theta$ . Again, the effect of the stratification becomes clear as  $|\theta|$  is increased; at small  $|\theta|$ , mixing has taken place, in a similar way to when  $\theta = 0$  and thin boundary layers have formed as a result of the fixed entropy boundary conditions. As  $|\theta|$  is increased, less mixing is able to take place and there remain strong entropy gradients across the layer. Hence, increasing the strength of the stratification makes it harder for the convection to redistribute the entropy.

Taking an average of  $s_{\text{tot}}$  (over  $y$  and time) leads to the profiles shown in figure 7.6. The dashed lines show the basic state profiles, and the solid lines show the equivalent (i.e., for the same  $\theta$ ) profiles after the simulations have been carried out; each colour represents a different  $\theta$ . We see that, for all  $\theta$ , the convection acts to make the layer closer to being isentropic, but, how close it gets depends on  $\theta$ . In other words, when  $|\theta|$  is small, e.g.,  $\theta = -0.37$ , most of the layer is

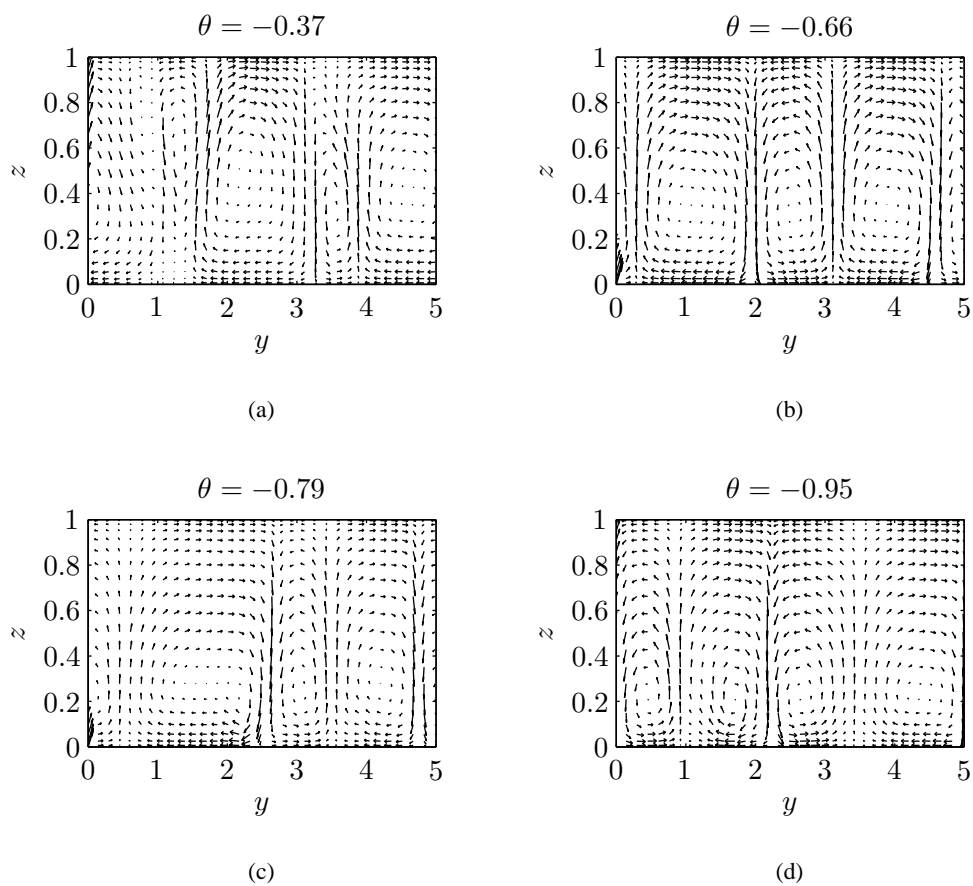


Figure 7.4: Velocity plots indicating the direction of flow in the layer for different  $\theta$ . In (a)  $\theta = -0.37$ , in (b)  $\theta = -0.66$ , in (c)  $\theta = -0.79$  and in (d)  $\theta = -0.95$ . In all cases  $Pr = 1$  and  $Ra = 5 \times 10^5$ . The asymmetry of the layer increases with  $|\theta|$ .

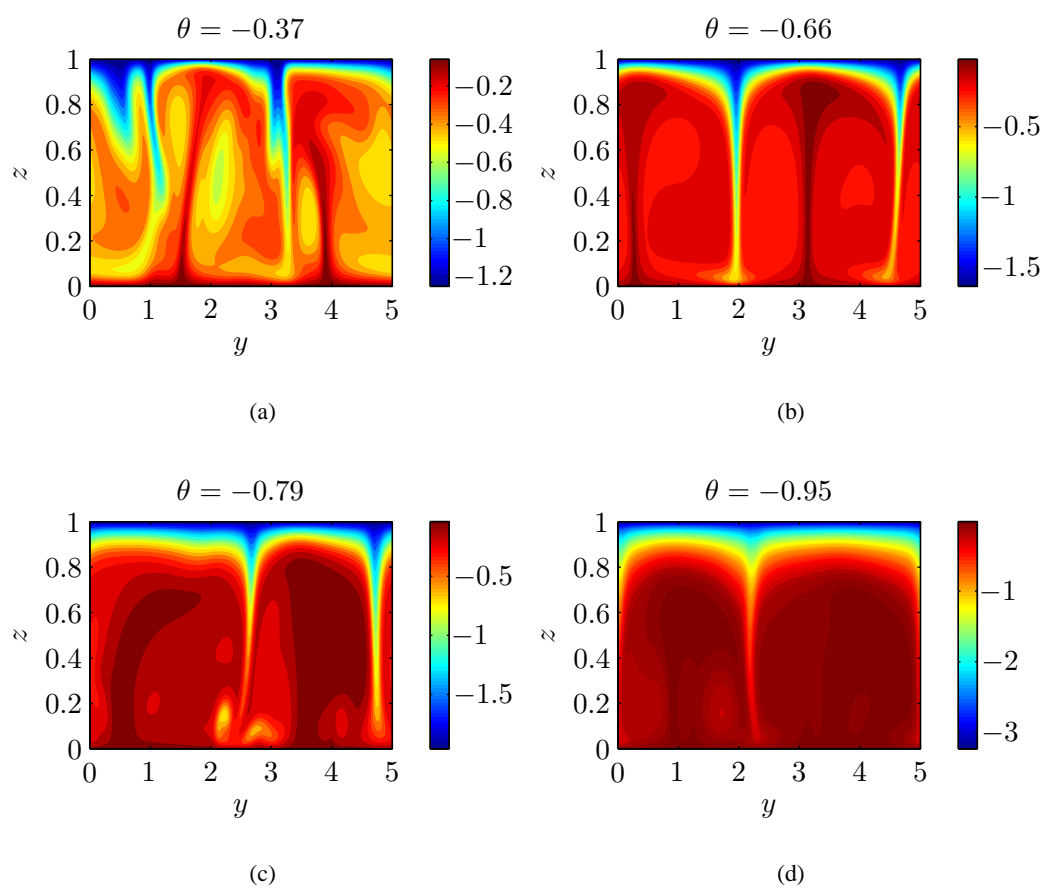


Figure 7.5: Contours of the total entropy,  $\bar{s} + s$ , corresponding to the velocity plots in figure 7.4. In (a)  $\theta = -0.37$ , in (b)  $\theta = -0.66$ , in (c)  $\theta = -0.79$  and in (d)  $\theta = -0.95$ . In all cases  $Pr = 1$  and  $Ra = 5 \times 10^5$ . The amount of mixing that occurs in the layer decreases as  $|\theta|$  increases.

isentropic because the layer is well mixed, though there are small regions close to the boundaries where the entropy distribution changes. But, as  $|\theta|$  is increased, the size of the isentropic region decreases and the upper region remains stratified; this effect increases with  $|\theta|$ . It should be noted that we expect the entropy distribution to become more uniform as the degree of supercriticality is increased, and so to compare the different  $\theta$ , we should perform the same analysis of  $s_{tot}$  at fixed  $Ra/Ra_c$ , as opposed to fixed  $Ra$ . However, here, the critical Rayleigh number is only slightly changed as  $\theta$  is changed and so all cases are such that  $14.2 < Ra/Ra_c < 15.4$ , and therefore we take this analysis to be valid without having to repeat for fixed  $Ra/Ra_c$ .

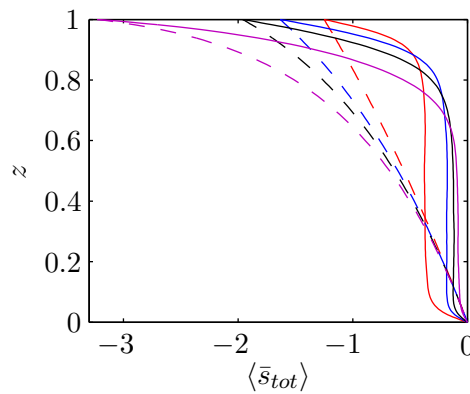


Figure 7.6: Vertical structure of the mean entropy,  $\bar{s}_{tot}$ , for the parameters used in figure 7.5. In red,  $\theta = -0.37$ , in blue,  $\theta = -0.66$ , in black,  $\theta = -0.79$  and in purple,  $\theta = -0.95$ . The dashed lines correspond to the basic state entropy and the solid lines to  $\bar{s}_{tot}$  after the simulations have been carried out.

Next, we consider the effect of increasing  $|\theta|$  on the kinetic energy of the system. From the definition of  $KE_{pert}$  in section 5.7.2, we see that it depends explicitly on  $\bar{\rho}$ . For  $\theta = 0$ ,  $\bar{\rho} = 1$  for all  $z$ , but as  $|\theta|$  is increased,  $\bar{\rho} \leq 1$  for all  $z$ , and is only equal to one on the bottom boundary. In other words, the total mass in the layer is decreased as  $|\theta|$  is increased, and this, by definition, will result in a decreased kinetic energy. But,  $\theta$  also has an impact on  $\mathbf{u}$ , and so it is not clear what will happen to the kinetic energy as  $|\theta|$  is varied. To see what happens, we plot two cases in figure 7.7: one of the cases is from the chaotic regime ( $Ra = 2 \times 10^5$ , crosses) and the other is from the relaxation oscillation regime ( $Ra = 5 \times 10^5$ , dots). For the relaxation oscillation case, as  $|\theta|$  is increased, the energy in the perturbations exhibits an increase until  $|\theta| \sim 0.6$ , and then the energy decreases in a more rapid fashion compared to the rate of increase in the energy that occurred at small  $|\theta|$ . As discussed previously, we would expect a decrease in the energy with

increasing  $|\theta|$  due to the decrease in  $\bar{\rho}$ , but for  $|\theta| \lesssim 0.6$  the energy is increasing and so this must be due to an increase in the fluid velocity. This increase is likely to be, in part, a result of the decrease in  $Ra_c$  in this region of  $\theta$  space, so that, as  $|\theta|$  is increased, there is a small increase in supercriticality which we would expect to lead to larger velocities, but this increase is small and so may not be the only contributing effect.

The time-averaged kinetic energy of the chaotic solutions ( $Ra = 2 \times 10^5$ ) possess a similar behaviour, except that there is not the increase in kinetic energy for small  $|\theta|$  that is seen for the relaxation oscillation solution ( $Ra = 5 \times 10^5$ ), the more rapid decrease of kinetic energy with increasing  $|\theta|$  as seen in the relaxation oscillation case, does occur at higher  $|\theta|$  though.

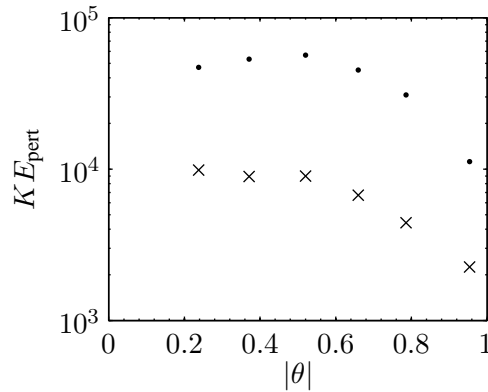


Figure 7.7: Kinetic energy in the perturbations as a function of  $\theta$  for  $Pr = 1$  and  $Ra = 2 \times 10^5$  (crosses), from the chaotic regime and  $Ra = 5 \times 10^5$  (dots), from the relaxation oscillation regime.

### 7.2.1 Mean flows

As was the case in the previous chapter, we are interested in analysing the mean flows driven by the system. In this case, we are particularly interested in the effect of stratification on the mean flows. Figure 7.8 shows plots of the energy in  $\bar{u}$  and  $\bar{v}$  as a function of  $\theta$ , for  $Pr = 1$  and  $Ra = 5 \times 10^5$ . The red symbols represent the kinetic energy as calculated using the mean measure and the blue symbols represent the kinetic energy as calculated using the variability measure (see equations (5.7.165) and (5.7.166) respectively for definitions of these quantities). Also plotted is the ratio of the energy in the mean flow to the energy in the perturbations (as given in figure 7.7). This should give us a guide as to whether the behaviour of the energy in the mean flows reflects

the behaviour of the energy in the perturbations, or if there is some other process affecting the mean flows. As before, we use both the mean and variability measures of the energies to quantify the behaviour, where the mean measure is given by the red crosses and the variability measure by the blue dots. First, if we consider  $\bar{u}$ , we see that as  $|\theta|$  is increased, the variability measure increases slightly, before decreasing. The ratio follows a similar pattern suggesting that for small  $|\theta|$ , the energy in  $\bar{u}$  increases slightly more than it does in the perturbations and at larger  $|\theta|$  the energy in  $\bar{u}$  is decreased more than it is in the perturbations. The mean measure of the energy in  $\bar{u}$  gives a different perspective: for the smaller  $|\theta|$  (less than approximately 0.5), there is a clearer increase in the energy in  $\bar{u}$ , the ratio also exhibits this steeper increase and so the mean energy in  $\bar{u}$  increases more over this range of  $|\theta|$  than the energy in the perturbations does. After  $|\theta| \approx 0.5$ , the mean measure of the energy in  $\bar{u}$  decreases, but the ratio remains roughly constant, which suggests the decrease in energy of the mean is due to the influence of increasing  $|\theta|$  on the whole system, rather than any particular influence of the larger stratifications on the correlations driving  $\bar{u}$ . Note also, as  $|\theta|$  is increased, the mean and variability measures of  $\bar{u}$  become much closer, suggesting that the stratification acts to drive more systematic mean flows. By contrast,  $\bar{v}$  is systematic for all  $|\theta|$ . Examining the variability measure of  $\bar{v}$  shows that it remains roughly constant until  $|\theta| \approx 0.65$ , at which point it then decreases with increasing  $|\theta|$ . The behaviour when  $|\theta| \leq 0.65$  of  $\bar{v}$  is thought to be as a consequence of the effect of increasing  $|\theta|$  on the whole system because the ratio to kinetic energy in the perturbations remains roughly constant throughout this region. But, when  $|\theta| > 0.65$ , there is a decrease in both the variability measure of the mean energy and the ratio, implying that it is the mean that is decreased more than the perturbations. For  $\bar{v}$ , the mean measure follows much the same path as the variability measure and therefore the same comments can be made about it.

As described in section 7.2, there is a difference in the time-dependent behaviour of the kinetic energy in the chaotic and relaxation oscillation cases. Therefore, it is interesting to consider whether this difference is also present in the mean flows driven by the convection. To investigate this, we plot  $\bar{v}$  as a function of  $z$  and  $t$  for  $\theta = -0.79$  in each of the two regimes, the results are shown in figure 7.9. In (a), the solution is from the chaotic regime and in (b), the solution is from the relaxation oscillation regime. In (a), for the chaotic solution, the distribution of strong positive flow in the top half of the plane is fairly even, whereas in (b), for the relaxation oscillation solution, there are short regions of strong mean flow consistent with the bursting profile we observed in figure 7.2 (b). There is a clear asymmetry across the layer depth which was not present in the Boussinesq examples we examined (see for example, figure 6.14); we shall now investigate this asymmetry further. For this purpose, we will focus on the chaotic regime, as for

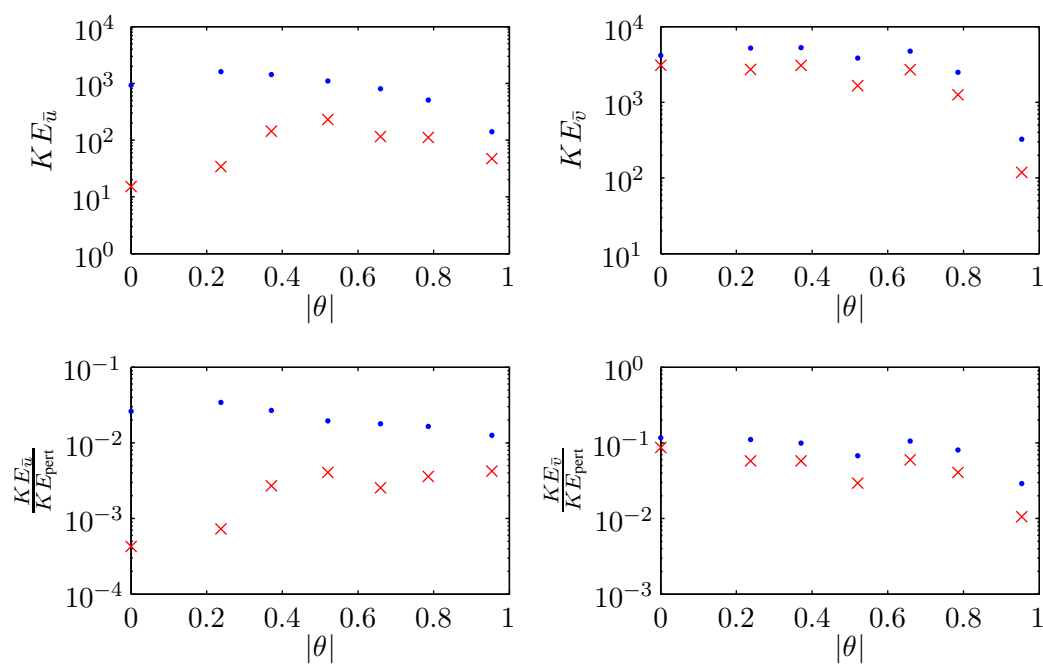


Figure 7.8: Energy in the mean flows  $\bar{u}$  and  $\bar{v}$  as calculated by the mean measure (red crosses) and the variability measure (blue dots) for the case corresponding to figure 7.7, i.e.,  $Pr = 1$  and  $Ra = 5 \times 10^5$ .

reasons mentioned before, we are able to work with time-averages more confidently.

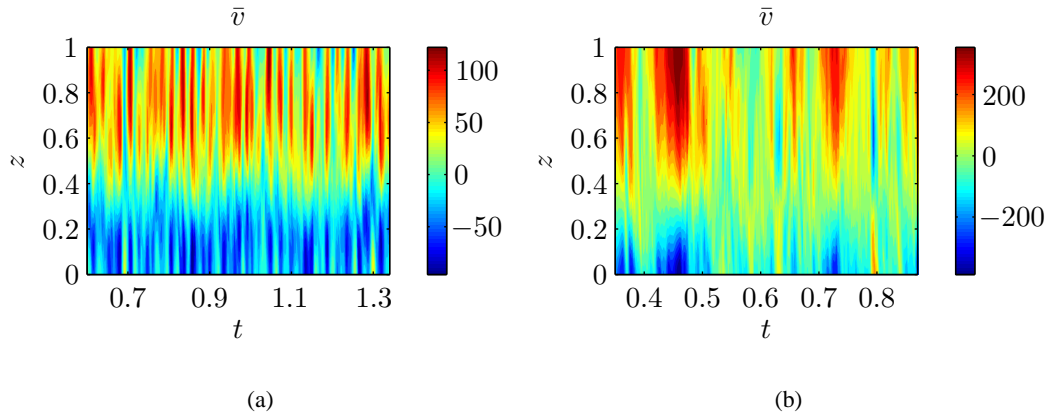


Figure 7.9: Contour plots of  $\bar{v}$  in two different regimes. In (a) the solution is chaotic and in (b) the solution is from the relaxation oscillation regime. In both cases,  $Pr = 1$ ,  $\theta = -0.79$  with  $Ra = 2 \times 10^5$  in (a) and  $Ra = 5 \times 10^5$  in (b).

Before considering such time-averages, we consider the time-dependent mean flows,  $\bar{u}(z, t)$  and  $\bar{v}(z, t)$ , for three different stratifications. Contour plots of these flows are shown in figure 7.10. In (a),  $\theta = -0.24$ , and the density at the bottom of the layer is just 1.5 times the density at the top of the layer; in (b),  $\theta = -0.66$ , and the density at the bottom of the layer is five times the density at the top of the layer, and in (c),  $\theta = -0.79$ , the density at the bottom of the layer is ten times the density at the top of the layer. As alluded to before, the most noticeable difference is the extent of the asymmetry in the layer. For example, the positive flow of  $\bar{v}$  in the upper half-plane only just penetrates down into the lower half-plane for small  $|\theta|$ , but the stronger stratification becomes, the further it penetrates into the layer.  $\bar{u}$  is more time-dependent and harder to interpret than  $\bar{v}$ , but the asymmetry is still evident. From figure 7.10, another effect of increasing the stratification appears to be that the maximum magnitude of the flow decreases as  $|\theta|$  increases, but the flows become more systematic.

To quantify these properties, we consider the mean and variation of the flows in time, and see how they vary with  $\theta$ , and also the depth at which they are calculated, i.e., how they vary with  $z$ . In figure 7.11, we plot the time-averaged mean for  $\bar{u}$  and  $\bar{v}$  along with error bars corresponding to the standard deviation ( $\sigma$ ) from that mean. In (a), the stratification is small, with  $\theta = -0.24$ , and in (b), the stratification is much stronger, with  $\theta = -0.79$ . In (a), for  $\bar{u}$ , we see that  $\sigma$  is smallest near to mid-layer and grows as we move out towards the boundaries, but in (b),  $\sigma(\bar{u})$  is smallest at a deeper layer. This behaviour is also seen in  $\sigma(\bar{v})$ , where for small  $|\theta|$ ,  $\sigma$  is fairly even across

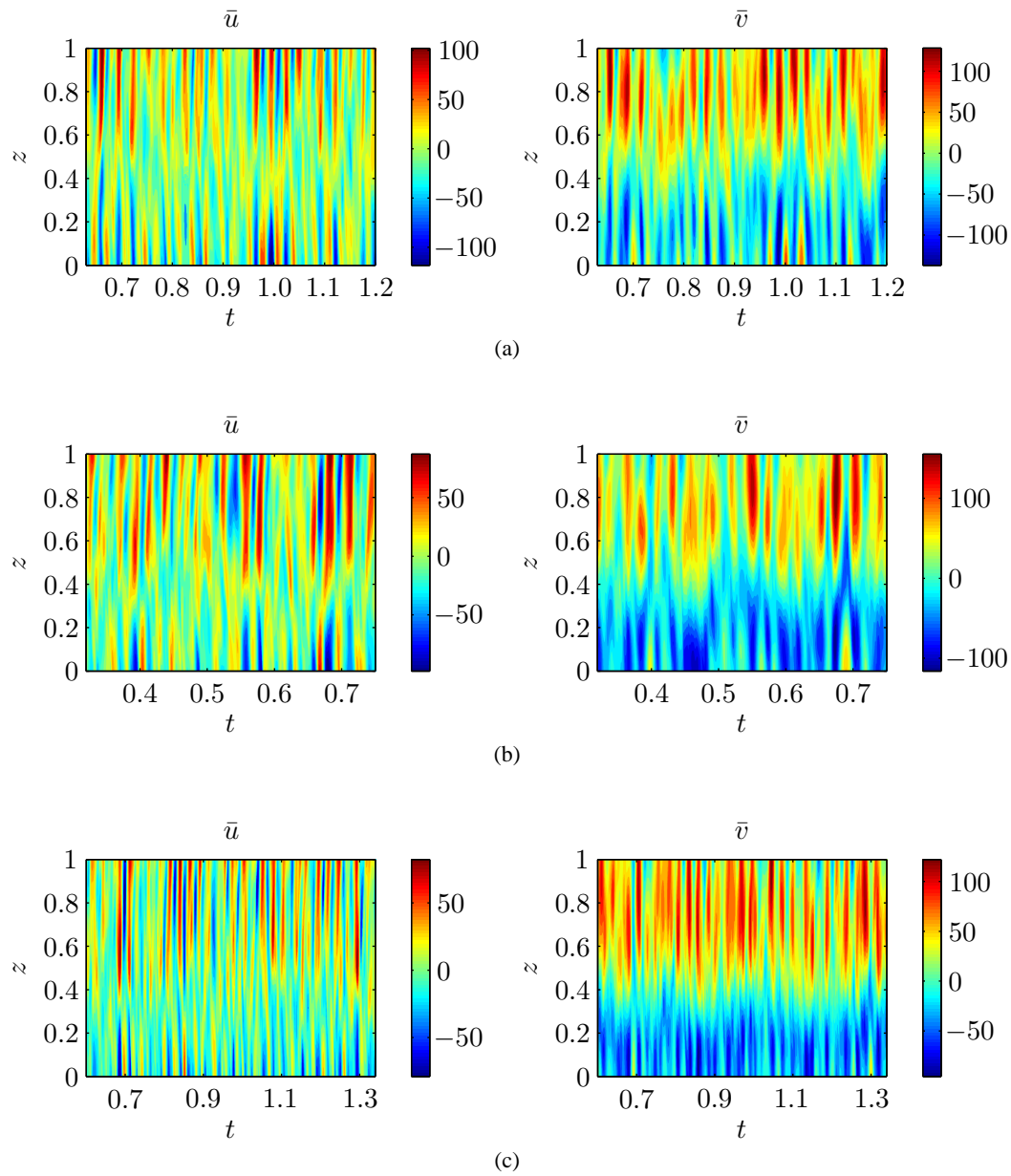


Figure 7.10: Contour plots of the mean flows  $\bar{u}$  and  $\bar{v}$ . In (a)  $\theta = -0.24$ , in (b)  $\theta = -0.66$  and in (c)  $\theta = -0.79$ . In all cases  $Pr = 1$  and  $Ra = 2 \times 10^5$ .

the layer but with its smallest value at approximately mid-layer, but for  $\theta = -0.79$  the smallest  $\sigma$  is found at much smaller  $z$ . Note also, the mean of  $\bar{u}$  and  $\bar{v}$  is close to zero at  $z = 0.5$  in (a), but there is a significant flow at  $z = 0.5$  in (b). These measures characterise the behaviour we saw in the time-dependent plots in figure 7.10. As a percentage of its mean,  $\sigma(\bar{u})$  is larger than  $\sigma(\bar{v})$ , indicative of the more intermittent behaviour of  $\bar{u}$  we also observed in figure 7.10.

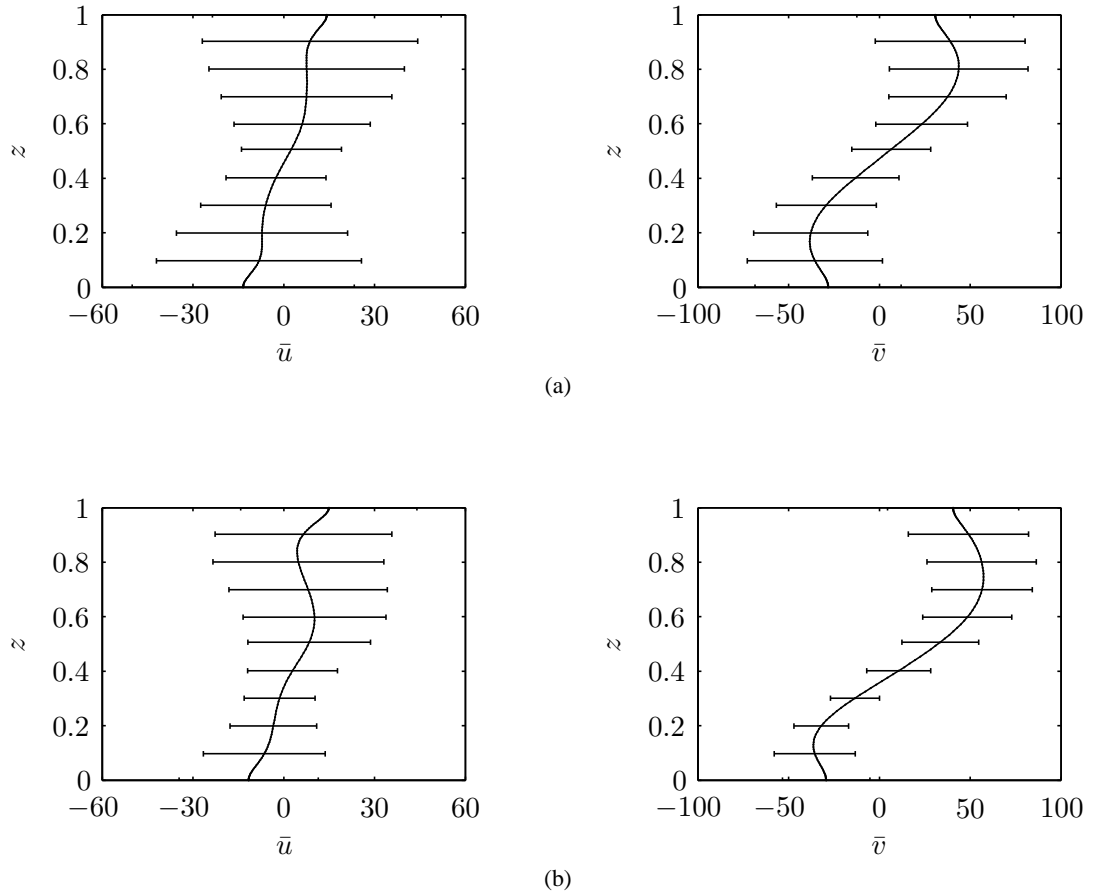


Figure 7.11: Mean (black curve) and standard deviation (error bars) of  $\bar{u}$  and  $\bar{v}$  for  $Pr = 1$ ,  $Ra = 2 \times 10^5$ , (a)  $\theta = -0.24$  and (b)  $\theta = -0.79$ . As  $|\theta|$  is increased the more systematic flow occurs at lower  $z$ .

Comparing figure 7.11 (a) and (b), it appears that the standard deviation at a fixed  $z$  is reduced as  $|\theta|$  is increased, this is particularly evident at the lower layers (smaller  $z$ ). To examine this statement more closely, we plot the standard deviation in  $\bar{u}$  and  $\bar{v}$  as a function of  $z$ , for different  $\theta$ . The results are shown in figure 7.12, where the black lines correspond to the smallest density contrast across the layer ( $\theta = -0.24$ ), then purple ( $\theta = -0.37$ ), then orange ( $\theta = -0.66$ ), then turquoise ( $\theta = -0.79$ ) and finally blue ( $\theta = -0.95$ ). The more systematic flows have the

smallest standard deviations as they fluctuate less about their mean. From the plots we see that generally, the stronger the stratification, the more systematic the flow, particularly in the lower part of the plane. It is also evident that for  $\sigma(\bar{v})$ , the minimum of the standard deviation occurs at a deeper level in the layer as  $|\theta|$  is increased. For  $\sigma(\bar{u})$ , the trend is not so clear, however, the flows corresponding to larger  $|\theta|$  have a minimum at a lower  $z$  than the flows corresponding to smaller  $|\theta|$ . Therefore, there are fewer fluctuations at lower levels with increasing  $|\theta|$ , and it is this that results in the larger time-averaged mean at this level.

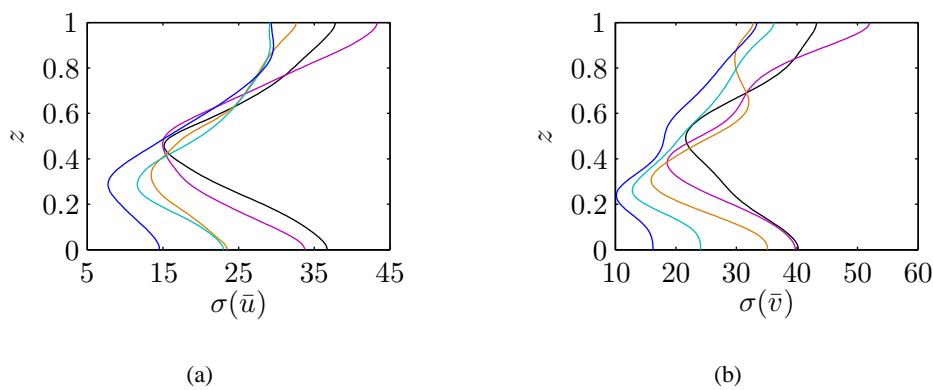


Figure 7.12: Standard deviation of (a)  $\bar{u}$  and (b)  $\bar{v}$  as a function of layer depth for different stratifications. In black  $\theta = -0.24$ , in purple  $\theta = -0.37$ , in orange  $\theta = -0.66$ , in turquoise  $\theta = -0.79$  and in blue  $\theta = -0.95$ .

Figure 7.13 gives the time-averaged profiles of  $\bar{u}$  (top) and  $\bar{v}$  (bottom) for different  $\theta$ . It is not clear from the plots if there is an obvious relationship between  $\bar{u}$  and  $\theta$ . However, it can be seen that  $\bar{u}$  is zero at increasingly deeper levels in  $z$  as  $|\theta|$  is increased. For  $\bar{v}$ , in the upper half-plane, if we ignore the  $\theta = -0.95$  solution, then the strongest stratifications give rise to the largest  $\bar{v}$ . This behaviour is not reflected in the lower half-plane. The maximum magnitude of the  $\theta = -0.95$  solution in the upper and lower half-planes is smaller than the maxima of the solutions for the other stratifications. We also see that, as  $|\theta|$  is increased, the maximum value of  $\bar{v}$  in the lower half-plane tends to occur at deeper levels. As for  $\bar{u}$ , the time-averaged plots of  $\bar{v}$  show that the value of  $z$  at which positive flow becomes negative flow, i.e., the layer depth at which the mean flow is zero, becomes smaller as the stratification is increased, this is in agreement with the time-dependent plots in figure 7.10.

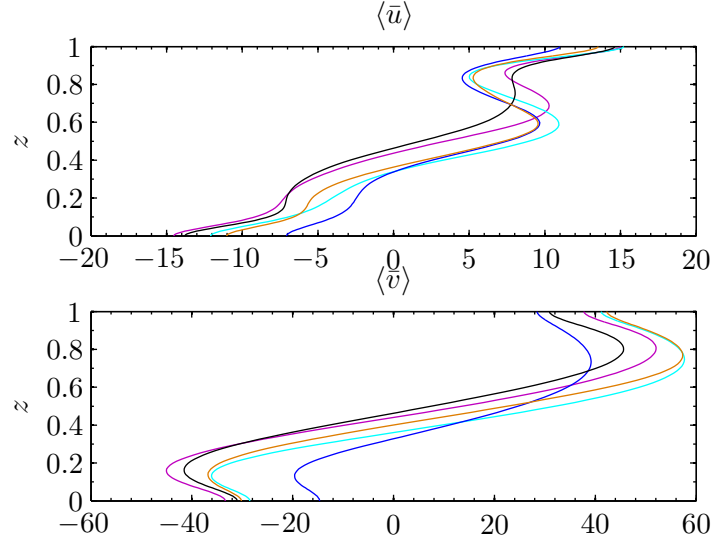


Figure 7.13: Time-averaged mean flows  $\langle \bar{u} \rangle$  (top) and  $\langle \bar{v} \rangle$  (bottom) as a function of  $z$ . In this case  $Pr = 1$ ,  $Ra = 2 \times 10^5$  and in black  $\theta = -0.24$ , in purple  $\theta = -0.37$ , in orange  $\theta = -0.66$ , in turquoise  $\theta = -0.79$  and in blue  $\theta = -0.95$ .

## 7.2.2 Mean flow equations

Taking a horizontal average of the  $x$  and  $y$  components of the momentum equation (2.4.142) gives us equations governing the mean flows. This is analogous to section 6.3.3, however, here we must remember the new definition of  $\psi$  involving  $\bar{\rho}$  and that  $\bar{\rho}$  is now a function of  $z$  (see section 5.7).

On taking such horizontal averages, we obtain the following equations

$$Pr \bar{\rho} \bar{u} = \frac{Pr}{Ta^{\frac{1}{2}} \sin \phi} \frac{\partial}{\partial z} \left( \bar{\rho} \frac{\partial \bar{v}}{\partial z} \right) - \frac{1}{Ta^{\frac{1}{2}} \sin \phi} \frac{\partial (\bar{\rho} \overline{v w})}{\partial z}, \quad (7.2.1)$$

$$Pr \bar{\rho} \bar{v} = -\frac{Pr}{Ta^{\frac{1}{2}} \sin \phi} \frac{\partial}{\partial z} \left( \bar{\rho} \frac{\partial \bar{u}}{\partial z} \right) + \frac{1}{Ta^{\frac{1}{2}} \sin \phi} \frac{\partial (\bar{\rho} \overline{u w})}{\partial z}, \quad (7.2.2)$$

where we have averaged in time and assumed a steady state so that  $\frac{\partial}{\partial t} \langle \bar{u} \rangle = \frac{\partial}{\partial t} \langle \bar{v} \rangle = 0$ . Notice the presence of  $\bar{\rho}$  in the equations, and also that when  $\bar{\rho} = 1$ , i.e.,  $\theta = 0$ , equations (7.2.1) and (7.2.2) reduce to the mean flow equations in the Boussinesq case, as given by equations (6.3.3) and (6.3.4). In contrast to (6.3.3) and (6.3.4), the mean flow terms on the left-hand sides are now multiplied by  $\bar{\rho}$ . The viscous term (first term on the right-hand sides) also have a  $\bar{\rho}$  multiplying the  $\frac{\partial \bar{v}}{\partial z}$ ,  $\frac{\partial \bar{u}}{\partial z}$  before the second derivative is taken. Similarly, the Reynolds stress terms (second term on right-hand sides), have a  $\bar{\rho}$  multiplying the correlations  $\overline{v w}$ ,  $\overline{u w}$ , before the vertical derivative is taken.

As we have just mentioned, there is a factor of  $\bar{\rho}$  in the mean flow terms of equations (7.2.1) and

(7.2.2). This means that, in theory, for two different  $\theta$ , if the driving terms on the right-hand side are of the same size, then the case with the largest  $|\theta|$  will yield the largest  $\bar{u}$  and  $\bar{v}$ , i.e., if  $Pr\bar{\rho}\bar{u}$  is the same for two different  $\bar{\rho}$  (fixed  $Pr$ ) then  $\bar{u}$  will be larger for the smaller  $\bar{\rho}$  (equivalent to larger  $|\theta|$ ). To see this, we plot each of the terms of equations (7.2.1) and (7.2.2) in figure 7.14; for (a)  $\theta = 0$  and (b)  $\theta = -0.79$ . In addition, we plot  $\bar{u}$  and  $\bar{v}$  (without the  $Pr\bar{\rho}$  factors) in red, but for  $\theta = 0$ , the mean flow term is also the overall mean flow since  $Pr = 1$ , therefore no red line is visible in this case. However, for  $\theta \neq 0$ , there is a difference between the mean flow term and the mean flow itself. In both (a) and (b), the strong dominance of the RS terms (orange) is clear. It is also evident that the viscous term (green) is more important in determining  $\bar{u}$  than it is  $\bar{v}$ , as it was in the Boussinesq case. It is clear that the RS terms are bigger in the  $\theta = 0$  case and this results in the mean flow terms being bigger for  $\theta = 0$ . However, because for  $\theta = -0.79$ ,  $\bar{\rho} \leq 1$  across the layer,  $\bar{u}$  and  $\bar{v}$  are actually bigger for  $\theta = -0.79$ . This effect is most prominent at the top of the layer, where the fluid mass is at its lowest.

Figure 7.14 highlights that the dominant balance is between the RS and mean flow terms. Therefore, if we examine how the RS terms are affected by  $\theta$ , it should help us to understand how the mean flows are affected by  $\theta$ . We begin by considering the time-dependent RS terms. Figure 7.15 shows contours of the RS terms as a function of  $z$  and time for three different stratifications. In (a), the layer has a mild stratification and  $\theta = -0.24$ , in (b), the stratification is increased to  $\theta = -0.66$  and in (c), the stratification is strong such that  $\theta = -0.79$ . The left-hand column of plots is of the RS term that drives  $\bar{u}$  and the right-hand column of plots is of the RS term that drives  $\bar{v}$ . We see that the term driving  $\bar{v}$  is more systematic than the term driving  $\bar{u}$ , this is to be expected since  $\bar{v}$  is more systematic than  $\bar{u}$ . Also evident, is the asymmetry introduced when  $\theta \neq 0$ , and this asymmetry gets stronger as  $|\theta|$  is increased. For example, the positive band in the upper half-plane of  $\frac{\partial}{\partial z}(\bar{\rho}\bar{u}\bar{w})$  increases in depth as  $|\theta|$  is increased. The behaviour of these RS terms is similar to that of  $\bar{u}$  and  $\bar{v}$  (shown in figure 7.10), emphasising the strong correlation between the RS terms and the mean flows. They, of course, will not be identical as the dominant balance in the mean flow equations is between the RS term and the mean flow term, i.e., between the RS term and  $Pr\bar{\rho}\bar{u}$ , and not just  $\bar{u}$ , and so the  $Pr\bar{\rho}$  factor needs to be taken into account. There is also slight modification by the viscous term, especially in the boundary layers.

Taking time averages of the RS terms gives the profiles shown in figure 7.16. The top plot shows the RS term that drives  $\bar{u}$  and the bottom plot shows the RS term that drives  $\bar{v}$ , for different  $\theta$ , for  $Pr = 1$  and  $Ra = 2 \times 10^5$ , i.e., for the same cases as in figure 7.13. For the RS term driving  $\bar{u}$ , at the top of the layer, the size of the term decreases with increasing  $|\theta|$  - this could be a result of

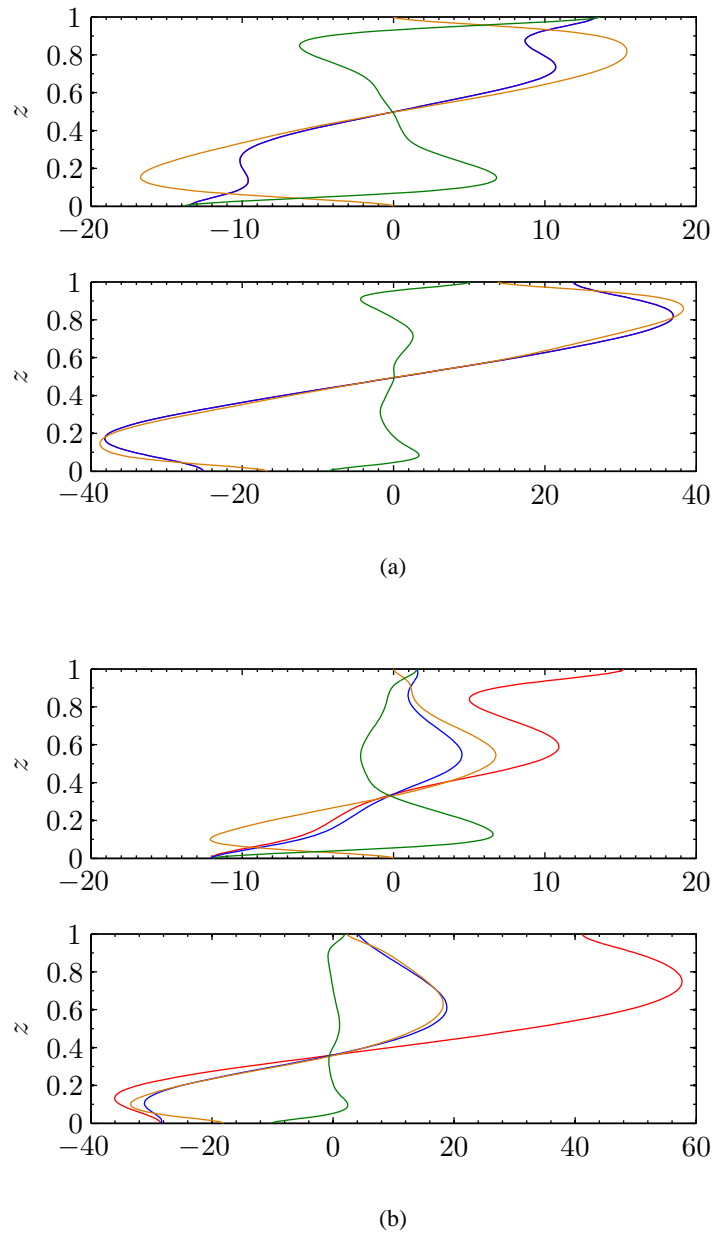


Figure 7.14: Terms of the mean flow equations (7.2.1) (top axes) and (7.2.2) (bottom axes) as a function of  $z$  for  $Pr = 1$ ,  $Ra = 2 \times 10^5$  and in (a),  $\theta = 0$ , whilst in (b),  $\theta = -0.79$ . The blue lines represent the mean flow terms, the orange the RS terms, the green the viscous terms and red the mean flows  $\bar{u}$  and  $\bar{v}$ . In case (a), the mean flow terms are equivalent to the mean flows themselves.

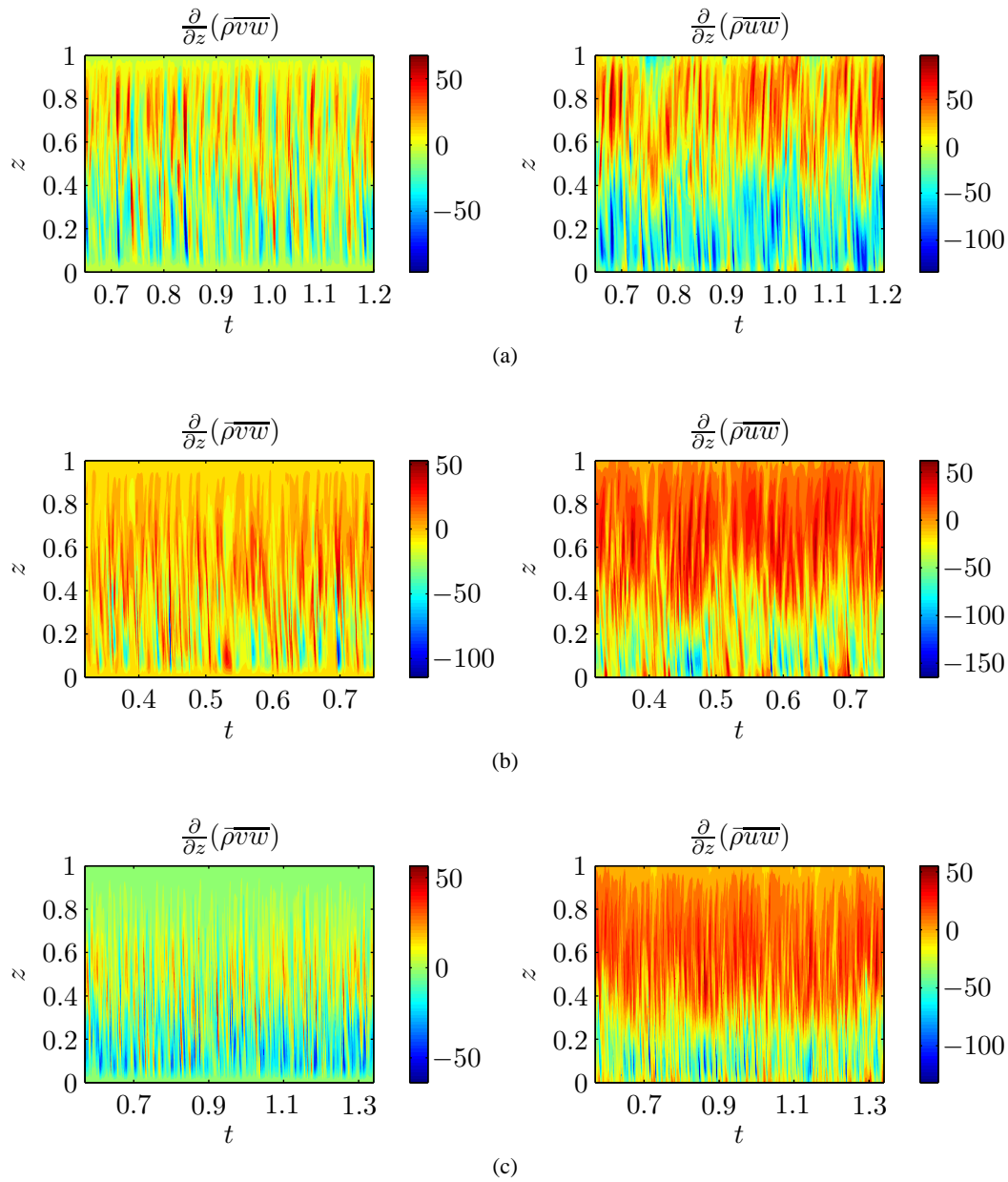


Figure 7.15: Left-hand column: Contour plots of the RS term  $\frac{\partial}{\partial z}(\overline{\rho v w})$  that drive  $\bar{u}$ . Right-hand column: Contour plots of the RS term  $\frac{\partial}{\partial z}(\overline{\rho u w})$  that drive  $\bar{v}$ . In (a),  $\theta = -0.24$ , in (b),  $\theta = -0.66$  and in (c),  $\theta = -0.79$  and in all cases,  $Pr = 1$  and  $Ra = 2 \times 10^5$ . They correspond to the mean flows depicted in figure 7.10.

the decrease in  $\bar{\rho}$  with increased  $|\theta|$ . We remark that the difference between the different  $|\theta|$  cases is most prominent at the top of the layer. At the bottom of the layer,  $\theta = 0$  gives the largest RS term and  $\theta = -0.95$  the smallest with the other  $\theta$  cases in between but with no obvious pattern as there is at the top of the layer. These RS terms drive  $\bar{u}$  as given in the top plot of figure 7.13.

The bottom plot of figure 7.16 shows the RS term that drives  $\bar{v}$ . Again, in the top portion of the layer, it is clear that  $\theta = 0$  gives the largest RS term and that as  $\theta$  is increased, the size of the term decreases. In the bottom half of the layer,  $\theta = -0.95$  clearly gives the smallest term but there is no obvious trend as  $|\theta|$  is increased, which is in contrast to the behaviour of the  $\bar{v}$  shown in figure 7.13. However, this is to be expected, since the RS term drives  $Pr\bar{\rho}\bar{v}$  (as given by equation 7.2.2) and so  $\bar{v}$  is obtained by dividing through by  $Pr\bar{\rho}$ . Therefore, since for larger  $|\theta|$ ,  $\bar{\rho}$  is smaller at the top of the layer,  $\bar{v}$  will be larger there (assuming everything else is fixed). Despite  $\theta = -0.95$  corresponding to the smallest  $\bar{\rho}$  at  $z = 1$ ,  $\bar{v}$  is smaller for  $\theta = -0.95$  than for the other cases, this is because the RS term is significantly smaller. Close to the bottom of the layer,  $\bar{\rho}$  varies only slightly between all the  $\theta$  cases, and therefore the mean flows reflect the same order of size as the RS terms at the bottom of the layer.

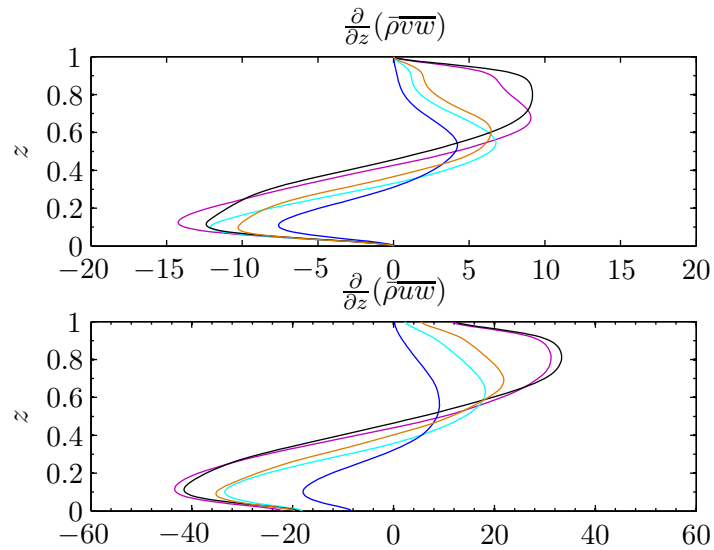


Figure 7.16: Time-averaged RS terms that drive  $\bar{u}$  (top) and  $\bar{v}$  (bottom) as a function of  $z$ . In this case  $Pr = 1$ ,  $Ra = 2 \times 10^5$  and in black  $\theta = -0.24$ , in purple  $\theta = -0.37$ , in orange  $\theta = -0.66$ , in turquoise  $\theta = -0.79$  and in blue  $\theta = -0.95$ . These plots correspond to the mean flows in figure 7.13.

As we did for  $\bar{u}$  and  $\bar{v}$ , we can analyse the mean and standard deviation of the time series of the RS terms, to see if they behave in a similar way to the time series of the mean flows. The results

for cases with  $Pr = 1$  and  $Ra = 2 \times 10^5$  are shown in figure 7.17 for a weak stratification, (a)  $\theta = -0.24$ , and a stronger stratification, (b)  $\theta = -0.79$ . In (a), the stratification is small and we see that the distribution of RS terms has approximately the same standard deviation across the layer. This was also the case for the standard deviation of the distribution of  $\bar{u}$  and  $\bar{v}$  in the small stratification case, see figure 7.11 (a). In the case of stronger stratification, see figure 7.17 (b), where  $\theta = -0.79$ , the standard deviation of the RS terms is larger at the bottom of the layer than it is at the top. This is different to the standard deviation of the mean flows for the same parameters (cf. figure 7.11 (b)) where the standard deviation was larger at the top of the layer than it was at the bottom. This difference can be explained by remembering that the RS terms balance with the mean flow terms and not just the mean flow and therefore the factor of  $\bar{\rho}$  in the mean flow term has to be considered. More specifically, (see e.g., DeGroot & Schervish (2002))

$$\sigma(\bar{\rho}\bar{u}) = |\bar{\rho}|\sigma(\bar{u}), \quad (7.2.3)$$

at each  $z$ , for all  $\theta$ . Therefore, since  $\bar{\rho}$  increases as  $z$  decreases, if  $\sigma(\bar{u})$  decreases with  $z$  by a smaller amount than  $\bar{\rho}$  increases, then  $\sigma(\bar{\rho}\bar{u})$  will increase as  $z$  is decreased. This provides an explanation of how the standard deviation of the RS terms can increase as  $z$  is decreased, whilst the standard deviation of the mean flows decreases with  $z$ .

### 7.2.3 Linear approximation

Mean flow generation is a nonlinear process. As we have seen, it relies upon quantities such as the Reynolds stresses, which are the product of perturbations, e.g.,  $\overline{\rho u w}$ . Such products are ignored in a linear calculation. However, it is interesting to consider the differences between the RS terms as calculated from the solutions of the linear perturbation equations (cf. chapter 4) and as calculated from the fully nonlinear equations (as done in previous sections of this chapter). Such a calculation will give us an indication as to whether the behaviour of the system can be captured without the need for a full nonlinear calculation. The results for two cases are shown in figure 7.18, for different  $Ra$  and  $\theta$ . For case (a), the linear calculation provides a rough estimate for the RS terms when  $\theta = -0.37$  but, as  $|\theta|$  is increased, the agreement between the linear and nonlinear calculations becomes poorer. In other words, increasing the stratification causes the nonlinearities to become more important so that the linear calculation becomes a worse approximation. In case (b),  $Ra$  is increased by a factor of five. Comparing the linear and nonlinear calculations now shows a poor agreement, even for the smaller  $|\theta|$ . This is due to the increased supercriticality and therefore the increased nonlinearity.

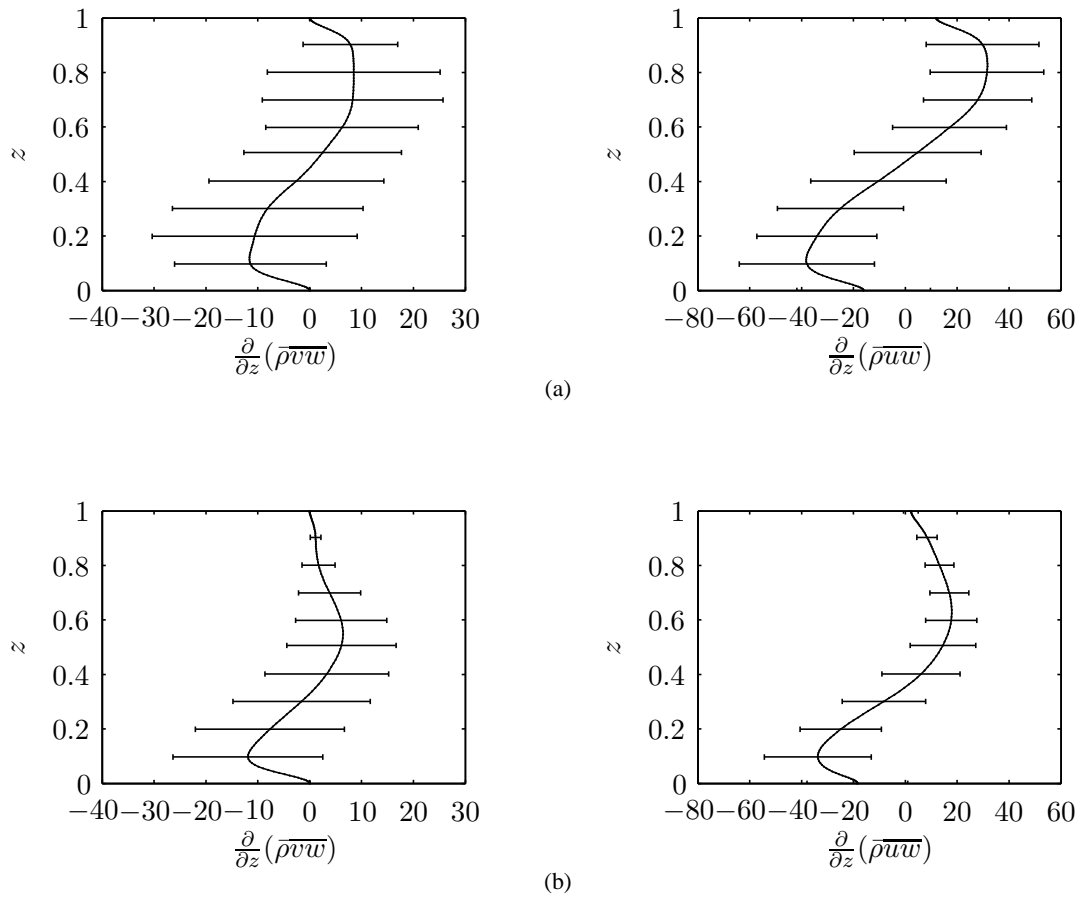


Figure 7.17: Mean (black curve) and standard deviation (error bars) of the RS terms that drive  $\bar{u}$  (left) and  $\bar{v}$  (right) for  $Pr = 1$ ,  $Ra = 2 \times 10^5$  and (a)  $\theta = -0.24$ , (b)  $\theta = -0.79$ .

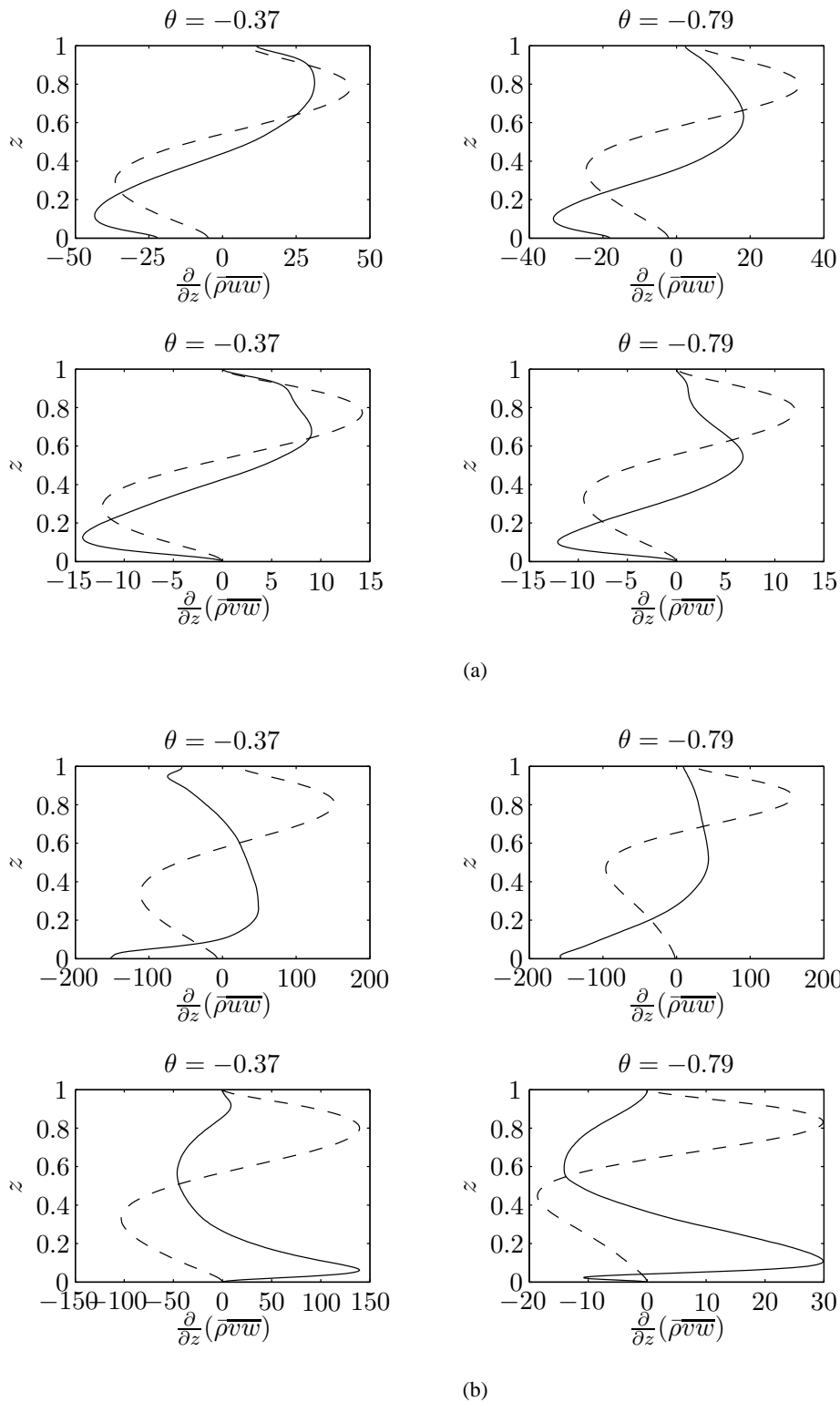


Figure 7.18: The RS terms calculated from the nonlinear code (solid lines) and the RS terms calculated from linear eigenfunctions (dashed lines) for  $Pr = 1$  and (a)  $Ra = 2 \times 10^5$ , (b)  $Ra = 10^6$ . The agreement is generally poor. The linear calculation provides a rough estimate at  $\theta = -0.37$  and  $Ra = 2 \times 10^5$  but the approximation gets worse as  $|\theta|$  and  $Ra$  are increased.

We note that in particular, the interaction of the mean flow with the fluctuations is neglected in the linear calculation. A quasi-linear calculation could be performed to capture this interaction between the mean and fluctuation quantities whilst still neglecting the terms quadratic in the fluctuation quantities, to see if this is capable of capturing the large-scale dynamics. Also, a slightly simpler calculation would be to take the mean flows calculated by the nonlinear code and impose them in a linear calculation. Both these calculations are beyond the scope of this thesis but are discussed further in Chapter 9.

### 7.3 Summary

In this chapter we extended the investigation of convection-driven mean flows in Chapter 6, to allow for the possibility of the layer being continuously stratified. As mentioned before, this a more realistic situation for many physical applications in which we are interested (see Chapter 1). We found that increasing  $Ra$  and  $|\theta|$  eventually led to a subtle change in regime, from chaotic convection to a regime where bursting is evident. By examining solutions from both of these regimes, we found an asymmetry in the layer that develops when  $\theta \neq 0$ , the asymmetry becoming more prominent as  $|\theta|$  is increased.

Studying the dependence of the energy in the mean flows on  $\theta$ , led to the conclusion that most of the change is likely a result of the effect changing  $\theta$  has on the whole system, and not a specific effect changing  $\theta$  has on the correlations responsible for the mean flows. The asymmetries introduced in the anelastic simulations are evident in the vertical structure of the mean flows. Analysis of the time-dependent mean flows shows that the flow in the upper half-plane penetrates further into the lower half-plane as  $|\theta|$  is increased. A statistical analysis of the mean flow distribution gave that the standard deviation is smallest at a lower level in the layer as  $|\theta|$  is increased. Also, it was shown that, in general, the standard deviation is decreased, as the strength of the stratification is increased, making for more systematic mean flows when  $|\theta|$  is larger.

To consider what was driving the mean flows, we derived the mean flow equations, which are a modified form of the ones discussed in Chapter 6; now the mean flow equations contain a  $\bar{\rho}$  factor to allow for the density stratification. We showed that the Reynolds stress term is indeed the term responsible for the mean flow driving, but that they actually drive  $Pr\bar{\rho}\bar{u}$  and  $Pr\bar{\rho}\bar{v}$  and the mean flows result as a consequence. This means that, at the top of the layer, because the mass is reduced there and the vertical velocity is increased in order to transport heat, the mean flow is

amplified. The time-dependent RS terms exhibit the same asymmetries as observed in the mean flow case, but the standard deviation for the RS terms is different from the the mean flows, this is again because of the  $\bar{\rho}$  factor in the mean flow term.

We finished with an investigation of whether the RS terms as calculated using the linear eigenfunctions could approximate the actual RS terms. It was found this agreement was moderate at small  $|\theta|$  and  $Ra$ , but only got worse as  $|\theta|$  or  $Ra$  was increased, an indication that the nonlinear processes become more important in these cases. An interesting investigation would be to see if this nonlinear behaviour could be captured in a quasi-linear calculation, this is discussed further in section 9.2.

## Chapter 8

# Nonlinear rotating convection in the presence of a horizontal magnetic field

### 8.1 Introduction

In this chapter, we extend the work of Chapter 6 by introducing a horizontal magnetic field to the system. We derived the full nonlinear equations for this setup in Chapter 2, in Chapter 3 we presented the linear theory and in Chapter 5, specifically section 5.6, we described the numerical method used to solve the nonlinear governing equations. Before we present results from the nonlinear simulations, we restate the governing equations and the boundary conditions, for ease of reference. From equations (5.6.132)-(5.6.138), the equations are given by

$$\begin{aligned} \frac{\partial \omega}{\partial t} - Pr \nabla^2 \omega = Pr Ta^{\frac{1}{2}} (\cos \phi u_y + \sin \phi u_z) + Ra Pr \frac{\partial \theta}{\partial y} + J(\psi, \omega) \\ - Q \zeta Pr \left( J(A, j) - \frac{\partial j}{\partial y} \sin \alpha \right), \end{aligned} \quad (8.1.1)$$

$$\frac{\partial \theta}{\partial t} - \nabla^2 \theta = J(\psi, \theta) - \frac{\partial \psi}{\partial y}, \quad (8.1.2)$$

$$\begin{aligned} \frac{\partial u}{\partial t} - Pr \nabla^2 u = Pr Ta^{\frac{1}{2}} \left( \cos \phi \frac{\partial \psi}{\partial y} + \sin \phi \frac{\partial \psi}{\partial z} \right) + J(\psi, u) \\ + Q \zeta Pr \left( \frac{\partial B_1}{\partial y} \sin \alpha - J(A, B_1) \right), \end{aligned} \quad (8.1.3)$$

$$\nabla^2 \psi = -\omega, \quad (8.1.4)$$

$$\frac{\partial B_1}{\partial t} - \zeta \nabla^2 B_1 = \frac{\partial u}{\partial y} \sin \alpha - J(A, u) + J(\psi, B_1), \quad (8.1.5)$$

$$\frac{\partial A}{\partial t} - \zeta \nabla^2 A = J(\psi, A) + \frac{\partial \psi}{\partial y} \sin \alpha, \quad (8.1.6)$$

where we have taken  $T_y = U = 0$ , as we will ignore thermal wind effects in this chapter. The boundary conditions for this system are given by

$$\omega = \psi = \frac{\partial u}{\partial z} = \theta = A = \frac{\partial B_1}{\partial z} = 0 \quad \text{on } z = 0, 1. \quad (8.1.7)$$

Whilst these equations allow for the possibility of the magnetic field being oriented in any horizontal direction, we take  $\alpha = \frac{\pi}{2}$  throughout this chapter, so that the imposed field is purely in the  $y$ -direction. We also fix  $Ta = 10^5$ ,  $\phi = \frac{\pi}{4}$  and the length of the computational box by setting  $L = 5$ , unless otherwise stated. We initially consider  $Pr = 1$  and  $\zeta = 1.1$ , but the effect of changing  $Pr$  and  $\zeta$  will be considered in later sections.

## 8.2 Numerical results

First, we briefly consider the effect of a horizontal magnetic field on the evolution of the variables of the MHD system. We then examine the effect of the field on the mean flows driven (see section 8.2.1). To see the effect of the magnetic field on the system, we start with a hydrodynamic simulation (equivalent to  $Q = 0$ ) and increase  $Q$  at fixed  $Ra$ , thus increasing the strength of the magnetic field. We calculate the kinetic and magnetic energies as a function of  $Q$ , the results for the case where  $Pr = 1$ ,  $\zeta = 1.1$  and  $Ra = 5 \times 10^5$  are shown in figure 8.1. As expected, as the strength of the field is increased, the magnetic energy of the system is also increased, whilst the kinetic energy is decreased. Since the basic state field lies in the  $y$ -direction, any attempt by a flow in the  $x$ -direction to draw out field lines is opposed by the field. This results in the flow in the  $x$ -direction being reduced and hence contributes to the decrease in the kinetic energy we observe.

The different symbols used in figure 8.1 denote different types of solution; crosses denote chaotic solutions and dots denote steady solutions. In this case, the small  $Q$  solutions are chaotic, but as  $Q$  is increased, the solutions eventually become steady. Since the effect of increasing  $Q$  is to increase the critical Rayleigh number (see section 3.6.3), for fixed  $Ra$ , the larger  $Q$  solutions are less supercritical and so the move to steady solutions might be expected.

To visualise the flow and the magnetic field as  $Q$  is increased, we have plotted contours of the streamfunction  $\psi(y, z)$  and the flux function  $A(y, z)$ , at a snapshot in time, for three different values of  $Q$  (see figure 8.2). In (a),  $Q = 100$ , and therefore the solution only differs slightly from the solution in the purely hydrodynamic case and is chaotic; in (b),  $Q = 1500$ , and the solution is still chaotic but, from figure 8.1, this solution occurs just before the solutions go steady. In

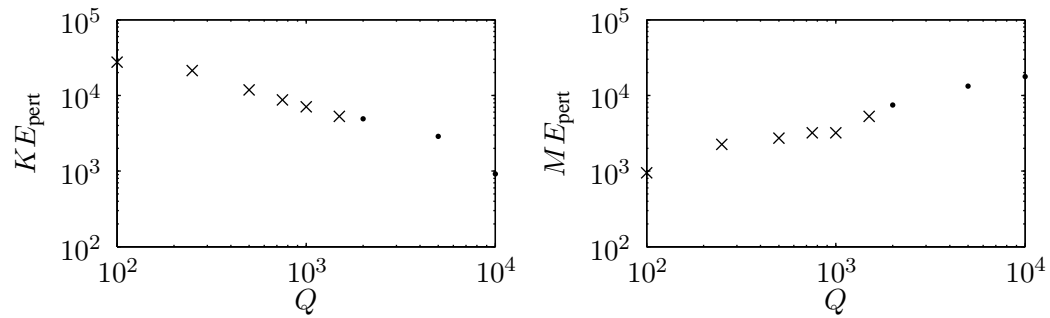


Figure 8.1: Kinetic energy (left) and magnetic energy (right) in the perturbations plotted against  $Q$  for  $Pr = 1$ ,  $\zeta = 1.1$ ,  $Ra = 5 \times 10^5$ . Solutions from the chaotic regime are marked with a cross and solutions from the steady regime with a dot.

(c),  $Q = 10000$  and these solutions are now steady. We see that as  $Q$  is increased, the field organises, and reduces the magnitude of, the flow, so that it eventually becomes steady. In doing so, the length scale of the solution increases from being such that three pairs of negative and positive cells fit in the box at  $Q = 100$  to just one pair fitting in the box by  $Q = 10000$ . A linear calculation of the wavenumber of the fastest growing mode for the cases in figure 8.2 gives:  $l = 6$  for case (a),  $l = 5$  for case (b) and  $l = 3$  for case (c), and so the nonlinear terms have acted to increase the length scale of the solutions we observe.

### 8.2.1 Mean flows

In order to investigate the effect of the magnetic field on the mean flows driven, we consider the kinetic energy in the mean flows as a function of  $Q$ . Figure 8.3 shows the results for the same parameters as in figure 8.1. The mean measure of the kinetic energy is shown in red and the variability measure is shown in blue (calculated using the formulae in section 5.5.3), and as in figure 8.1, the different symbols represent a different type of solution. We note that, at small  $Q$ , as expected, the behaviour is close to that of the purely hydrodynamic system discussed in Chapter 6. In both the chaotic and the steady regimes, we see that the variability measure of  $\bar{u}$  and  $\bar{v}$  is decreased as  $Q$  is increased, but in the chaotic regime, the mean of  $\bar{u}$  increases and the mean of  $\bar{v}$  decreases. Therefore, increasing  $Q$  has increased the level to which  $\bar{u}$  is systematic but reduced the overall energy in the flow.  $\bar{v}$  is more systematic than  $\bar{u}$  throughout the chaotic regime, this can be seen from the fact that the mean and the variability measures are much closer in value for  $\bar{v}$  than they are for  $\bar{u}$ . Now, if we consider the ratio of the energy in the mean to the kinetic energy in

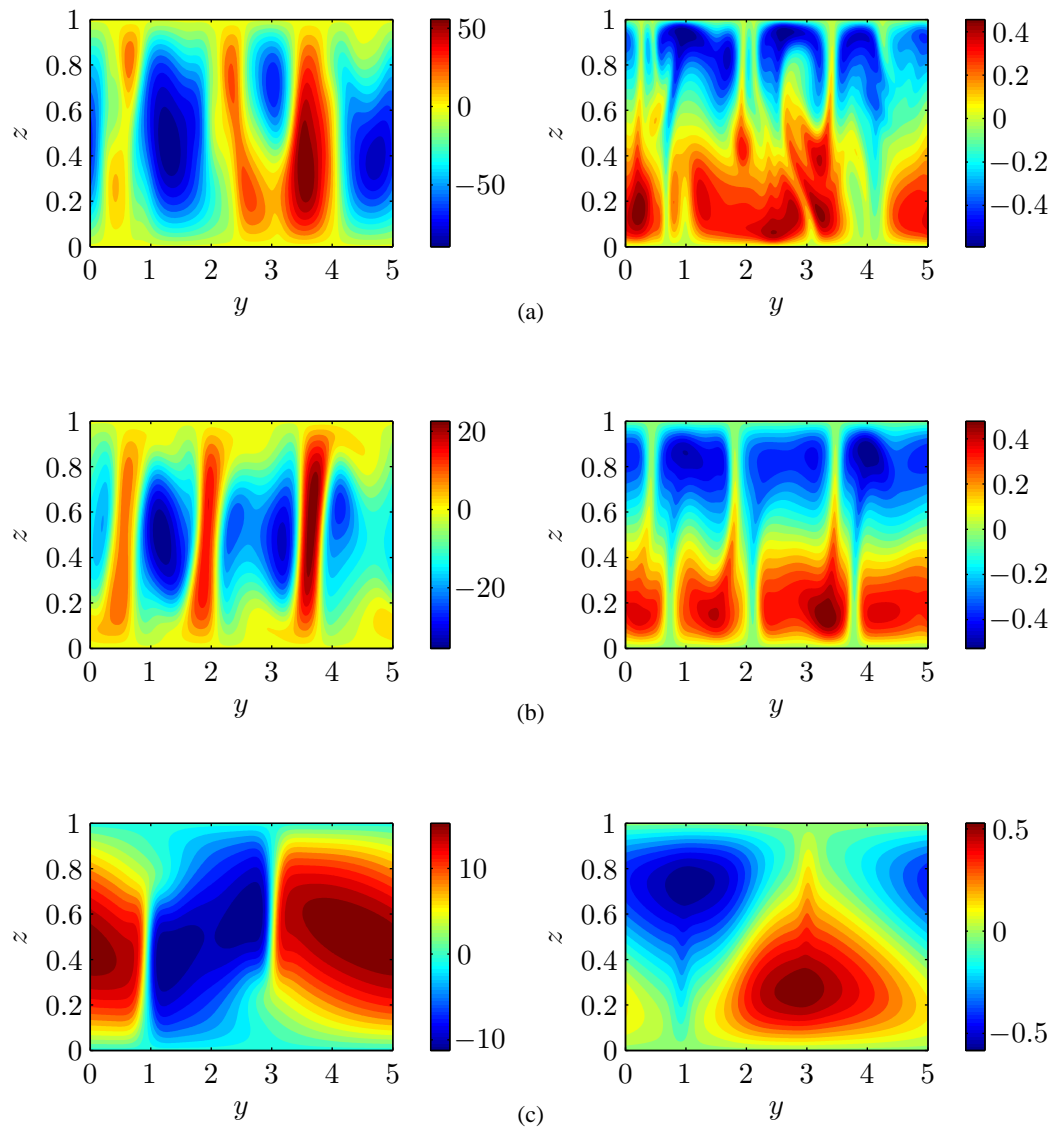


Figure 8.2: Contours of  $\psi(y, z)$  (left-hand column) and  $A(y, z)$  (right-hand column) at a snapshot in time for  $Pr = 1$ ,  $\zeta = 1.1$ ,  $Ra = 5 \times 10^5$  and in (a)  $Q = 100$ , in (b)  $Q = 1500$  and in (c)  $Q = 10000$ . (a) and (b) correspond to chaotic solutions and (c) is a steady solution.

the perturbations (see bottom row of figure 8.3) we see that, in the chaotic regime, the ratio of the variability measure of  $\bar{u}$  to  $KE_{\text{pert}}$  is fairly constant and so the mean flow decreases at the same rate as the perturbations. The ratio of the mean measure of  $\bar{u}$  to  $KE_{\text{pert}}$ , however, is increasing in the chaotic regime because of the increase in  $KE_{\langle\bar{u}\rangle}$  with  $Q$  in the chaotic regime. For both measures, the ratio of the energy in  $\bar{v}$  to the energy in the perturbations exhibits a decrease as  $Q$  is increased, which suggests that  $\bar{v}$  is decreased more than the perturbations are decreased by the field. In the steady regime, both  $KE_{\bar{u}}$  and  $KE_{\bar{v}}$  decrease sharply at first and then more slowly, this results in a ratio that decreases for smaller  $Q$  before increasing with larger  $Q$ .

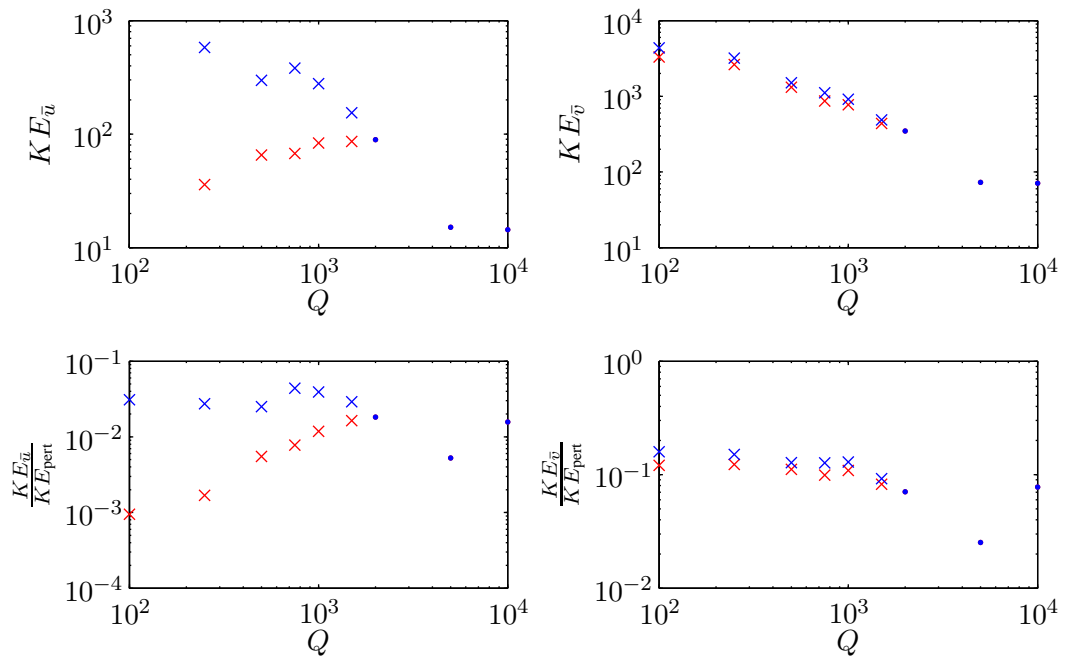


Figure 8.3: Kinetic energies in the mean flow for  $Pr = 1$ ,  $\zeta = 1.1$ ,  $Ra = 5 \times 10^5$  and a range of  $Q$ . The top row gives the mean measure of the energy in  $\bar{u}$  (left) and  $\bar{v}$  (right) in red and the variability measure of the energy in blue. Chaotic solutions are marked with a cross and steady solutions with a dot. The bottom row gives the ratio of the energy in the mean flow to the kinetic energy in the perturbations.

As well as analysing the energy contained in the mean flows, it is worth studying the time-dependent mean flows because this can give important information about the nature of the flows that may not be captured in the time-averaged quantities. For example, figure 8.4 shows  $\bar{u}$  and  $\bar{v}$  as a function of  $z$  and  $t$  for a case when the field strength is (a) small ( $Q = 100$ ), and (b) larger ( $Q = 1500$ ). Both examples are taken from the chaotic regime of the examples used in figure 8.2.

For small  $Q$ , case (a), the mean flows are very similar to some of the cases we saw in Chapter 6 (e.g., fig 6.14), which is of no surprise as when  $Q = 0$ , we reduce to the hydrodynamic system studied in Chapter 6. In particular, we see that  $\bar{v}$  is more systematic than  $\bar{u}$  and is predominantly positive in the upper half-plane and predominantly negative in the lower half-plane. In case (b), the magnetic field strength has been increased and we see that the nature of  $\bar{u}$  and  $\bar{v}$  has changed. Firstly, let us consider  $\bar{v}$ , whilst there is still a band of positive flow in the upper half-plane and a band of negative flow in the lower half-plane, the bands do not extend all the way to the top and bottom boundaries, as they did when  $Q = 100$  (a). As  $Q$  has increased, boundary layers have formed where the flow has been significantly reduced. The behaviour that causes this change to occur will be discussed in section 8.2.4. Secondly, we also observe a change in the nature of  $\bar{u}$ ; boundary layers are also formed in this case, a layer of positive flow at the top boundary and a layer of negative flow at the bottom boundary. But, in contrast to  $\bar{v}$ , the flow is largest in these layers. Further away from the boundaries, a negative band is evident in the top half of the plane and a positive band in the lower half of the plane. These bands are more coherent than any seen in  $\bar{u}$  when  $Q = 100$ , this highlights the fact that increasing  $Q$  organises the flow into having a more systematic nature. It should also be noted that the overall magnitude of the flows is decreased as  $Q$  is increased, contributing to the decrease in the variability measure with increasing  $Q$ .

To examine the vertical structure of  $\bar{u}$  and  $\bar{v}$  as a function of  $z$ , and its dependence on  $Q$ , we plot the time-averaged mean flows in figure 8.5. We expect these plots to be more informative when considering  $\bar{v}$  than when considering  $\bar{u}$ , as, from the time-dependent plots, we know that  $\bar{u}$  is highly fluctuating about zero, however, we still examine both cases. All parameters are held constant and we explore a range of  $Q$  from zero to 10000, each value of  $Q$  is shown in a different colour. First, note how the size of  $\bar{v}$  changes as  $Q$  is increased; from the bottom plot in figure 8.5 we see that, a small addition of field ( $Q = 100$ , red) increases the size of  $\bar{v}$  (compared with  $Q = 0$ , blue) but then further increases in  $Q$  decrease the magnitude of the maximum value of  $\bar{v}$ . A slight change in the vertical structure of  $\bar{v}$  is also evident. As  $Q$  is increased from zero to 1000, the layer depths at which the maxima occur move towards the mid-layer depth, as we saw in figure 8.4. From  $Q = 2000$  to 10000, the solutions are steady and perhaps should be considered separately, though the  $Q = 2000$  and  $Q = 5000$  cases do have a similar structure, again with their maxima closer to the mid-layer depth than in the low  $Q$  cases. For  $\bar{v}$ , the  $Q = 10000$  case stands out, as the direction of flow has reversed and the structure is different. This will be examined in more detail in section 8.2.4.

As expected, the change in structure of  $\bar{u}$  is trickier to interpret as  $\bar{u}$  is more time-dependent. It

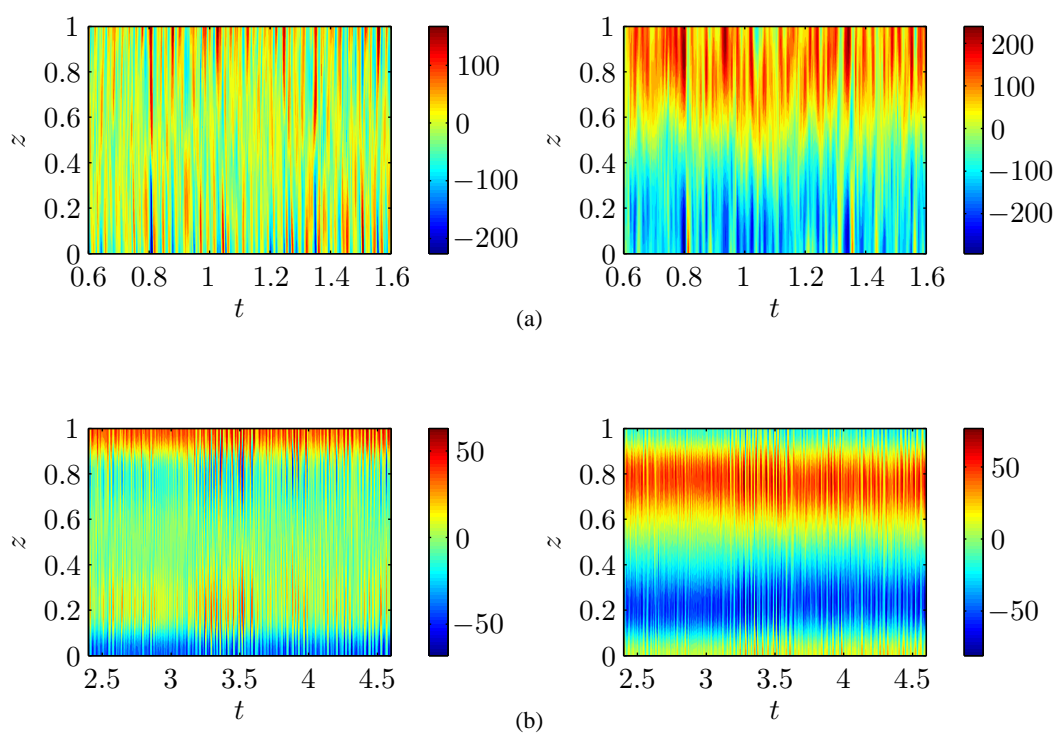


Figure 8.4: Time-dependent  $\bar{u}$  (left) and  $\bar{v}$  (right) for  $Pr = 1$ ,  $\zeta = 1.1$ ,  $Ra = 5 \times 10^5$  and (a)  $Q = 100$ , (b)  $Q = 1500$ .

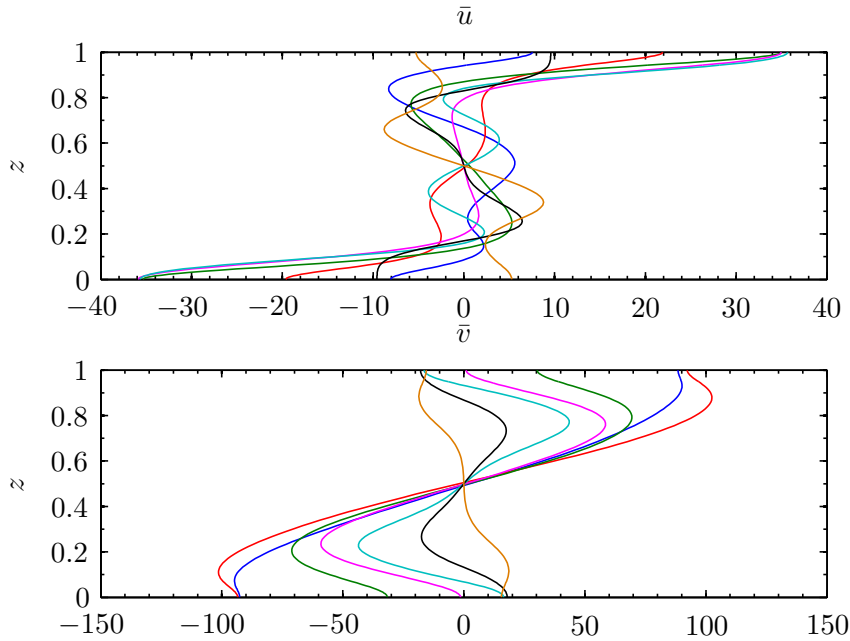


Figure 8.5:  $\bar{u}$  (top) and  $\bar{v}$  (bottom) for  $Pr = 1$ ,  $\zeta = 1.1$ ,  $Ra = 5 \times 10^5$ . Each  $Q$  is represented by a different colour; blue represents  $Q = 0$ , red represents  $Q = 100$ , green represents  $Q = 500$ , pink represents  $Q = 1000$ , light blue represents  $Q = 2000$ , black represents  $Q = 5000$  and orange represents  $Q = 10000$ .  $Q = 0$  to  $Q = 1000$  are chaotic solutions, whereas  $Q = 2000$  to  $Q = 10000$  are steady solutions. Notice that  $\bar{v}$  is bigger than  $\bar{u}$ .

is clear though, from the top plot of figure 8.5, that as  $Q$  is increased, the strength of the flow in the boundary layers is increased in the chaotic regime. This is likely to be the reason for the increase in  $KE_{\langle \bar{u} \rangle}$  with  $Q$  that was seen in figure 8.3. In the bulk of the fluid, there appear to be a number of changes in the direction of the flow as  $Q$  is increased, for example between  $Q = 2000$  (light blue) and  $Q = 5000$  (black) the flow changes direction. So  $Q$  not only decreases the kinetic energy in the mean flows, it can also change the direction of the mean flow. What causes the change in vertical structure of the flows we observe in figure 8.5 will be examined in section 8.2.4. Finally, by comparing the sizes of  $\bar{u}$  and  $\bar{v}$ , in figure 8.5, we see that  $\bar{v}$  is larger than  $\bar{u}$  in all cases.

## 8.2.2 Mean fields

In addition to the mean flows, we investigate the behaviour of the mean fields,  $\bar{B}_1$  and  $\bar{B}_2$ , as  $Q$  is increased. Figure 8.6 shows contours of  $\bar{B}_1$  and  $\bar{B}_2$  as a function of  $z$  and time, for the

same parameters as used in figure 8.4. Note, we have plotted the total magnetic field, i.e., the basic state magnetic field plus the perturbation magnetic field. We recall that the basic state field imposed throughout this chapter is purely in the  $y$ -direction. In (a),  $Q = 100$ , and so the imposed magnetic field strength is small. From the plot of  $\bar{B}_2(z, t)$  in this case, we see that the magnetic field has been expelled to the boundaries, leaving the bulk of the layer with almost zero magnetic field. For  $\bar{B}_1(z, t)$ , there was no imposed field in this direction and so the field in the  $x$ -direction has resulted from the evolution of the system. It is true in this case also that the magnetic field is strongest close to the boundaries. In (b), the initial field strength is increased so that  $Q = 1500$ . In this case, the magnetic field in the basic state is expelled to the boundaries, as it was for  $Q = 100$ , but to a lesser extent and so there remains a field in the bulk of the layer.  $\bar{B}_1$  reflects this behaviour too.

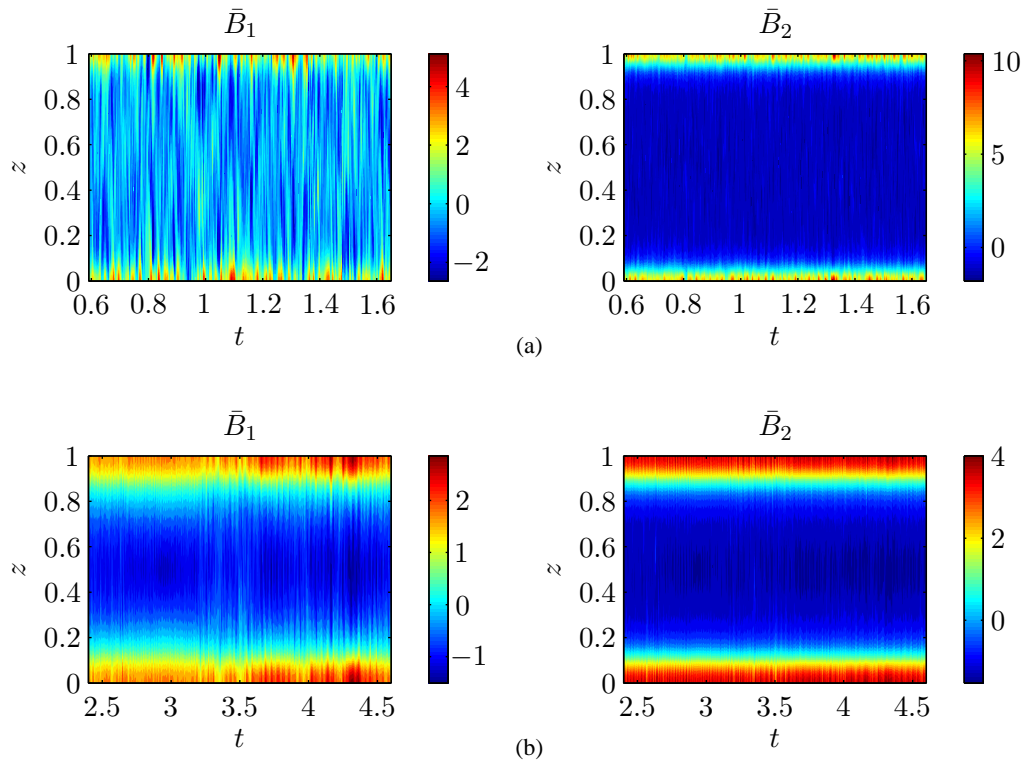


Figure 8.6: Time-dependent  $\bar{B}_1$  (left) and  $\bar{B}_2$  (right) for  $Pr = 1$ ,  $\zeta = 1.1$ ,  $Ra = 5 \times 10^5$  and (a)  $Q = 100$ , (b)  $Q = 1500$ .

To examine the expulsion to the boundaries of the magnetic field for other values of  $Q$ , we consider the time-averaged profiles of the components of the magnetic field. In figure 8.7, we plot  $\langle \bar{B}_1 \rangle$  (top axes) and  $\langle \bar{B}_2 \rangle$  (bottom axes) for  $Pr = 1$ ,  $\zeta = 1.1$ ,  $Ra = 5 \times 10^5$  and  $Q = 100$  (red),  $Q = 500$  (green),  $Q = 1000$  (pink),  $Q = 2000$  (light blue),  $Q = 5000$  (black) and

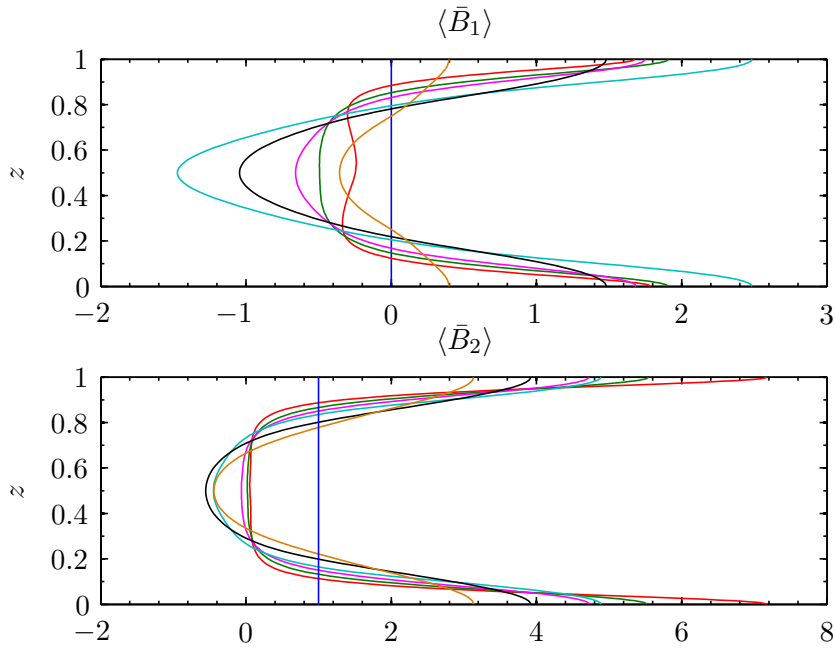


Figure 8.7:  $\bar{B}_1$  (top) and  $\bar{B}_2$  (bottom) for  $Pr = 1$ ,  $\zeta = 1.1$ ,  $Ra = 5 \times 10^5$ . Each  $Q$  is represented by a different colour; red represents  $Q = 100$ , green represents  $Q = 500$ , pink represents  $Q = 1000$ , light blue represents  $Q = 2000$ , black represents  $Q = 5000$  and orange represents  $Q = 10000$ . In blue is the basic state magnetic field,  $\mathbf{B}_{BS} = (0, 1, 0)$ .  $Q = 100$  to  $Q = 1000$  are chaotic solutions, whereas  $Q = 2000$  to  $Q = 10000$  are steady solutions.

$Q = 10000$  (orange). We also show the corresponding component of the basic state field in the  $x$  and  $y$  directions (blue). From the plots of  $\langle \bar{B}_2 \rangle$ , it is clear that the smaller  $Q$ , the more magnetic field is expelled to the boundaries. As we saw from the time dependent plots in figure 8.6, for  $Q = 100$ , the bulk of the layer has almost zero magnetic field in the  $y$ -direction. As  $Q$  is increased, it becomes harder for the magnetic field to be moved to the boundaries; as we see from figure 8.7, the larger  $Q$  solutions have significant field across the whole layer.  $\langle \bar{B}_1 \rangle$  increases in size at  $z = 0.5$  with  $Q$  in the chaotic regime, but decreases in size at  $z = 0.5$  with increasing  $Q$  in the steady regime. We also see that the boundary layers are thinnest for small  $Q$ . The consequences of magnetic field being expelled to the boundaries arise from the fact that, if there is little, or no, magnetic field in the bulk of the layer, it will be unable to affect the mean flow there. We will analyse the competition between the flows and the fields in section 8.2.4.

### 8.2.3 Increasing $Ra$

Before investigating what is responsible for the behaviour of the mean flows and mean fields, we increase  $Ra$  to  $Ra = 5 \times 10^6$ , to see if we observe similar behaviour at larger  $Ra$ . The kinetic energies in the mean flows for  $Ra = 5 \times 10^6$  are shown in figure 8.8. There are now extra solution regimes appearing; in addition to the chaotic and steady regimes from the previous case, we have a relaxation oscillation regime which is slightly different to the chaotic regime (as described in section 6.2 and 7.2) and solutions in this regime are denoted by a plus sign, we also have periodic solutions arising, these are shown by the square symbols. For  $Q \lesssim 750$ , the solutions are shown as steady on the plot, but at this  $Ra$ , the degree of supercriticality is high and so the numerical code has to take small time steps in order to converge, therefore, it may be that we need to integrate for longer for the solutions to become chaotic. We have decided, it might be best to ignore these small  $Q$  solutions. As with the  $Ra = 5 \times 10^5$  case, the solutions go steady after a chaotic regime, and here, if  $Q$  is increased even further, the solutions become periodic.

In the chaotic and relaxation oscillation regimes, both measures of the energy in  $\bar{u}$  and  $\bar{v}$  decrease as  $Q$  increases. But, if we consider the ratio of the energy in  $\bar{u}$  to the energy in  $KE_{\text{pert}}$  we see a difference between the chaotic and relaxation oscillation regimes. In the relaxation oscillation regime, the ratio is roughly constant before decreasing, as  $Q$  is increased, therefore the mean is reduced by the field more than the perturbations are. In contrast, in the chaotic regime, the ratio increases with  $Q$  and so  $\bar{u}$  is decreased less than the perturbations are by the field. For  $\bar{v}$ , the ratio in the relaxation oscillation regime is roughly constant and so the decrease in the energy in  $\bar{v}$  is probably as a direct result of the decrease in the energy in  $v$ . In the chaotic regime, the ratio decreases as  $Q$  is increased, indicating that the energy in the mean is decreased more by the field than the energy in the perturbations is.

In both the steady and periodic regimes (large  $Q$ ), the energy in both  $\bar{u}$  and  $\bar{v}$  is decreased as  $Q$  is increased but the ratio of the energy in  $\bar{u}$  to the energy in the perturbations is roughly constant. This is in contrast to  $\bar{v}$  where, in this regime, the energy in the mean and the ratio decrease as  $Q$  is increased.

### 8.2.4 Mean flow equations

In an analogous way to the purely hydrodynamic system (see section 6.3.3), we derive the mean flow equations by taking a horizontal average of the  $x$  and  $y$  components of the momentum

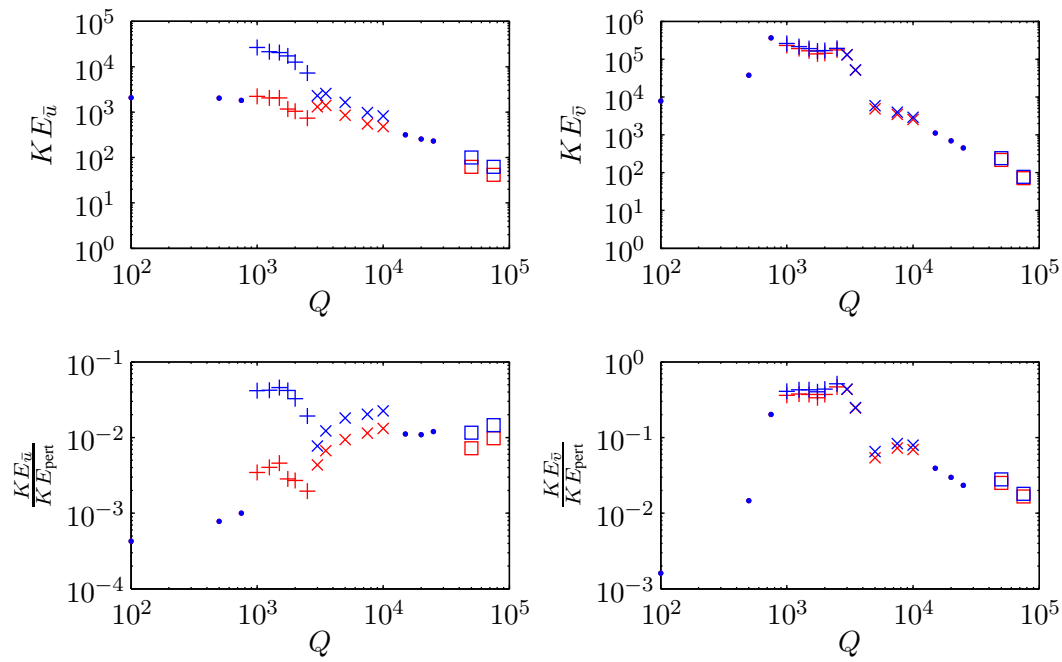


Figure 8.8: Kinetic energies in the mean flow for  $Pr = 1$ ,  $\zeta = 1.1$ ,  $Ra = 5 \times 10^6$  and a range of  $Q$ . The top row gives the mean measure of the energy in  $\bar{u}$  (left) and  $\bar{v}$  (right) in red and the variability measure of the energy in blue. Chaotic solutions are marked with a cross, relaxation oscillation solutions with a plus sign, periodic solutions with a square and steady solutions with a dot. The bottom row gives the ratio of the energy in the mean flow to the kinetic energy in the perturbations.

equations to give

$$Pr\bar{u} = \frac{Pr}{Ta^{\frac{1}{2}} \sin \phi} \frac{\partial^2 \bar{v}}{\partial z^2} - \frac{1}{Ta^{\frac{1}{2}} \sin \phi} \frac{\partial \overline{vw}}{\partial z} + \frac{Pr\zeta Q}{Ta^{\frac{1}{2}} \sin \phi} \frac{\partial \overline{B_2 B_3}}{\partial z}, \quad (8.2.8)$$

$$Pr\bar{v} = -\frac{Pr}{Ta^{\frac{1}{2}} \sin \phi} \frac{\partial^2 \bar{u}}{\partial z^2} + \frac{1}{Ta^{\frac{1}{2}} \sin \phi} \frac{\partial \overline{uw}}{\partial z} - \frac{Pr\zeta Q}{Ta^{\frac{1}{2}} \sin \phi} \frac{\partial \overline{B_1 B_3}}{\partial z}, \quad (8.2.9)$$

where we have taken time averages and assumed a statistically steady state so that  $\frac{\partial}{\partial t} \langle \bar{u} \rangle = \frac{\partial}{\partial t} \langle \bar{v} \rangle = 0$ . These equations are of a similar form as the hydrodynamic mean flow equations, (6.3.1) and (6.3.2), with the derivatives of the Reynolds stresses  $\overline{uw}$  and  $\overline{vw}$  helping to drive the flows, but, in addition, there is an extra term in each equation, proportional to  $Q$ . The terms  $\overline{B_1 B_3}$  and  $\overline{B_2 B_3}$  are known as the Maxwell stresses and are a contributing factor when considering what drives, or inhibits, the mean flows. Note, it is the correlations of the flow and the field in the  $x$ -direction with the flow and field in the  $z$ -direction that dictate the flow in the  $y$ -direction. Similarly, it is the correlations of the flow and the field in the  $y$ -direction with the flow and field in the  $z$ -direction that dictate the flow in the  $x$ -direction. We will refer to the term on the left-hand sides of the equations as the mean flow term, the first term on the right-hand sides as the viscous term, the second term on the right-hand sides as the Reynolds stress (RS) term and the last term on the right-hand sides as the Maxwell stress (MS) term.

In the previous section, we saw that increasing  $Q$  had an effect on the size and structure of the mean flows. To understand what is dictating this change, we plot each of the terms of the mean flow equations, (8.2.8) and (8.2.9), as a function of  $z$ . The plots are shown in figure 8.9 for (a)  $Q = 100$ , (b)  $Q = 1500$  and (c)  $Q = 10000$ . In blue are the mean flow terms; in orange are the RS terms; in black are the MS terms and in green are the viscous terms.

First, let us consider the case when the field strength is small,  $Q = 100$ . In the bottom plot of (a), we can see  $\bar{v}$  is clearly driven by the RS term, with the MS and viscous terms making only a small contribution. We see that the extrema of the RS terms are close to the boundaries resulting in a mean flow with maximum value close to the boundaries. Similarly, from the top plot of (a),  $\bar{u}$  is driven by the Reynolds stress term. However, in this case there is a larger contribution from the viscous term, resulting from the fact that  $\bar{v}$  is greater than  $\bar{u}$ , and as a result  $\bar{u}$  is a less systematic flow than  $\bar{v}$ . The MS term, when  $Q = 100$ , is small compared to the other terms. For small  $Q$ , the MS term is expected to be small for two reasons: firstly, the MS term is proportional to  $Q$  and secondly, we saw in figures 8.6 and 8.7 that for  $Q = 100$ ,  $\bar{B}_2$  is small in the bulk, suggesting that the correlations  $\overline{B_2 B_3}$  are likely to be small in the bulk too. Since the MS term is small, we are left with a similar balance as seen in the hydrodynamic case, (see e.g., figure 6.18).

Increasing  $Q$  to  $Q = 1500$  gives the balance shown in case (b).  $\bar{v}$  is clearly still driven by the RS term but the MS term is larger now. In particular, the MS term is most significant close to the top and bottom boundaries, and since it is acting in the opposite direction to the RS term there, it reduces size of the mean flow driving and so  $\bar{v}$  is relatively small in these boundary layer regions compared to  $\bar{v}$  in the bulk of the layer. At this  $Q$ , the magnetic field is strongest near the boundaries (cf. figure 8.7) and because the magnitude of  $Q$  is large enough, the MS term is significant at the boundaries, resulting in the behaviour we observe. Some field exists in the bulk and so the MS terms have started to have an effect there too. Furthermore, the increase in the effect of the MS term, along with the fact that the maximum of the RS term has moved towards the middle of the layer (compared with smaller  $Q$ ), mean that the maximum of  $\bar{v}$  has also moved towards the mid-layer depth. This explains what was causing the behaviour observed in the time-dependent plots of figure 8.4.

For  $\bar{u}$ , the increase in  $Q$  has resulted in an increase in the MS term affecting it, and also a decrease in the RS term driving it. These RS and MS terms now, along with the viscous term, roughly balance in the bulk of the layer to result in a relatively small  $\bar{u}$  there. At the boundaries, there are relatively large viscous boundary layers and since close to the boundaries the RS and MS terms are small, it follows that  $\bar{u}$  has boundary layers where the flow is largest, in agreement with the plots in figure 8.4 and 8.5.

Increasing  $Q$  further, to  $Q = 10000$  (see figure 8.9 (c)), leads to the MS terms becoming the dominant terms. Magnetic field is no longer expelled to the boundary, this fact combined with the large  $Q$  means that the MS terms are dominant across the whole layer. The RS term still contributes to the form of  $\bar{v}$  but it is the MS term that dominates the structure. It is for this reason,  $\bar{v}$  is in the opposite direction for  $Q = 10000$  than it is for the other  $Q$  shown in figure 8.5. For  $\bar{u}$ , the MS term is now larger than the viscous term, with the RS term being the smallest of the three terms and so it is the MS term that dominates  $\bar{u}$ .

Hence, we have shown that the field can act to change the direction of the flow through changing which terms in equations (8.2.8) and (8.2.9) are dominant. In the cases examined, increasing  $Q$  does not appear to change the direction of the mean flow by changing the direction of the Reynolds stresses.

We have seen that the relative size of the RS and MS terms determines the size and structure of the mean flows driven. It is interesting to see how the size of these terms changes with  $Q$ . We

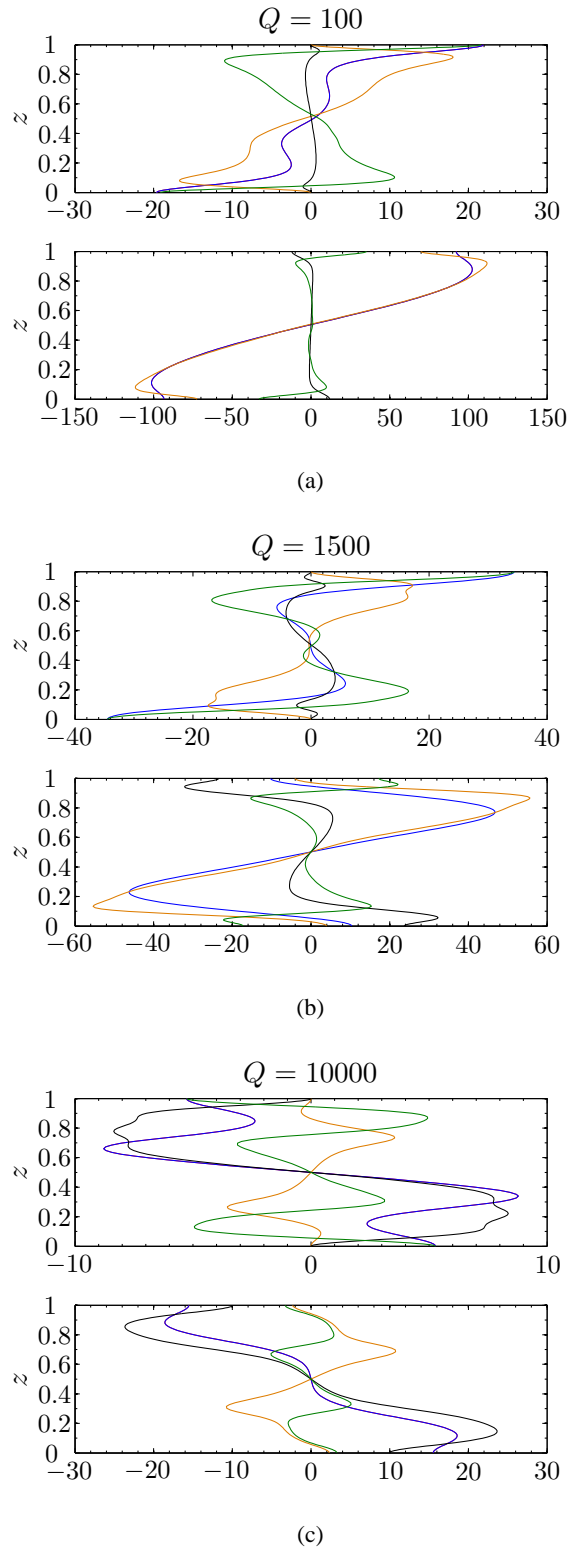


Figure 8.9: Terms of the mean flow equations, (8.2.8) (top) which drive  $\bar{u}$ , and (8.2.9) (bottom) which drive  $\bar{v}$ , plotted for different  $Q$  and  $Pr = 1$ ,  $\zeta = 1.1$  and  $Ra = 5 \times 10^5$ . In orange are the RS terms, in black are the MS terms, in green are the viscous terms and in blue are the mean flow terms.

define typical sizes of these terms as follows:

$$|RSx| = \left( \int_0^1 \langle (\frac{\partial}{\partial z} \overline{uw})^2 \rangle dz \right)^{\frac{1}{2}}, \quad |RSy| = \left( \int_0^1 \langle (\frac{\partial}{\partial z} \overline{vw})^2 \rangle dz \right)^{\frac{1}{2}}, \quad (8.2.10)$$

$$|MSx| = QPr\zeta \left( \int_0^1 \langle (\frac{\partial}{\partial z} \overline{B_1 B_3})^2 \rangle dz \right)^{\frac{1}{2}}, \quad |MSy| = QPr\zeta \left( \int_0^1 \langle (\frac{\partial}{\partial z} \overline{B_2 B_3})^2 \rangle dz \right)^{\frac{1}{2}}. \quad (8.2.11)$$

In figure 8.10 we plot the sizes of the RS, MS and viscous terms from equations (8.2.8) (left) and (8.2.9) (right). We also include the ratio of the typical size of the RS and MS terms to  $KE_{\text{pert}}$  and  $ME_{\text{pert}}$  respectively, so that we can assess whether the behaviour of the mean correlations reflects that of the perturbations, or if there is another process occurring that is affecting the mean. The red symbols represent the RS terms, the black the MS terms and the green the viscous terms. Note, the plots in the left-hand column of each subfigure are the typical sizes of the terms that dictate  $\bar{u}$ , and the plots in the right-hand column are the typical sizes of the terms that dictate  $\bar{v}$ .

In the  $Ra = 5 \times 10^5$  case, (plot (a)), from the right-hand side plots, we see that the RS term in equation (8.2.9), which drives  $\bar{v}$ , decreases with increasing  $Q$ , whilst the MS term increases, this supports the fact that as  $Q$  is increased the size of  $\bar{v}$  is decreased (cf. figure 8.3). Note also that the viscous term is roughly constant throughout the chaotic regime and decreases significantly in the steady regime. We see that the RS term dominates  $\bar{v}$  until  $Q \approx 5000$  and then the MS and RS terms are of roughly equal importance. If  $Q$  is increased further, to  $Q = 10000$ , then the MS term becomes the dominant term. This is reflected in the behaviour of the different terms, as seen in figure 8.9. The left-hand side plots of figure 8.10 (a) show that, for  $\bar{u}$ , the viscous term plays a larger role, in agreement with before. Also, up until the largest  $Q$  ( $Q = 10000$ ), the RS term and the viscous term dominate and it is their combination that determines the size of  $\bar{u}$ . As with the terms driving  $\bar{v}$ , for  $Q = 10000$ , the MS term has become the dominant term and this determines  $\bar{u}$ . For the RS term, the ratios of the correlations to the kinetic energy in the perturbations slightly increase, and so the decreases in the correlations are less than the decrease in the perturbations. For the MS term, the ratios of the correlations to the magnetic energy in the perturbations slightly decrease, and so the increase in the correlations is less than in the perturbations.

Examining the equivalent plots for increased  $Ra = 5 \times 10^6$ , see figure 8.10 (b), we find, for the terms driving  $\bar{v}$  (right-hand side), in the relaxation oscillation/chaotic regimes the RS term decreases as  $Q$  increases. In comparison to the RS term, the MS term and the viscous term are relatively unchanged. Up until  $Q$  is approximately 25000, the RS term is the largest, but after this value of  $Q$ , the MS term becomes increasingly dominant. For the terms driving  $\bar{u}$  (left-hand side), in the relaxation oscillation and chaotic regimes, the RS term is decreasing with increasing

$Q$ , whilst the MS term is slightly increasing - this explains the decrease in  $KE_{\bar{u}}$  as  $Q$  is increased. As in the smaller  $Ra$  case, the viscous term is more important for determining  $\bar{u}$  than it is for  $\bar{v}$ . Considering the ratio of the mean correlations to the perturbation energies (figure 8.10 (b), bottom row) gives us that the magnetic field correlations are increasing with  $Q$  less than the magnetic field perturbations are. In the chaotic regime, the ratio of the size of the RS terms to  $KE_{\text{pert}}$  is changed slightly by  $Q$ ; the ratio of the RS term driving  $\bar{v}$  to  $KE_{\text{pert}}$  is decreasing (in the chaotic regime) and the ratio of the RS term driving  $\bar{u}$  to  $KE_{\text{pert}}$  is increasing with  $Q$ . This behaviour is reflected in the behaviour of the kinetic energy in the mean flows.

### 8.2.5 Linear approximation

In an analogous way to section 7.2.3, we compare the differences between the RS and MS terms as calculated using the eigenfunctions obtained from the linear code (cf. section 3.3) with the actual RS and MS terms calculated from the fully nonlinear code (as in this chapter). Figure 8.11 shows the RS and MS terms as calculated from the nonlinear code (solid lines) and as calculated from the linear code (dashed lines). The amplitude of the linear eigenfunctions is normalised so that its maximum value coincides with the maximum value of the nonlinear (correct) terms.

As mentioned previously, the critical Rayleigh number is increased as  $Q$  is increased, and so for fixed  $Ra$ , the larger  $Q$  solutions lie in a less supercritical regime, we would therefore expect the linear behaviour to match that of the nonlinear calculation more closely. Indeed, for  $Q = 10000$  (c), the linear calculation provides a reasonable approximation to the nonlinear one. There is however, some evidence of nonlinear effects even at this  $Q$ , for example, the narrowing of the jet profile that can be seen in the nonlinear calculation is not captured in the linear case. For smaller  $Q$ , the agreement between the linear and nonlinear cases is worse, especially in the MS term. The MS term affecting  $\bar{u}$ , i.e.,  $\frac{\partial}{\partial z} \overline{B_2 B_3}$ , is well approximated in the bulk of the fluid but the agreement breaks down close to the boundary layers. This appears to be because the linear calculation is not capturing the expulsion of magnetic field that occurs in the nonlinear system for small  $Q$  (cf. figures 8.6, 8.7).

The largest discrepancy between the nonlinear and linear calculations occurs for the MS term affecting  $\bar{v}$ , i.e.,  $\frac{\partial}{\partial z} \overline{B_1 B_3}$ . In fact, the difference is so large that the linear calculation does not capture the actual behaviour in any way (at small  $Q$ ), this MS term therefore, must result from a nonlinear process. The poor performance of the linear calculation in approximating the nonlinear RS and MS terms at small  $Q$ , could be rectified by considering the interaction of the mean flow

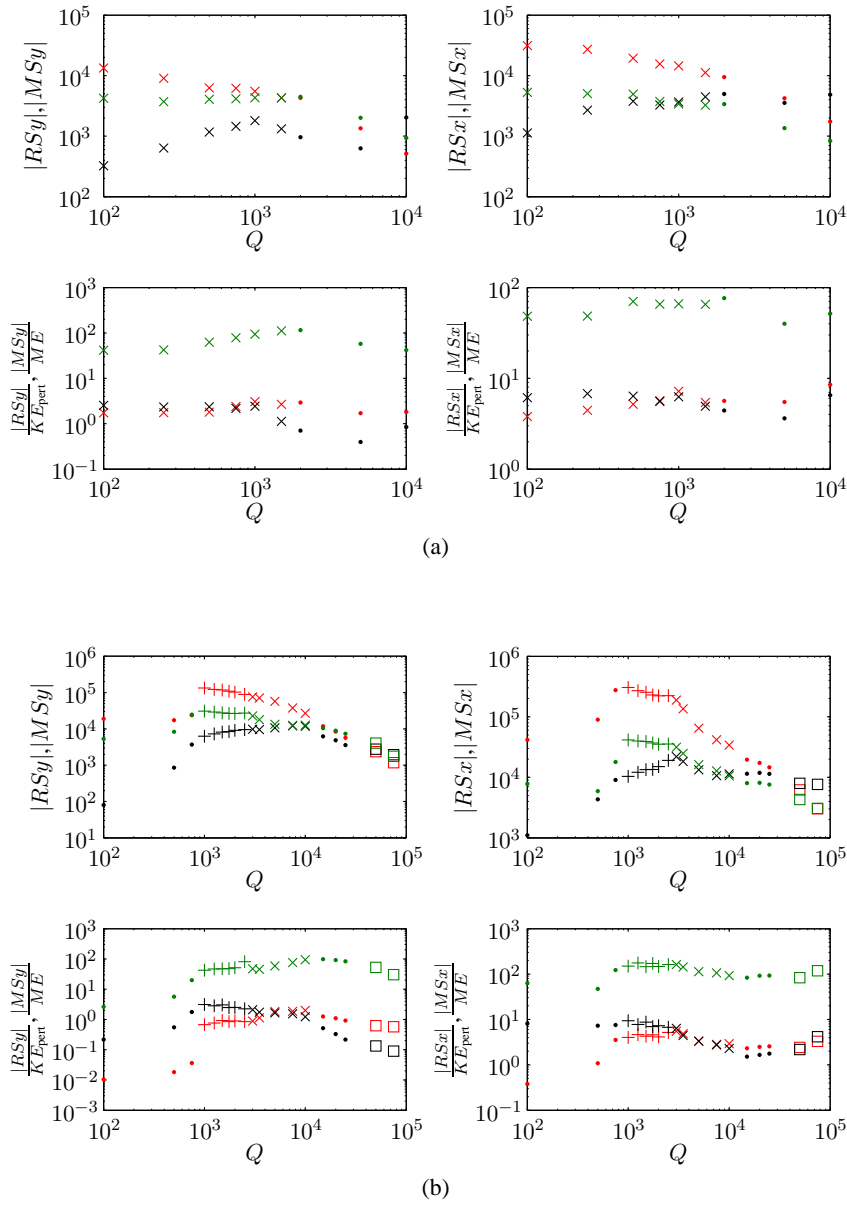


Figure 8.10: Typical sizes of the terms in the mean flow equations (as given by (8.2.10) and (8.2.11)). In red are the RS terms, in black the MS terms and in green the viscous terms for  $Pr = 1$ ,  $\zeta = 1.1$  and (a),  $Ra = 5 \times 10^5$  and (b),  $Ra = 5 \times 10^6$ . The different symbols represent the same solution regimes as they did in figures 8.3 and 8.8.

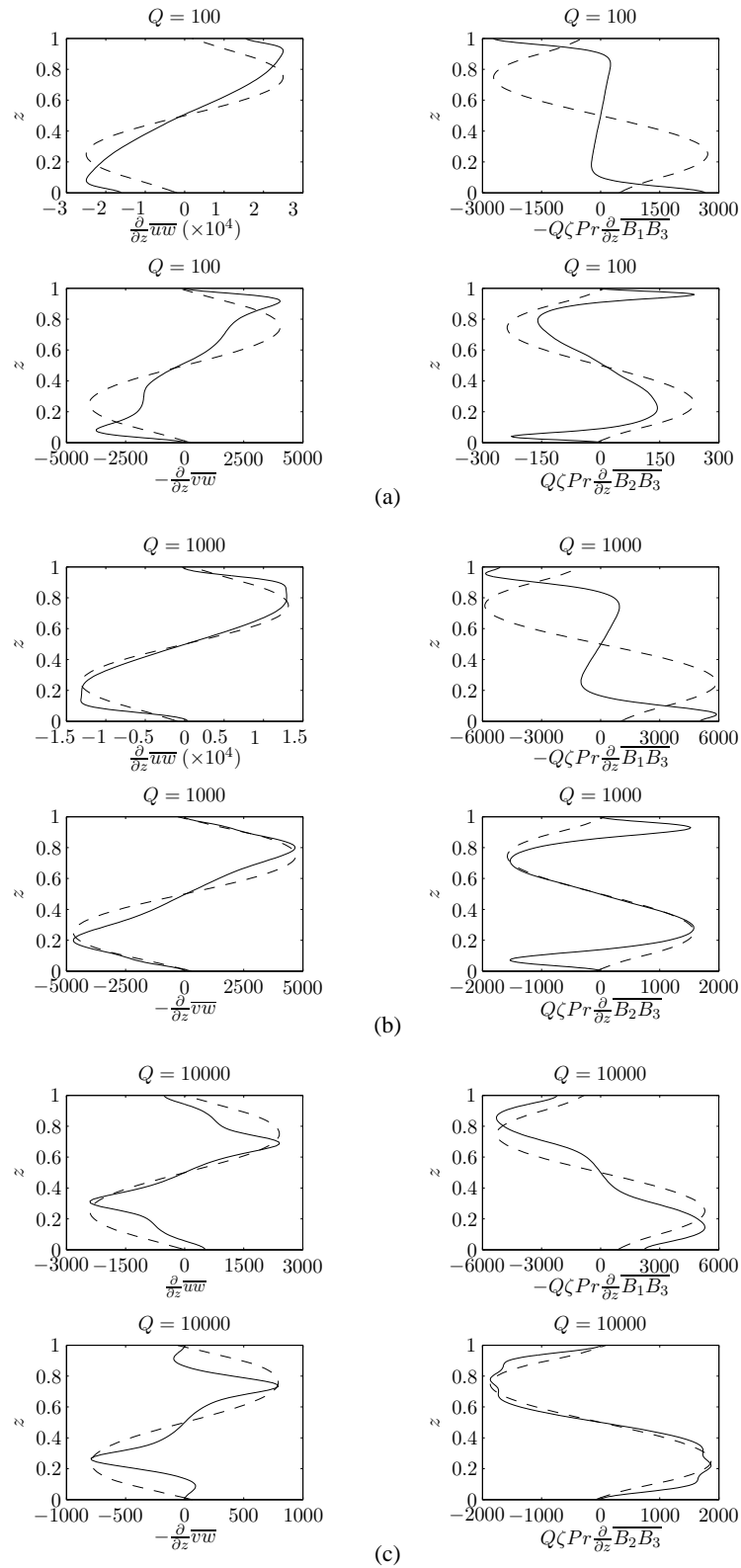


Figure 8.11: The RS terms (left-hand column) and MS terms (right-hand column) calculated from the nonlinear code (solid lines) and the RS terms calculated from linear eigenfunctions (dashed lines) for  $Pr = 1$ ,  $\zeta = 1.1$ ,  $Ra = 5 \times 10^5$  and (a)  $Q = 100$ , (b)  $Q = 1000$  and (c)  $Q = 10000$ . The agreement is better for larger  $Q$ .

and field with the fluctuations. Further possibilities for examining this will be discussed in Chapter 9.

### 8.2.6 Effect of $\zeta$

In this section, we examine the effect of decreasing  $\zeta$ . We do this by considering  $\zeta = 0.1$ , unless otherwise stated, and we draw comparisons with the  $\zeta = 1.1$  regime investigated in the previous sections.

The kinetic energy in the mean flows for a small  $\zeta$  case are shown, as a function of  $Q$ , in figure 8.12. On comparison with the energies in the  $\zeta = 1.1$  case (figure 8.3), we see that the behaviour of the two cases is similar. The main difference, however, is that the solutions remain chaotic for all  $Q$  in the small  $\zeta$  case. From figure 8.12, it is especially clear that there are two different regimes; for  $Q \lesssim 2000$ , the decrease in the kinetic energy of  $\bar{v}$  is roughly matched by the decrease in the total kinetic energy and so the ratio of the two is roughly constant, but for  $Q \gtrsim 2000$ , the ratio is decreasing and so the energy in  $\bar{v}$  is being decreased by the field more than the energy in the perturbations is. The flow in the  $x$ -direction ( $\bar{u}$ ) is affected in a different way; for small  $Q$ , the mean measure is increased, whilst the variability measure is decreased slightly, i.e., the field is not only reducing the magnitude of the flow slightly, but it is organising it into a more coherent state. The variability measure of  $KE_{\bar{u}}$  is decreasing but only slightly more than the energy in the perturbations and so the ratio is approximately constant.

By analysing the time-dependent mean flows, we found that they are of a similar form to those found when  $\zeta = 1.1$ , especially for small  $Q$ . We show the cases when  $Q = 10000$  and  $Q = 50000$  for  $\zeta = 0.1$  in figure 8.13. The similarity at small  $Q$  is to be expected as  $\zeta$  appears with  $Q$  in the equations and so if  $Q$  is small, then the MS term will play a less important role. Furthermore, as  $Q$  is increased, we found that a larger  $Q$  had to be reached in the  $\zeta = 0.1$  case before the same flow structure was apparent as in the  $\zeta = 1.1$  case. For example, the boundary layers in  $\bar{u}$  and  $\bar{v}$  (seen in figure 8.4 (b) but not 8.4 (a)) are not seen until  $Q \approx 10000$  for the  $\zeta = 0.1$  case (see figure 8.13 (a)), this can again be explained by the fact that  $\zeta$  appears with  $Q$  in the equations and so it is their product that is a measure of the applied field.

As was highlighted in figure 8.12, for small  $\zeta$ , the chaotic regime persists for much higher  $Q$ . We find that, within the chaotic regime, there is a change in the form of the mean flows. After  $Q \approx 20000$ , we see this change in the structure of the flows, we show an example of this for  $Q = 50000$ , see figure 8.13 (b). We notice a large change in the structure of the flows for this

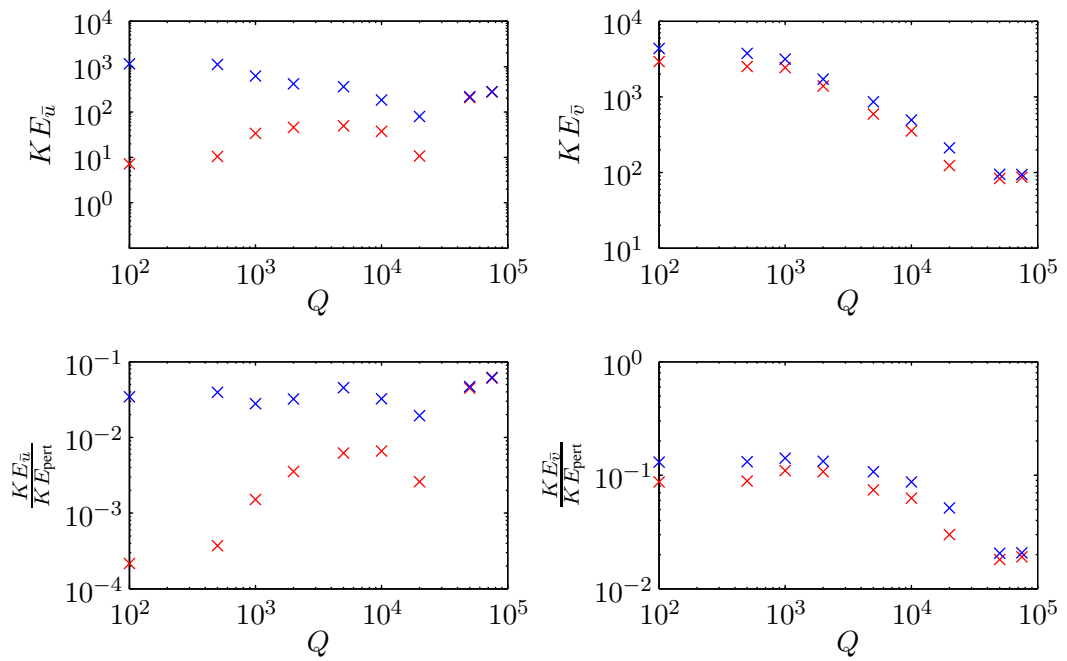


Figure 8.12: Kinetic energies in the mean flow for  $Pr = 1$ ,  $\zeta = 0.1$ ,  $Ra = 5 \times 10^5$  and a range of  $Q$ . The top row gives the mean measure of the energy in  $\bar{u}$  (left) and  $\bar{v}$  (right) in red and the variability measure of the energy in blue. Chaotic solutions are marked with a cross and steady solutions with a dot. The bottom row gives the ratio of the energy in the mean flow to the energy in the perturbations.

value of  $Q$ , compared with the flows for  $Q = 10000$  (8.13 (a)). For  $\bar{v}$ , the positive and negative banded structure in the bulk of the fluid, that was present at smaller  $Q$ , no longer exists, instead a wide band of mostly positive flow is observed. The flow is less time-dependent, i.e., there are fewer fluctuations in the flow, and also, the flow at the boundaries is much stronger than in the smaller  $Q$  case. Furthermore, the overall size of the flow is reduced in the larger  $Q$  case.  $\bar{u}$  has changed from being a highly fluctuating flow to one consisting of less time-dependent jets. The flow at the boundaries is still the strongest, but in this case, both boundaries have negative flow, whereas in (a) the top boundary has positive flow close to it. Hence, increasing  $Q$  has not only decreased the magnitude of the mean flows but it has changed the vertical structure of the flows.

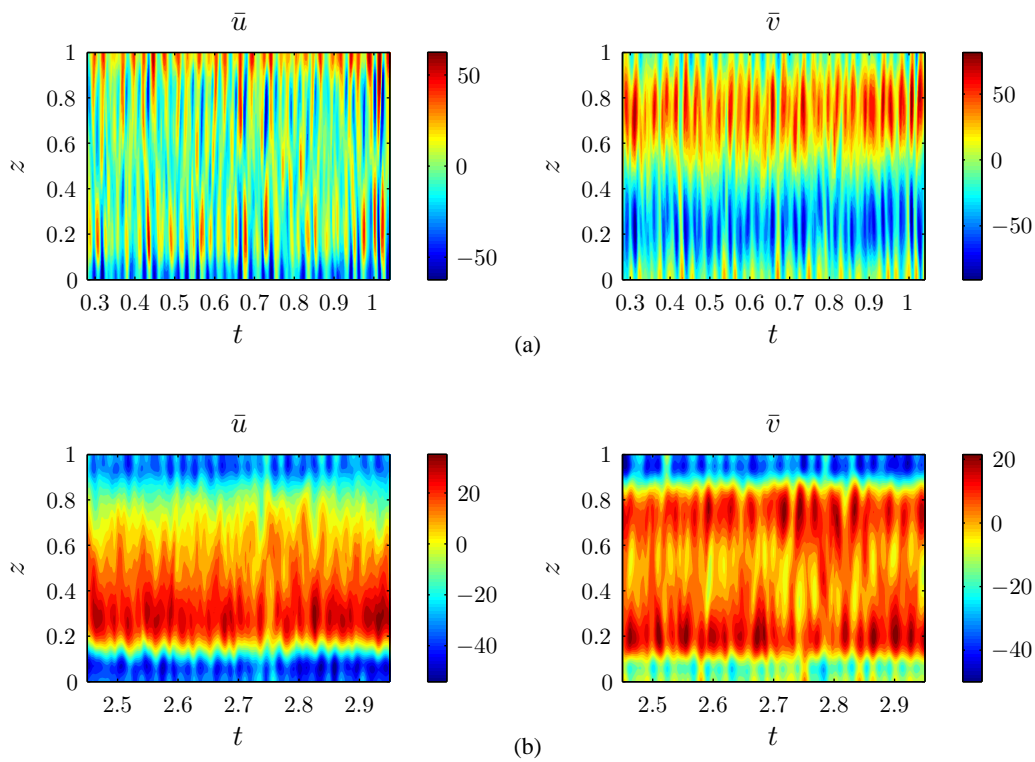


Figure 8.13:  $\bar{u}$  (left) and  $\bar{v}$  (right) for  $Pr = 1$ ,  $\zeta = 0.1$ ,  $Ra = 5 \times 10^5$  and (a)  $Q = 10000$ , (b)  $Q = 50000$ .

If we consider the size and structure of the terms driving the mean flows seen in figure 8.13, i.e., if we consider the terms of the mean flow equations (8.2.8) and (8.2.9), then for flows such as the ones given in figure 8.13 (a), we find a similar balance of terms to in figure 8.9 (b) and so we do not show the plots again here, however, we recap the main points. For case (a), the RS term is free to drive  $\bar{v}$  in the bulk of the layer, but the field expelled to the boundaries results in a MS term that opposes the RS term there and causes relatively little flow at the boundaries. In contrast, for  $\bar{u}$ ,

the terms cancel in the bulk of the layer and the flow is small there, but larger viscous boundary values result in a larger mean  $\bar{u}$  close to the boundaries.

For the large  $Q$  case of figure 8.13 (b), i.e.,  $Q = 50000$ , the terms of the mean flow equations must be different, in order to result in the different mean flows we observe. The results for this case are shown in figure 8.14.  $\bar{u}$  (top plot) is clearly dominated by the MS term; the MS term has two strong, negative boundary layers and a positive band in the interior, closely resembling the mean flow term,  $Pr\bar{u}$ .  $\bar{v}$  is determined from the terms shown on the bottom set of axes. The boundary layers present in the viscous and MS terms at the top of the layer combine to give the strong negative flow we observe there, whilst close to the bottom boundary, the viscous and MS terms approximately cancel to give a much smaller flow. In the interior, the structure of  $\bar{v}$  is not clearly dominated by any one term and results from a balance of all three terms.

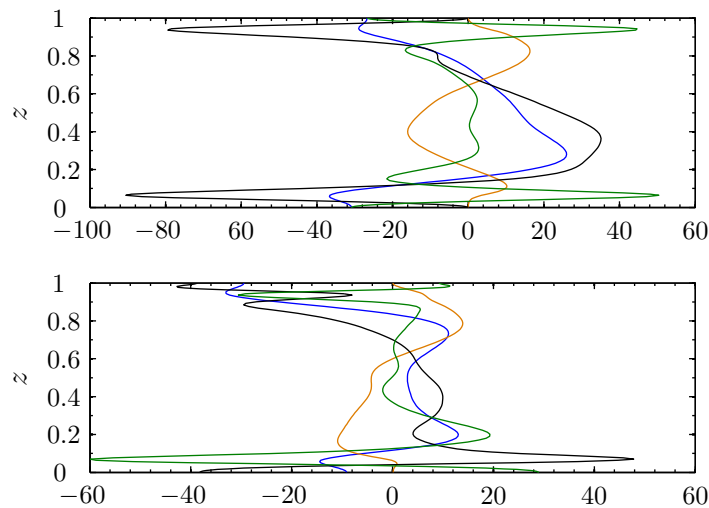


Figure 8.14: Terms of the mean flow equations, (8.2.8) (top) which drive  $\bar{u}$ , and (8.2.9) (bottom) which drive  $\bar{v}$ , for  $Pr = 1$ ,  $\zeta = 0.1$ ,  $Q = 50000$  and  $Ra = 5 \times 10^5$ . In orange are the RS terms, in black are the MS terms, in green are the viscous terms and in blue are the mean flow terms.

By considering the relative size of the RS and MS terms, as defined by (8.2.10) and (8.2.11) respectively, we can examine the value of  $Q$  at which the terms first balance. Figure 8.15 displays a plot of the ratio of the MS terms to the RS terms against  $Q$ , for different  $\zeta$ . From the plots, we see that the RS terms are balanced by the MS terms at larger  $Q$  for smaller  $\zeta$ . This may be explained from the mean flow equations (8.2.8) and (8.2.9), as the MS term has a  $Pr\zeta Q$  factor multiplying the  $z$ -derivative of the Maxwell stresses, therefore, assuming the Maxwell stresses are themselves not changed too much by  $\zeta$ , a larger  $Q$  will be needed for the MS term to have the

same effect at smaller  $\zeta$ .

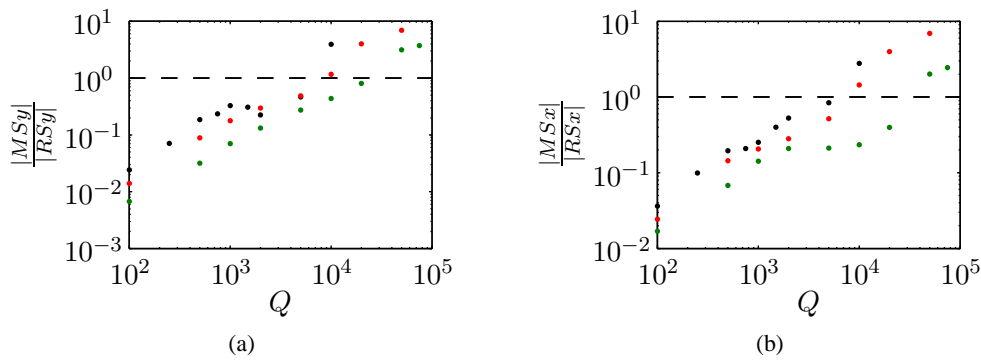


Figure 8.15: Ratio of the typical sizes of MS to RS terms that drive (a)  $\bar{u}$  and (b)  $\bar{v}$ , as a function of  $Q$ , for  $Pr = 1$  and  $Ra = 5 \times 10^5$ . In black,  $\zeta = 1.1$ , in red,  $\zeta = 0.5$  and in green,  $\zeta = 0.1$ .

To see if changing  $\zeta$  has any effect on the systematic nature of the mean flows, we consider the standard deviation,  $\sigma$ , in  $\bar{u}$  and  $\bar{v}$  at fixed  $z$ . The results are shown in figure 8.16. In (a), we plot  $\sigma$  against  $Q$ , and in (b), we plot  $\sigma$  against  $\zeta Q$ . We have considered two different  $\zeta$ , in black  $\zeta = 1.1$  and in green  $\zeta = 0.1$ . It is clear from the plots in (a) that, as  $Q$  is increased, the standard deviation in  $\bar{u}$  and  $\bar{v}$  is decreased for both  $\zeta$ . As described before, this is because the increase in field strength causes the flow to become more aligned and hence become more systematic, which leads to a reduced standard deviation. As explained before, a smaller  $\zeta$  requires a larger  $Q$  for the MS term to achieve the same effect as for the larger  $\zeta$ . In fact, if we plot the standard deviation against  $\zeta Q$  instead, see figure 8.16 (b), then the standard deviation for the two  $\zeta$  are much closer in size. In particular, for smaller  $\zeta Q$ , the  $\zeta = 0.1$  solutions have the smaller standard deviation and are therefore more systematic (at fixed  $\zeta Q$ ), but as  $\zeta Q$  is increased the standard deviations for the two  $\zeta$  considered become closer and are almost equal in magnitude.

### 8.2.7 Effect of $Pr$

In this section, we decrease  $Pr$  to 0.1 which, as mentioned on numerous occasions, is more physically relevant. For this work, we fix  $\zeta = 0.5$ ; with  $Pr = 0.1$ , this results in a magnetic Prandtl number of  $Pm = 0.2$ , this is in contrast to  $Pm = 0.91$  and  $Pm = 10$  for the cases studied in sections 8.2.1 and 8.2.6 respectively.

In contrast to previous examples (e.g., figure 8.1), when  $Pr = 0.1$ ,  $\zeta = 0.5$  and  $Ra = 5 \times 10^5$ , the kinetic energy does not monotonically decrease with increasing  $Q$ , at fixed  $Ra$ , see figure 8.17 (a).

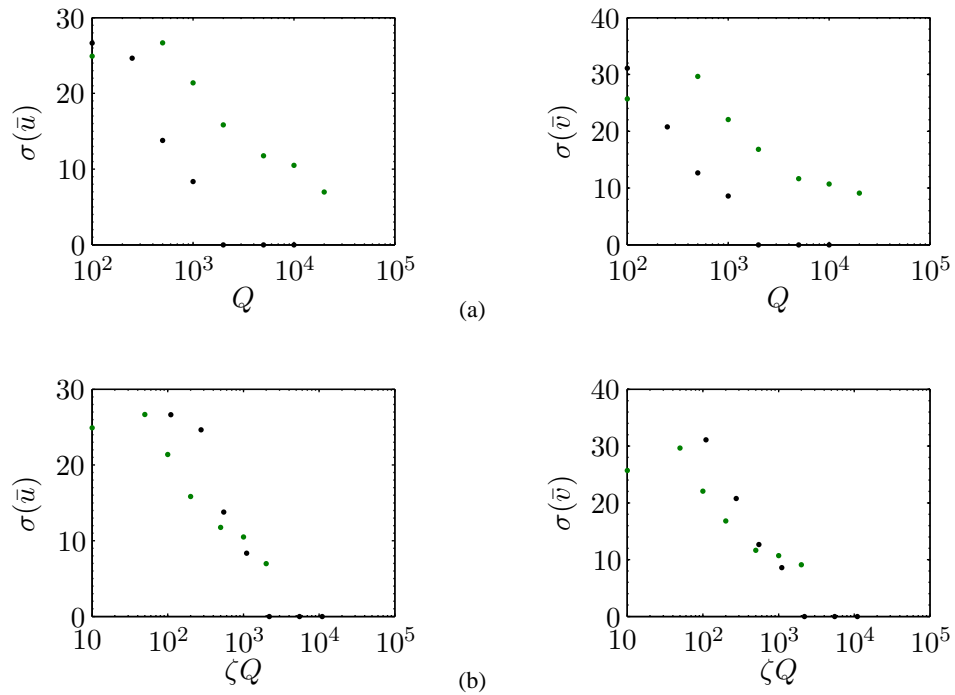


Figure 8.16: Standard deviation,  $\sigma$ , in  $\langle \bar{u} \rangle$  (left) and  $\langle \bar{v} \rangle$  (right) as a function of (a)  $Q$  and (b)  $\zeta Q$ , for  $Pr = 1$ ,  $Ra = 5 \times 10^5$  and  $\zeta = 1.1$  (black) and  $\zeta = 0.1$  (green).

Instead, there is a decrease in the kinetic energy with increasing  $Q$  in the chaotic regime, but an increase in the kinetic energy with  $Q$  in the quasi-periodic regime. The reasons for this behaviour are not obvious and require further investigation. However, if we consider the dependence of the magnetic energy on  $Q$ , we obtain the plot shown in figure 8.17 (b), the behaviour in this case is qualitatively the same as seen in previous examples (e.g., figure 8.1), i.e., the magnetic energy is monotonically increasing with  $Q$  for all  $Q$  shown.

To see what behaviour is contributing to the rise in kinetic energy at high  $Q$ , we plot the kinetic energies of the mean flows  $\bar{u}$  and  $\bar{v}$ , as calculated by the mean and variability measures; the results are shown in figure 8.18. Also shown are the ratios of the energies in the mean flows to the energy in the perturbations. As in figure 8.17, crosses represent chaotic solutions and triangles represent quasi-periodic solutions. In the chaotic regime, as  $Q$  is increased, the variability measure of both  $\bar{u}$  and  $\bar{v}$  decreases, demonstrating that the field acts to reduce the magnitude of the flow in both directions, just as it did for larger  $Pr$ . The mean energy is also reduced with increased  $Q$  for  $\bar{u}$ , but there is a slight increase in the mean energy of  $\bar{v}$ . Comparing these plots with those for  $Pr = 1$  (see figure 8.3) we see that  $\bar{u}$  is more systematic for  $Pr = 0.1$ , as the mean and variability measures are closer in magnitude, but  $\bar{v}$  is less so. The ratio of the variability measure

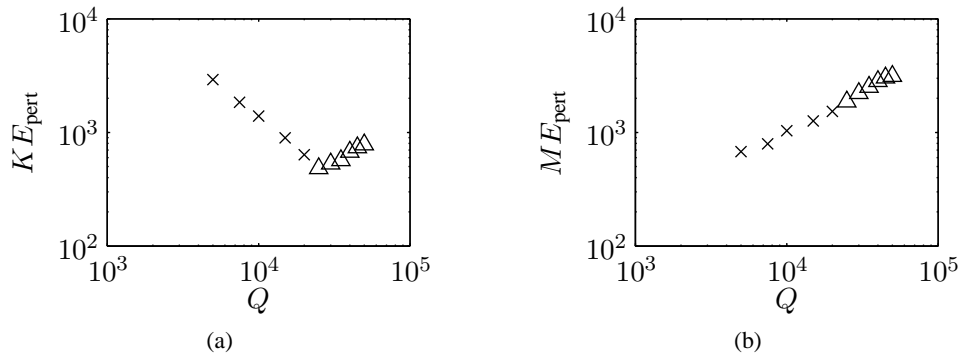


Figure 8.17: Energies in the kinetic energy and magnetic energy for  $Pr = 0.1$ ,  $\zeta = 0.5$ ,  $Ra = 5 \times 10^5$  and a range of  $Q$ . Chaotic solutions are marked with a cross and quasi-periodic solutions with a triangle.

to the kinetic energy in the perturbations in the chaotic regime, is roughly constant in both cases, indicating that the decrease in the mean velocity is matched by a decrease in perturbation velocity. The decrease in  $KE_{\langle \bar{v} \rangle}$  with increased  $Q$  is not as severe as the decrease in  $KE_{\text{pert}}$  since the ratio of the two increases slightly with  $Q$ . The increase in the ratio  $\frac{KE_{\langle \bar{v} \rangle}}{KE_{\text{pert}}}$  is due to the fact that  $KE_{\langle \bar{v} \rangle}$  increases but  $KE_{\text{pert}}$  decreases as  $Q$  is increased. When  $Q$  is large enough, the solutions become quasi-periodic. In this regime, the kinetic energy in both measures of  $\bar{u}$  and  $\bar{v}$  increases with  $Q$ , as does the kinetic energy in the perturbations. However, the growth with  $Q$  in the kinetic energy in the mean flows is more than in the perturbations, as seen from the fact that the ratios are also increasing in this regime.

To investigate whether this type of behaviour is evident for other  $Ra$  close to  $Ra = 5 \times 10^5$ , we examine the change in the average  $KE_{\text{pert}}$ ,  $ME_{\text{pert}}$ ,  $\theta^2$  and  $Nu$  with  $Ra \in [10^5, 5 \times 10^5]$ , for two different  $Q$ . Considering first the kinetic energy in the perturbations as a function of  $Ra$ , for  $Q = 25000$  and  $Q = 50000$  (figure 8.19 (a)), we observe that for  $Ra \lesssim 3.5 \times 10^5$ , the smaller  $Q$  solutions are the most energetic, this is in line with what we might expect as, the smaller  $Q$  is, the smaller  $Ra_c$  is, and hence the smaller  $Q$  solution is more supercritical (at fixed  $Ra$ ). However, this argument breaks down, in this case, at larger  $Ra$ , where the  $Q = 50000$  solutions are the more energetic. We also notice that, the growth is uniform for the larger  $Q$  solutions whereas for the  $Q = 25000$  solutions, the growth appears to occur in two stages. From figure 8.19 (b), the magnetic energy of the  $Q = 25000$  solutions also grows in two different stages, in contrast to the  $Q = 50000$  solutions, where the growth is more uniform. The magnetic energy of the  $Q = 25000$  solution is smaller than the  $Q = 50000$  solution for all  $Ra$ , this agrees with what we would

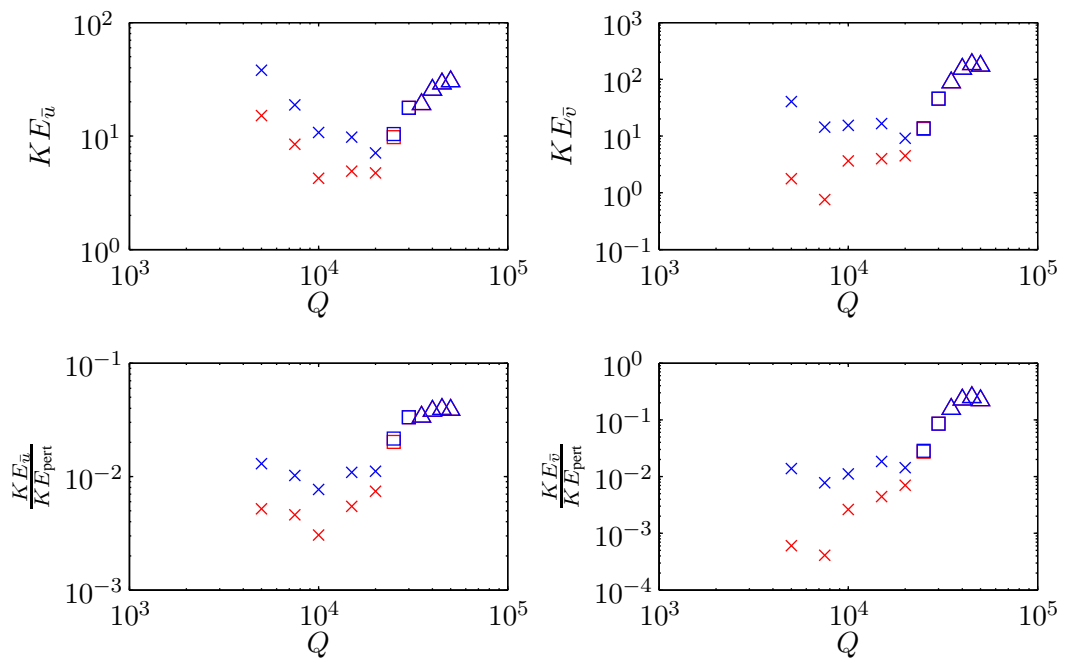


Figure 8.18: Energies in the mean flow for  $Pr = 0.1$ ,  $\zeta = 0.5$ ,  $Ra = 5 \times 10^5$  and a range of  $Q$ . The mean measure of the energy is given in red and the variability measure in blue. Chaotic solutions are marked with a cross and quasi-periodic solutions with a triangle. The bottom row presents the ratios of the energies in the mean flows to the energy in the perturbations.

expect as, from the definition (see equation (5.6.145)),  $ME_{\text{pert}}$  is proportional to  $Q$ . We also see that, from figure 8.19 (c), the thermal energy as measured by  $\theta^2$ , is reduced at large  $Ra$  for the smaller  $Q$ . The slowing in the rate of increase, or the decrease of the energies for  $Q = 25000$  at larger  $Ra$  means that dissipation in the system must be larger there, so as not to violate the law of conservation of energy.

As we have done previously (e.g., Chapter 6), we can consider the Nusselt number,  $Nu$ , as a measure of the effectiveness of the convection at transporting heat. We plot  $Nu$  against  $Ra$  in figure 8.19 (d), and we notice that, even at larger  $Ra$ ,  $Nu$  is larger for  $Q = 25000$  and so the system with relatively small kinetic energy has found an efficient way to transport heat via convection. This can be compared with the large  $Nu$  solutions found in section 6.2.4, though there, there was an obvious change in the length scale of the solution that is not present here. Also in contrast to the large  $Nu$  solutions in section 6.2.4, here, the change to solutions that are more efficient at transporting heat by convection, occurs within the chaotic regime whereas in section 6.2.4, the change coincided with a change of regime from chaotic to steady.

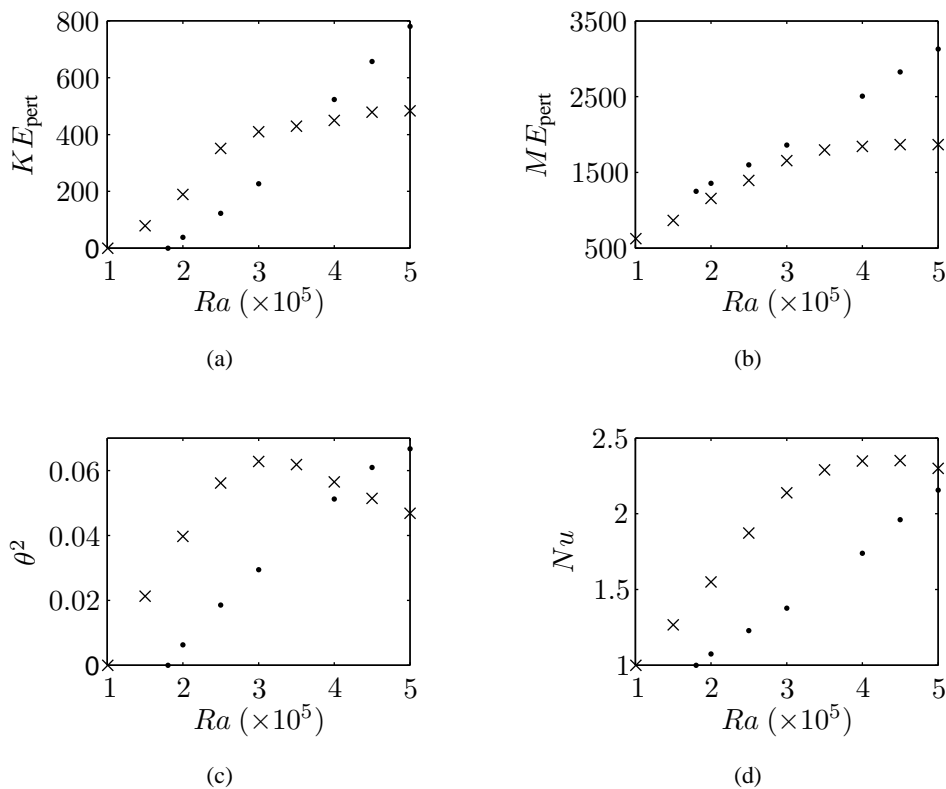


Figure 8.19:  $KE_{\text{pert}}$  (a),  $ME_{\text{pert}}$  (b),  $\theta^2$  (c) and  $Nu$  (d) as a function of  $Ra$  for  $Pr = 0.1$ ,  $\zeta = 0.5$  and  $Q = 25000$  (crosses),  $Q = 50000$  (dots).

From figures 8.17 and 8.18, it is clear that there are two distinct regimes. For  $Q \lesssim 20000$ , the solutions are chaotic and the energy in the mean flow decreases with increasing  $Q$ , but for  $Q \gtrsim 20000$ , the solutions are quasi-periodic and the energy in the mean flow increases with  $Q$ . Here, we consider the change in the form of the mean flows as we move between the two regimes. In figure 8.20 (a), time-dependent  $\bar{u}$  (left-hand side) and  $\bar{v}$  (right-hand side) are shown for  $Q = 20000$ . We see that  $\bar{u}$  consists of four alternating bands: a positive and negative jet in the bulk and two smaller jets at the boundaries, one positive and one negative.  $\bar{v}$  is made up of two distinct bands in the interior and smaller boundary layer jets, where the flow is reduced. These flows are of the form of the chaotic solutions we saw in figure 8.4 (b) and in figure 8.13 (a). The slight difference being that  $\bar{u}$  is more systematic in the small  $Pr$ ,  $\zeta$  case and  $\bar{v}$  is less systematic. A larger  $Q$  is needed to achieve such a flow pattern in this case than is needed in the larger  $Pr$  cases. As when considering the effect of  $\zeta$  in section 8.2.6, this can be explained by the  $Pr\zeta Q$  factor in the MS term of the mean flow equations. In figure 8.20 (b), the time-dependent  $\bar{u}$  (left-hand side) and  $\bar{v}$  (right-hand side) are shown for a solution from the quasi-periodic regime. The less time-dependent nature of these flows is evident and we see that, instead of two jets of opposite direction occurring in the interior, one larger scale, negative band is present.

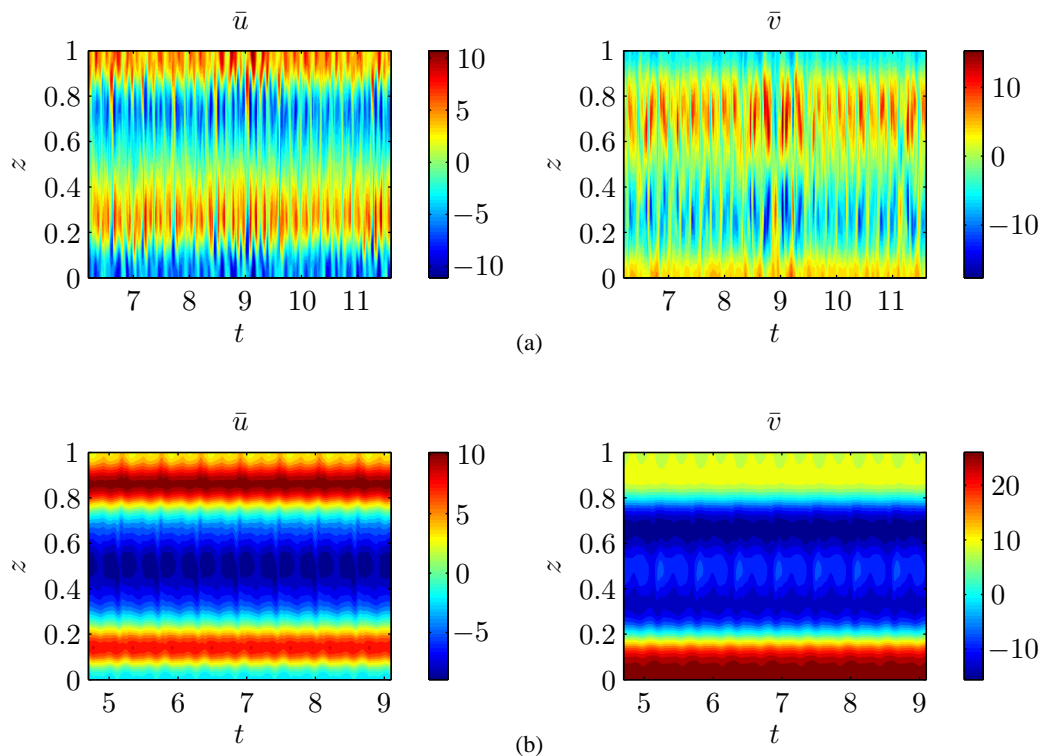


Figure 8.20: Time-dependent  $\bar{u}$  (left) and  $\bar{v}$  (right) for  $Pr = 0.1$ ,  $\zeta = 0.5$ ,  $Ra = 5 \times 10^5$  and (a)  $Q = 20000$ , (b)  $Q = 35000$ .

In a similar way to before, we analyse the terms of the mean flow equations (8.2.8) and (8.2.9) to see what is responsible for driving the flows we observed in figure 8.20. Analysis of the terms that drive the flows in figure 8.20 (a) gives a similar balance to the terms shown in figure 8.14 (b) and therefore we do not repeat this analysis here. But we analyse the terms that drive the flows in figure 8.20 (b), as these are different to the ones discussed in other cases. Each term of the mean flow equations is shown in a different colour in figure 8.21; the terms driving  $\bar{u}$  are in the top plot and the terms driving  $\bar{v}$  in the bottom plot. The structure of  $\bar{u}$  is dominated by the MS term, but the other terms contribute to give the structure we observe. Recall that the RS and MS terms actually dictate  $Pr\bar{u}$  and  $Pr\bar{v}$  and so even though the driving terms are small, a significant flow is produced since  $Pr < 1$ . By considering the terms that drive  $\bar{v}$ , we see that the vertical structure of  $\bar{v}$  is not dominated by one particular term.

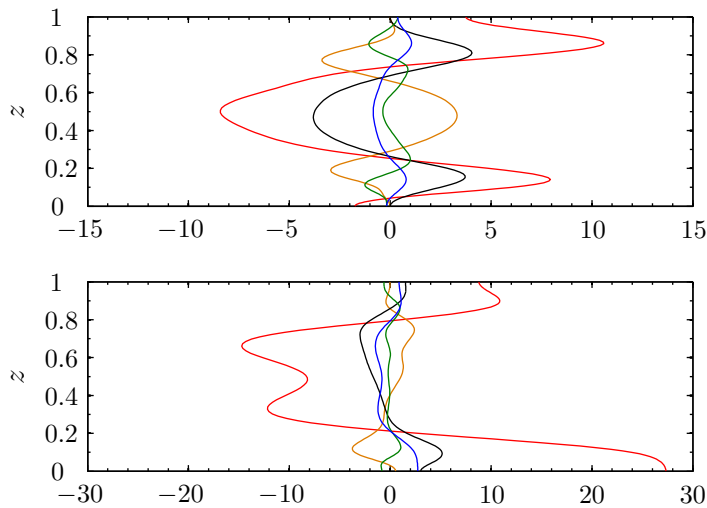


Figure 8.21: Terms of the mean flow equations, (8.2.8) (top) which drive  $\bar{u}$ , and (8.2.9) (bottom) which drive  $\bar{v}$ , for  $Pr = 0.1$ ,  $\zeta = 0.5$ ,  $Q = 35000$  and  $Ra = 5 \times 10^5$ . In orange are the RS terms, in black are the MS terms, in green are the viscous terms, in blue are the mean flow terms and in red are the mean flows themselves.

As we have seen throughout, it is the Reynolds stresses that drive the mean flows, and as the magnetic field is increased, the Maxwell stresses become more important and modify the flows. By comparing the typical size of the RS and MS terms, as defined by (8.2.10) and (8.2.11), we can see at which value of  $Q$  the two balance. In figure 8.22 we show the ratio of MS to RS terms as a function of  $Q$  for two  $Pr$  and  $\zeta = 0.5$ ,  $Ra = 5 \times 10^5$ . As was the case for small  $\zeta$ , the small  $Pr$  system requires a larger  $Q$  for the MS term to balance the RS term.

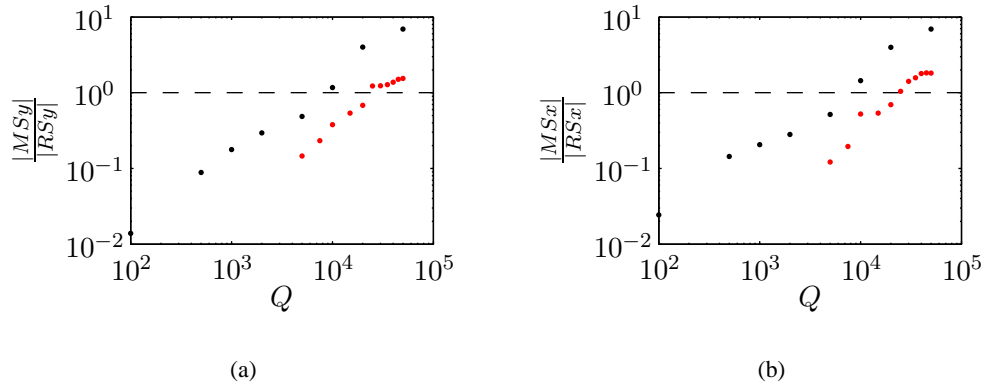


Figure 8.22: Ratio of the typical sizes of MS to RS terms that drive (a)  $\bar{u}$  and (b)  $\bar{v}$ , as a function of  $Q$ , for  $\zeta = 0.5$  and  $Ra = 5 \times 10^5$ . In black,  $Pr = 1$  and in red,  $Pr = 0.1$ .

### 8.3 Summary

The aim of this chapter was to examine the effect of a horizontal magnetic field on convection in a plane layer model with a tilted rotation vector. We found that, in general, as the strength of the magnetic field was increased, the kinetic energy of the system decreased and the magnetic energy increased. Although, for small  $Pr$  and  $\zeta$ , we found a region of parameter space where the kinetic energy increased with  $Q$ . We also found that, for  $\zeta = 1.1$ , whilst the small  $Q$  solutions were chaotic, there was a move towards steady solutions, as  $Q$  was increased. With this change, came the move to larger-scale solutions, with the preferred wave number decreasing. On comparison with the wavenumber expected from linear theory, it was found that nonlinear effects cause the scale of the solutions to increase.

We investigated the effect of the magnetic field on the mean flows driven. For  $Pr = 1$ ,  $\zeta = 1.1$ , the field reduced the magnitude of the flows but increased the systematic nature of them, i.e., they became less time-dependent. The small  $Q$ , chaotic flow in the plane, that is,  $\bar{v}$ , was found to consist of a band of positive flow in the upper half-plane and a band of negative flow in the lower half-plane. This persisted when  $Q$  was increased, however, in these cases the flow did not extend all the way to the boundaries and boundary layers of relatively slow flow were formed.

By studying the mean fields in the system, we demonstrated that, at small  $Q$ , magnetic field was expelled to the boundaries, but as  $Q$  was increased this expulsion became more difficult. This meant that there was little magnetic field left in the bulk of the layer to inhibit the mean flows in these cases.

As was the case in Chapters 6 and 7, we derived the mean flow equations, in order to see what dictated the size and structure of the mean flows. The mean flow equations were similar to the mean flow equations in the hydrodynamic system, the only difference being, the addition of an extra term due to the magnetic field. This Maxwell stress term became increasingly important for determining the mean flows as  $Q$  was increased, for two reasons. Firstly, the MS term was proportional to  $Q$  and so had a larger influence for larger  $Q$ , secondly, less field was expelled to the boundaries in these cases and so the correlations were likely to be higher. We showed that at small  $Q$ , the RS term dominates and is able to drive a significant flow; at moderate  $Q$ , there is a balance in the interior of the layer and so the flow is dominated by boundary layers and for large  $Q$ , the MS term dominated and produced a small, yet systematic flow.

We considered what happens when more realistic parameter regimes were reached, i.e., smaller  $Pr$  and smaller  $Pm$ . We saw that, the effect of decreasing  $\zeta$  was to allow chaotic solutions to exist for a larger range of  $Q$ . We also found that in some cases the behaviour of the small  $\zeta$  solutions matched that of the  $\zeta = 1.1$  solutions but only when  $Q$  was increased, this was due to the presence of  $\zeta Q$  in the MS term. Unlike in the  $\zeta = 1.1$  case, the MS term was able to dominate the RS term whilst the solutions were still in the chaotic regime. When this was the case, we found that the mean flows were less time-dependent and that the interior flow was mostly of one sign, rather than forming an alternating jet structure as seen at smaller  $Q$ .

Decreasing  $Pr$ , whilst keeping  $Pm$  small, gave similar results. In particular, a larger  $Q$  was needed to achieve the same behaviour as for larger  $Pr$  because of the  $Pr\zeta Q$  factor in the MS term. In the case we examined, the solutions became quasi-periodic at large  $Q$  and these were accompanied by an increase in the kinetic energy of the system and a change in the vertical structure of the flow. As was the case in the hydrodynamic system, we demonstrated that, for small  $Pr$ , even if the driving terms are relatively small, a significant mean flow is still produced.

Finally, a linear calculation of the RS and MS terms led to the conclusions that as  $Q$  is increased, the nonlinear RS and MS terms can be well approximated by the linear eigenfunctions, however, some behaviour is still not captured. For example, the expulsion of flux to the boundaries is not captured by the linear calculation. The increase in agreement of the linear and nonlinear calculations with  $Q$  is to be expected since the solutions are less supercritical in this case and so the nonlinearities are not expected to be so large. We discuss extensions to this work in Chapter 9.

## Chapter 9

# Conclusions

### 9.1 Summary of results and discussion

In this thesis, we have investigated the interaction of convection with rotation and magnetic fields. In particular, we have focussed on the mean flows driven in a plane layer model of a convecting body. In Chapter 1, we introduced some of the many examples of where mean flows occur in nature, e.g., the differential rotation in the solar convection zone, and the mechanisms for driving them. As we discuss our work in the following paragraphs, we aim to relate the work we have done back to the initial problems that initially motivated their interest.

As a mathematical framework for our study, we presented the setup and governing equations of our model for studying convection in a plane layer in Chapter 2. The model was based upon that used by Hathaway *et al.* (1980) and was intended as a local approximation to a region around a latitude on a spherical body, so that the rotation vector was oblique to gravity. The major shortcoming of such a local model is its inability to describe the global behaviour of the body, a full spherical model would be more appropriate for such a study. However, important information about the underlying physical processes involved in rotating convection can still be extracted from a local model such as the one used in this thesis. The boundary conditions we elected to impose were impenetrable and stress free, chosen as they are less restrictive to mean flow generation than rigid boundaries and they are more realistic to stellar interiors. This distinguished our work from that of Hathaway *et al.* (1980) who assumed rigid boundaries. In reality, the boundaries of the convection zone are much more complex. For example, the outer boundary of the convection zone is coupled to the solar atmosphere and close to this boundary, convective motions, when considered with other physical processes there, lead to the granulation that is observed at the

surface. The imposed impenetrable boundary conditions of our model also prevent any flux across the boundary which again is a simplification. At the base of the convection zone, where the convection zone meets the tachocline, there is overshooting of convection towards the radiative zone, this is not possible with such idealised boundary conditions but can be modelled in more global models with more complex boundary conditions. For study of a single region, like the one in this thesis, impenetrable and stress free boundary are not too restrictive and allow us to make progress easily.

For simplicity, our study began by using the Boussinesq approximation which assumes a small layer depth ( $d$ ) compared to the pressure scale height of the system ( $H$ ) and so pressure variations may be neglected. This approximation is not a particularly good one for the Sun and other astrophysical objects since there are many pressure scale heights in the layer height (for example,  $H$  is less than 1% of the solar radius in the convection zone (Fan (2004))) and so pressure fluctuations should not be neglected. This led us to introduce the anelastic approximation whereby the constraint  $\frac{d}{H} \ll 1$  is relaxed, but the typical speeds are still considered small compared to the sound speed so that sound waves are filtered out. This is an accurate approximation for the Sun except for near surface layers where velocities associated with granulation can exceed the sound speed (Miesch (2005)).

Using the mathematical description from Chapter 2, we considered convection in the linear regime under the Boussinesq approximation (see Chapter 3). We examined three cases: (i) where there was no magnetic field or thermal wind present, (ii) where there was a thermal wind but no field and (iii) where there was a horizontal magnetic field but no thermal wind. The linear problem is an important one to examine before solving the nonlinear problem as, whilst it is unable to capture physical effects that result from nonlinear interactions, the linear model is able to tell us about some physical aspects of the system such as the conditions at onset of convection. In (i), we built upon the work of Hathaway *et al.* (1980) by considering  $Pr < 1$ . Our motivation for considering the small  $Pr$  case came from the fact that, in an astrophysical context,  $Pr$  is often tiny, e.g., at the bottom of the convection zone it is believed that  $Pr \sim 10^{-6} - 10^{-7}$  (Ossendrijver (2003)). Computational constraints prevent us from reaching such a small number but, in the linear work, we considered  $Pr$  as small as  $6 \times 10^{-3}$ . The main findings of the linear work were that the tilted rotation vector had more of an effect on convection in the  $y$ - $z$  plane (EW rolls) than it did on convection in the  $x$ - $z$  plane (NS rolls) but that, even at small  $Pr$ , the NS rolls remained the preferred ones. Also, in agreement with Hathaway *et al.* (1980), in (ii), we found that the addition of a thermal wind could switch the preference from NS to EW rolls, as even a small  $T_y$  stabilised

NS rolls and destabilised EW rolls. In (iii), we added a horizontal magnetic field to (i) and found different solutions existed, depending on whether  $Pr$  and  $\zeta$  were greater or less than unity. A larger range of oscillatory solutions were found when  $Pr < 1$  and  $\zeta < 1$ . As already discussed, in the Sun,  $Pr \ll 1$ , but so is  $\zeta$ , with a value of  $\zeta \sim 10^{-4}$  (Ossendrijver (2003)) suggesting that the oscillatory modes are relevant in the Sun. To finish Chapter 3, we considered three-dimensional perturbations to a basic state and found in some cases oblique rolls were actually preferred at onset, but in other cases, the two-dimensional modes were preferred.

In Chapter 4, we added stratification to the plane layer system of Chapter 3 for which the anelastic approximation was more suitable than the Boussinesq approximation. This amounted to adding the effects of a tilted rotation vector to the linear anelastic problem as described in Mizerski & Tobias (2011). The main result was that stratification, when a tilted rotation vector was present, broke the up-down symmetry when three-dimensional modes, or two-dimensional modes in the  $x$ - $z$  plane (NS), were considered. However, the up-down symmetry was not broken when two-dimensional modes in the  $y$ - $z$  plane (EW) were considered. This had the result of the critical modes occurring with a preferred positive or negative critical frequency, so that the preferred modes were left or right travelling waves when the symmetry was broken but, when it was not broken, the preferred modes were standing waves. We proved this to be true regardless of the boundary conditions considered. We found that in the NS case, whether solutions with positive or negative frequency were preferred, depended on  $Ta$ .

In order to investigate the nonlinear effects of convection, in particular the driving of mean flows, we developed a two-dimensional pseudospectral nonlinear numerical code to solve the governing equations. The details of the numerical methods used were given in Chapter 5. We assumed periodicity in the horizontal direction which is inaccurate in reality, but provides an efficient way of solving the local model and therefore allows us to gain insight into otherwise inaccessible problems. In the vertical direction, we used a Chebyshev expansion allowing extra points close to the boundaries and therefore better boundary layer resolution. By setting up the problem as we did, we were able to solve the matrix systems in a relatively efficient way, thanks to a well-developed algorithm of Thual (1986). However, we were still restricted by limited resolution and therefore a restricted parameter regime. Parallelising the code would help with this, allowing us to reach more realistic parameters although truly accurate parameters such as  $Pr \sim 10^{-7}$  are still a way from being achieved by even the most sophisticated models.

The first five chapters set the groundwork for the study of mean flow generation by convection. In Chapters 6-8, we carried out this study. In Chapter 6, we focussed on nonlinear hydrodynamic

convection under the Boussinesq approximation. As  $Ra$  was increased, and thus the degree of nonlinearity in the system increased, the solutions underwent a number of bifurcations en route to chaos. However, for a sufficiently tilted rotation vector and small enough  $Pr$ , further increases in  $Ra$  led to the solutions becoming steady again in what turned out to be large-scale solutions that were efficient at transporting heat by convection. Whilst this is an interesting result in the two-dimensional system, we believe that these large-scale solutions were a result of the two-dimensional nature of the problem we had set up and in a fully three-dimensional simulation such large-scale, steady solutions are unlikely to exist.

By tilting the rotation vector, we found non-trivial correlations which led to systematic mean flows, with a vertical rotation vector such correlations are small on averaging. By taking horizontal spatial and time averages, we derived the mean flow equations which isolated the Reynolds stress (RS) term responsible for the driving of mean flows. A smaller  $Pr$  was found to result in smaller RS terms but the presence of a  $Pr$  factor in the mean flow equations ensures that larger mean flows could result for smaller  $Pr$ . As described before, numerical limitations result in orders of magnitude difference between the size of the Prandtl number used computationally and those occurring in reality. Despite this, knowledge about the fundamental interactions involved in mean flow generation has been gained from this study and presented in this thesis.

In the second part of Chapter 6, we considered the addition of a thermal wind, via a horizontal temperature gradient, as an approximation to latitudinal temperature gradients that occur, for example, in stars. This studying of mean flow generation when a shear flow results from a horizontal temperature gradient in a self-consistent manner is a novel approach which does not appear in the literature. In this case, we found that, the addition of a thermal wind resulted in more energetic flows and even when  $\phi = \frac{\pi}{2}$ , the RS terms still generated systematic mean flows. The thermal wind parameter was shown not to appear explicitly in the mean flow equations but act through an implicit modification of the correlations. The convection either extracted energy from, or put energy into, the thermal wind shear; for smaller  $Pr$ ,  $\phi$  and  $Ta$  it tended to extract energy from the thermal wind shear.

For almost all the cases we studied, when mean flows were driven, the flow in the  $y$ - or meridional direction ( $\bar{v}$ ) was larger than the flow in the  $x$ - or zonal direction ( $\bar{u}$ ). However, for example, in the Sun, meridional circulations are much smaller than the zonal, differential rotation. One reason for this discrepancy comes from the fact we are using a local plane layer model with periodic horizontal boundary conditions and therefore, flow in the  $y$ - direction at one end of the computational box is matched by flow at the other end, resulting in superficially large flows. In

fact, meridional circulation in the solar convection zone is a global circulation and so we cannot expect to capture such behaviour in a local model. More realistic geometries would be needed to rectify this.

We extended the Boussinesq model of mean flow generation to include the effects of stratification and, as in the linear case, employed the anelastic approximation. The results of this work were presented in Chapter 7. We demonstrated that the stratification led to an asymmetry in the vertical structure of the mean flow across the layer; flow from the upper half-plane penetrated further into the lower half-plane as the strength of the stratification was increased. It was also found that the flows were more systematic at lower levels in the layer and with increased stratification.

In Chapter 8, we finished our study with an investigation of the opposing of mean flows by a horizontal magnetic field. We showed that, in general, an increase in magnetic field strength was met with a decrease in the strength of the mean flows. However, the field did act to organise the flow and increase the level to which it was systematic. In addition, the magnetic field could act to change the structure of the mean flows, including their direction. We also showed that, at small  $Q$ , magnetic field was expelled to the boundary, leaving relatively small amounts of field in the bulk. This meant systems with small  $Q$  were still able to drive strong, unopposed flows in the bulk of the layer. Analysis of the terms driving the flows highlighted a balance between the RS and Maxwell stress (MS) terms that was responsible for the size and structure of the mean flows. As the magnetic field strength was increased, magnetic field could no longer be expelled to the boundaries and so the RS terms were opposed by the MS terms, and hence the flows resulted from a balance between the two terms. When the MS terms dominated, only very small mean flows were generated, although they were shown to be very systematic. It was the balance of the RS, MS and viscous terms that dictated the direction of the flow. In particular, if, as  $Q$  was increased, the direction of the mean flow changed, then this was a result of the balance of the terms changing and not that e.g., the RS terms had changed direction.

To investigate if the nonlinear behaviour of the RS and MS terms could be captured by a simpler, linear calculation, we compared the RS and MS terms as calculated from the linear eigenfunctions with the actual RS and MS terms as calculated by the nonlinear code. In general, the agreement was found to be poor and so the linear study does neglect interactions that are crucial in determining the full dynamics of the system. Of course, there is no reason why the linear calculation should be a good approximation. However, there are extensions to this idea, i.e., to see if any of the large-scale dynamics of the system can be captured without performing the full nonlinear calculation. We describe some of these extensions in the next section.

We conclude this section by highlighting what we consider to be the most interesting, new results:

1. In the linear anelastic study of Chapter 4, we showed numerically the existence of a hidden symmetry. Upon breaking the up-down symmetry via a vertical density stratification, and through tilting the rotation vector from the vertical, when considering convection rolls in the plane of the tilted rotation vector (EW rolls), the linear growth rates still occurred as complex conjugate pairs. That is, there was no preference for left or right travelling waves as there was when NS rolls were considered in the asymmetric setup. We proved this result to be true for any natural boundary conditions.
2. In Chapter 6, when considering the interaction of convection with a thermal wind shear, resulting from a horizontal temperature gradient, we found that, whether the convection extracted energy from, or put energy into, the shear, depended upon the parameters of the system. In particular, for small  $Pr$  and  $\phi$ , the convection tended to extract energy from the thermal wind.
3. The investigation of mean flow generation in a stratified layer in Chapter 7, showed that a stratification leads to an asymmetry in the layer. Flows in the lower part of the plane were more systematic than those in the upper part of the plane. Furthermore, in contrast to the Boussinesq case, the flow speed was non-zero at the mid-layer depth, instead, it was zero deeper in the layer.
4. In Chapter 8, an imposed horizontal magnetic field was shown not only to inhibit mean flow generation, but also to change the vertical structure of the flow as the field strength was increased. More specifically, in some cases, the direction of the mean flow was actually reversed.

## 9.2 Further work

As with most studies, there are many natural extensions to the work in this thesis that have yet to be carried out. We have mentioned some of these as we discussed our work in the previous section, however, there are many more. In this section we describe the ones we envisage undertaking next.

As described at the end of the last section, we showed that a linear calculation of the RS terms generally provided a poor agreement with a nonlinear calculation of them. We would like to find a way of capturing the key dynamics without having to solve the full nonlinear equations, as they

are computationally demanding to solve. One reason for the inaccuracy in the linear calculation is that it neglects the interaction between the mean flow and the fluctuations and also the mean field and the fluctuations (amongst others). Therefore, to see if this interaction is responsible for any of the behaviour we see in the full nonlinear system, we could impose the mean flows generated from a nonlinear calculation on the linear equations and carry out a linear analysis, in a similar way to the one performed when a thermal wind produced a basic state flow (as in section 3.5). Building on this idea, another interesting extension would be to perform the quasi-linear calculation which involves splitting the perturbations into a mean and fluctuating part and then neglecting the terms in the equations that are quadratic in the fluctuations. This is a technique employed by Srinivasan & Young (2012), for example. This would allow us to determine whether the interaction between the means and the fluctuations dictate the large-scale features of the system dynamics or whether it is essential to include the interactions between the fluctuations themselves in a full nonlinear calculation.

In Chapter 8, we considered mean flow generation in rotating magnetoconvection. An extension to this work, which we did not have time to carry out, would be to consider what happens when a horizontal temperature gradient is also present, so that a thermal wind is also present. Also, it would be interesting to examine the differences that occur for other field orientations, whilst keeping the field in the horizontal plane. Both of these extensions are already accounted for in the way we set up the problem and in the equations we derived. The former of these extensions involves repeating the simulations for  $T_y \neq 0$  and the latter involves changing the parameter  $\alpha$ .

The work undertaken in this thesis has been predominantly two-dimensional. A natural development then, would be to extend the work to include a third spatial dimension. An easy way to do this would be to assume periodicity in the second horizontal direction, i.e., introduce an  $x$ -direction to be treated as the  $y$ -direction was in this study. This would add a few subtleties to the numerical procedure, but in principle, the same numerical algorithm could be used on the three-dimensional problem. In reality though, the code would need parallelising, so as to be able to solve the equations in a realistic amount of time.

Finally, as we mentioned in Chapter 1, mean flows are thought to be important in the generation of large-scale magnetic fields in the Sun, but their role is not fully understood. Ponty *et al.* (2001), considered the kinematic dynamo problem by driving a flow through shearing the bottom boundary of a plane layer. Further work we would like to pursue, is to extend the work of Ponty *et al.* (2001) by considering the kinematic dynamo problem with the mean flows that emerge self-consistently from the turbulence in our model. Furthermore, extending to three dimensions would

allow us to consider the nonlinear dynamo problem. Recent work (Tobias & Cattaneo (2013)) showing that systematic oscillating magnetic fields can be generated, relies on an imposed shear flow. Again, the model discussed in this thesis, does not require this imposition as a shear flow is driven self-consistently by the convection and so could provide the basis for a dynamo study.

It is clear that the complex nature of physical problems involving the interaction of convection, rotation and magnetic fields is difficult to comprehend fully. It is hoped that by considering a simplified model of the large-scale dynamics, the work in this thesis provides some insight into the underlying physical processes occurring in such problems, and that similar future work will help to explain phenomena such as the large-scale mean flows we observe across the Universe today.

# Bibliography

- ANDERSON, E., BAI, Z., BISCHOF, C., BLACKFORD, S., DEMMEL, J., DONGARRA, J., DU CROZ, J., GREENBAUM, A., HAMMERLING, S., MCKENNEY, A., *et al.* 1999. *LAPACK Users' guide*. Siam.
- ARTER, W. 1983. Nonlinear convection in an imposed horizontal magnetic field. *Geophysical and Astrophysical Fluid Dynamics*, **25**, 259–292.
- AURNOU, J., HEIMPEL, M., & WICHT, J. 2007. The effects of vigorous mixing in a convective model of zonal flow on the ice giants. *Icarus*, **190**, 110–126.
- BATCHELOR, G. K. 1953. The conditions for dynamical similarity of motions of a frictionless perfect-gas atmosphere. *Quarterly Journal of the Royal Meteorological Society*, **79**, 224–235.
- BATCHELOR, G. K. 2000. *An introduction to fluid dynamics*. Cambridge university press.
- BÉNARD, H. 1900. Étude expérimentale des courants de convection dans une nappe liquide. Régime permanent: tourbillons cellulaires. *J. Phys. Theor. Appl.*, **9**, 513–524.
- BÉNARD, H. 1901. Les tourbillons cellulaires dans une nappe liquide.-Méthodes optiques d'observation et d'enregistrement. *J. Phys. Theor. Appl.*, **10**, 254–266.
- BERKOFF, N. A. 2011. *The Anelastic Approximation: Magnetic Buoyancy and Magnetoconvection*. Ph.D. thesis, University of Leeds, UK.
- BERKOFF, N. A., KERSALÉ, E., & TOBIAS, S. M. 2010. Comparison of the anelastic approximation with fully compressible equations for linear magnetoconvection and magnetic buoyancy. *Geophysical and Astrophysical Fluid Dynamics*, **104**, 545–563.
- BOUSSINESQ, J. 1903. *Théorie analytique de la chaleur: mise en harmonie avec la thermodynamique et avec la théorie mécanique de la lumière*. Vol. 2. Gauthier-Villars.
- BOYD, J. 2001. *Chebyshev and Fourier Spectral Methods*. Dover.

- BRACHET, M. E., MEIRON, D. I., ORSZAG, S. A., NICKEL, B. G., MORF, R. H., & FRISCH, U. 1983. Small-scale structure of the Taylor-Green vortex. *Journal of Fluid Mechanics*, **130**, 411–452.
- BRAGINSKY, S. I., & ROBERTS, P. H. 1995. Equations governing convection in earth's core and the geodynamo. *Geophysical and Astrophysical Fluid Dynamics*, **79**, 1–97.
- BROWN, B. P., BROWNING, M. K., BRUN, A. S., MIESCH, M. S., NELSON, N. J., & TOOMRE, J. 2007. Strong dynamo action in rapidly rotating stars. *AIP Conference Proceedings*, **948**, 271–278.
- BROWN, B. P., BROWNING, M. K., BRUN, A. S., MIESCH, M. S., & TOOMRE, J. 2008. Rapidly rotating stars and active regions of convection. *The Astrophysical Journal*, **689**, 1354.
- BROWN, B. P., MIESCH, M. S., BROWNING, M. K., BRUN, A. S., & TOOMRE, J. 2011. Magnetic cycles in a convective dynamo simulation of a young solar-type star. *The Astrophysical Journal*, **731**, 69.
- BROWNING, M. K. 2008. Simulations of dynamo action in fully convective stars. *The Astrophysical Journal*, **676**, 1262.
- BROWNING, M. K., MIESCH, M. S., BRUN, A. S., & TOOMRE, J. 2006. Dynamo action in the solar convection zone and tachocline: pumping and organization of toroidal fields. *The Astrophysical Journal Letters*, **648**, L157.
- BRUMMELL, N. H., & HART, J. E. 1993. High Rayleigh number  $\beta$ -convection. *Geophysical & Astrophysical Fluid Dynamics*, **68**, 85–114.
- BRUMMELL, N. H., HURLBURT, N. E., & TOOMRE, J. 1996. Turbulent compressible convection with rotation. I. Flow structure and evolution. *The Astrophysical Journal*, **473**, 494.
- BRUMMELL, N. H., HURLBURT, N. E., & TOOMRE, J. 1998. Turbulent compressible convection with rotation. II. Mean flows and differential rotation. *The Astrophysical Journal*, **493**, 955.
- BRUN, A. S., & TOOMRE, J. 2002. Turbulent convection under the influence of rotation: sustaining a strong differential rotation. *The Astrophysical Journal*, **570**, 865.
- BRUN, A. S., BROWNING, M. K., & TOOMRE, J. 2005a. Simulations of core convection in rotating A-type stars: magnetic dynamo action. *The Astrophysical Journal*, **629**, 461.

- BRUN, A. S., BROWNING, M. K., & TOOMRE, J. 2005b. Simulations of core convection in rotating A-type stars: magnetic dynamo action. *The Astrophysical Journal*, **629**, 461.
- BUSSE, F. H. 1970. Thermal instabilities in rapidly rotating systems. *Journal of Fluid Mechanics*, **44**, 441–460.
- BUSSE, F. H. 1976. A simple model of convection in the Jovian atmosphere. *Icarus*, **29**, 255–260.
- CANUTO, C., HUSSAINI, M. Y., QUARTERONI, A., & ZANG, T. A. 1993. *Spectral Methods in Fluid Dynamics*. Dover.
- CANUTO, C., HUSSAINI, M. Y., QUARTERONI, A., & ZANG, T. A. 2006. *Spectral Methods: Fundamentals in Single Domains*. Springer.
- CASTAING, B., GUNARATNE, G., HESLOT, F., KADANOFF, L., LIBCHABER, A., THOMAE, S., WU, X-Z., ZALESKI, S., & ZANETTI, G. 1989. Scaling of hard thermal turbulence in Rayleigh-Bénard convection. *Journal of Fluid Mechanics*, **204**, 1–30.
- CHAN, K. L. 2001. Rotating convection in f-planes: Mean flow and Reynolds stress. *The Astrophysical Journal*, **548**, 1102.
- CHANDRASEKHAR, S. 1961. *Hydrodynamic and Hydromagnetic Stability*. Dover.
- CHINI, G. P., & COX, S. M. 2009. Large Rayleigh number thermal convection: Heat flux predictions and strongly nonlinear solutions. *Physics of Fluids*, **21**, 083603.
- CHO, J. Y. K., & POLVANI, L. M. 1996. The morphogenesis of bands and zonal winds in the atmospheres on the giant outer planets. *Science*, **273**, 335–337.
- CHRISTENSEN, U. R. 2001. Zonal flow driven by deep convection in the major planets. *Geophysical research letters*, **28**, 2553–2556.
- CHRISTENSEN, U. R. 2002. Zonal flow driven by strongly supercritical convection in rotating spherical shells. *Journal of Fluid Mechanics*, **470**, 115–133.
- CHRISTENSEN-DALSGAARD, J. 2002. Helioseismology. *Rev. Mod. Phys.*, **74**, 1073–1129.
- CLUNE, T. C., ELLIOTT, J. R., MIESCH, M. S., TOOMRE, J., & GLATZMAIER, G. A. 1999. Computational aspects of a code to study rotating turbulent convection in spherical shells. *Parallel Computing*, **25**, 361–380.
- COLLIER CAMERON, A., DONATI, J-F., & SEMEL, M. 2002. Stellar differential rotation from direct star-spot tracking. *Monthly Notices of the Royal Astronomical Society*, **330**, 699–706.

- DAVIDSON, P. A. 2001. *An introduction to magnetohydrodynamics*. Vol. 25. Cambridge university press.
- DEGROOT, M. H., & SCHERVISH, M. J. 2002. *Probability and statistics*. Addison Wesley.
- DEROSA, M. L. 2001. *Dynamics in the Upper Solar Convection Zone*. Ph.D. thesis, University of Colorado, US.
- DONATI, J-F., & COLLIER CAMERON, A. 1997. Differential rotation and magnetic polarity patterns on AB Doradus-. *Monthly Notices of the Royal Astronomical Society*, **291**, 1–19.
- DONATI, J-F., COLLIER CAMERON, A., HUSSAIN, G. A. J., & SEMEL, M. 1999. Magnetic topology and prominence patterns on AB Doradus. *Monthly Notices of the Royal Astronomical Society*, **302**, 437–456.
- DORMY, E., SOWARD, A. M., JONES, C. A., JAULT, D., & CARDIN, P. 2004. The onset of thermal convection in rotating spherical shells. *Journal of Fluid Mechanics*, **501**, 43–70.
- DOWLING, T. E., & INGERSOLL, A. P. 1989. Jupiter's Great Red Spot as a shallow water system. *Journal of the Atmospheric Sciences*, **46**, 3256–3278.
- DRAZIN, P. G., & REID, W. H. 1981. *Hydrodynamic stability*. Cambridge university press.
- DREW, S. J., JONES, C. A., & ZHANG, K. 1995. Onset of convection in a rapidly rotating compressible fluid spherical shell. *Geophysical & Astrophysical Fluid Dynamics*, **80**, 241–254.
- ELLIOTT, J. R., MIESCH, M. S., & TOOMRE, J. 2000. Turbulent solar convection and its coupling with rotation: The effect of Prandtl number and thermal boundary conditions on the resulting differential rotation. *The Astrophysical Journal*, **533**, 546.
- ELTAYEB, I. A. 1972. Hydromagnetic convection in a rapidly rotating fluid layer. *Proceedings of the Royal Society of London. A. Mathematical and Physical Sciences*, **326**, 229–254.
- ELTAYEB, I. A. 1975. Overstable hydromagnetic convection in a rotating fluid layer. *Journal of Fluid Mechanics*, **71**, 161–179.
- EVONUK, M. 2008. The role of density stratification in generating zonal flow structures in a rotating fluid. *The Astrophysical Journal*, **673**, 1154.
- FAN, Y. 2004. Magnetic fields in the solar convection zone. *Living reviews in solar physics*, **1**, 1.

- FRIGO, M., & JOHNSON, S. G. 2005. The design and implementation of FFTW3. *Proceedings of the IEEE*, **93**, 216–231.
- FRIGO, M., & JOHNSON, S. G. 2012. *FFTW3.3.3 Users Manual*. Massachusetts Institute of Technology.
- GALLOWAY, D. J., & WEISS, N. O. 1981. Convection and magnetic fields in stars. *The Astrophysical Journal*, **243**, 945–953.
- GILLILAND, R. L., BROWN, T. M., CHRISTENSEN-DALSGAARD, J., KJELDEN, H., AERTS, C., APPOURCHAUX, T., BASU, S., BEDDING, T. R., CHAPLIN, W. J., CUNHA, M. S., *et al.* 2010. Kepler asteroseismology program: introduction and first results. *Publications of the Astronomical Society of the Pacific*, **122**, 131–143.
- GLATZMAIER, G. A., EVONUK, M., & ROGERS, T. M. 2009. Differential rotation in giant planets maintained by density-stratified turbulent convection. *Geophysical and Astrophysical Fluid Dynamics*, **103**, 31–51.
- GLATZMAIER, G. A. 2013. *Introduction to Modeling Convection in Planets and Stars: Magnetic Field, Density Stratification, Rotation*. Princeton University Press.
- GLATZMAIER, G. A., & ROBERTS, P. H. 1996. An anelastic evolutionary geodynamo simulation driven by compositional and thermal convection. *Physica D: Nonlinear Phenomena*, **97**, 81–94.
- GOUGH, D. O. 1969. The Anelastic Approximation for Thermal Convection. *Journal of Atmospheric Sciences*, **26**, 448–456.
- GROTE, E., & BUSSE, F. H. 2001. Dynamics of convection and dynamos in rotating spherical fluid shells. *Fluid Dynamics Research*, **28**, 349–368.
- GUCKENHEIMER, J., & HOLMES, P. 1983. *Nonlinear oscillations, dynamical systems, and bifurcations of vector fields*. Vol. 42. New York Springer Verlag.
- GUILLOT, T., STEVENSON, D. J., HUBBARD, W. B., & SAUMON, D. 2004. The interior of Jupiter. *Jupiter: The Planet, Satellites and Magnetosphere*, 35–57.
- HADLEY, G. 1735. Concerning the Cause of the General Trade-Winds: By Geo. Hadley, Esq; FRS. *Philosophical Transactions*, **39**, 58–62.

- HAMMEL, H. B., RAGES, K., LOCKWOOD, G. W., KARKOSCHKA, E., & DE PATER, I. 2001. New measurements of the winds of Uranus. *Icarus*, **153**, 229–235.
- HAMMEL, H. B., DE PATER, I., GIBBARD, S., LOCKWOOD, G. W., & RAGES, K. 2005. Uranus in 2003: Zonal winds, banded structure, and discrete features. *Icarus*, **175**, 534–545.
- HATHAWAY, D. H. 2010. The Solar Cycle. *Living Reviews in Solar Physics*, **7**.
- HATHAWAY, D. H., & SOMERVILLE, R. C. J. 1983. Three-dimensional simulations of convection in layers with tilted rotation vectors. *Journal of Fluid Mechanics*, **126**, 75–89.
- HATHAWAY, D. H., & SOMERVILLE, R. C. J. 1986. Nonlinear interactions between convection, rotation and flows with vertical shear. *J. Fluid Mech*, **164**, 91–105.
- HATHAWAY, D. H., & SOMERVILLE, R. C. J. 1987. Thermal convection in a rotating shear flow. *Geophysical & Astrophysical Fluid Dynamics*, **38**, 43–68.
- HATHAWAY, D. H., TOOMRE, J., & GILMAN, P. A. 1979. Convective Instability when the Temperature Gradient and Rotation Vector are Oblique to Gravity. I. Fluids without Diffusion. *Geophysical and Astrophysical Fluid Dynamics*, **13**, 289–316.
- HATHAWAY, D. H., TOOMRE, J., & GILMAN, P. A. 1980. Convective instability when the temperature gradient and rotation vector are oblique to gravity. II - Real fluids with effects of diffusion. *Geophysical and Astrophysical Fluid Dynamics*, **15**, 7–37.
- HEIMPEL, M., AURNOU, J., & WICHT, J. 2005. Simulation of equatorial and high-latitude jets on Jupiter in a deep convection model. *Nature*, **438**, 193–196.
- HEPWORTH, B. J. 2014. *Nonlinear two-dimensional Rayleigh-Bénard convection*. Ph.D. thesis, University of Leeds, UK.
- HUGHES, D. W., ROSNER, R., & WEISS, N. O. 2007. *The Solar Tachocline*. Cambridge University Press.
- HURLBURT, N. E., MATTHEWS, P. C., & PROCTOR, M. R. E. 1996. Nonlinear Compressible Convection in Oblique Magnetic Fields. *The Astrophysical Journal*, **457**, 933.
- JEFFREYS, H. 1926. The stability of a layer of fluid heated below. *The London, Edinburgh, and Dublin Philosophical Magazine and Journal of Science*, **2**, 833–844.
- JEFFREYS, H. 1928. Some cases of instability in fluid motion. *Proceedings of the Royal Society of London. Series A*, **118**, 195–208.

- JONES, C. A. 2011. Planetary magnetic fields and fluid dynamos. *Annual Review of Fluid Mechanics*, **43**, 583–614.
- JONES, C. A., & KUZANYAN, K. M. 2009. Compressible convection in the deep atmospheres of giant planets. *Icarus*, **204**, 227–238.
- JONES, C. A., ROBERTS, P. H., & GALLOWAY, D. J. 1990. Compressible convection in the presence of rotation and a magnetic field. *Geophysical & Astrophysical Fluid Dynamics*, **53**, 145–182.
- JONES, C. A., SOWARD, A. M., & MUSSA, A. I. 2000. The onset of thermal convection in a rapidly rotating sphere. *Journal of Fluid Mechanics*, **405**, 157–179.
- JONES, C. A., ROTVIG, J., & ABDULRAHMAN, A. 2003. Multiple jets and zonal flow on Jupiter. *Geophysical research letters*, **30**.
- JONES, C. A., KUZANYAN, K. M., & MITCHELL, R. H. 2009. Linear theory of compressible convection in rapidly rotating spherical shells, using the anelastic approximation. *Journal of Fluid Mechanics*, **634**, 291–319.
- JULIEN, K., & KNOBLOCH, E. 1998. Strongly nonlinear convection cells in a rapidly rotating fluid layer: the tilted f-plane. *Journal of Fluid Mechanics*, **360**, 141–178.
- KING, E. M., STELLMACH, S., & AURNOU, J. M. 2012. Heat transfer by rapidly rotating Rayleigh–Bénard convection. *Journal of Fluid Mechanics*, **691**, 568–582.
- KING, ERIC M, STELLMACH, STEPHAN, NOIR, JEROME, HANSEN, ULRICH, & AURNOU, J. M. 2009. Boundary layer control of rotating convection systems. *Nature*, **457**, 301–304.
- LANTZ, S. R. 1992. *Dynamical Behavior of Magnetic Fields in a Stratified, Convecting Fluid Layer*. Ph.D. thesis, Cornell University, Ithaca, USA.
- LANTZ, S. R., & FAN, Y. 1999. Anelastic Magnetohydrodynamic Equations for Modeling Solar and Stellar Convection Zones. *ApJS*, **121**, 247–264.
- LIMAYE, S. S. 1986. Jupiter: New estimates of the mean zonal flow at the cloud level. *Icarus*, **65**, 335–352.
- LIU, Y., & ECKE, R. E. 1997. Heat transport scaling in turbulent Rayleigh–Bénard convection: effects of rotation and Prandtl number. *Physical review letters*, **79**, 2257.

- MALKUS, W. V. R. 1954. Discrete transitions in turbulent convection. *Proceedings of the Royal Society of London. Series A. Mathematical and Physical Sciences*, **225**, 185–195.
- MALKUS, W. V. R., & VERONIS, G. 1958. Finite amplitude cellular convection. *Journal of Fluid Mechanics*, **4**, 225–260.
- MAUNDER, E. W. 1904. Note on the distribution of sun-spots in heliographic latitude, 1874–1902. *Monthly Notices of the Royal Astronomical Society*, **64**, 747–761.
- MIESCH, M. S. 2005. Large-scale dynamics of the convection zone and tachocline. *Living Reviews in Solar Physics*, **2**, 1–139.
- MIESCH, M. S., ELLIOTT, J. R., TOOMRE, J., CLUNE, T. L., GLATZMAIER, G. A., & GILMAN, P. A. 2000. Three-dimensional spherical simulations of solar convection. I. Differential rotation and pattern evolution achieved with laminar and turbulent states. *The Astrophysical Journal*, **532**, 593.
- MIZERSKI, K. A., & TOBIAS, S. M. 2011. The effect of stratification and compressibility on anelastic convection in a rotating plane layer. *Geophysical and Astrophysical Fluid Dynamics*, **105**, 566–585.
- MOORE, D. R., & WEISS, N. O. 1973. Two-dimensional Rayleigh-Benard convection. *Journal of Fluid Mechanics*, **58**, 289–312.
- NATIONAL RESEARCH COUNCIL. 1997. *Space Weather: A Research Perspective*. The National Academies Press.
- NATIONAL RESEARCH COUNCIL. 2008. *Severe Space Weather Events—Understanding Societal and Economic Impacts: A Workshop Report*. The National Academies Press.
- NEWHOUSE, S., RUELLE, D., & TAKENS, F. 1978. Occurrence of strange Axiom A attractors near quasi periodic flows on  $T^m$ ,  $m \geq 3$ . *Communications in Mathematical Physics*, **64**, 35–40.
- OGURA, Y., & PHILLIPS, N. A. 1962. Scale analysis of deep and shallow convection in the atmosphere. *Journal of the atmospheric sciences*, **19**, 173–179.
- ORSZAG, S. A. 1971. On the elimination of aliasing in finite-difference schemes by filtering high-wavenumber components. *Journal of the Atmospheric sciences*, **28**, 1074–1074.

- OSSENDRIJVER, M. 2003. The solar dynamo. *The Astronomy and Astrophysics Review*, **11**, 287–367.
- PÉREZ-HOYOS, S., SÁNCHEZ-LAVEGA, A., FRENCH, R. G., & ROJAS, J. F. 2005. Saturn's cloud structure and temporal evolution from ten years of Hubble Space Telescope images (1994–2003). *Icarus*, **176**, 155–174.
- PEYRET, R. 2002. *Spectral Methods for incompressible viscous flow*. Springer.
- PONTY, Y., GILBERT, A. D., & SOWARD, A. M. 2001. Kinematic dynamo action in large magnetic Reynolds number flows driven by shear and convection. *Journal of Fluid Mechanics*, **435**, 261–287.
- PORCO, C. C., WEST, R. A., MCEWEN, A., DEL GENIO, A. D., INGERSOLL, A. P., THOMAS, P., SQUYRES, S., DONES, L., MURRAY, C. D., JOHNSON, T. V., *et al.* 2003. Cassini imaging of Jupiter's atmosphere, satellites, and rings. *Science*, **299**, 1541–1547.
- PORCO, C. C., BAKER, E., BARBARA, J., BEURLE, K., BRAHIC, A., BURNS, J. A., CHARNOZ, S., COOPER, N., DAWSON, D. D., DEL GENIO, A. D., DENK, T., DONES, L., DYUDINA, U., EVANS, M. W., GIESE, B., GRAZIER, K., HELFENSTEIN, P., INGERSOLL, A. P., JACOBSON, R. A., JOHNSON, T. V., MCEWEN, A., MURRAY, C. D., NEUKUM, G., OWEN, W. M., PERRY, J., ROATSCH, T., SPITALE, J., SQUYRES, S., THOMAS, P., TISCARENO, M., TURTLE, E., VASAVADA, A. R., VEVERKA, J., WAGNER, R., & WEST, R. 2005. Cassini Imaging Science: Initial Results on Saturn's Atmosphere. *Science*, **307**, 1243–1247.
- PRIEST, E. R. 1984. *Solar magnetohydrodynamics*. Dordrecht: Reidel.
- PROCTOR, M. R. E., & WEISS, N. O. 1982. Magnetoconvection. *Reports on Progress in Physics*, **45**, 1317–1379.
- PROCTOR, M. R. E., WEISS, N. O., THOMPSON, S. D., & ROXBURGH, N. T. 2011. Effects of boundary conditions on the onset of convection with tilted magnetic field and rotation vectors. *Geophysical and Astrophysical Fluid Dynamics*, **105**, 82–89.
- RASHID, F., JONES, C. A., & TOBIAS, S. M. 2008. Hydrodynamic instabilities in the solar tachocline. *Astronomy and Astrophysics*, **488**, 819.

- RAYLEIGH, LORD. 1916. On convection currents in a horizontal layer of fluid, when the higher temperature is on the under side. *The London, Edinburgh, and Dublin Philosophical Magazine and Journal of Science*, **32**, 529–546.
- ROBERTS, P. H. 1968. On the thermal instability of a rotating-fluid sphere containing heat sources. *Philosophical Transactions of the Royal Society of London. Series A, Mathematical and Physical Sciences*, **263**, 93–117.
- ROBERTS, P. H., & JONES, C. A. 2000. The onset of magnetoconvection at large Prandtl number in a rotating layer I. Finite magnetic diffusion. *Geophysical and Astrophysical Fluid Dynamics*, **92**, 289–325.
- ROSSBY, H. T. 1969. A study of Bénard convection with and without rotation. *Journal of Fluid Mechanics*, **36**, 309–335.
- ROTVIG, J., & JONES, C. A. 2006. Multiple jets and bursting in the rapidly rotating convecting two-dimensional annulus model with nearly plane-parallel boundaries. *Journal of Fluid Mechanics*, **567**, 117–140.
- ROXBURGH, N. T. 2007. *Anelastic convection in an inclined magnetic field*. Ph.D. thesis, University of Cambridge, UK.
- SAITO, N., & ISHIOKA, K. 2011. Interaction between thermal convection and mean flow in a rotating system with a tilted axis. *Fluid Dynamics Research*, **43**, 065503.
- SCHMIDT, R. J., & MILVERTON, S. W. 1935. On the instability of a fluid when heated from below. *Proceedings of the Royal Society of London. Series A, Mathematical and Physical Sciences*, **152**, 586–594.
- SCHOU, J., ANTIA, H. M., BASU, S., BOGART, R. S., BUSH, R. I., CHITRE, S. M., CHRISTENSEN-DALSGAARD, J., DI MAURO, M. P., DZIEMBOWSKI, W. A., EFF-DARWICH, A., *et al.* 1998. Helioseismic studies of differential rotation in the solar envelope by the solar oscillations investigation using the Michelson Doppler Imager. *The Astrophysical Journal*, **505**, 390.
- SCOTT, R. K., & POLVANI, L. M. 2007. Forced-dissipative shallow-water turbulence on the sphere and the atmospheric circulation of the giant planets. *Journal of the Atmospheric Sciences*, **64**.

- SHAMPINE, L. F., KIERZENKA, J., & REICHELT, M. W. 2000. Solving boundary value problems for ordinary differential equations in MATLAB with bvp4c. *Tutorial notes*.
- SPIEGEL, E. A., & VERONIS, G. 1960. On the Boussinesq approximation for a compressible fluid. *The Astrophysical Journal*, **131**, 442.
- SPIEGEL, E. A., & ZAHN, J-P. 1992. The solar tachocline. *Astronomy and Astrophysics*, **265**, 106–114.
- SRINIVASAN, K., & YOUNG, W. R. 2012. Zonostrophic Instability. *Journal of the atmospheric sciences*, **69**.
- STEVENSON, D. J., & SALPETER, E. E. 1976. Interior models of Jupiter. *Pages 85–112 of: IAU Colloq. 30: Jupiter: Studies of the Interior, Atmosphere, Magnetosphere and Satellites*, vol. 1.
- STIX, M. 2004. *The Sun: An Introduction*. Springer.
- SUKORIANSKY, S., GALPERIN, B., & DIKOVSKAYA, N. 2002. Universal spectrum of two-dimensional turbulence on a rotating sphere and some basic features of atmospheric circulation on giant planets. *Physical review letters*, **89**, 124501.
- TEED, R., JONES, C., & HOLLERBACH, R. 2010. Rapidly rotating plane layer convection with zonal flow. *Geophysical and Astrophysical Fluid Dynamics*, **104**, 457–480.
- TEED, R. J., JONES, C. A., & HOLLERBACH, R. 2012. On the necessary conditions for bursts of convection within the rapidly rotating cylindrical annulus. *Physics of Fluids*, **24**, 066604.
- THOMAS, J. H., & WEISS, N. O. 2008. *Sunspots and starspots*. Vol. 46. Cambridge University Press Cambridge.
- THUAL, O. 1986. *Transition vers la turbulence dans des systemes dynamiques apparentes a la convection*. Ph.D. thesis, Univresit de Nice-Sophia Antipolis.
- TOBIAS, S. M. 2002. The solar dynamo. *Philosophical Transactions of the Royal Society of London. Series A: Mathematical, Physical and Engineering Sciences*, **360**, 2741–2756.
- TOBIAS, S. M., & CATTANEO, F. 2013. Shear-driven dynamo waves at high magnetic Reynolds number. *Nature*, **497**, 463–465.
- TOBIAS, S. M., & WEISS, N. O. 2007. The solar dynamo and the tachocline. *Page 319 of: The solar tachocline*, vol. 1. Cambridge University Press Cambridge.

- TOOMRE, J., ZAHN, J-P., LATOUR, J., & SPIEGEL, E. A. 1976. Stellar convection theory. II- Single-mode study of the second convection zone in an A-type star. *The Astrophysical Journal*, **207**, 545–563.
- TREFETHEN, L. N. 2000. *Spectral methods in MATLAB*. Vol. 10. Siam.
- VALLIS, G. K. 2006. *Atmospheric and oceanic fluid dynamics: fundamentals and large-scale circulation*. Cambridge University Press.
- VASAVADA, A. R., & SHOWMAN, A. P. 2005. Jovian atmospheric dynamics: An update after Galileo and Cassini. *Reports on Progress in Physics*, **68**, 1935.
- VERONIS, G. 1959. Cellular convection with finite amplitude in a rotating fluid. *Journal of Fluid Mechanics*, **5**, 401–435.
- VERONIS, G. 1966. Large-amplitude Bénard convection. *Journal of Fluid Mechanics*, **26**, 49–68.
- VERONIS, G. 1968. Rapidly rotating plane layer convection with zonal flow. *Geophysical and Astrophysical Fluid Dynamics*, **104**, 457–480.
- VINCENT, A. P., & YUEN, D. A. 1999. Plumes and waves in two-dimensional turbulent thermal convection. *Physical Review E*, **60**, 2957.
- VINCENT, A. P., & YUEN, D. A. 2000. Transition to turbulent thermal convection beyond  $Ra = 10^{10}$  detected in numerical simulations. *Physical Review E*, **61**, 5241.
- WARD, F. 1966. Determination of the Solar-Rotation Rate from the Motion of Identifiable Features. *The Astrophysical Journal*, **145**, 416.
- WARNEFORD, E. S., & DELLAR, P. J. 2014. Thermal shallow water models of geostrophic turbulence in Jovian atmospheres. *Physics of Fluids*, **26**, 016603.
- WILLIAMS, D. R. 2004. Sun Fact Sheet. *NSSDC Planetary Fact Sheets, NASA Goddard*, Available from URL: <http://nssdc.gsfc.nasa.gov/planetary/factsheet/sunfact.html>.
- WILLIAMS, D. R. 2007. Jupiter Fact Sheet. *NSSDC Planetary Fact Sheets, NASA Goddard*, Available from URL: <http://nssdc.gsfc.nasa.gov/planetary/factsheet/jupiterfact.html>.
- WILLIAMS, G. P. 1979. Planetary circulations: 2. The Jovian quasi-geostrophic regime. *Journal of the Atmospheric Sciences*, **36**, 932–969.
- ZHANG, K. 1992. Spiralling columnar convection in rapidly rotating spherical fluid shells. *Journal of Fluid Mechanics*, **236**, 535–556.